Experimental and Computational Investigation of the Performance of the Braced Ductile Shear Panel

A DISSERTATION

SUBMITTED TO THE FACULTY OF THE

UNIVERSITY OF MINNESOTA

BY

Davide Giannuzzi

IN PARTIAL FULFILLMENT OF THE REQUIREMENTS

FOR THE DEGREE OF

DOCTOR OF PHILOSOPHY

Roberto Ballarini

June, 2016

Acknowledgements

I would like to express my sincere gratitude to my adviser Professor Roberto Ballarini, for giving me the opportunity to work with him on this research project, and for the support he provided me during these five years. Furthermore, he always believed in my potentialities, and for this reason alone I can consider myself fortunate to have had him as my academic adviser. Thanks to Professors Arturo Schultz, Henryk Stolarski, and Ellad Tadmor, for serving on my committee. I am also grateful to Professor Jia-Liang Le, for his help in supporting my studies during the last year. I would also like to acknowledge Dr. Arthur Huckelbridge for providing valuable guidance during the early stages of this research. I greatly appreciate the assistance of Paul Bergson during the development and execution of the experimental portion of this work.

I would also like to thank the friends and fellow graduate students at the University of Minnesota, who I had the fortune to meet and with whom I shared many happy moments. Special thanks go to Bing Xue, for being a fantastic office mate, always eager to help.

As I step into a new chapter in my life, I feel blessed for the amazing people I have met during these years in Minnesota and who became some of my closest friends: you are my family away from home. I am infinitely grateful to my girlfriend, for sharing with me the ups and downs of these last years, for her love and patience, and for always being able to make any day a bit better.

Lastly, I would not have been able to do this without the love and unconditioned support of my parents. Their help during my years as a graduate student, has done more for me than what I could ever be able to express in words, *grazie.*

Abstract

This thesis presents the investigation of the performance of a new ductile seismic resistant steel bracing system, called the Braced Ductile Shear Panel (BDSP), which can be used to provide the necessary lateral strength to steel braced frame buildings in high seismic areas. The proposed system is comprised of a sacrificial rectangular shear panel, connected to the frame by four short concentric braces. The BDSP is envisioned as an economical alternative to more expensive bracing systems, while still providing increased design control and similar performance levels. First, the development of the BDSP concept is illustrated, and equations are developed to predict the elastic and plastic response of the shear panel based on its geometry by means of a reduced model, and a numerical parametric study. To validate the results of the computational study, an experimental program is conducted on a half-scale steel frame braced with a BDSP. Ten shear panel specimens with varying geometry are tested under quasi-static cyclic lateral loading. The data from this program is then used to verify the accuracy of the results obtained from a detailed three-dimensional finite element model, which is later used to compute the response of the BDSP systems. Finally, the design of the BDSP system for a sample 12-story office building is presented. The design is then evaluated by conducting nonlinear dynamic analyses, following the methodology in FEMA P-695. This work shows that the Braced Ductile Shear Panel can achieve high level of ductility, and it can, in fact, represent a viable, economical alternative to provide a building with the necessary lateral strength.

Table of Contents

List of Tables

List of Figures

Chapter 1
Introduction

1.1 Background

Structures in areas associated with high seismic activity are required to resist strong lateral forces resulting from earthquake triggered ground accelerations. In a typical scenario a building – or any other structure rising above ground – must resist smaller, frequent earthquakes as well as large, less frequent earthquake. The structure must have not only enough strength and stiffness to resist frequent events with little or no damage, but also adequate ductility –or another form of damping– to economically and efficiently ensure stability and safety during major events. In a system that undergoes large inelastic deformations, the energy dissipation provided by ductile mechanisms dampens the dynamic response of the structure, effectively limiting structural demands. The next-generation seismic lateral force resisting systems (LFRS) should require performance beyond ensuring life-safety and collapse prevention. They should also protect the primary gravity load resisting system by limiting damage to easily replaceable elements so that the structure can be repaired following a major earthquake and remain operational following a moderate earthquake. Limiting or preventing damage to its non-structural elements and equipment is also desirable from an operational and monetary standpoint. In today's steel buildings the most frequently used steel structural systems are the moment resisting frame (MRF) and the concentrically braced frame (CBF).

MRFs are flexible, economical structures that get their ductility capacity from beam flexure and panel zone yielding. The relatively large flexibility of these systems results in larger inter-story

drifts, which could lead to severe P-δ effects. Yielding of the beams and the column panel zones in MRFs cause extensive yielding and damage to the primary gravity-load system, and make replacement of damaged area expensive and complicated (Gupta and Krawinkler 1999). CBFs are an attractive alternative to MRFs since they allow increasing the stiffness of the structure, therefore reducing inter-story and total drifts. However, the increase in stiffness – required to control drift – results in increased base shear when the structure is subject to seismic ground motion, thus requiring the members to be designed for higher loads. The larger demand in terms of capacity leads to a cost increase which quickly becomes uneconomical for bigger, taller structures. A solution to the problem of balancing stiffness and limiting force demands on the members, is offered by dissipative bracing systems.

1.2 Existing Dissipative Braced Frames Systems

A variety of energy dissipating bracing systems are available and have been implemented worldwide for seismic protection of buildings. Systems that rely on plastic energy dissipation are commonly used in steel frames. In these systems, energy is dissipated when bracing members or specially designed devices reach their yield point and deform plastically. Some of these systems are currently included in the *Seismic Provisions for Structural Steel Buildings* (AISC 2010a) and their behavior and performance are summarized below.

Two other dissipative systems which are not part of the current seismic specification are included in this review because of their relevance and similarities with this research, the Added Damping And Stiffness (ADAS) system and the Japanese shear panel system.

1.2.1 Ordinary and Special Concentrically Braced Frames

Ordinary Concentrically Braced Frames (OCBFs) and Special concentrically braced frames (SCBFs) are a stiff, strong and economical alternative for bracing a steel frame. However their ductility and energy dissipation capacities are limited by the buckling of the braces in compression, even when installed in pair with a tension brace (Figure 1-1.a-b). In order to achieve better ductility,

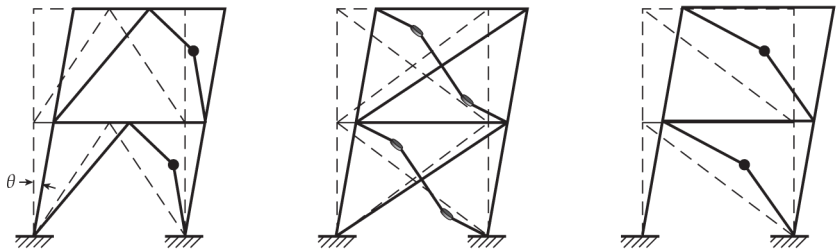

Figure 1-1: Ordinary and Special Concentrically Braced Frames configurations and yielding mechanisms (a) V-bracing; (b) X-bracing; (c) Diagonal Bracing

SCBFs can be used in place of OCBF. SCBFs have more stringent detailing requirements aimed at increasing their ductility capacity, like ensuring that gussets plates are ductile enough to allow for rotation at the braces ends following compression buckling without fracturing. However, the behavior of SCBFs is still affected by the poor performance of the compression member. In fact, after the compression brace buckles, the system needs to undergo a large drift in the opposite direction to cancel the P-δ effects on the brace and recover the full axial tension stiffness of the element (Lumpkin et al. 2012).

1.2.2 Eccentrically Braced Frames

Eccentrically Braced Frames (EBFs) are characterized by a stable hysteretic response under cyclic loading and provide a good amount of energy dissipation (Hjelmstad and Popov 1983). This category of dissipative systems relies on yielding of a segment of the floor beam (link) for energy dissipation (Figure 1-2). The nonlinear response of the system depends on the ratio *e/L* where *e* is

the length of the dissipative element and *L* is the width of the braced bay. For low values of *e/L* the link yields primarily in shear and the ductility of the system is larger. However, a low value of the link to beam length ratio results in larger drifts of the frame. Vice versa: longer links limit the drift index but exhibit worse ductile behavior due to a mainly flexural yielding mode.

The major drawback of these systems is that a strong seismic loading would yield and significantly deform the link – which is part of the primary gravity load system – and likely result in significant damage to the floor system. Since the link is part of the gravity load system, replacement of the link portion of the beam is complicated, making the replacement process expensive.

Moreover, the design and detailing of the link is also complicated by the kinematics of the dissipative mechanism, which induces both shear and flexural forces into the short element (Hjelmstad and Popov 1984).

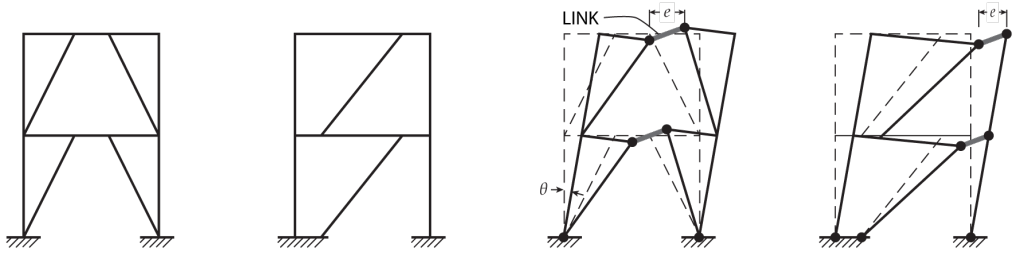

Figure 1-2: Eccentrically Braced Frames.
(a) Chevron and diagonal configurations; (b) Plastic mechanisms

1.2.3 Special Plate Shear Walls

In a Special Plate Shear Wall (SPSW) system a steel sheet is used as an infill to brace steel frames against lateral loading. The steel sheet is usually attached to the boundary beams and columns with bolted connection for the entire length of the members. SPSWs provide significant inelastic deformation capacity primarily through web plate yielding and as plastic-hinge formation in the ends of horizontal boundary elements (Figure 1-3).

Under cyclic loading however, the drift-force response of the system exhibits pinching due to the buckling of the compressed diagonals in the steel web. Once this happens, the frame undergoes a large drift before developing the tension field action in the buckled plate and regain stiffness and energy dissipation behavior.

Another disadvantage of the SPSW is its interaction with the boundary elements. The steel web transfers several forces and moments to the surrounding columns and beams when subjected to lateral loading. Local buckling of the column can occur if not properly detailed, and the relatively large drifts required to develop the tension field action often lead to formation of plastic hinges in the beams, which are still part of the gravity load frame.

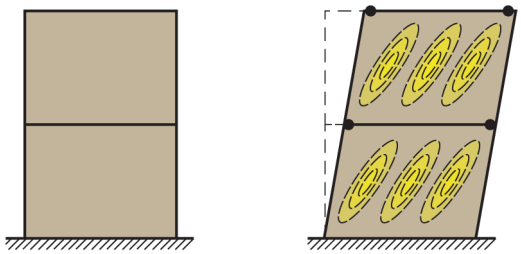

Figure 1-3: Steel Plate Shear Wall.
(a) Braced frame; (b) Plastic mechanism and tension field action

1.2.4 Buckling-Restrained Braced Frames

Buckling-Restrained Braced Frames (BRBF) systems have been used in recent years as primary lateral force resisting elements in both new construction and seismic retrofit projects. They consists of a steel core that provides the resisting force and will yield in both tension and compression under lateral loading and a steel casing filled with concrete which prevents the core from buckling, thus allowing the core to behave symmetrically in tension and compression (Figure 1-4).

BRBFs were originally developed in Japan after several decades of research, and have become a popular structural system worldwide since the late 1990's. Their first application in the United

States was in 2000 at University of California-Davis. BRBFs overcome much of the shortcomings of SCBFs, delivering a ductile and stable hysteretic behavior (Merritt et al. 2003). While they allow for some economy by providing an increased ductility when compared to SCBFs, buckling-restrained braces are costly because they are still a proprietary design produced in the United States by few manufacturers. Additionally, the design parameters to control the systems lateral stiffness and strength (cross-sectional area and brace length) are somewhat constrained by configurations available at the manufacturer.

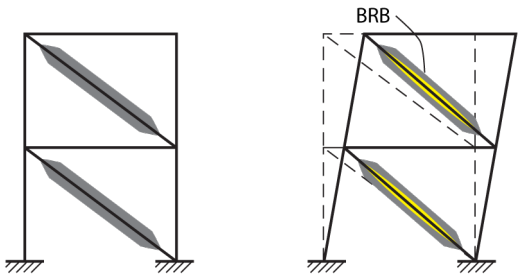

Figure 1-4: Buckling-Restrained Braced Frame
(a) undeformed configuration; (b) plastic mechanism

1.2.5 Other Systems

Shear panel systems such as those illustrated in Figure 1-5 (different configurations are possible) have been used for high-rise buildings in Japan since the 1990's. In many cases, shear panel systems in Japan use low-yield-point-steel (Saeki et al. 1998) to ensure that plastic deformation is strictly contained within the shear panels, and the systems are designed to supplement the underlying moment resisting frame. Among currently available systems and systems studied in the past, the shear panel system most closely resembles the system object of this study. However, this Japanese system has not been adopted widely in the US practice, perhaps due to the small energy dissipation capacity or the substantial cost premium.

Past research has also investigated various steel devices that undergo yielding in different ways and can be designed to provide either supplemental passive energy dissipation or the primary lateral force resistance. The added damping and stiffness (ADAS) concept (Bergman and Goel 1987; Whittaker et al. 1991) consists of X-shaped steel plates that undergo flexural yielding in double curvature (Figure 1-6). The similar triangular added damping and stiffness device (TADAS) consists of triangular shaped steel plates that also undergo flexural yielding but in single curvature (Tsai et al. 1993). Both systems are often designed attached to the underside of a beam with a vertical slotted hole to prevent axial forces from developing on the plates from gravity loads. Such devices have been shown to provide very ductile hysteretic behavior if proper fabrication

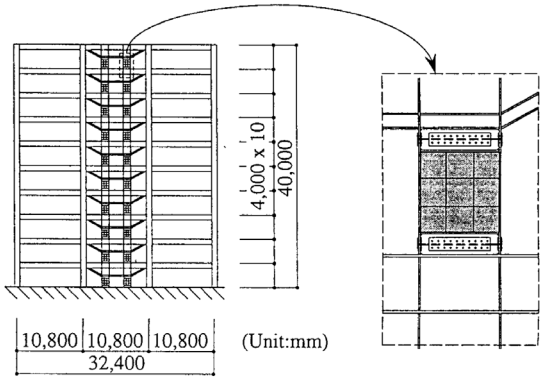

Figure 1-5: Low-yield shear panel.
(a) Prototype building including shear panels; (b) Shear panel detail (Nakashima 1995)

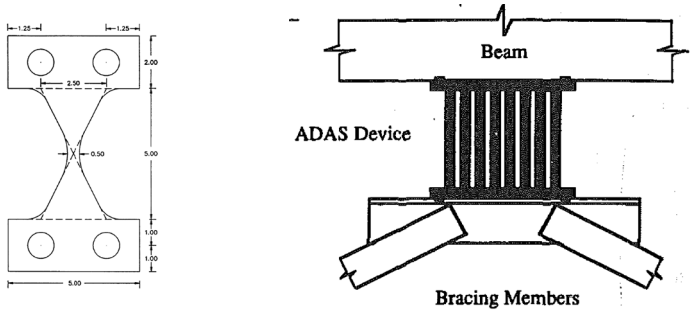

Figure 1-6: ADAS Device.
(a) ADAS X-shaped element; (b) Device installation example (Whittaker et al. 1991)

tolerances and weld details are achieved. These devices require out-of-plane bracing at the plate end that is not connected to the beam.

1.3 Objective of Research

The previous paragraph outlined the most commonly used dissipative lateral force resisting systems along with their strength and drawbacks. While these systems have been developed to satisfy a life safety performance objective, they likely would be difficult to design to achieve desirable seismic performance throughout the building while providing replaceable ductile components. Economic seismic steel lateral force resisting systems capable of reduced drift, controllable force capacity, stable hysteretic energy dissipation, and replaceable structural details are needed for the next-generation seismic systems. The objective of this research is to investigate a new dissipative framing system for steel buildings that can provide adequate stiffness and ductility and at the same time protect the gravity-load frame from damage. The system would also limit plastic deformations – and thus damage – to an easily replaceable framing member.

The proposed system utilizes a rectangular panel connected to the frame by four short concentric braces as a sacrificial dissipative element. A conceptual sketch of the system is shown in Figure 1-7. The panel is designed to undergo shear deformations when the frame is subject to inter-story drift and to yield in shear when the lateral force reaches the design value. In this regard this system is similar to the Japanese shear panel previously discussed, but differs from it because of the position of the panel inside the frame which is now concentrically placed in the center of the frame instead of being attached at the beam midpoint. This configuration prevents bending moments from developing in the device before yielding and extremely reduces the entity of secondary bending moments once the web yields and a plastic mechanism is activated. The length of the four connecting braces is also reduced in this system, thus allowing for use of lighter steel section given the reduction in slenderness with respect to buckling of these members.

The concentrically braced configuration also allows the complete development of the plastic capacity of the panel without the need for out-of-plane lateral bracing on the panel. The braces in tension can in fact easily provide enough restraint against lateral buckling of the panel.

When isolated from the rest of the system, the rectangular shear panel can be seen as acting as a smaller, more compact SPSW. On the other hand, the slenderness of the web plate in the proposed system is significantly smaller when compared to the web of a full sized steel plate shear wall (either stiffened or unstiffened), which results in a more stable hysteretic behavior and better mitigation of undesirable post-buckling effects such as pinching of the drift-force response.

The rectangular panel at the core of the proposed system is envisioned as being replaceable, therefore acting as a structural fuse. To achieve this, the panel is attached to the four braces by means of bolted connections.

Since this system can be seen as a hybrid of a buckling-restrained braced frame and a steel shear panel system, it is referred to hereafter as the Braced Ductile Shear Panel (BDSP) system.

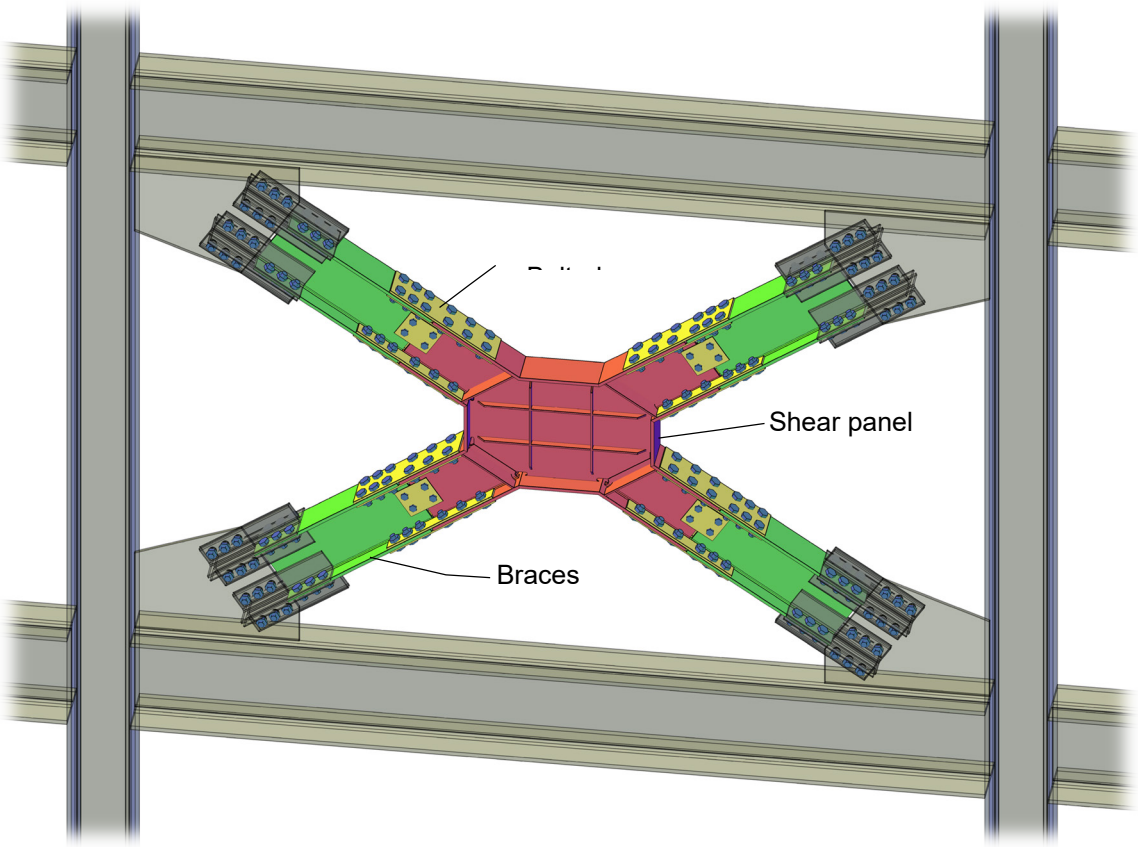

Figure 1-7: Concept of the proposed system

1.4 Dissertation Overview

In the next chapter, a selection of previous works on shear panels and shear links is presented, with an emphasis on literature that provided most useful for the design and prediction of the BDSP system. Chapter 3 will introduce a reduced, simplified model used to design the experimental specimen and summarize the results of parametric finite element analyses carried out during the conceptual design phase. Chapter 4 illustrates the experimental program; it includes a full description of the process used to design the specimens and details about the instrumentation and loading protocol. Chapter 5 lists the results of the tests in terms of total force and lateral drift, and presents a discussion of the initiation and evolution of yielding and damage in the specimens along with pictures of the tested specimens. The data obtained from the experimental program is analyzed in Chapter 6. The data is compared to the models previously introduced, and new expressions are

proposed for predicting the stiffness, ultimate strength and energy dissipation capacity of the shear panels. A comparison between the results from the experimental investigation and the results obtained from finite element analyses is presented in Chapter 7. Finally, Chapter 8 provides an example of a viable design process, and system level performance of the proposed system. The performance is evaluated following the methodology given in FEMA P-695.

Chapter 2
Literature Review

2.1 Introduction

A large number of studies have been conducted in the past on various steel devices designed to dissipate energy in structures by plastic deformations. Most of these studies concern Eccentrically Braced Frames links, Added Damping And Stiffness devices and their triangular iterations (ADAS and TADAS), and in more recent years Steel Plate Shear Walls and Buckling Restrained Braces. Some of these studies, mostly from Japanese authors, have explored the performance as energy dissipation elements of square and rectangular panels, connected in several ways to the gravity frame. However, most of these studies only explored the behavior of said devices with numerical simulations, and when experimental tests were performed, they were conducted on reduced subassemblies, consisting of the sole device and the loading elements. These works showed that well designed steel panels can achieve good ductility and energy dissipation when loaded in shear, and are therefore suitable for use as dampers for seismic applications. The most significant data from past research concerns the geometrical and detailing requirements for satisfactory performance of the devices. The following review presents a selection of works from the vast amount of literature on the topic of panels loaded in shear, intended to highlight the key results that have been used in the development of the present work, while also identifying the limits of the experimental tests performed in the past and the difference with the BDSP system object of the present study.

2.2 Nakashima (1995)

Nakashima (1995) performed tests on six shear panels made of low-yield steel, with variable loading conditions and width-to-thickness ratio. The panels are envisioned by the author to be used

in a pillar-like configuration with the bottom side of the panel attached directly to the floor girder and the top side connected to the upper story with more structural members, as shown in Figure 2-1(a). As summarized in Table 2-1, three panels were tested under monotonic loading, while three identical panels were tested under cyclic loading. The geometry of the specimen is shown in Figure 2-1(b) and consists of a web made of low-yield steel and four flanges that surround the shear panel. The clear dimensions of the panel are 344 mm x 344 mm, and the thickness is one of 6, 9 or 12 mm. The vertical and horizontal flanges are 19 mm and 28 mm in thickness, respectively, and 200 mm wide. The tests were performed on the shear panel directly attached to the loading and reaction frames as shown in Figure 2-1(c). The loading protocol used during the test defined as shear angle in the panel is shown in Figure 2-1(d). The experiments showed that the panel were able to dissipate ample amount of energy. In particular, because of the significant strain hardening behavior of low-yield steel, the amount of energy dissipated was 1.5 to 2.0 times the dissipated energy predicted by an elastic-perfectly plastic stress strain model. Plate buckling under cyclic loading was observed in the two most slender specimens (LP06CY and LP09CY) while no buckling was observed in the LP12CY specimen. However, pinching of the shear force-deformation curve was observed only for the panel having width-to-thickness ratio of 58, and no pinching was observed for the other two panels up to a drift angle of 0.0588. Figure 2-2 shows the normalized shear force versus drift angle curves for the cyclically loaded tests. The shear force H is calculated by the author as the difference between the measured total lateral force and the flanges contribution, and is normalized by the value yielding shear force Hy obtained multiplying the panel web cross-sectional area by the yielding shear stress.

Nominal thickness of Shear Panel	6 mm	9 mm	12 mm
Width-to-thickness ratio	58.0	37.4	28.2
Monotonic loading test	LP06MN	LP09MN	LP12MN
Repeated loading test	LP06CY	LP09CY	LP12CY

Table 2-1: Shear panel specimens table (Nakashima 1995)

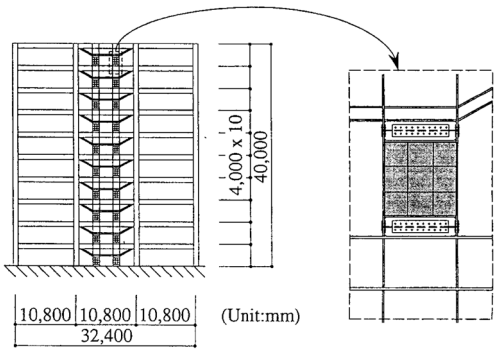

(a)

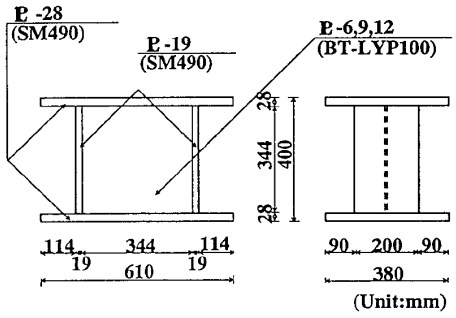

(b)

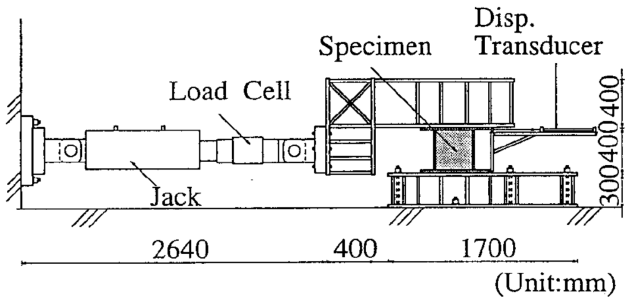

(c)

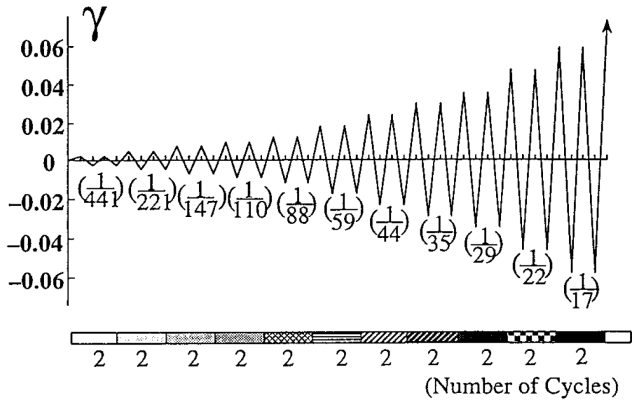

(d)

Figure 2-1: Nakashima tests
(a) Specimens geometry; (b) Test setup (Nakashima 1995)

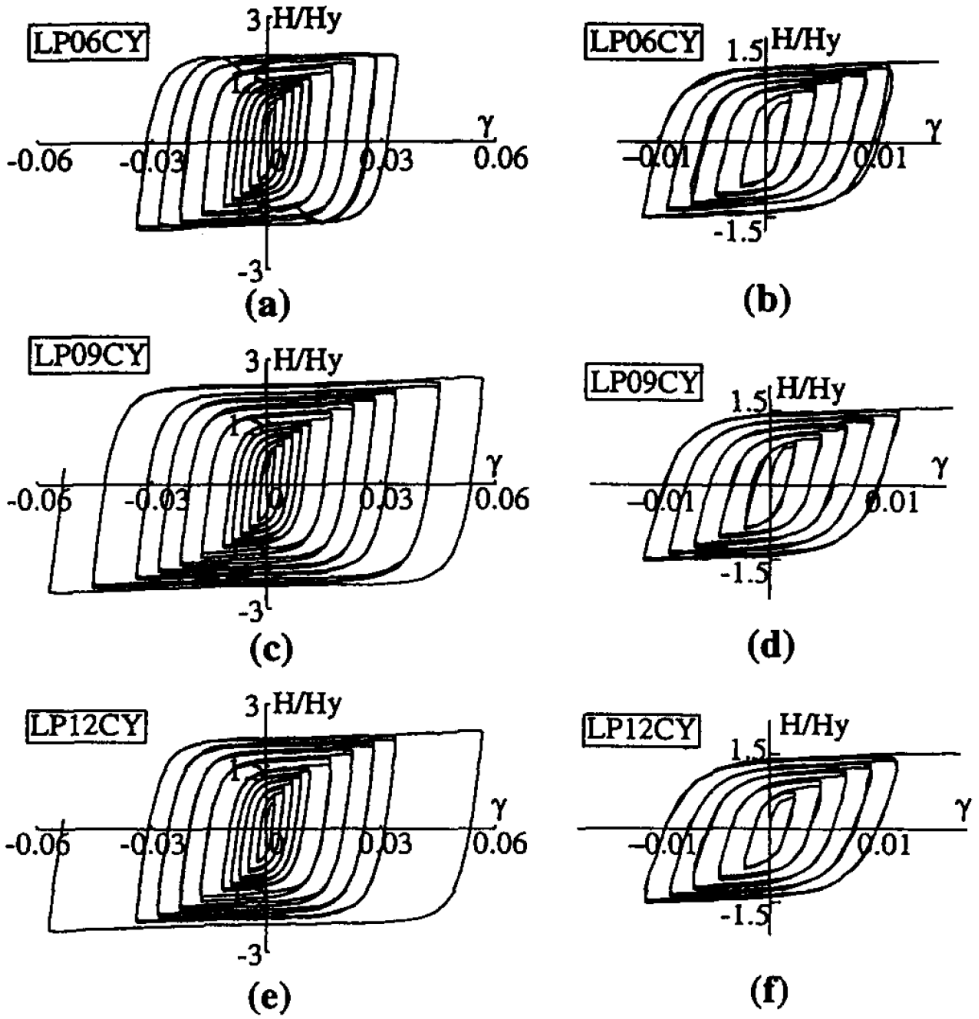

Figure 2-2: Shear Force versus Drift Angle Obtained from Cyclic Tests (Nakashima 1995) (a) LP06CY; (b) LP12CY (close-up); (c) LP09CY; (d) LP09CY (close-up); (e) LP12CY; (f) LP12CY (close-up)

2.3 Rai and Wallace (1998)

Rai and Wallace (1998) investigated a beam-like shear link made of aluminum for earthquake resistant structures. The authors chose aluminum for its low yield stress, which in turn allows for thicker shear webs more resistant to plate buckling. The proposed device is developed to be used in a chevron configuration, positioned between the underside of a steel girder and the top of the chevron braces, see Figure 2-3(a). The authors performed tests on several 1:4 scaled down

specimens made of two different aluminum alloys (0.2% yield stress equal to 35MPa and 53Mpa). The scaling factor resulted in relatively small specimens, 152 mm long and 45 mm deep. Both stiffened and unstiffened specimens were tested, a schematic of a typical specimen and its dimensions are shown in Figure 2-3(b). The tests were performed on the link alone at variable cycling frequencies of 0.01, 5, 10 and 17Hz. All the specimens exhibited good energy dissipation capacity and stable force-displacement response up to buckling. After buckling the stiffness of the panel started deteriorating. The authors found the energy dissipation behavior of the devices to be insensitive to loading frequencies in the considered range; the experimental shear stress-strain curves for different loading frequencies are shown in Figure 2-3(c). The shear force-deformation relationship was also similar for the two aluminum alloys used. The authors remark that for this type of device bolt-slip on the connection was proven critical given the smoothness of the aluminum surfaces when compared to steel, and that special coatings or surface preparations should be mandated. Differential thermal expansion and contraction of the steel and aluminum parts should also be taken into account when designing the pretension force in the fasteners. The problem of galvanic corrosion due to the steel-aluminum coupling is also raised by the writers.

Table 2-2: Aluminum shear link specimens (Rai and Wallace 1998)

Test feature	Specimen number	Web material	Geometric dimensions (mm)	Stiffener details	Cycling frequency
Material selection	1	3003-O	$d_w = 45.2$	No Stiffener	Pseudo-static
	2	3003-O	$t_w = 1.6$	End stiffener only	Pseudo-static
	3	3003-O	$b_f = 31.8$	End + intermediate stif.	Pseudo-static
	5	6061-O	$t_f = 3.2$	End stiffener only	Pseudo-static
	6	6061-O	$l = 152.4$	End + intermediate stif.	Pseudo-static
Strain rate effects	7	3003-O	$d_w = 45.2$	End stiffener only	5 Hz
	8	3003-O	$t_w = 1.6$		5 Hz
	9	3003-O	$b_f = 63.5$		5 Hz
	10	3003-O			10 Hz
	11	3003-O	$t_f = 3.2$		10 Hz
	12	3003-O	$l = 152.4$		17 Hz
	13	3003-O			0.01 Hz
	14	3003-O			17 Hz

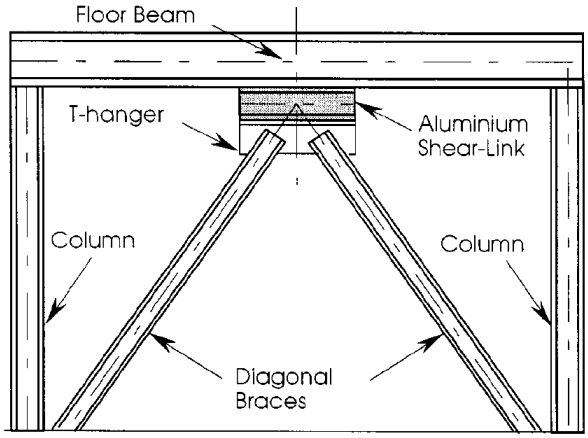

(a)

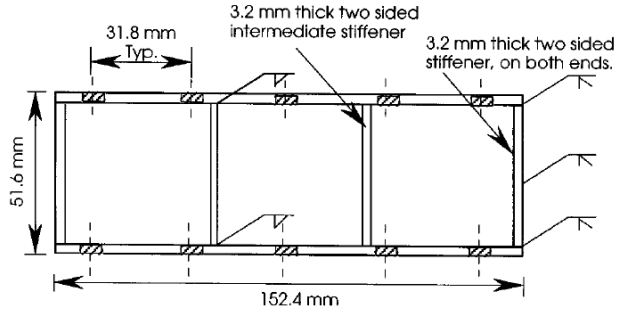

(b)

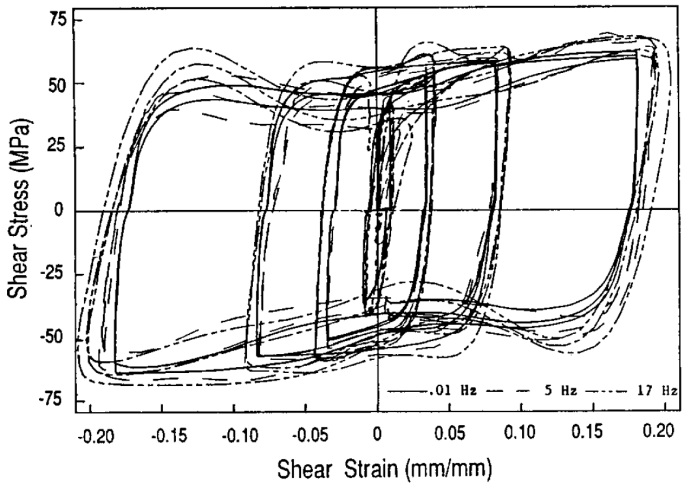

(c)

Figure 2-3: Aluminum shear links (Rai and Wallace 1998)
(a) Proposed system configuration; (b) Typical test specimen; (c) Strain-stress curves for different loading frequencies from tests

2.4 Tanaka and Sasaki (2000)

Tanaka and Sasaki (2000) performed an extensive experimental investigation on full-scale shear panels made of ultra-low-yield steel (yield stress 100MPa or 15ksi). The authors tested square and rectangular panels, both stiffened and unstiffened, with varying width-to-thickness ratio. A rectangular specimen with stiffeners is shown in Figure 2-4(a). A total of sixteen specimens were tested, their properties are listed in Table 2-3. Three different testing apparatuses were used to statically load the specimens as shown Figure 2-4(c). Type A and B have the panel specimens directly bolted to rigid loading blocks. In the Type C setup, the panels are connected to two elastic supporting elements instead, similarly to the way the authors propose they would be installed in a building, that is in the pillar-type configuration shown in Figure 2-4(b). The tests showed a stable response of all the specimens under cyclic loading, with moderate pinching of the most slender panels. However, all the specimens provided large energy dissipation before reaching failure. Failure mode of the panels was dependent on the width-to-thickness ratio of the specimens: fracture initiated in the middle of the panel for slender specimens (or subpanel for stiffened specimens) due to plate buckling and reversed out-of-plane displacements under cyclic loading, while in panels with lower width-to-thickness ratio fracture initiated at the toe of the boundary weld.

Table 2-3: Specimens table (Tanaka and Sasaki 2000)

Specimen	d (mm)	H (mm)	t_w (mm)	b_f (mm)	t_f (mm)	t_r (mm)	h_r (mm)	d/t_w $[d/t_w]_{eq}$	Type of loading
L1SR020	167	164	8.6	100	8.5	--	--	19.3	A
L1SR040	249	249	6	101	8.8	--	--	41.2	A
L1SR050	249	248	4.9	100	8.8	--	--	50.7	A
L1SR060	249	249	4	100	8.8	--	--	62.2	A
L2SR033	300	300	9	101	11.9	--	--	33.1	B
L2SR050	300	299	6.2	101	12	--	--	48	B
L3RR085	668	384	5.1	175	16	--	--	[85.8]	C
L3RR185	668	384	5.1	175	16	6	50	[63.7]	C
L3RR285-1	668	384	5.1	175	16	6	50	[48.3]	C
L3RR385	668	384	5.1	175	16	6	50	[43.0]	C
L3RR285-2	668	384	5.1	175	16	6	50	[48.3]	C
L3RR285-3	668	384	5.1	175	16	6	50	[48.3]	C
L4RR385-1	668	400	6	175	16	6	50	[37.2]	B
L4RR385-2	668	400	6	175	16	6	50	[37.2]	B
L4RR385-3	668	400	6	175	16	6	50	[37.2]	B
L4RR385-4	668	400	6	175	16	6	50	[37.2]	B

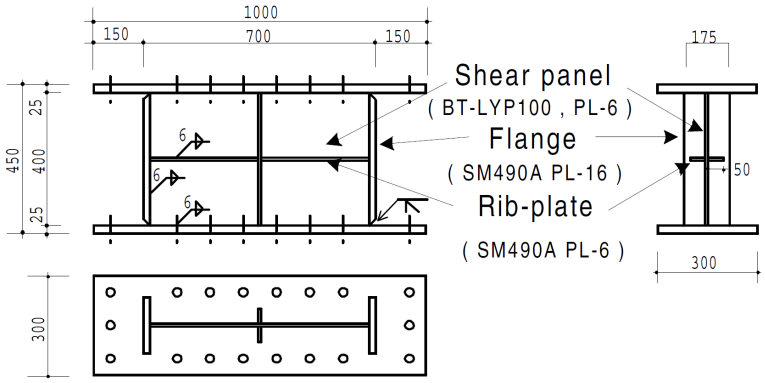

(a)

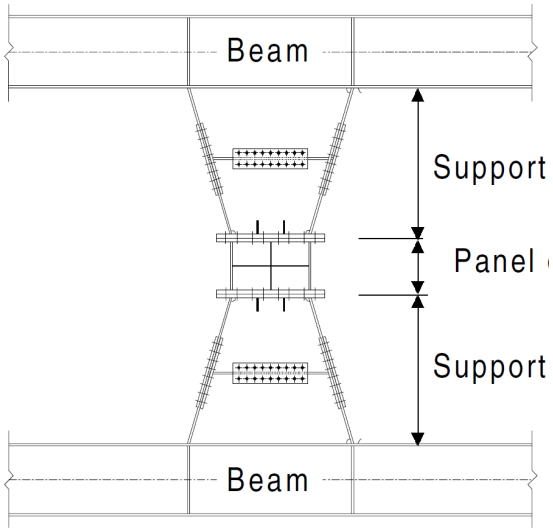

(b)

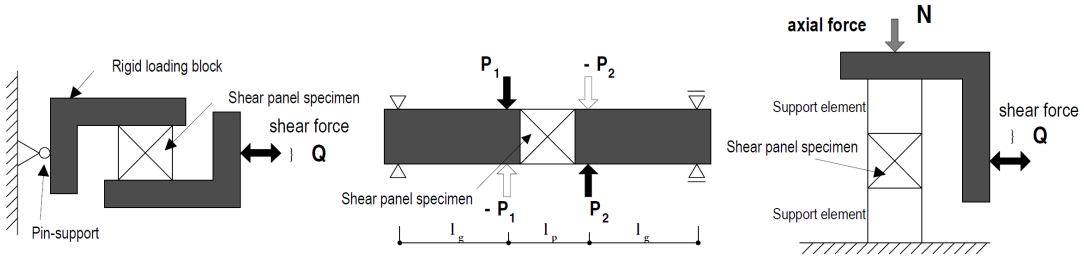

(c)

Figure 2-4: Square and rectangular specimens (Tanaka and Sasaki 2000)
(a) Typical specimen geometry; (b) Pillar type shear panel configuration;
(c) Experimental testing apparatuses

2.5 McDaniel, Uang and Seible (2003)

McDaniel et al. (2003) tested two shear links as part of the design of the new San Francisco-Oakland Bay Bridge east span. The two full scale shear link tested were representative of the shear links designed for use in the main tower. The main tower was designed as four column members intermittently connected to each other in both directions by the shear links. One transverse link, Type 1, and one longitudinal link, Type 3, were tested to evaluate the link force and deformation capacities. The links were constructed as built-up I-section beams and included a shear deformable region in the center and a connection region on each side. The cross section dimensions were the same for the two links, while the deformable region length varied, see Figure 2-5(a)-(b). The deformable regions webs were made of ASTM A709 Grade 50 steel, while the connection regions were constructed using A709 Grade HPS70W high-performance steel. The higher strength steel combined with an increase in thickness in the connection regions was used to limit plastic deformations to the deformable region. The tests showed a stable response and a good energy dissipation capacity of the two links, which were able to sustain shear strains up to 20 times the yield shear strain and a total shear deformation of 0.06 rad, Figure 2-5(c)-(d). The authors observed a brittle fracture in both specimens at failure. The fracture initiated at the end of the vertical fillet weld connecting the transverse stiffener to the web of the link, and then propagated at higher-deformation levels to the web of the link. This type of brittle fracture had not been previously reported in the literature. The authors noted that the cracks in the two full-scale link specimens occurred at the ends of vertical welds of the intermediate stiffeners, near the highly restrained location where the flange-to-web groove weld and the vertical and horizontal fillet welds of the stiffeners met. As a way to mitigate this effect, the authors proposed to terminate the weld further from the web-flange-stiffener intersection. The effectiveness of this solution was investigated by the researchers with a series of monotonically loaded finite element simulations, which were used to explore the relationship between the distance of the weld from the toe of the web-flange weld, and the stress demand at the end of the vertical fillet weld. By looking at the hydrostatic stress and

the equivalent plastic strain PEEQ the authors concluded that terminating the fillet weld at a distance equal or greater to three time the web thickness leads to a reduction of 40% in hydrostatic stress and 60% in cumulative plastic strain when the links are subjected to a 0.07rad shear deformation. A plot of this trend is shown in Figure 2-5(e).

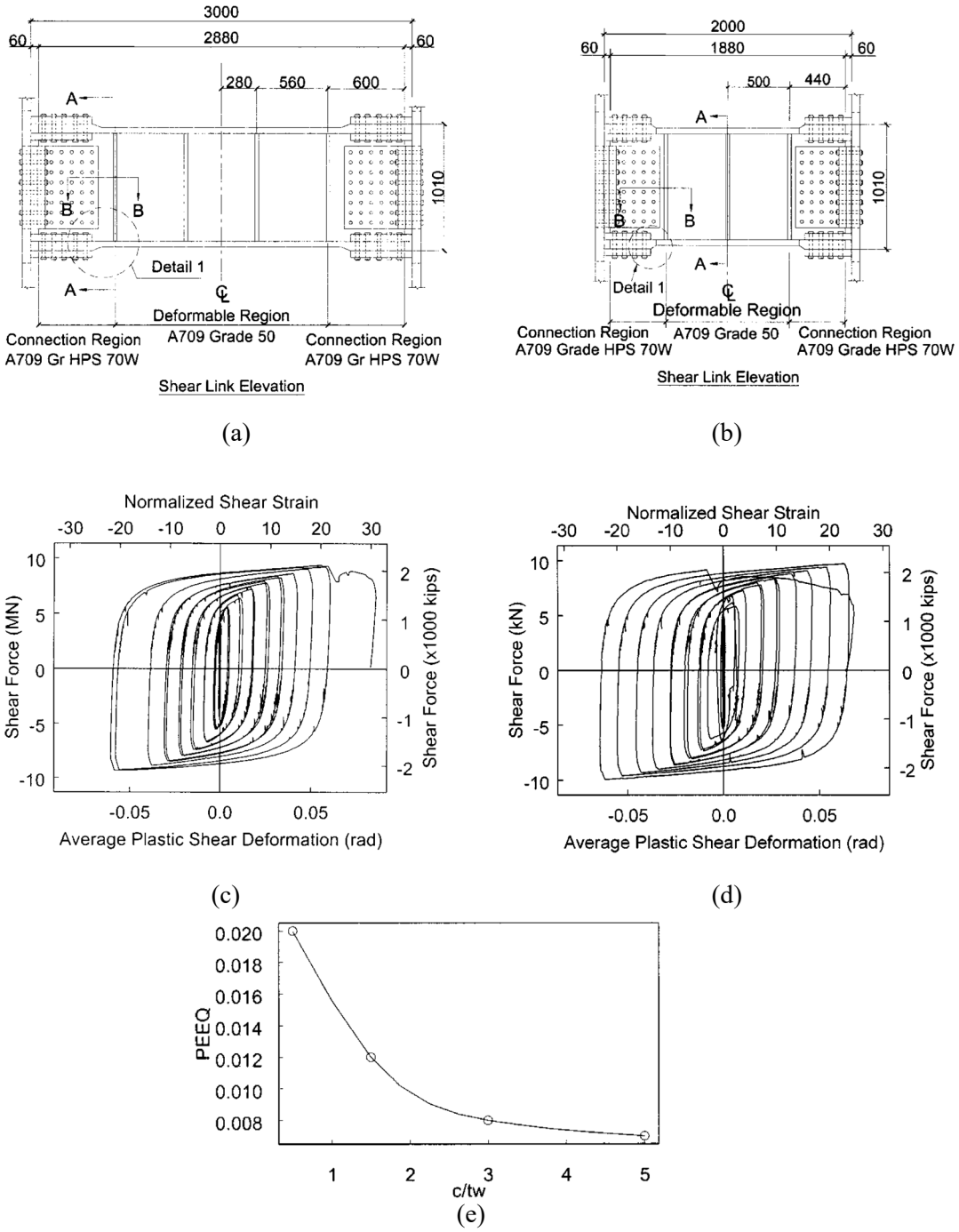

Figure 2-5: Cyclic Testing of Built-up Steel Shear Links (McDaniel et al. 2003) (a) TYPE 1 Shear link; (b) TYPE 3 Shear link; (c) TYPE 1 link experimental results; (d) TYPE 3 link experimental results; (e) PEEQ versus distance *c* relationship from FEAs

2.6 Chen, Ge and Usami (2006)

Chen *et al.* conducted a numerical investigation on the hysteretic performance of stiffened shear panels. Finite element simulations were used to analyze a series of shear panels with 1, 2 and 3 two-way stiffeners under cyclic loading. The slenderness of the web R_w was employed as the key parameter of the study. The authors also analyzed the sensitivity to the ratio of stiffener rigidity to optimum stiffener rigidity, γ_s/γ_s^*, the ratio of flange thickness to web thickness, and aspect ratio α. The slenderness parameter R_w is defined as

$$R_w = \frac{b_i}{t_w}\sqrt{\frac{12(1-\nu^2)\tau_y}{k_s\,\pi^2\,E}} \qquad \text{with } k_s = 5.35 + \frac{4}{\alpha^2} \tag{2-1}$$

where b_i is the width of the subpanels created by the stiffeners. In their sensitivity study the authors concluded that practical values of the aspect ratio, between 0.5 and 1.5, do not affect the response of the panels significantly. The stiffeners rigidity, on the other hand, affects the performance of the panels by modifying the maximum shear stress in the web. The authors recommend the use of a value $\gamma_s/\gamma_s^* = 3.0$ to ensure that the full capacity of the panel is developed, as shown in Figure 2-6 where the average shear stress in the panel is plotted against the normalized shear deformation for different values of the stiffener rigidity. The stiffener rigidity γ_s and optimum stiffener rigidity γ_s^* are defined as

$$\gamma_s = \frac{EI_s}{b_w D_w} \tag{2-2}$$

$$\gamma_s^* = \left(\frac{23.1}{(n_L+1)^{2.5}} - \frac{1.35}{(n_L+1)^{0.5}}\right)\frac{\left(1+\alpha^{3/(n_L+1)-0.3}\right)^{2(n_L+1)-1}}{1+\alpha^{5.3-0.6(n_L+1)-3/n_L+1}} \tag{2-3}$$

where n_L is the number of stiffeners, I_s is the moment of inertia of the stiffeners cross-section, b_w is the width of the panel, and D_w is the flexural rigidity of the panel web. Once the sensitivity to these parameters had been investigated, the authors conducted a series of FEM analyses on shear panels with 1, 2 and 3 two-way stiffeners under cyclic loading, with the slenderness parameter R_w

ranging from 0.2 to 0.7. The results of these simulations showed that all the panels possessed good ductility up to $\gamma/\gamma_y = 20$, except for the case with $R_w = 0.7$ in which the shear strength began deteriorating at $\gamma/\gamma_y = 12$ and significant local buckling occurred. The cyclic shear stress-shear strain envelopes for the case $n_L = 2$ are shown in Figure 2-6(b), where the effect of the web slenderness can be seen. The authors also note that during their simulations, panels with $R_w = 0.6$ showed pinching of the curve at large deformation, although the energy dissipation capacity was not significantly affected. Therefore, they concluded that for the purpose of plastic energy dissipation, the slenderness of the panel webs be limited to be $R_w \leq 0.5$.

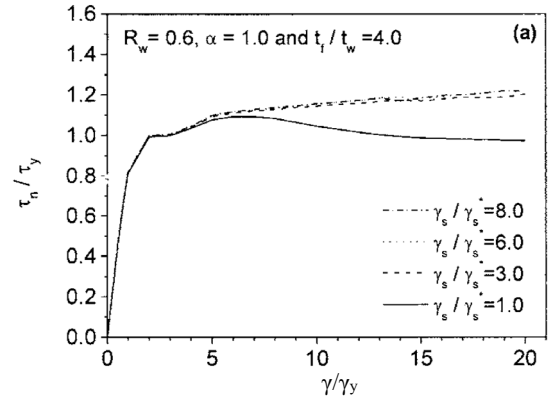

(a)

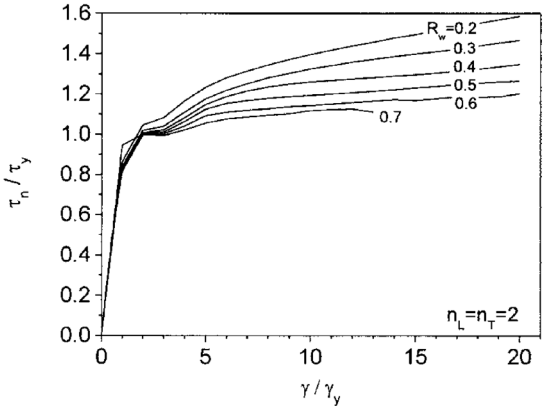

(b)

Figure 2-6: Stiffened shear panels performance under cyclic loading (Chen et al. 2006)
(a) Effect of stiffener rigidity on average shear stress envelope;
(b) Cyclic shear stress-shear strain envelopes for different R_w

Chapter 3
Preliminary Analyses and Conceptual Design

3.1 Introduction

This chapter presents the analytical and computational models used to characterize the behavior of the Braced Ductile Shear Panel system and to guide the design and detailing of the dissipating device.

First, a simplified two-dimensional analytical model is presented which allows the calculation of some basic but fundamental parameters of the response of the bracing system, such as shear stress, yielding load and stiffness. The predictions of this model are then compared against the results of numerical simulations obtained with a detailed three-dimensional finite element model.

The same finite element model—which includes material and geometrical nonlinearities—is also used to investigate the effect on the system response of other variables, including initial imperfections, buckling mode and connection type, which would otherwise be unviable to investigate using low resolution models. Lastly, this section also describes how the output of the computational analyses is brought into the final phase in the conceptual design of the BDSP – the detailing and optimization of the BDSP geometry.

3.2 Simplified Model

A preliminary model of a single frame braced with a BDSP system is obtained by modeling the shear panel as a rectangular planar element, and the beams, columns and braces with beam elements. In order to simplify the model for use during the initial phase, the connection between the braces and the surrounding frame can be assumed to be moment-free, regardless of the type of connection that will be realized in the real frame. This assumption can be justified by observing that (1) at least in the elastic range the expected drifts are so small that no significant moment would

arise in the frame, (2) the braces flexural stiffness will likely be much smaller than the ones of the beams and columns, (3) the braces are designed to have their centerline coincident with the intersection of the framing members' centerlines. Further reduction of the model is achieved by neglecting the axial deformation in beam and column elements.

According to this model, the response of the system when subjected to a lateral load can be divided into two uncoupled contributions: the first due to the surrounding frame, if the beam-column connections are moment connections; the second due to the bracing system. In the following discussion, the frame contribution will be neglected and the sole bracing system will be considered, however the response of the surrounding elements could be superimposed at any point.

Another feature of the model as described is that consecutive corners of the frame – and therefore the ends of the braces that attach to them – are constrained to maintain the same relative distance due to the assumed axial inextensibility of beams and columns.

The resulting system is shown Figure 3-1 along with the relevant dimensions in the undeformed and deformed configuration. In this representation the beams and columns in the frame are replaced by rigid constraints shown in gray. Using this model, relationships between loading, displacements, stresses and strains can be worked out which can be used to design the bracing system.

The load is translated as a horizontal lateral force V_{sp} to the upper nodes of the system. Under the assumption of uniform distribution of shear stresses in the rectangular panel, equilibrium of the system when cut horizontally through the panel gives the equation shown in (3-1), where τ is the shear stress, and b and t_w are the width and thickness of the panel.

$$V_{sp} = \tau\, b\, t_w \tag{3-1}$$

The series configuration between the panel and the braces allows now to calculate the lateral load to cause first yielding of the panel web V_{ysp} by substituting the yielding shear stress τ_y in the previous equation:

$$V_{ysp} = \tau_y\, b\, t_w \tag{3-2}$$

Using the Von Mises yield surface and a shear-only stress state, the yield shear stress can be written as:

$$\tau_y = \sigma_y/\sqrt{3} \tag{3-3}$$

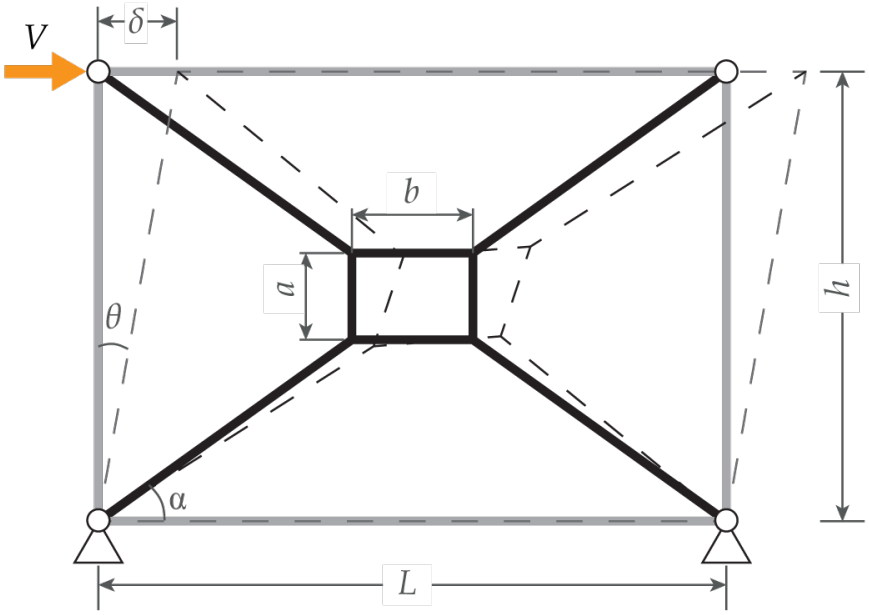

Figure 3-1: Bracing only simplified model

The lateral drift at yielding is also needed to completely define the elastic domain of the bracing system response. In the elastic range the lateral drift δ can be expressed as $\delta = F/K_X$ where K_X is the generalized stiffness of the entire bracing system. Using the simplified model, the value of the stiffness parameter can be calculated with a simple elastic energy equation, the result is shown in (3-4, where K_{panel} and K_{br} are respectively the shear stiffness of the panel and the axial stiffness of the braces (or total axial stiffness of the elements connecting the shear panel to the frame).

$$K_X = \left(\frac{1}{K_{panel}} + \frac{1}{K_{br}}\right)^{-1} \tag{3-4}$$

To obtain (3-4), the previously introduced constraint was used which eliminates relative displacement between the two upper nodes was used. This constraint—together with the chosen

boundary conditions—creates an anti-symmetry in the model, which was leveraged to neglect in-plane deformations in the panel beside the shearing one. Once this is taken into account the panel is reduced to a shear-only element and its stiffness can be written as shown in (3-5).

$$K_{panel} = \frac{G_s \, t_w \, b}{a} \tag{3-5}$$

The contribution of the connecting elements to the total stiffness K_{br} can be difficult to estimate when the geometry of the connection is complex. The generalized stiffness with respect to the bracing axis of all the element in the series (gusset plates, splicing angles and plates, braces) has to be calculated. Equation (3-6) shows the value of K_{br} when only the braces are considered and the gusset plates and other connecting elements are neglected.

$$K_{br} = \cos^2 \alpha \frac{E_s \, A_{br}}{L_{br}} \tag{3-6}$$

The drift to cause first yield – which defines the extent of the elastic region of the response – can be calculated by dividing the yielding lateral load V_{ysp} by K_X:

$$\delta_y = \frac{V_{ysp}}{K_X} = \frac{\tau_y \, b \, t_w}{K_X} \tag{3-7}$$

Once the shear panel is pushed past its elastic domain, the response of the system is controlled by the nonlinear elastic-plastic response of the panel material. At this point the simplified model is no longer suitable to describe this complex behavior. However an estimate of the ultimate load for the bracing system can be obtained by substituting the shear stress in (3-1) with τ_u – the maximum shear stress for the panel web. The plot in Figure 3-2 graphically sums up the results obtained using this model.

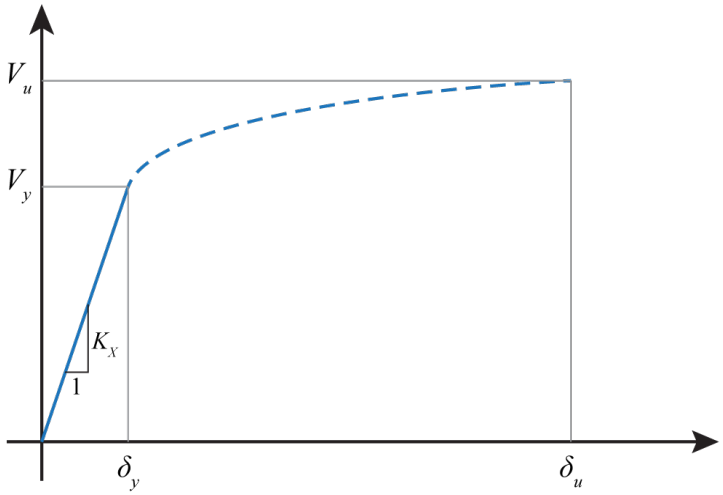

Figure 3-2: Force-Displacement response parameters

3.3 Finite Element Analyses

3.3.1 Model Geometry

The three-dimensional finite element model of the bracing system is created using planar 4-nodes shell elements exclusively. At this point in the investigation the model is built up by two unique geometries: the shear panel and the connecting brace.

The geometrical model for the shear panel includes all the elements that will be part of the finished structural element, such as transverse stiffeners, boundary flanges and end stiffeners (when present). The thickness of the in-plane elements varies between the stubs and the panel to reflect the different thickness of the beam web and the actual panel web. Similarly, different material models are assigned to different portions of the panel to reflect the different steel grades used. The average size of the mesh is 0.5 inches throughout the panel. A typical geometry is shown in Figure 3-3, while the mesh associated with it is shown in Figure 3-4.

The complete model is assembled by connecting one panel to four different instances of the brace geometry. Each brace is attached to the shear panel by means of a kinematic constraint between opposing nodes on the panel I-beam stubs and the brace end.

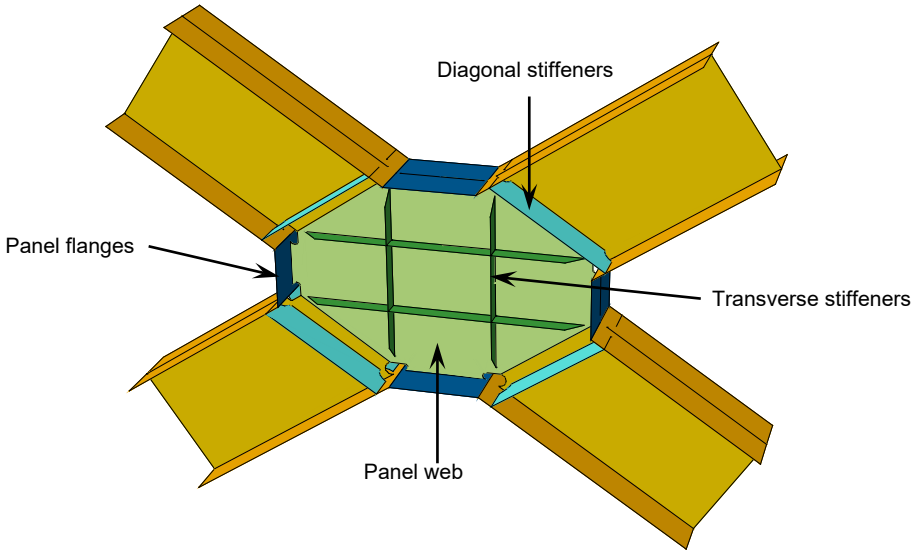

Figure 3-3: Shear panel model geometry

3.3.2 Material Models

Two material models are used in the finite element model to define the elastic and plastic properties of the two steel grades used. For the members made out of Grade 50 steel, which are not expected to experience stresses larger than the yield stress and therefore not undergo any plastic deformation, a simple elastic-perfectly plastic model is used with yield stress $f_y = 50\ ksi$.

A more refined model was instead using for the shear panel, since its behavior past the elastic limit will define the response of the system, and the accuracy of the results is directly related to the quality of the material model used. The model used for the panel web made of ASTM A36 steel is an elastic-plastic model, with embed nonlinear mixed isotropic-kinematic hardening. The strain rate is decomposed in elastic and plastic components, $\dot{\boldsymbol{\epsilon}} = \dot{\boldsymbol{\epsilon}}^{el} + \dot{\boldsymbol{\epsilon}}^{pl}$. The plastic behavior is controlled by the yield function $f(\boldsymbol{\sigma} - \boldsymbol{\alpha}) = \sigma^0$, where σ^0 is the size of the yield surface, $\boldsymbol{\sigma}$ is the stress tensor, and $\boldsymbol{\alpha}$ is the backstress tensor. The yield surface size for isotropic hardening follows the equation:

$$\sigma^0 = \sigma|_0 + Q_\infty\left(1 - e^{-\kappa\bar{\epsilon}^{pl}}\right)$$

and the function f is the von Mises yield criterion

$$f(\boldsymbol{\sigma} - \boldsymbol{\alpha}) = \sqrt{\frac{3}{2}(\boldsymbol{\sigma}^{dev} - \boldsymbol{\alpha}^{dev}) : (\boldsymbol{\sigma}^{dev} - \boldsymbol{\alpha}^{dev})}$$

where $\boldsymbol{\sigma}^{dev}$ is the deviatoric stress tensor, $\boldsymbol{\alpha}^{dev}$ is the deviatoric part of backstress, Q_∞ and κ are constants. The flow rule is associated, and the rate of plastic flow is defined by the relationship:

$$\dot{\bar{\epsilon}} = \frac{\partial f}{\partial \sigma} \sqrt{\frac{2}{3} \dot{\boldsymbol{\epsilon}}^{pl} : \dot{\boldsymbol{\epsilon}}^{pl}}$$

The parameters defining the model are fitted to a cyclic stress-strain curve, which models the behavior of structural steel under repeated cyclic loading (Cofie and Krawinkler 1985). The resulting yield stress is approximately 31 ksi. Two backstresses are used to define the kinematic hardening, with the *k-th* component defined as follows:

$$\dot{\boldsymbol{\alpha}}_k = \frac{C_k}{\sigma_0} (\boldsymbol{\sigma} - \boldsymbol{\alpha})\, \dot{\bar{\epsilon}}^{pl} - \gamma_k\, \boldsymbol{\alpha}\, \dot{\bar{\epsilon}}^{pl}$$

where C_k and γ_k are fitted parameters. In Figure 4 the results from finite element simulation of a cyclic uniaxial tensions-compression specimen are shown and compared to the literature result. The values of the four parameters and the constants are: $C_1 = 3480\, ksi$, $\gamma_1 = 400$, $C_2 = 200\, ksi$, $\gamma_2 = 10$, $Q_\infty = 5.1\, ksi$, $\kappa = 25$.

3.3.3 Boundary Conditions and Loading

Following the same considerations used when constructing the simplified model described in 3.2, the assembly is restrained against displacements in all directions at the bottom ends and allowed to move only in the X (horizontal) direction at the top. In addition, in order to investigate the effect that different type of connections between the braces and the braced frame can have on the behavior of the system, the models are analyzed with and without restraints against rotation of the braces about the Z-axis. This will reflect the effect of a full moment connection (i.e. a bolted or welded connection) or a pinned connection respectively. Rotations about the X- and Y-axis of the braces ends are not constrained. This reflects the assumption that the weak axis stiffness of the

braces will suffice to prevent out-of-plane buckling of the system and prevent damage to any structural element outside the panel. This will also allow to perform a capacity design of the connections between the braces and the braced frame without having to account for weak-axis bending moments in the braces.

The boundary conditions are defined with respect to four reference points located at the centroid of each brace extreme cross-section. The nodes on these cross-sections are tied together by a kinematic constraint and then associated to the motion of the reference point. In Figure 3-6 the thick crosses represent the reference points and the edges in yellow the areas tied to each point. This procedure allows to effectively model a pinned connection where the brace cross-section rigidly rotates around the reference point. At the same time a load or imposed displacement can be applied to the reference point without creating artificial stress concentrations.

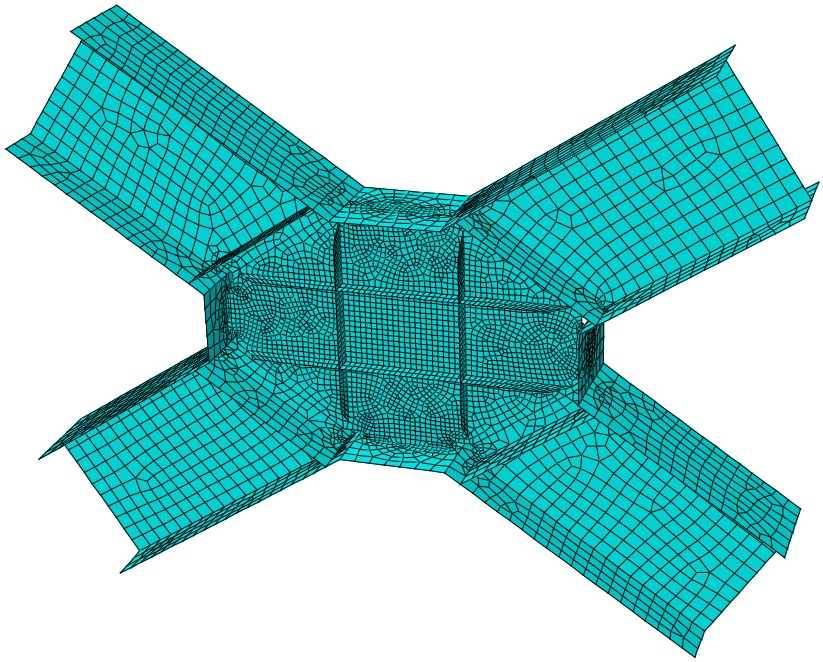

Figure 3-4: Shear panel typical mesh

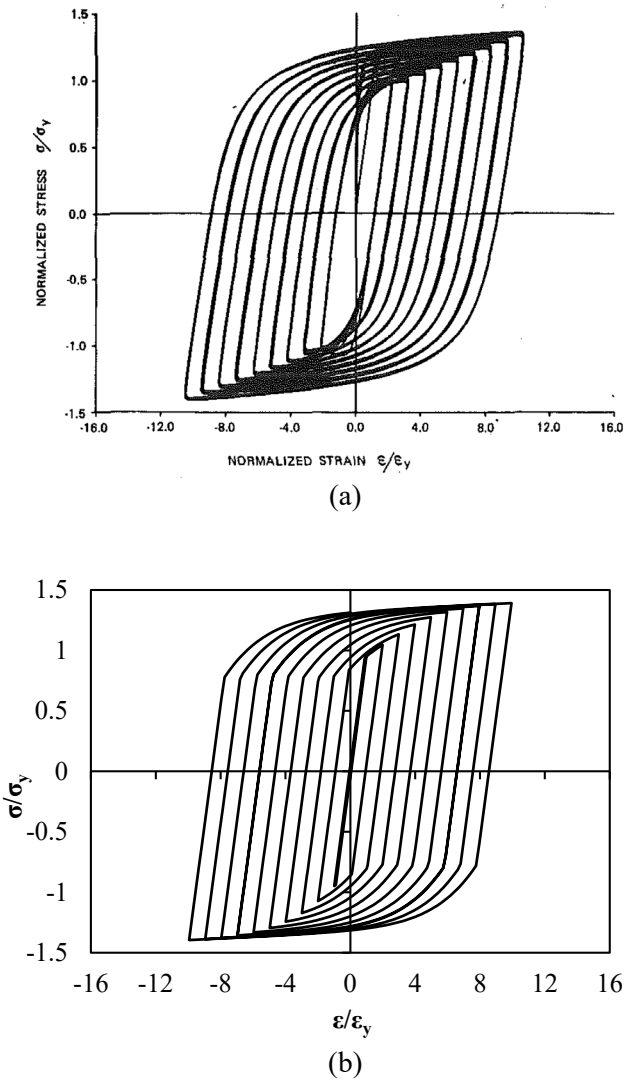

Figure 3-5: Normalized stress-strain curves
(a) Cofie and Krawinkler 1985; (b) Finite element model

3.3.4 Analysis Procedures

3.3.4.1 Elastic Buckling

The finite element model was used during the initial investigation of the system behavior to identify the dominant buckling modes for different geometries. This investigation was completed

by performing linear elastic buckling analyses in ABAQUS on parametric models, varying the braces sections, the panel dimensions and the arrangement of transverse stiffeners on the panel web.

For these analyses a unit horizontal reference load *F* was distributed to the two upper reference point at the braces end (see Figure 3-6). The first 10 buckling modes, associated with the 10 lowest critical loads, were calculated for each model.

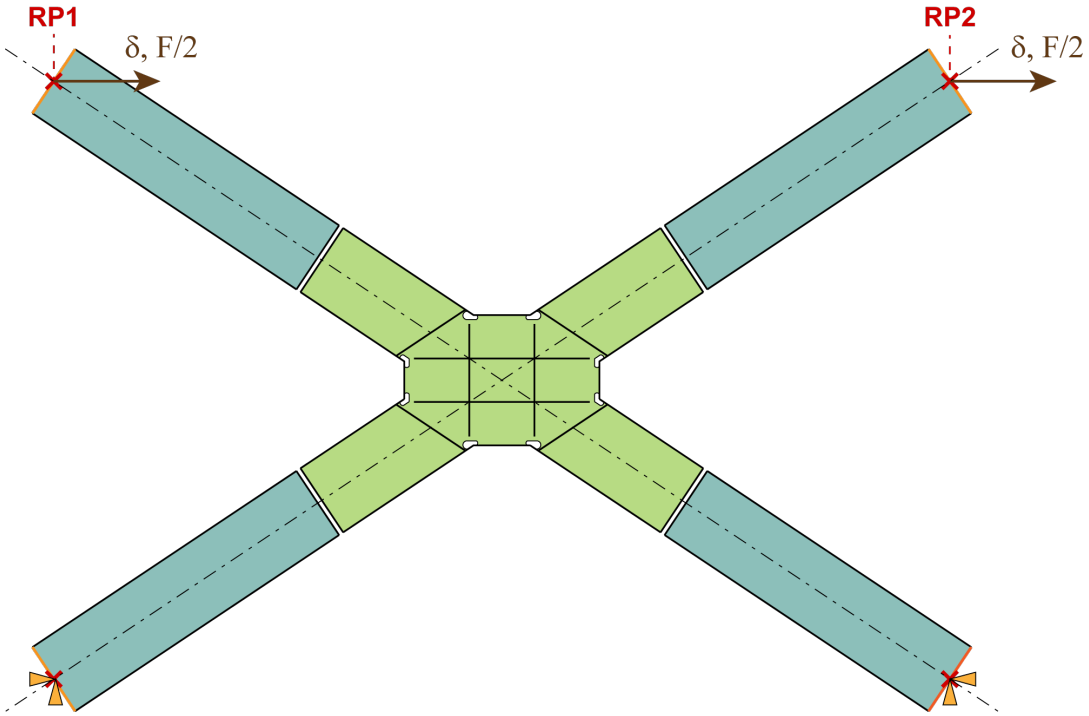

Figure 3-6: Finite element model: boundary conditions, loading and example geometry

3.3.4.2 Cyclic Loading

The response of the system under lateral, cyclic drift was evaluated by nonlinear quasi-static finite element analyses. For these analyses, the horizontal drift was set as imposed displacement at the two reference points RP1 and RP2 (Figure 3-6). This is consistent with the assumption of neglecting the beam axial deformation made previously for the simplified model.

To evaluate the response of the system, a cyclic, constant amplitude horizontal displacement loading was applied to the reference points. The amplitude was equal to fifteen times the drift to cause first yield. Although this loading scheme is not representative of a real drift history scenario

when the system is installed in a frame subject to seismic shaking, it was chosen to magnify the negative effects of repeated cyclic loading and explore stiffness degradation and post-buckling behavior of the system.

3.4 Results

In this section the main results obtained from the parametric study on the finite element model of the BDSP are presented. The principal results about the response of the bracing system are the shape and load associated with the elastic buckling, the characteristics of the cyclic force-displacement response, and the energy dissipation capacity of the system. A more detailed discussion of these results can be found in Giannuzzi *et al.* (Giannuzzi et al. 2014).

An estimate of the loads associated with elastic buckling is made using a linearized version of the finite element model. The finite element analyses showed that the most critical buckling mode for the geometries and dimensions considered is either the global out-of-plane buckling of two aligned braces about their weak axis or local shear buckling of the BDSP web. Simulations of numerous model geometries suggested that systems which exhibit out-of-plane buckling are associated with decreased stiffness and unsatisfactory performance under cyclic loading. In Figure 15 the history of the horizontal reaction force at one of the supports (end of brace) is shown for two systems with different dominating buckling mode. The only difference between the models is the section of the braces. In this plot a positive value of the horizontal reaction causes the attaching brace to be tensioned. The brace-buckling dominated system has worse performance in carrying load through the compression brace: the stiffness rapidly degrades with cyclic loading. Note that for the purpose of this study, a constant amplitude loading protocol is used as to increase the rate of the stiffness degradation. It follows, that to increase the performance of the system, the design of the system must prevent out-of-plane of the braces.

On the other hand, the theoretical critical load for shear buckling of a rectangular plate is equal to:

$$V_{sh} = K \cdot \pi^2 \cdot \frac{D}{a^2} \cdot b \tag{3-8}$$

$$D = \frac{E \cdot {t_w}^3}{12(1 - \nu^2)} \tag{3-9}$$

where K is a function of boundary conditions:

$$K = \begin{cases} 5.34 + 4.0\dfrac{a^2}{b^2} & simply\ supported \\ 8.98 + 5.6\dfrac{a^2}{b^2} & fully\ restrained \end{cases} \tag{3-10}$$

and b, a and t_w are the width, height and thickness of an unstiffened plate respectively (or the dimensions of the regions that the plate is divided into by the transverse stiffeners), and E and ν are the steel's Young's modulus and Poisson ratio. The results from parametric numerical simulations on panels with different geometries, have shown that the critical load of the panel can be estimated using Equation (3-8). In fact, as shown in Figure 3-7 for a selection of thirty simulations, the elastic buckling load for the shear panels is bound by the two loads calculated for the two different boundary conditions, and therefore the two expressions of Kin (3-9).

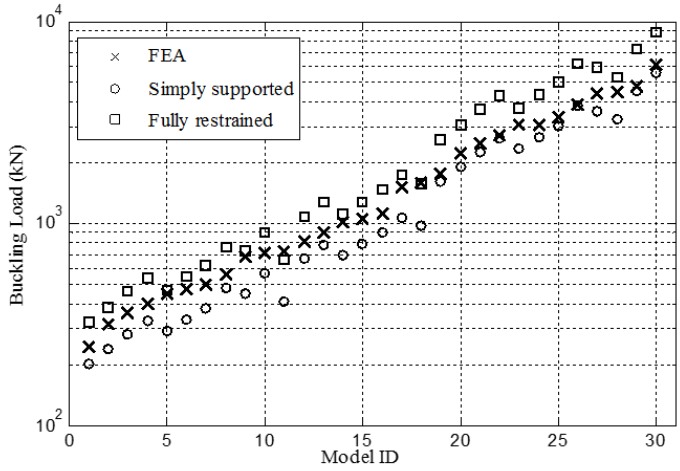

Figure 3-7: Comparison of buckling loads obtained from FEA with predicted loads (Giannuzzi et al. 2014)

The main result from the numerical parametric investigation is given by the response of the BDSP system when subjected to a lateral story drift. That is, the relationship between the applied lateral drift δ and the lateral force in the bracing. The analyses showed that Equation (3-2) is an accurate estimate of the yielding load. The force-displacement data was used to develop an expression to estimate the ultimate load of the bracing system: while neglecting the contribution coming from the flanges surrounding the BDSP web, one can assume that at the ultimate load the whole shear panel is yielded, and reached its maximum shear stress. These results suggested a bilinear approximation of the force-displacement behavior of a system with given dimensions. The first segment, corresponding to the elastic region, starts at the origin and ends at the point identified by the drift and the lateral load to cause first yielding; the second segment continues from that point to the ultimate drift and load coordinates. The equations used to calculate these points can be solved for the BDSP dimensions, thus allowing the selection of geometries that will result in force-displacement behaviors satisfying practical needs.

The effect of initial imperfections on the initial and cyclic response of the system has also been studied using finite element analyses. It has been found that the system behavior is not sensitive to the imperfections amplitude. The size of the imperfections influences the number of cycles needed for the system to stabilize after inelastic buckling begins. However, the final response is practically the same for the different amplitudes. The initial imperfections will push the system to displace following the dominant buckling shape, after yielding of the web reduced the sectional stiffness. Initially, the amplitude of the out-of-plane deflections increases with each load cycle. After 3 to 6 cycles this trend ends, and the amplitude remains constant for the following cycles. This behavior can be seen in the plot in Figure 3-8, where the axial force in one of the braces under cyclic loading is plotted for different initial imperfection amplitudes (compression if positive). The braces in the model with no imperfections are able to carry more compression in the initial cycles compared to the system with imperfections. However, after a small amount of cycles the responses of the two models collapse to the same curve.

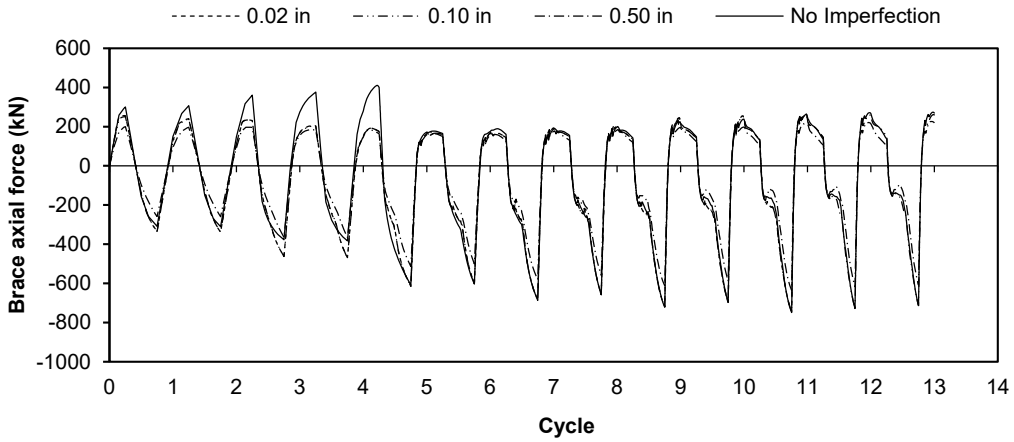

Figure 3-8: Effect of initial imperfections on system response

Another result obtained from the preliminary analyses is the proof that the design of the system leads to the concentration of plastic strains only in the BDSP. The braces remain elastic during lateral loading, thus they can be be reused. Figure 3-9 illustrates the evolution of the cumulative equivalent plastic strain (PEEQ). From this figure it can be seen that plastic strains are present in the shear panel alone. The PEEQ index is a positive scalar quantity used as a measure of plastic strains throughout the analysis at each integration point. The quantity is defined as the absolute value of the equivalent plastic strain rate.

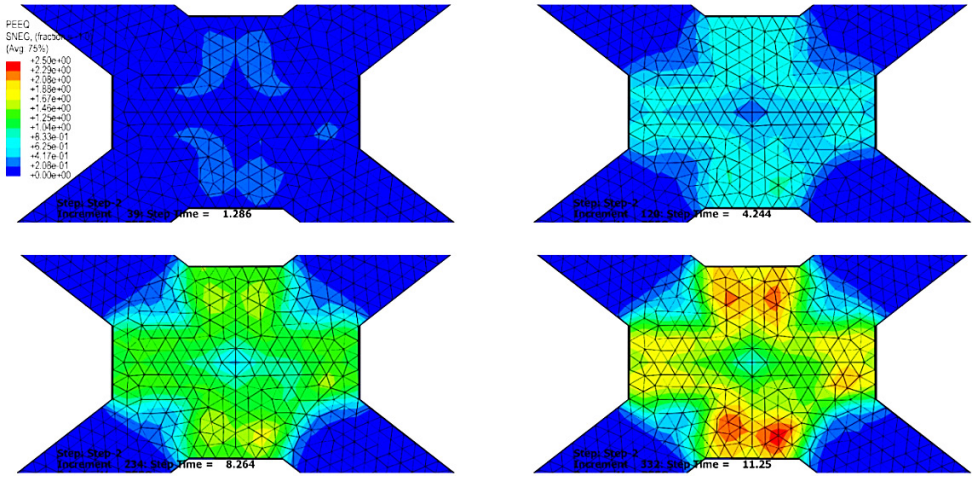

Figure 3-9: Cumulative equivalent plastic strain at different instants

Chapter 4
Experimental Program

4.1 Introduction

The previous chapter described the conceptual design of the new bracing system based on analytical and numerical analyses, targeted at understanding and predicting the elastic, buckling and plastic behavior. The performance of the BDSP as a dissipative sacrificial element, however, could not be completely estimated by these techniques alone. Some variables that could affect the response and energy dissipation capacity of the system could not be included in the numerical models, at least not without dramatically increasing the complexity and computational demand of the simulations. One example would be the response of critical welds under cyclic loading, the inherent stress concentration and the resulting life under low-cycle fatigue. At the same time, the uniqueness of the new systems limits the amount of data that can be reused from literature. These considerations led to the experimental program described in this chapter, aimed at evaluating the performance of the BDSP system. A general description of the testing frame is given in section 4.3, while the details of the design process are illustrated in section 4.4.

4.2 T. V. Galambos Structural Engineering Laboratory Description

The T. V. Galambos Structural Engineering Laboratory provides a 60’ by 160’ strong floor and a 20’ strong wall on the East end of the floor. At the time of testing three different experimental setups, including the BDSP, were present in the facility. Therefore some of the choices for the experimental setup were justified by limitations resulting from the need of coordinating with the other projects. The actuator used for loading, part of the laboratory equipment, is an MTS Hydraulic Actuator, model 244.51, with a maximum load rating of 220 kips and stroke of 5 inches. Figure 4-1 shows the West half of the facility with the first BDSP specimen in place.

4.3 Specimen and Braced Frame Description

As previously introduced, the main objective of the experimental investigation was to collect enough data to evaluate the behavior of the BDSP, and its interaction with the other members in the structure, to confirm and validate the prediction of the numerical analyses, and compare its energy dissipation capacity to other systems. The laboratory tests are primarily expected to provide information regarding the lateral force-drift response of the systems, the capacity and performance of the bolted connection between the panel and the braces, the yielding locations, the ductility under repeated loading and the dominating failure modes. In order to gather this data, it was decided to test a BDSP-braced frame under quasi-static cyclic lateral loading. To explore the dependency of the response variables on the shear panel geometry, a series of tests on multiple panels was required. Since the BDSP system – by design – is expected to provide enough stiffness and drift control to protect the gravity frame from damage when subject to seismic loading, it was decided to test all the shear panel specimens using the same test frame, braces and connections for all the tests. Therefore, the frame had to be designed to ensure that none or minimum damage would occur under the expected most severe loading. Furthermore, this approach, beside its obvious economical advantage, would also allow to investigate the feasibility and easiness of replacing a heavily damaged panel in the presence of residual drifts and forces in the system. Due to economic and space constraints, a half-scale specimen of a one-bay one-story frame was chosen as the test specimen. A description of the testing frame and specimens is given in the following paragraphs, while the details of the design process are illustrated in section 4.4.

4.3.1 Shear Panel Specimens Description

Three main parameters that have major influence on the response of the BDSP system were identified: the shear panel width b, the shear panel web thickness t_w and the perforation ratio ρ (defined as the ratio between the sum of holes diameter in the horizontal direction $n \cdot D_h$ and the panel width). For each parameter, a set of feasible values was specified. The values were defined by taking into account a number of different constraints and limitations, and among these the ones

that largely controlled the design are: (1) maximum lateral force the actuator could transfer; (2) fabrication and constructability; (3) plate slenderness limitations. A total of ten specimens were designed and tested from ten combinations of the three parameters. Table 4-1 lists all the specimens in testing order along with their properties. In Table 4-2 a synoptic summary of the coverage of the parametric space is shown: in this table the specimen yielding load increase from right to left (increasing b, decreasing ρ) and from the top down (increasing t_w).

All the specimens are designed as a central octagonal panel web, two horizontal and two vertical panel flanges, and four short I-beam connecting stubs. A drawing of a typical specimen is shown in Figure 4-2 and detailed drawings for all the specimens can be found in Appendix A. The panel webs are all stiffened by two horizontal and vertical stiffeners, which divide up the web in nine subpanels. The panel web is fillet welded on both sides to the 3/8" thick horizontal and vertical flanges. Oblique stiffeners are provided at the end of the I-sections where these are attached to the web. Eight of the ten specimens have perforated webs: the web of these specimens are designed with five holes on five of the subpanels. The diameter of the holes is equal to the perforation ratio ρ multiplied by the width of the sub-panel (equal to $b/3$ for all the specimens).

Four W8X21 stubs (same section as the braces) were used as the four connecting elements. The flanges of these sections were CJP-welded to the horizontal and vertical flanges of the panel, while the webs were butt welded to the specimen panel web. For the slip-critical bolted connection to the brace, each flange has six 3/4" long slotted holes, in the longitudinal direction, and the web has two long slotted 1/2" holes. The long slotted holes were used to facilitate construction, and to allow for the release of residual forces in the panel at the end of testing and disassembly. In fact, the slip caused by residual drift in the frame could force the bolts into bearing upon untightening, and make their removal impossible without the application of a balancing lateral force. This will also be used to investigate the replaceability of the BDSP after damage.

The thickness and depth of the stiffeners on the panel web were designed to achieve an optimal value of stiffening, and they vary across specimens. The values of stiffener thickness t_s and depth

d_s for each specimen are listed in Table 4-1, and their design is described in section 4.4. The stiffeners were stopped at a distance of one inch from the flanges and fillet welded to the web by single- or double-sided welds, depending on the plate thickness. The stiffeners are tapered at a 45 degrees angle at each end to reduce stress concentrations. Stiffeners on thin web plates, 1/8", where welded on one side only to limit warping of the web due to heating during the welding process.

4.3.2 Braced Frame Description

The braced frame specimen (Figure 4-3) has a bay width of 10' and a story height of 6' 8" (center-on-center). The beams and columns are both W8X40 sections made of ASTM A992 steel. The beams are attached to the columns by fully welded web and flanges connections; this type of connection was chosen to facilitate the construction and erection of the frame in the laboratory and avoid the need for field welding. The beam flanges were welded to the column by CJP weld, while fillet welds were used for the beam webs. Transverse stiffeners were provided in the column at points were the beam flanges attached to the flange.

The columns extend past the beams by 6" on the top side, and 1' on the bottom end. At this end, the columns were fillet welded to a 2 ½" thick steel base plate and stiffeners. Six oversized bolt holes on each base plate allowed the connection of the base plate to the floor plates with 1 ½" threaded rods to transfer the vertical loads to the strong floor. The transfer of the large horizontal force to the strong floor was realized by means of a 2" thick shear key fillet welded to the underside of the base plates, which would fit into a matching rectangular slot on the floor plates.

The short braces connecting the panel specimen to the frame are Grade A992 W8X21 sections 22-1/2" long. Six standard 3/4" bolt holes are provided at the end of each flange for the connections to the panel and gusset plate.

The gusset plates are made of 3/8" thick A572 Gr50 steel and are welded fillet welded to the beam alone. The vertical edge not attached to the column is stiffened by a 1/2" stiffener to avoid buckling of the gusset plate. The whole assembly is positioned at a distance of 5/8" from the column flange to prevent the column flange from getting in contact with the stiffener. The gusset plates are

not welded to the frame columns to avoid low-cycle fatigue damage to the gussets due to opening or closing of the beam-to-column joint when the frame is subjected to large drifts (Berman and Bruneau 2009). In fact, this type of strain in the gusset plates is due to compatibility rather than bracing forces and it could not be controlled by increasing the thickness of the gusset plates. Moreover, as shown by Berman and Bruneau for BRBs, this type of connection has other benefits to the overall response of the system such as decreasing the portion of story shear resisted by frame action, keeping the stiffness of the system closer to the analytical beam-column models and prevent out-of-plane buckling of the plates during "closing" of the beam-to-column joint. Twelve oversized bolt holes in a 3x4 pattern allow the connection of the brace to the gusset plate with a set of L3X3X1/4 angle sections.

4.4 Specimen and Braced Frame Design

This section described the process used to design the specimens and the braced frame for the experimental program. The main assumptions and the design philosophy are illustrated below, while detailed calculations and full results for one specimen are listed in Appendix C.

4.4.1 Shear Panels Design

As previously described, all the panels are made by four short I-sections, the web plate, the boundary flanges, the diagonal stiffeners and the transverse stiffeners. The web plate is dimensioned using the selected parameters, welded to the flanges with full strength fillet welds and to the I-section webs with butt welds.

The width, thickness and perforation ratio combinations of the panels were designed to explore a range of plate slenderness values R_w from 0.25 to 0.66. This range was chosen based on the work of Chen *et al*., in which the authors recommend values of plate slenderness between 0.2 and 0.6 to achieve good ductility under cyclic shear loading of stiffened plates. The slenderness parameter R_w is given in (Chen et al. 2006) as:

$$R_w = \frac{b_i}{t_w}\sqrt{\frac{12(1-\nu^2)\tau_y}{k_s\,\pi^2\,E}} \tag{4-1}$$

$$k_s = 5.35 + \frac{4}{\alpha^2} \tag{4-2}$$

Where α is the plate aspect ratio, b_i is the width of the subpanels.

The thickness and depth of the transverse stiffeners varies across the specimens as the stiffeners are designed to provide the same relative rigidity to the specimen webs. The stiffeners were dimensioned to provide three times the minimum optimum rigidity γ^*. The optimum rigidity of stiffeners for plates in shear is given by Chusilp and Usami (Chusilp and Usami 2002) and its expression is:

$$\gamma_s^* = \left(\frac{23.1}{(n_L+1)^{2.5}} - \frac{1.35}{(n_L+1)^{0.5}}\right)\frac{\left(1+\alpha^{3/(n_L+1)-0.3}\right)^{2(n_L+1)-1}}{1+\alpha^{5.3-0.6(n_L+1)-3/n_L+1}} \tag{4-3}$$

Where n_s is the number of stiffeners and α is the aspect ratio of the plate. The relative rigidity of stiffeners with respect to a plate can be calculated as:

$$\gamma_s = \frac{EI_s}{b \cdot D_w} \tag{4-4}$$

With I_s moment of inertia of the stiffeners and D_w plate flexural stiffness.

In their work, Chen *et al.* (Chen et al. 2006) recommend the use of stiffeners with a relative rigidity γ at least three times the optimum value γ_s^* to restore the full buckling strength of each subpanel. The stiffeners are tapered at a 45 degree angle and stopped 1" away from the flanges to reduce stress concentration at the weld.

The thickness of the boundary flanges is constant across all the specimen and equal to the thickness of the brace flanges.

The yielding and ultimate loads for each panel specimen were estimated using Equation (3-2), where the width b for panels with perforations is replaced by the effective width in shear, defined in (4-5), and the yielding shear stress is replaced by the maximum shear stress for the ultimate load calculation, giving Equations (4-6) and (4-7) .

$$b_{eff} = b \cdot (1 - \rho) \tag{4-5}$$

$$V_{ysp} = \tau_y \cdot t_w \cdot b \cdot (1 - \rho) \tag{4-6}$$

$$V_{usp} = \tau_u \cdot t_w \cdot b \cdot (1 - \rho) \tag{4-7}$$

The drift to cause yield δ_y was calculated using the global stiffness K_X defined in Equation (3-4 and a maximum drift equal to 10 times the yield drift δ_u was used as reference for subsequent ultimate state calculations. The calculated values of the loads and drifts, as well as stiffeners dimensions, are listed in Table 4-1.

Detailed drawings of all the panel specimens are included in Appendix A, and an example of calculations for one of the specimen panel (BDSP-24-2-00) can be found in Appendix C.

4.4.2 Braced Frame Design

The braced frame was designed using a capacity design approach, to ensure that it would undergo little to no damage and be reused for testing of all the ten panel specimens. The provisions of the *Specifications for Structural Steel Buildings* (AISC 2010b), hereafter *Specifications*, were used to check the strength of all the members and connections in the structure.

4.4.2.1 Loads and Member Demands

The ultimate load estimated with Equation (4-7) was used as the main parameter for the design of the braces axial capacity and for the slip-critical bolted connections. Under linear elastic assumptions, and following the simplified model described in 3.2, the design force in each of the braces can be calculated from the design horizontal shear in the panel V_{usp} as:

$$N_{u,X} = \frac{V_{usp}}{2 \cdot \cos \alpha} \tag{4-8}$$

However, numerical simulations showed that under large deformations the stiffness of the panel along the compression diagonal will decrease. As a results, the horizontal shear in the panel will be unequally distributed to the tension and compression diagonals, with the tension diagonal

carrying up to 50% force than the compression one. To account for this, a distribution factor κ = 1.5 was used. The force used for design is then calculated from the following expression:

$$N_{up,X} = \frac{V_{usp}}{\cos\alpha} \cdot \frac{\kappa}{\kappa + 1} \tag{4-9}$$

where for $\kappa = 1$ the symmetric response is obtained. The demands obtained using this factor are identified by the subscript 'up' as opposed to the ones calculated under symmetric distribution with subscript 'u'.

The demands in the rest of the frame were estimated by superimposing the forces and moments due to the elastic drift of the frame at maximum expected drift. Under the design drift δ_u, the lateral force due to frame action is:

$$V_{uf} = K_f \cdot \delta_u \tag{4-10}$$

$$K_f = \frac{24\ E\ I_{xB}\ I_{xC}}{(I_{xB} \cdot h + I_{xC} \cdot L) \cdot h^2} \tag{4-11}$$

where K_f is the frame stiffness.

The total external lateral force required at this drift level, that is the force needed from the actuator, is the sum of Equation (4-7) and (6-1):

$$V_u = V_{usp} + V_{uf} \tag{4-12}$$

The demands in the beams can then be calculated using expression (4-13) to (4-15):

$$N_{up,B} = V_u - V_{uf} \tag{4-13}$$

$$M_{up,B} = V_{uf} \cdot \frac{h}{4} \tag{4-14}$$

$$V_{up,B} = \frac{2 \cdot M_{up,B}}{L} + N_{up,X} \cdot \sin\alpha \tag{4-15}$$

while (4-16) to (4-18) are used to estimate forces and moments in the columns:

$$N_{up,C} = V_{up,B} \tag{4-16}$$

$$M_{up,C} = V_{uf} \cdot \frac{h}{4} \tag{4-17}$$

$$V_{up,C} = \frac{V_{uf}}{2} \tag{4-18}$$

4.4.2.2 Members capacity design

Beams, columns and braces are designed as member subject to axial force and bending moment, and their capacity is calculated following section H1 of the Specifications. The axial capacity ϕP_n of each member is calculated following Section E of the Specifications; the effective length factor K for beams and columns is conservatively taken as 1.0, while a conservative factor of 2.0 is used for the braces. The flexural capacity ϕM_n is calculated according to Section F of Specifications, and is controlled by Equation F2-1 which means all the sections can develop their full plastic capacity in pure strong-axis flexure. Finally, the interaction equations H1-1a and H1-1b are used to check the capacity of the sections when both axial load and bending moment are present.

$$\frac{P_u}{\phi P_n} + \frac{8}{9}\frac{M_u}{\phi M_n} \leq 1 \qquad \text{AISC (H1-1a)}$$

$$\frac{P_u}{2 \cdot \phi P_n} + \frac{8}{9}\frac{M_u}{\phi M_n} \leq 1 \qquad \text{(H1-1b)}$$

4.4.2.3 Connections design

All the bolted connections in the frame are designed as slip-critical connections to avoid wearing of bolt holes under reversed cyclic loading. These include the connection between the braces and the panel, realized with the use of doubler plates, and the connection between the braces and the gusset plates with angle sections. The capacity of each connection is checked according to Specifications, Section J3.

4.4.2.4 Gusset plate design

The gusset plates are designed to remain elastic under the maximum expected compressive and tensile forces, $P_u = \pm N_{up,X}$. The tensile strength of the gusset plate is estimated using the effective Whitmore area A_{we} shown in Figure 4-4(a). The yielding tensile strength is then calculated using the following expression:

$$R_n = A_w \cdot F_y \tag{4-19}$$

The buckling strength of the gusset plates is taken as the smaller of two values, one calculated using the Thornton Method and the other using the Modified Thornton Method (Thornton 1984). Both methods estimate the buckling strength of the gusset plate with two equations depending on the value of the Thornton slenderness parameter λ_t:

$$P_{cr} = \begin{cases} 0.658^{\lambda_t^2} \cdot A_e \cdot F_y & \text{if } \lambda_t \leq 1.5 \\ \dfrac{0.877}{\lambda_t^2} \cdot A_e \cdot F_y & \text{if } \lambda_t > 1.5 \end{cases} \tag{4-20}$$

$$\lambda_t = \frac{k\, L_t}{\pi\, t_g} \sqrt{\frac{12\, F_y}{E_s}} \tag{4-21}$$

where k is a restrain coefficient (taken as 1.2 because the gusset plate is stiffened on the free edge), L_t is the inflection length, and A_e is the effective area. For the Thornton Method the inflection length is taken as the minimum between the length L_2 and the average of L_1, L_2 and L_3 and the effective area is the Whitmore area, Figure 4-4(b). The Modified Thornton Method, instead, defines the length L_t as the distance between the last bolt and the beam flange, and the effective width used to calculate A_e is taken as the width obtained by projecting at a 45 degrees angle from the beginning to the end of the connection, as shown in Figure 4-4(c).

The gusset plates are welded to the beam flanges using 5/16" fillet welds. The demand on the welds is calculated by projecting the axial force in the braces onto the weld plane and adding the relative transport moment due to the original force eccentricity. The maximum throat area stress is then calculated as the resultant of the parallel stresses (due to the horizontal component of the load)

and the orthogonal stresses (due to the vertical component of the load and the transport moment). The maximum allowable stress in the weld is calculated using Equation J2-5 (Specifications). For the final capacity check a factor of 1.40 is applied to the demand stress to account for the uneven distribution of stresses in the weld length.

4.4.3 Experimental Setup Finite Element Model

The design of the experimental braced frame and specimens has been verified using a detailed finite element model of the experimental setup. This verification was used to check some of the assumptions made during design and identify possible issues due to local stress distribution. The same model will be used to validate the finite element analyses by comparing the predictions obtained from the simulations with the experimental results.

The model used for these analyses is similar to the one described in 0, since they both use shell elements to create the geometrical model of all the elements. However the current model expands on the previous model by including the braced frame, gusset plates, and the angle members used to connect the braces to the gusset plates, see Figure 4-5. The boundary conditions are modified to closely match the experimental setup ones. The restraints are now applied to the bottom end of each column, together with the base stiffeners edges, and all the nodes are pinned to the ground. The displacement load is still applied to one single reference point as before, but the reference node is now tied to the portion of the West column outside flange delimited by the column transverse stiffeners. The material models used are still the same as described in 3.3.2.

The results of the numerical simulations were satisfactory and confirmed the validity of the design, while no additional issues where highlighted by the detailed analyses.

4.5 Testing Apparatus

4.5.1 Strong Floor

The strong floor in the TVG Structural Engineering Laboratory is a 30” thick reinforced concrete slab. Pairs of 1 3/4” through holes allow anchoring of members to the floor by threaded

rods. The holes are distributed on a rectangular grid, spaced 40 inches in both directions. Each set of two holes is designed for a maximum load perpendicular to the floor of 125 kips.

4.5.2 Lateral Bracing

Lateral bracing is provided at both columns of the testing frame, detailed drawings shown in Appendix A, while a sketch of the assembly is shown in Figure 4-6.

The bracing consists of a truss-like frame that surrounds the column. Two W14X26 steel members serve as vertical elements of the truss. These are attached to the two short built-up double channel beams resting on the floor base plate with four 7/8" A325 structural bolts. The beams are fixed to the base plates by the rods running through the strong floor.

One L3X3X1/4 (horizontal) and one L4X4X1/2 (diagonal) on each of the W14X26 flanges complete the truss structure. The horizontal angles are bolted directly to the column flange with two 5/8" A325 structural bolts at each end, while the diagonals are attached with three ¾" A325 bolts to gusset plates CJP welded to the column flanges.

Bracing force is provided to the testing frame by two 1'x1' steel bearing plates that cantilever in from the truss vertical members. The plates are connected to the webs by four 3/4" threaded rods, fastened by one nut on each side of the W-section web to allow for precise fitting of the bearing plates against the testing frame. To reduce friction between the bearing plates and the braced columns, a sheet of PTFE plastic is used.

4.5.3 Reaction Frame

The reaction frame supports the actuator on West side and is designed to provide the necessary reaction forces. Detailed drawings are attached in Appendix A, while a schematic elevation of the frame is shown in Figure 4-7.

The actuator attaches to a W14X145 transfer beam with four 1-1/2" high-strength rods. In order to minimize deformations due to the large concentrated tensile force from the rods, transverse

stiffeners have been added to the W14 beam. The stiffeners also reduced the effect of prying due to flange deformation.

The transfer beam distributes the total force from the actuator to two equal triangular trusses, through a bolted connection to the truss columns with eight 7/8” A490 bolts on each side.

The columns are chosen from members available in the testing facility and are W12X120 sections. The diagonal members are W18X65 sections, which were also available in the structural laboratory. Both members are connected to the strong floor through a floor beam. The columns are connected to the floor member with two 1 1/8” A490 bolts. The diagonal truss element is connected with slip-critical connections to the column and the floor beam. Each connection required ten 7/8” A490 bolts.

The W10X100 floor beam – specifically designed for this project – is connected to the strong floor by six 1-1/2” Grade B7 rods. The rods are pretensioned in order to avoid slipping between the reaction frame and the floor.

4.5.4 Transfer Plate

A 2-1/8” thick A36 steel plate is used to attach the actuator to the West corner of the testing frame (Figure 4-8). The plate is designed to be connected to the actuator with four 1-1/2” rods, while eight 3/4” Grade B7 threaded rods transfer the load from the plate to the flanges of the West column. Long-slotted holes are provided for the 3/4” to allow leveling of the actuator and for easiness of construction.

During the design, it was noted that the large concentrated forces transferred from the bolts in tension to the flange of the W8X40 columns of the testing frame would cause significant local deformations. To prevent this situation it was decided to run the 3/4" threaded rods through both the flanges of the columns and pretension them against each one of the surface. Square plate washers (2½x2½x5/16) were included to increase the bearing surface. The two bottom rods, however, could only be fastened to the outermost flange only, due to the presence of the gusset plate, and they were replaced by 7/8” A490 bolts. The eccentricity in the connection stiffness

caused by this distribution of bearing forces was deemed negligible for this application. A drawing of the connection just described is shown in Figure 4-9.

4.6 Instrumentation

The response of the specimens was measured with several instruments, which included uniaxial strain gauges, rectangular strain rosettes, linear variable differential transformers (LVDTs) and string potentiometers (or string pots). A total of 72 data channels were recorded for each test at a rate of 1 Hz. A whitewash layer was applied onto the steel surfaces at locations where yielding was expected to happen. The whitewash, obtained by mixing lime and water, allows observation and monitoring of yielding of the painted areas.

During each test, photographs of the specimens were taken at regular intervals by a camera located on the north side of the specimen. Additional photographs were taken with a second camera during the observation pauses in the loading protocol.

The data reduction process used to obtain member internal forces and moments from the measured strains is illustrated in Appendix B.

Three types of strain gauges were used to estimate forces, moments and stress states on the specimen and the frame, all manufactured by Tokyo Sokki Kenkyuho Co. Ltd. Uniaxial strain gauges of type FLA-3-11 (gauge factor 2.12) were used to measure strains in one direction on the testing frame columns and beams, and the four braces. Rectangular strain rosettes of type FRA-3-11 (gauge factor 2.12) were used on braces #3 and #4 flanges and webs to obtain the full strain state including shear at these locations. Special post-yield strain rosettes YEFRA-5-11, capable of measuring strains up to about 10-15%, were used on the shear panel webs. All the strain gauges are three wires, temperature-integrated gauges. For the installation of the gauges the steel surfaces were prepared by removing the mill scale and then sanding down to a 220 grit. The gauges were installed using the manufacturer recommended adhesive. Drawings of the three types of sensors are shown in Figure 4-10.

Three LVDTs (Measurement Specialties, Inc., model HR2000) with ±2 inches range were installed across the shear panel to measure overall shear deformation of the panel, and one another LVDT was attached to the testing frame to measure the absolute drift. Two string pots (UniMeasure, model P1010) with a range of 10 inches were used across the testing frame to measure the overall frame deformation.

4.6.1 Actuator Instrumentation

The actuator used for loading is equipped with a load cell to measure the load transferred into the frame, and an LVDT that measures the actuator elongation. The measurement of this LVDT was used as feedback for loading rate control.

4.6.2 Specimen Instrumentation

Each shear panel was instrumented with three strain rosettes of type YFLA-5-11 on the south face. The sensors were installed on three of the sub-panels: center-middle, left-middle and top-center. For the specimens with perforated webs, the rosette was installed one inch away from the perforation edge in the horizontal direction, see Figure 4-11(a). For the panels without perforations the rosette was installed in the center of the sub-panel as shown in Figure 4-11(b).

In addition to the strain measurements, three LVDTs were installed on each panel to estimate the average shear deformation of the rectangle bounding the panel (the corners of this rectangle are defined by the intersection of the panel flanges). The LVDTs measured the change in length across the two diagonals and the top side of said rectangle as shown in Figure 4-12. This arrangement allows to calculate the average shear angle of the panel.

4.6.3 Braces Instrumentation

All the four braces in the frame were each instrumented with four linear strain gauges at one location. The gauges were installed 3/4 inch from the edge of each flange on the outer face as shown in Figure 4-14. This arrangement allows to estimation of the axial force, strong axis bending moment and weak axis bending moment for each brace.

Additionally, two of the braces are equipped with four strain rosettes each at the same location (Figure 4-14). These measurements of the complete two dimensional stress state on both the flanges outer faces and web allows to calculate an estimate of the strong and weak axis shear forces, and torsional moment. For the derivation see Appendix B. This instrumentation scheme was used to investigate the magnitude of any secondary moments that could arise in the braces under large drifts and after the panel loss of stiffness.

4.6.4 Columns Instrumentation

The two columns of the braced frame were instrumented with linear strain gauges outside each flange at two locations. This arrangement allows to calculate internal axial force, strong axis bending moment and shear as detailed in Appendix B. The locations chosen are located 1 foot from the beams flanges, see Figure 4-15.

4.6.5 Beam Instrumentation

The top beam of the braced frame was instrumented with six linear strain gauges. Two pairs of sensors were installed on the outside of the flanges at two locations far enough from the gusset plates edges so that shear can be assumed to be constant in within the measurement points. The remaining two gauges were installed on the outside face of the top flange in proximity of the beam-column joint. The exact location is shown in Figure 4-15. Like the column, the two pairs of gauges are used to estimate axial force, bending moment and shear in the central section of the beam, for details refer to Appendix B.

4.6.6 Drift Instrumentation

The overall drift of the frame with respect to the initial position was measured using an LVDT. The instrument was attached to the east column outer flange at the beam-column node level on one side, and to a fixed column on the other, refer to Figure 4-16. The LVDT in the actuator was not used as a measure of drift because the measurement also included the deflection due to compliance of the loading frame.

Three string-pots were also installed on the braced frame to measure the overall shear deformation. Two instruments measured the change in length along the two diagonal across the frame (Figure 4-13), the other string pot was installed between beam-column nodes along the top beam.

4.7 Loading Protocol

The load was applied to the braced frame through the transfer plate bolted to the top-west node. This setup requires the top beam to transfer a portion of the applied load to the east corner through axial force. This differs from what is likely to happen in a real structure where a slab would distribute the horizontal forces. However, since the effect on the BDSP system behavior and performance would be negligible this setup was deemed valid by the author. An alternative setup with the load applied separately to both top nodes was also explored. However, it was discarded due to laboratory space limitations on the setup footprint.

The lateral drift measured by the drift LVDT on the east corner was the control parameter used for the displacement controlled loading. The actuator internal LVDT was used as feedback for the loading rate, therefore, given the compliance of the loading frame, a systematic difference exists between the chosen loading rate and the actual drift rate of the frame.

The loading protocol used for testing is based on the ATC-24 loading protocol (ATC 1992). Figure 4-17 shows the lateral drift history for the first 24 cycles, while Table 4-3 lists the basic parameters for each set of cycles at constant amplitude. The protocol has six initial cycles at drift amplitude lower than yield drift δ_y (three cycles at $1/3\,\delta_y$ and $2/3\,\delta_y$), followed by three groups of three cycles each at δ_y, $2\delta_y$ and $3\delta_y$, followed by groups of two cycles with peak drift increasing by δ_y at each step until the end of the test. The number of cycles for each test varied depending on the stiffness degradation and damage accumulation observed.

It is worth noting at this moment that predicting the yield drift, which defines the loading protocol amplitude, requires very accurate numerical models. The finite element simulations of the

test setup, performed during the design of the experiments, allowed to get a more precise estimate of the elastic stiffness and yielding drift of the specimen than a purely analytical approach. Nevertheless, small differences between the predicted and experimental yielding drift were still present. These differences resulted in a loading history slightly offset from the targeted one.

The loading rate during the testing of each specimen was increased throughout the tests as the drift amplitude increased. The initial value of the loading rate for the first six cycles was 0.04 in/min (about 0.02 in/min drift rate, see above). The rate was then progressively increased, up to a maximum of 0.30 in/min for the tests with larger maximum drifts.

Table 4-1: Specimens table

Test No	Specimen ID	b (in)	a (in)	t_w (in)	ρ	t_s (in)	d_s (in)	$V_{y,sp}$ (kip)	K_{BDSP} (kip/in)	δ_y (in)
1	BDSP-20-2-40	20.0	13.3	1/8	0.40	3/16	1	30.3	1882	0.038
2	BDSP-24-2-40	24.0	16.0	1/8	0.40	3/16	1	36.4	1882	0.045
3	BDSP-20-2-25	20.0	13.3	1/8	0.25	3/16	1	37.9	2353	0.046
4	BDSP-24-2-25	24.0	16.0	1/8	0.25	3/16	1	45.5	2353	0.055
5	BDSP-20-3-40	20.0	13.3	3/16	0.40	3/16	1 1/2	49.6	1882	0.049
6	BDSP-20-2-0	20.0	13.3	1/8	0	3/16	1	55.3	3137	0.060
7	BDSP-24-3-40	24.0	16.0	3/16	0.40	3/16	1	54.6	1882	0.058
8	BDSP-20-3-25	20.0	13.3	3/16	0.25	3/16	1 1/2	56.9	2353	0.059
9	BDSP-20-4-40	20.0	13.3	1/4	0.40	1/4	1 3/4	60.6	2510	0.059
10	BDSP-24-2-0	24.0	16.0	1/8	0	3/16	1	60.6	3137	0.072

Table 4-2: Testing parametric space

Test No	$b = 20\ in$			$b = 24\ in$		
$t_w = 1/8\ in$	**1**	**3**	**6**	**2**	**4**	**10**
$t_w = 3/16\ in$	**5**	**8**		**7**		
$t_w = 1/4\ in$	**9**					
$\rho =$	0.40	0.25	0.00	0.40	0.25	0.00

Table 4-3: Cyclic loading protocol parameters

First cycle number at new drift level	1	4	7	10	13	16	18	20	22	24
Number of cycles	3	3	3	3	3	2	2	2	2	2
δ/δ_y	1/3	2/3	1	2	3	4	5	6	7	8

Figure 4-1: T. Galambos Structural Engineering Laboratory with first BDSP specimen

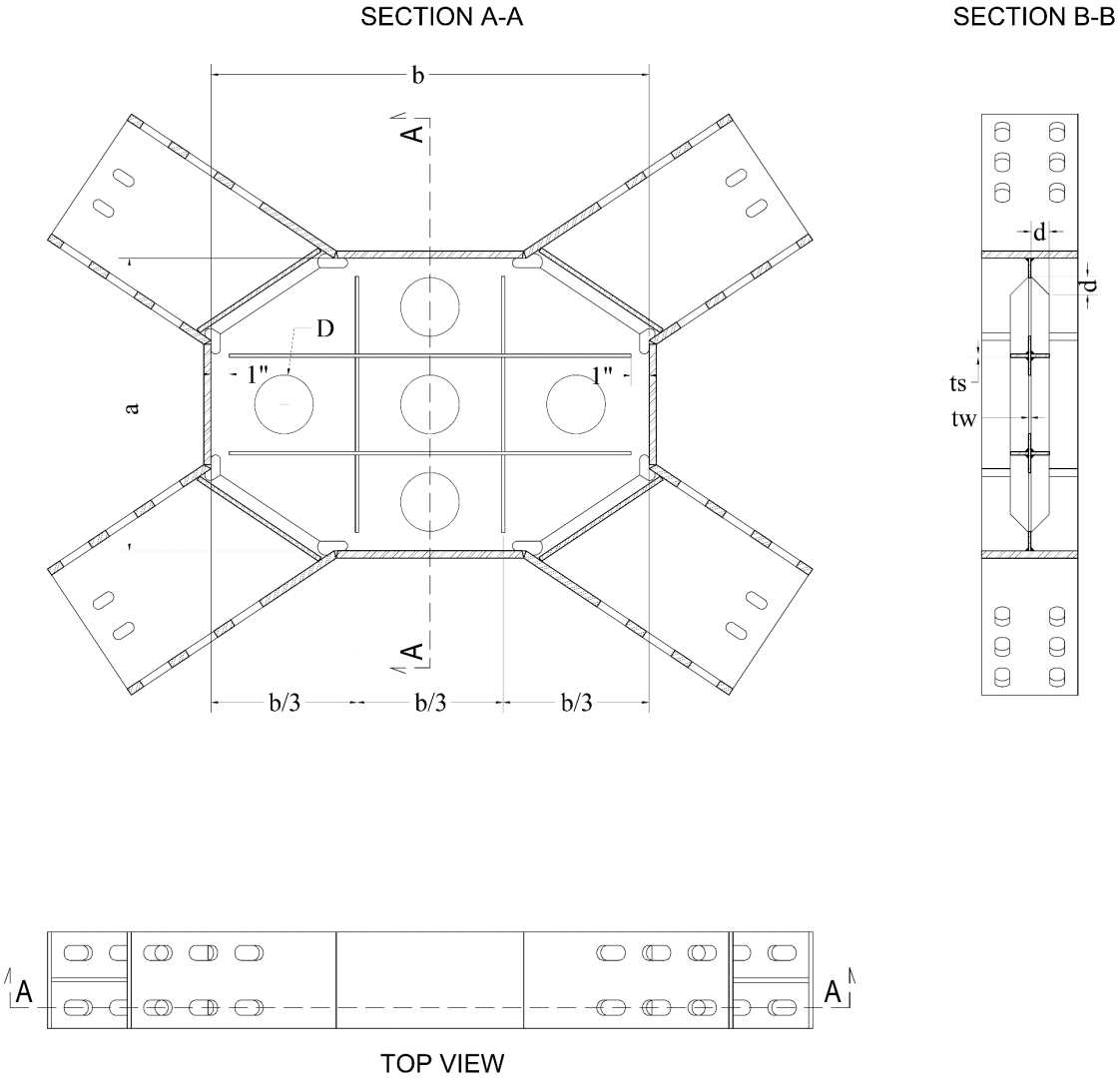

Figure 4-2: Typical BDSP Specimen and dimensions

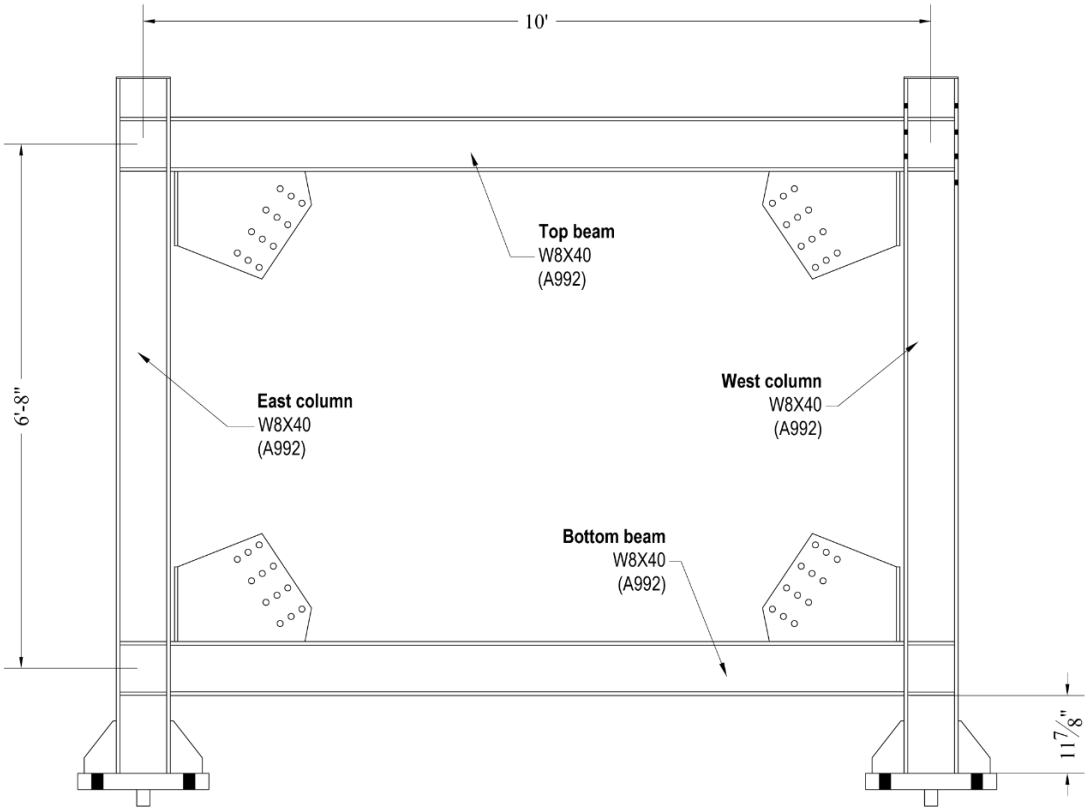

Figure 4-3: Braced frame elevation view

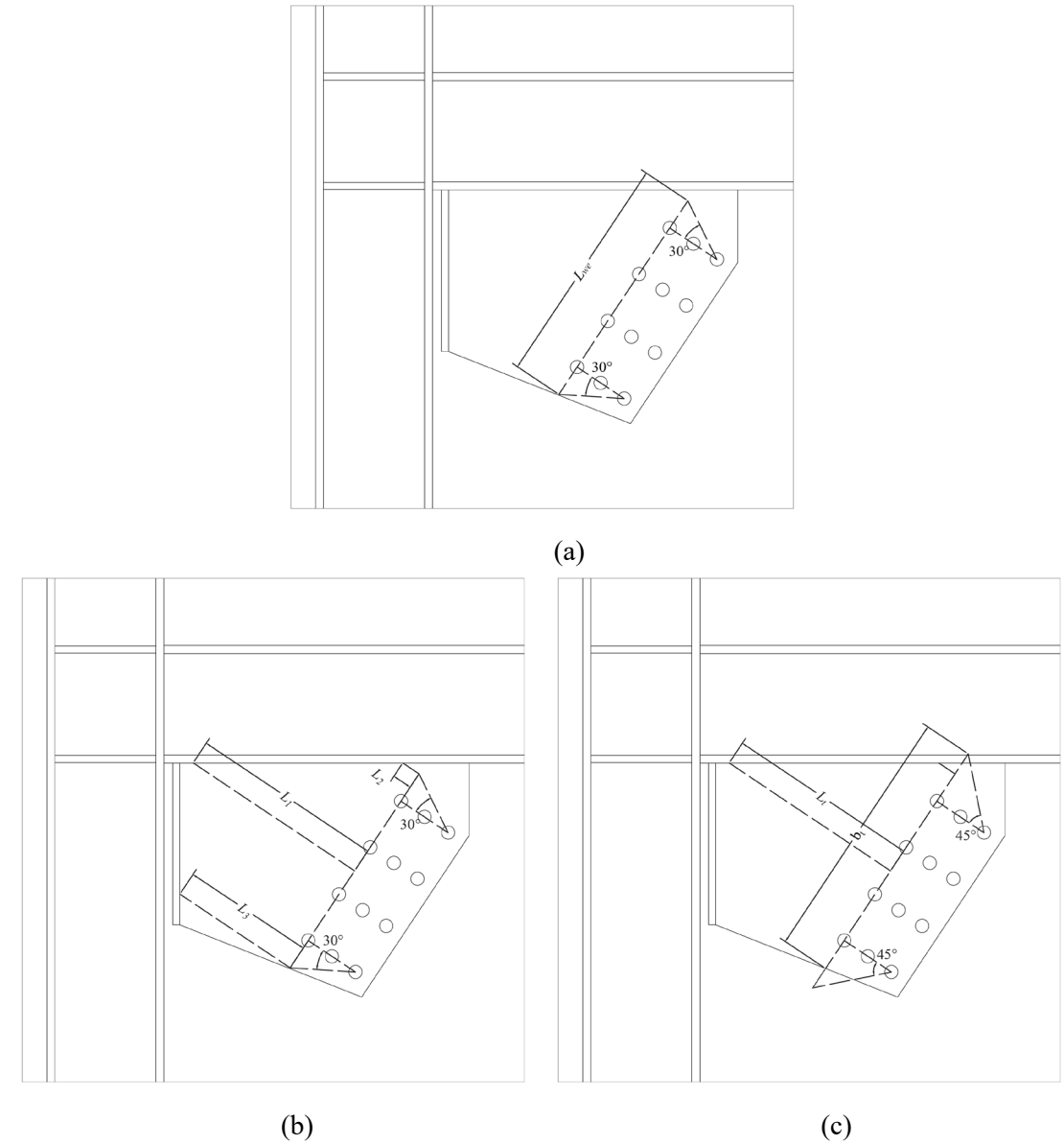

Figure 4-4: Gusset plate design dimensions
(a) Whitmore width; (b) Thornton Method; (c) Modified Thornton Method

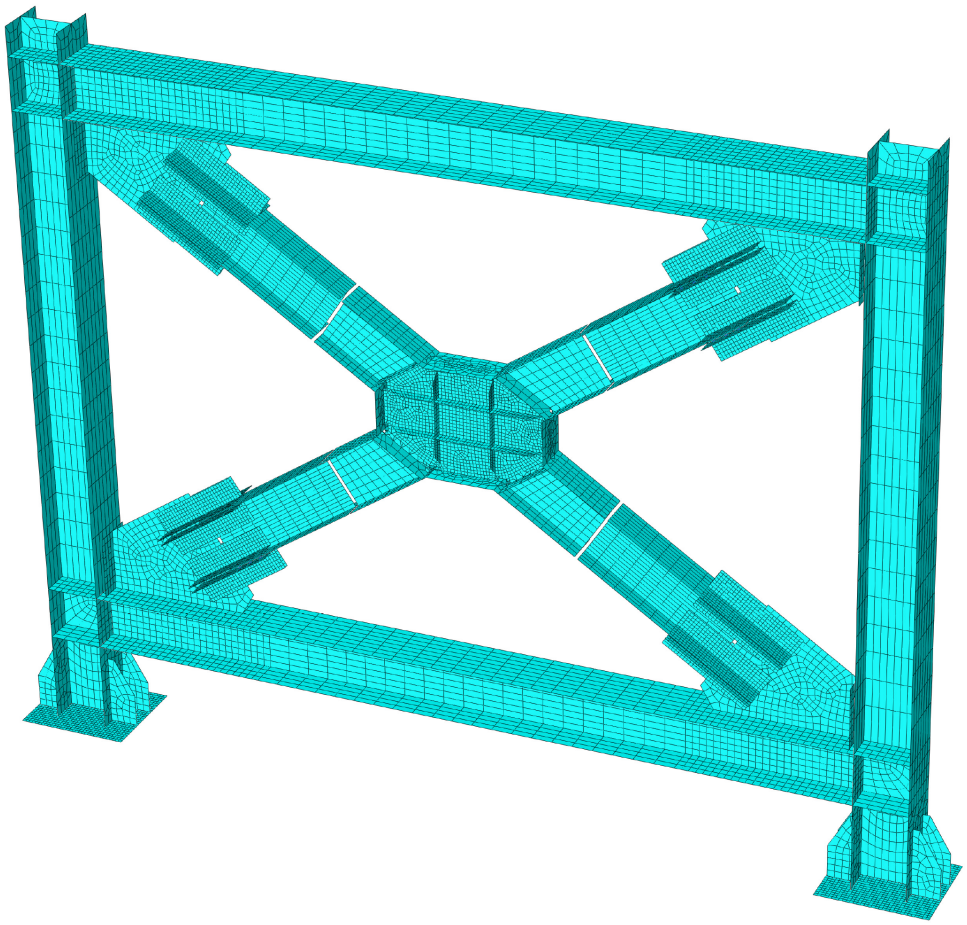

Figure 4-5: Experimental setup finite element model

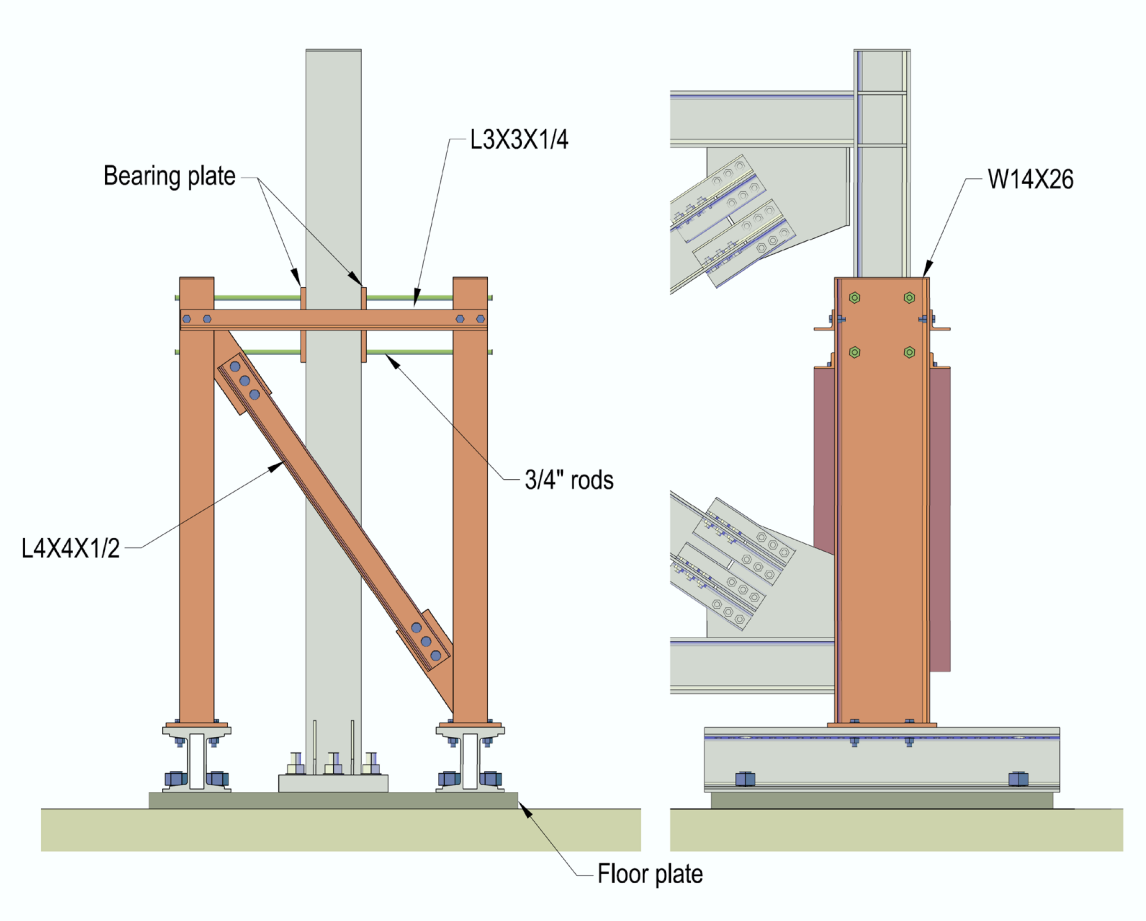

Figure 4-6: Lateral bracing, side and front view

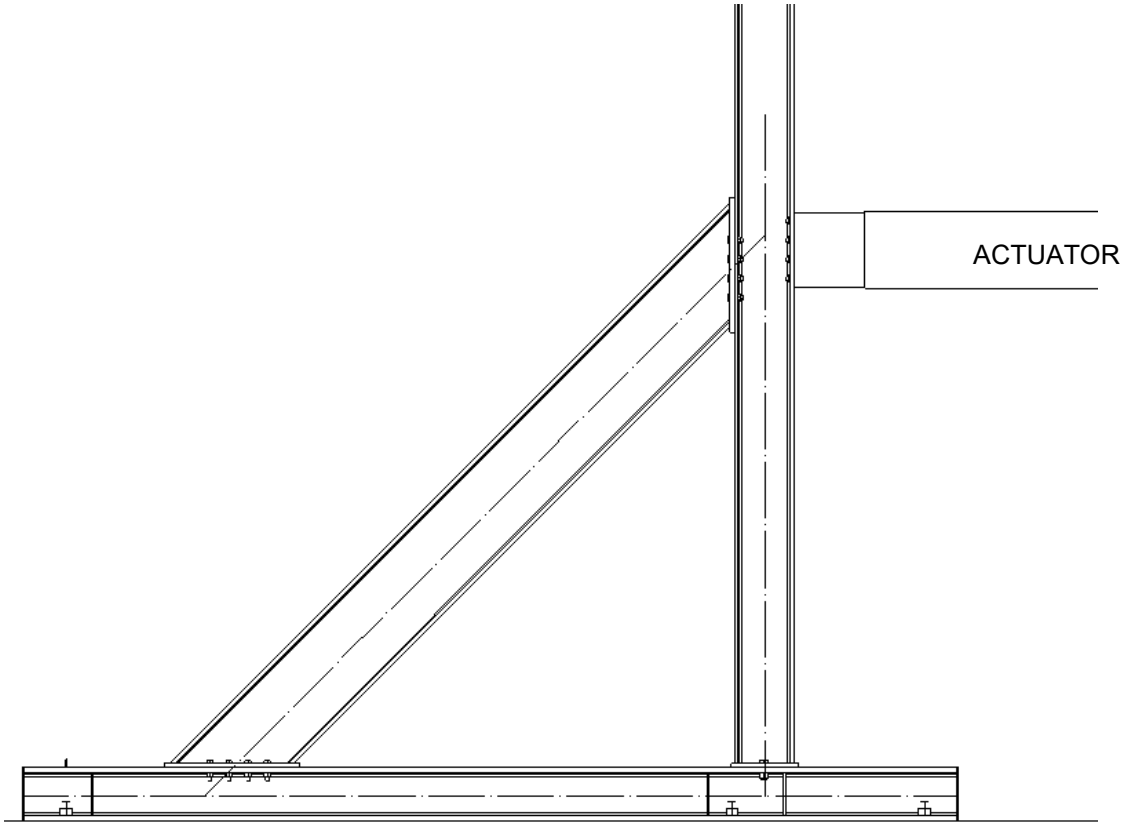

Figure 4-7: Reaction frame

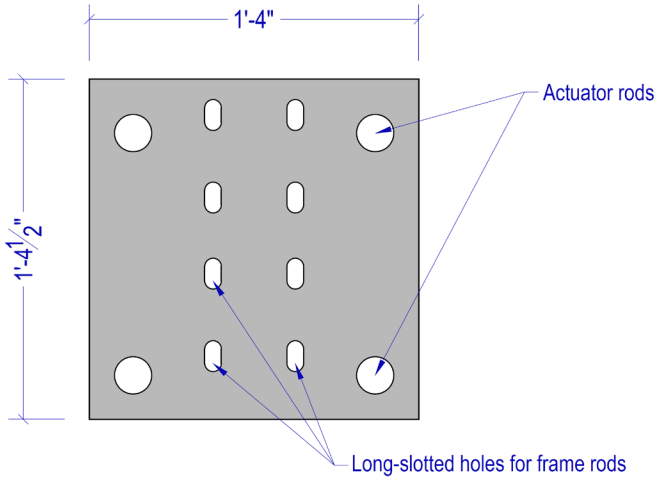

Figure 4-8: Transfer plate

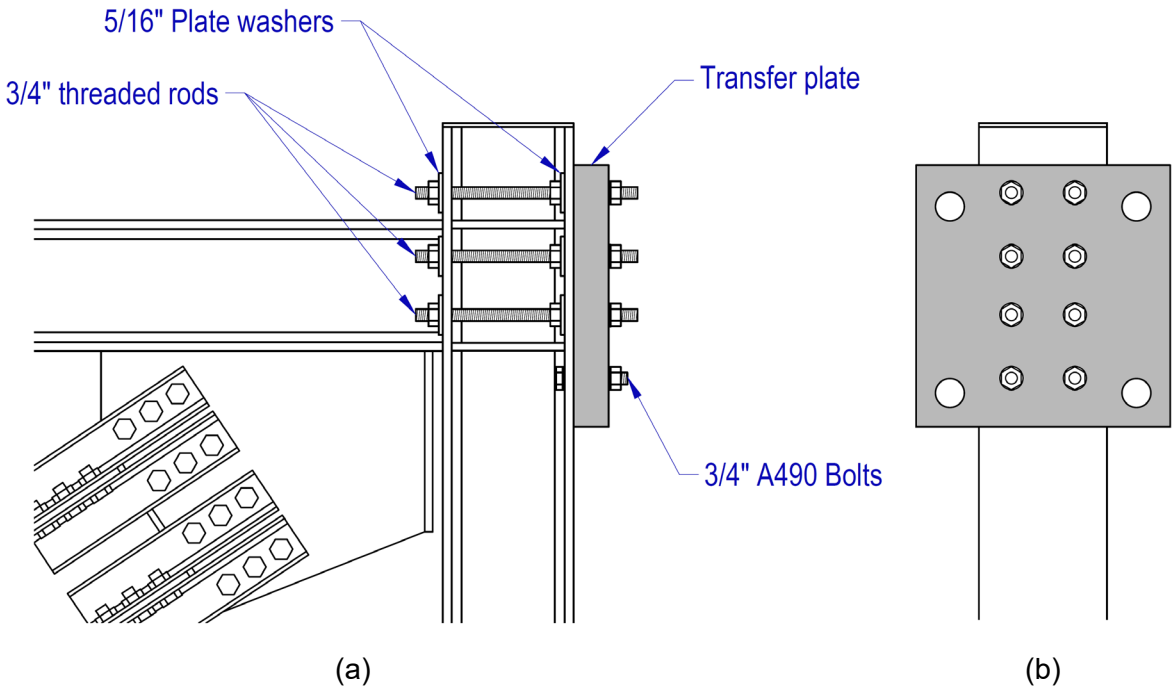

Figure 4-9: Transfer plate to testing frame connection detail: (a) North elevation; (b) East view.

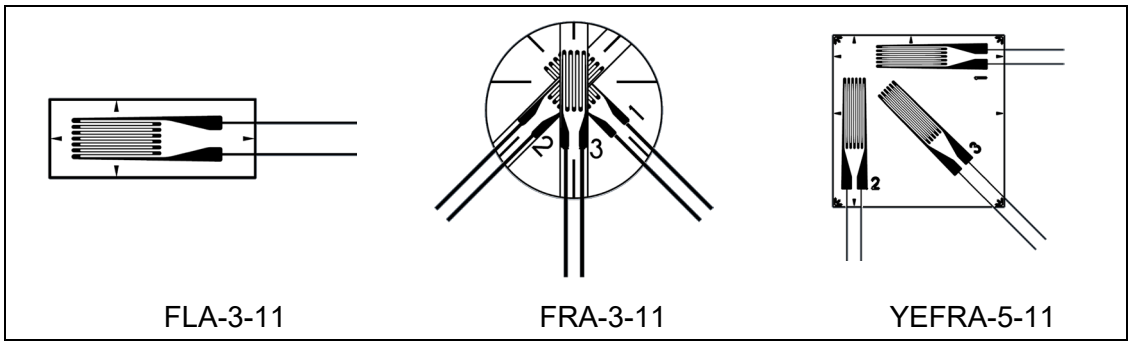

Figure 4-10: Strain gauges

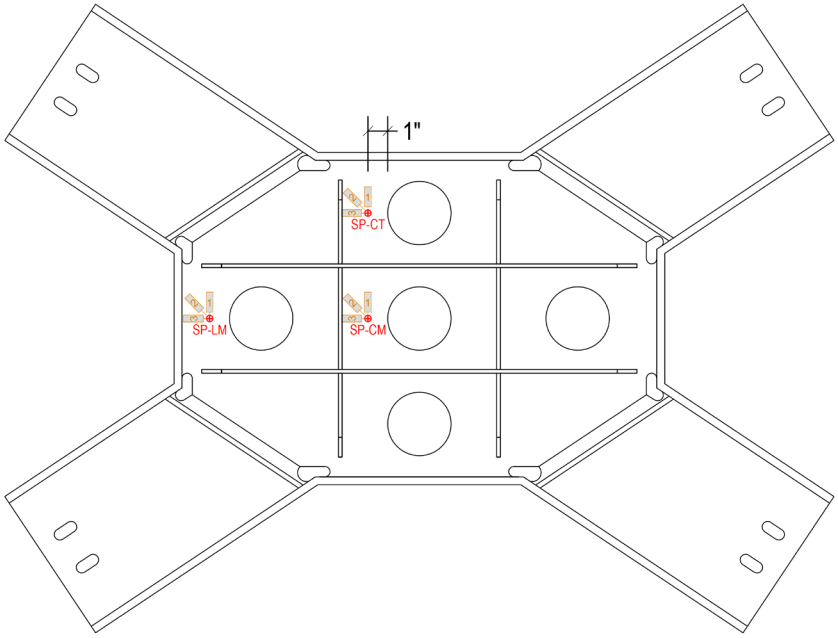

(a)

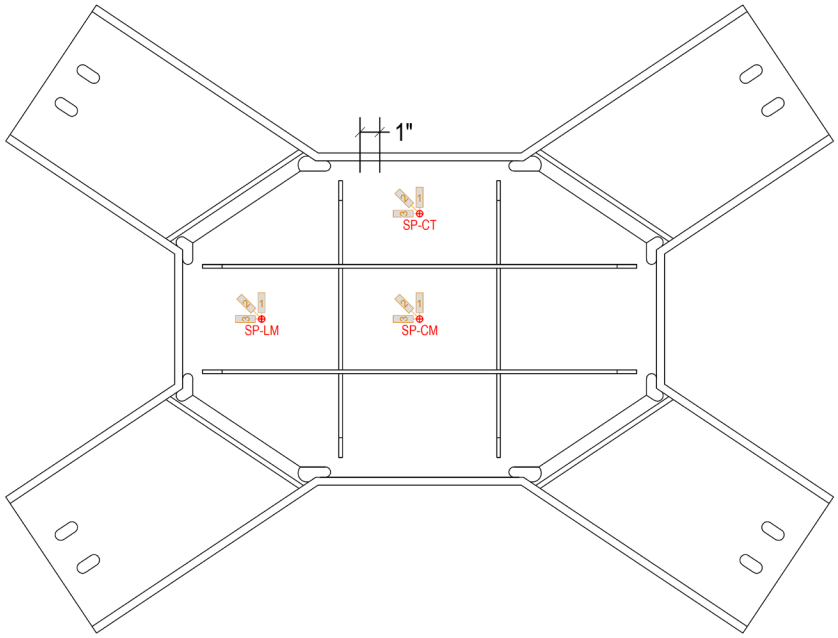

(b)

Figure 4-11: Specimens strain gauges rosettes locations
(a) Typical perforated panel; (b) Typical full panel

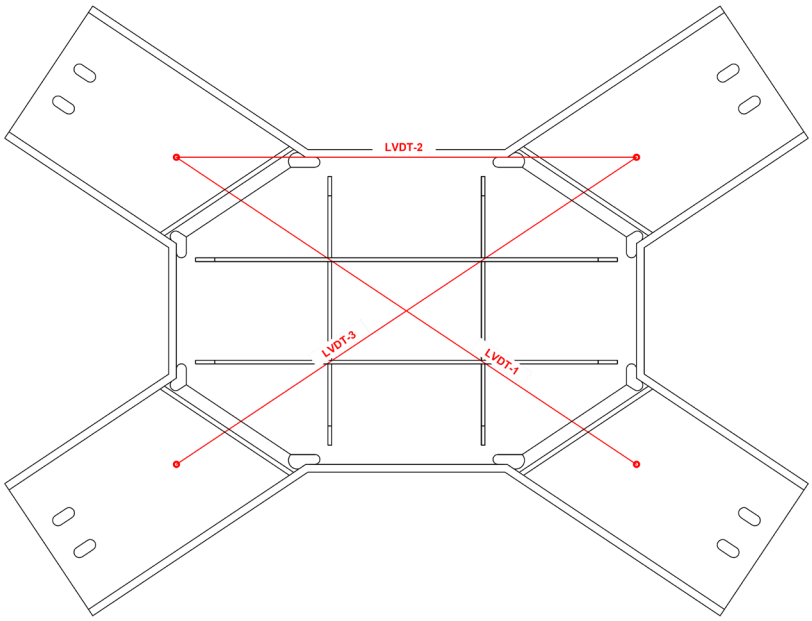

Figure 4-12: Specimens LVDT instrumentation

Figure 4-13: Diagonal string-pot installed on frame

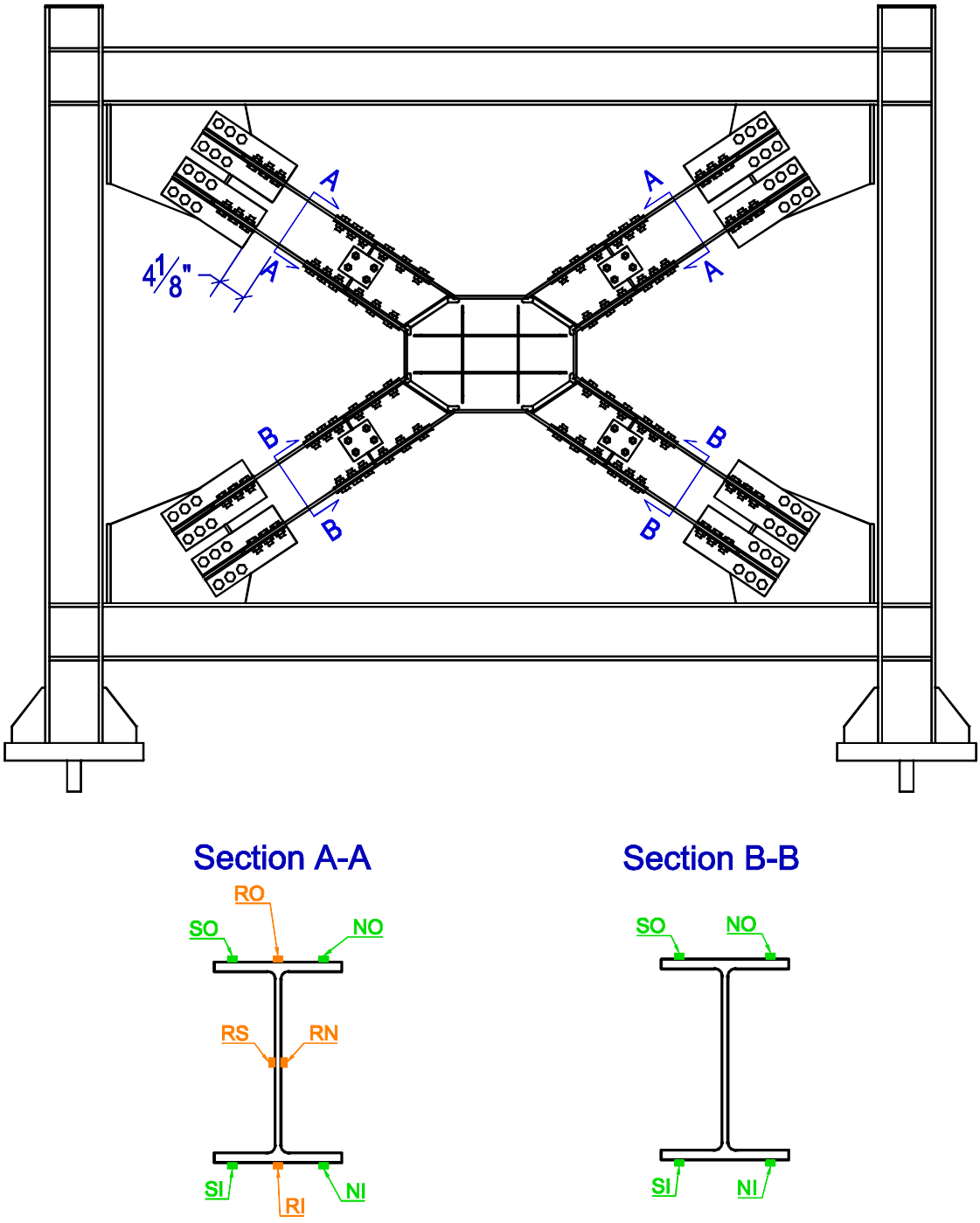

Figure 4-14: Braces strain gauges (green) and rosettes (orange) locations

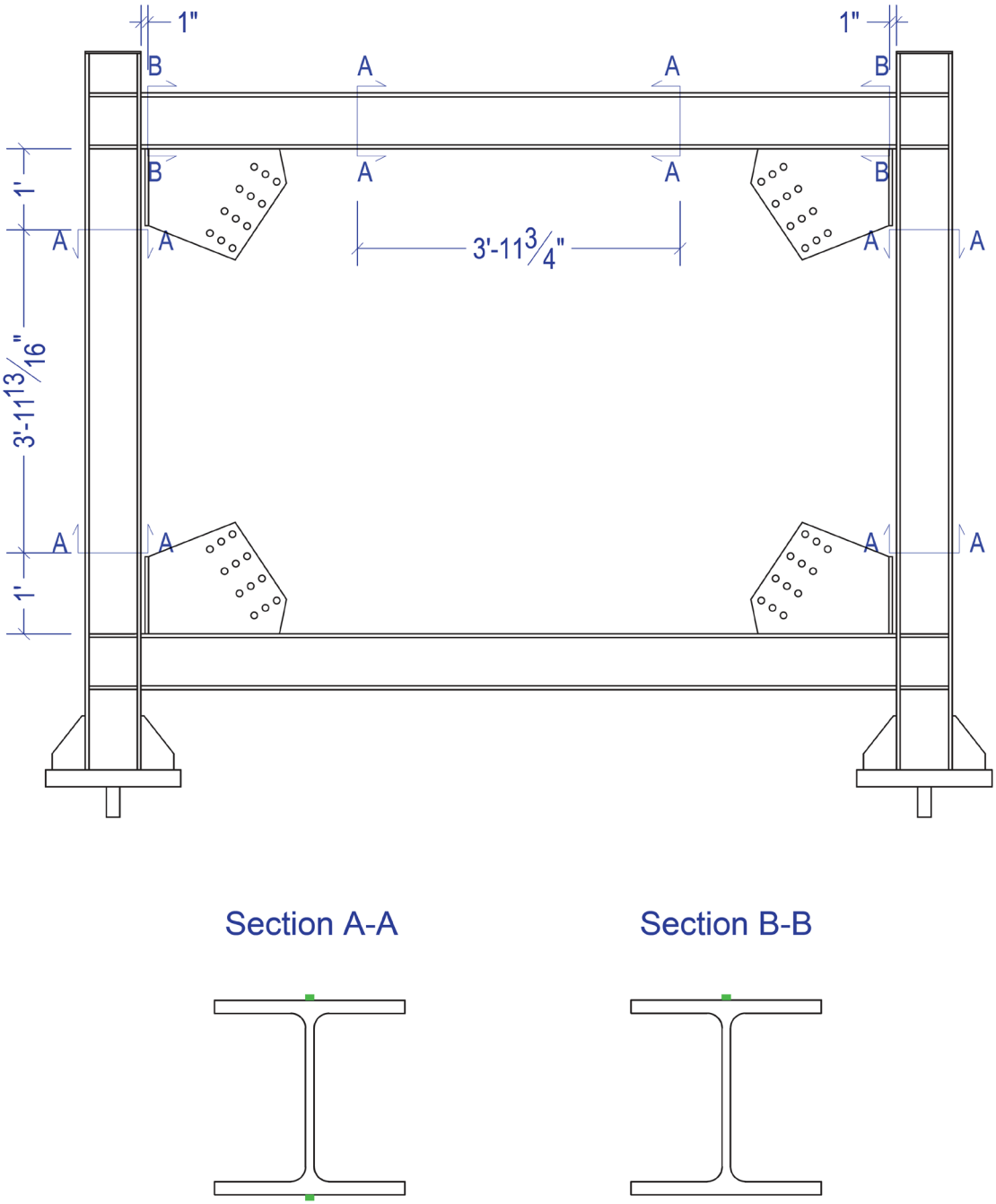

Figure 4-15: Strain gauges locations on braced frame

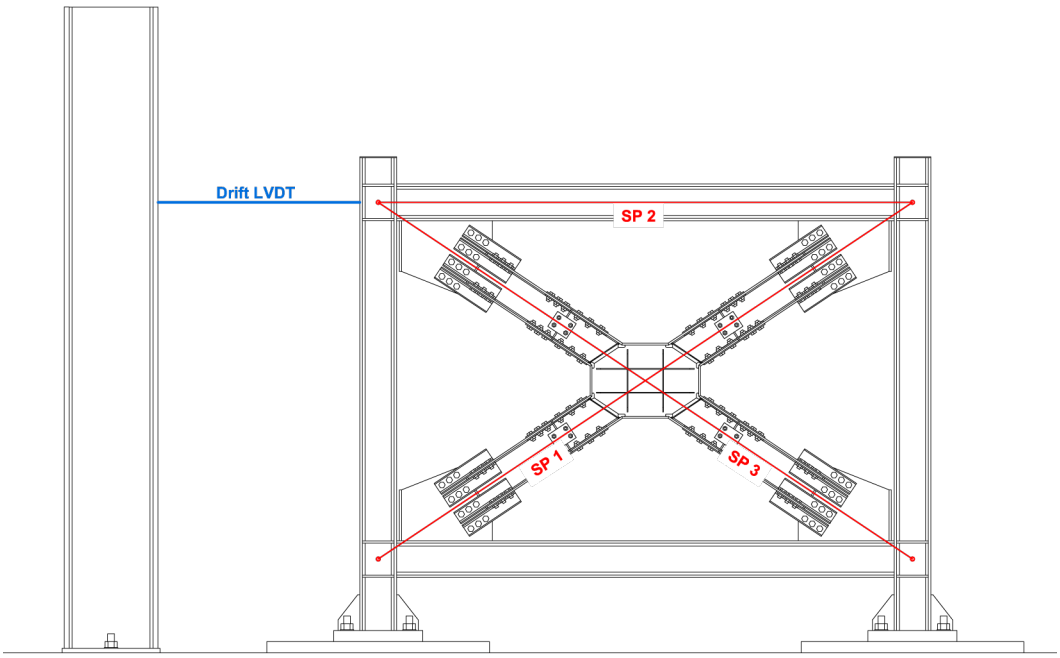

Figure 4-16: Drift instrumentation, string-pots (SP1, SP2, SP3) and LVDT

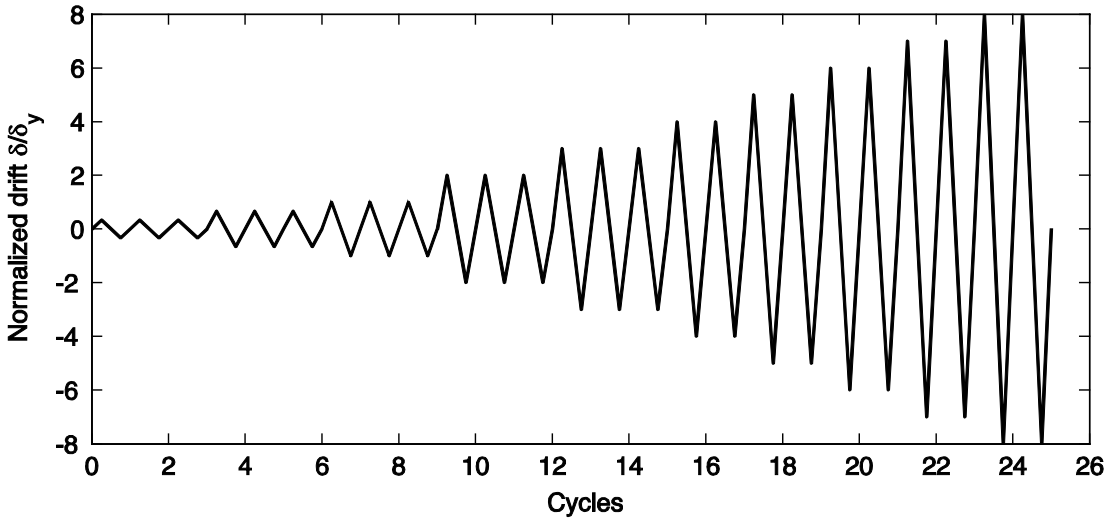

Figure 4-17: Cyclic loading protocol

Chapter 5
Experimental Results

5.1 Introduction

In this chapter the main results from the ten shear panel experiments are presented. These results include global force and displacements histories, description of the specimen performance, and observations of damage initiation and evolution. Observations were made before each lateral drift increment, therefore the exact point at which some of the damage not visible on camera occurred is not known. Chapter 6 contains a more complete analysis of the data from strain gauges and LVDTs, and provides a comparison with predictions and used models. The next two sections will introduce the names and abbreviations used in the description of the results, tables and plots, and describe the general response and main characteristics of the tests.

5.2 Nomenclature

The drift δ used as reference in the results is the braced frame absolute drift, measured as described in the previous chapter. The total lateral force V is the one measured by the actuator load cell and is therefore the sum of frame shear V_f and panel shear V_{sp}.

Yielding of the panels during the experiments was observed through the flaking of the whitewash applied to the webs. Out-of-plane displacements of the panel webs under large drifts was qualitatively evaluated during the test inspections.

The transverse stiffeners divide each shear panel in 9 subpanels, which are used as a reference system on the panel to track the initiation and evolution of yield and damage. Each subpanel is referred to using its relative position with respect to the panel web, by combining the horizontal position (one of Left, Center, Right) and the vertical position (Top, Middle, Bottom).

The braces are numbered 1 through 4, where 1 and 3 are parallel and are respectively the lower east and upper west braces, while 2 and 4 are respectively the lower west and upper east.

5.3 Introduction and Description of Tests Response

All the specimens exhibited a similar response to cyclic loading in terms of force-drift behavior. The main stages of the system response, common to all tests, are described below and provide the framework used to present the results.

- The first portion of the force-drift curve is composed by the linear elastic region traced during the first nine cycles ($\delta \leq \delta_y$).
- After yielding of the panel web has started, the curve gets into the post-yield response of the system. This region starts with a transition region, during which the tangent stiffness of the curve at each maximum cycle drift rapidly decreases, followed by a stable region where the tangent stiffness at cycles peaks is either constant or slowly decreasing.
- As drifts increase after the transition region, out-of-plane displacements of the panel web grow in amplitude. This creates a gradual loss of stiffness in the system, which can be more or less significant depending on the specimen. In the force-drift relationships this effect is visible as a reduction in slope of the hysteresis for each cycle or pinching of the curve, which in turns reduces the enclosed area and energy dissipation. Although these out-of-plane displacements can be observed for all specimens, the point in the loading history at which they can be seen, as well as their amplitude, varies across specimens. The point in the loading history at which the loss in stiffness starts to be visible is identified by the value T_1 set equal to the number of the last cycle before the stiffness loss.
- After several load reversals, damage in the form of cracks initiate in the most strained areas of the specimen and then steadily propagate with each drift increment. The time, location and propagation speed of damage varies for each specimen. As damage spreads in the specimen, a further reduction in stiffness and peak load of each cycle can be observed.

- The inelastic in-plane shear deformation of the webs tends to localize across three aligned subpanels. In six of the specimens the shear localized along the horizontal direction (subpanels LM, CM, RM), while four panels exhibited a vertical localization of deformations (subpanels CT, CM, CB).
- When damage has spread across the panel and significant loss in stiffness has occurred, the test is terminated.

It is important to note that the lateral total force taken into analysis at this time is the force read during testing from the actuator load cell, and it is therefore the sum of panel and frame shear ($V_f + V_{sp}$); therefore, the value and time of occurrence of the peak load do not necessarily correspond to the ones of the maximum panel shear V_{Sp}.

5.4 Test 1 - Specimen BDSP-20-2-40

The data from test 1 on specimen BDSP-20-2-40 is incomplete. During the startup process at the beginning of the second day of testing, the frame was accidentally loaded past the drift level prescribed by the loading protocol. Since data acquisition had not yet started when the loading happened, it was not possible to determine what was the maximum drift the frame sustained. Due to this important deviation from the experimental loading protocol, the remaining data from this test is not used in the rest of this study. The residual drift, after the error was discovered and the frame was unloaded can be seen in Figure 5-1. The lateral force-drift plot for the rest of the test, which was completed using a different, shorter loading history can be seen in Figure 5-2; the dashed line qualitatively shows the possible path of the load-displacement curve that was not recorded.

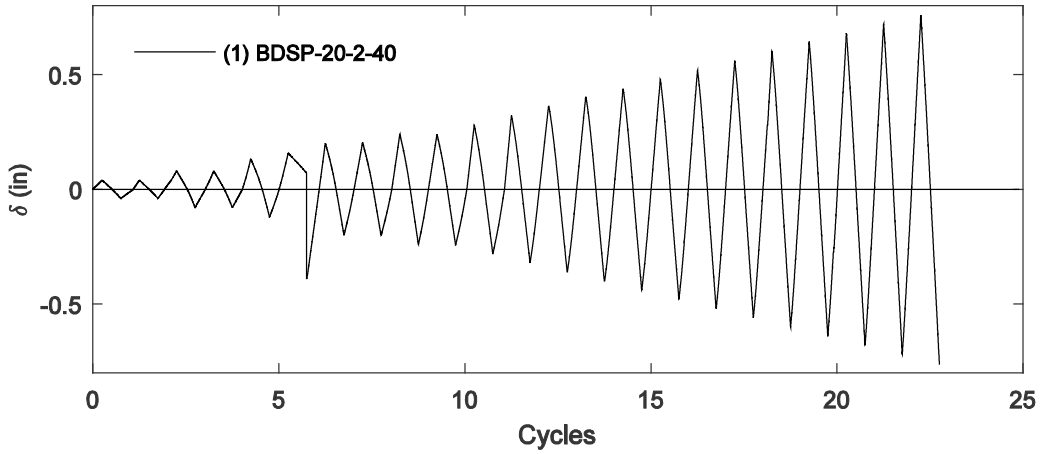

Figure 5-1: Test 1: Experimental lateral drift history

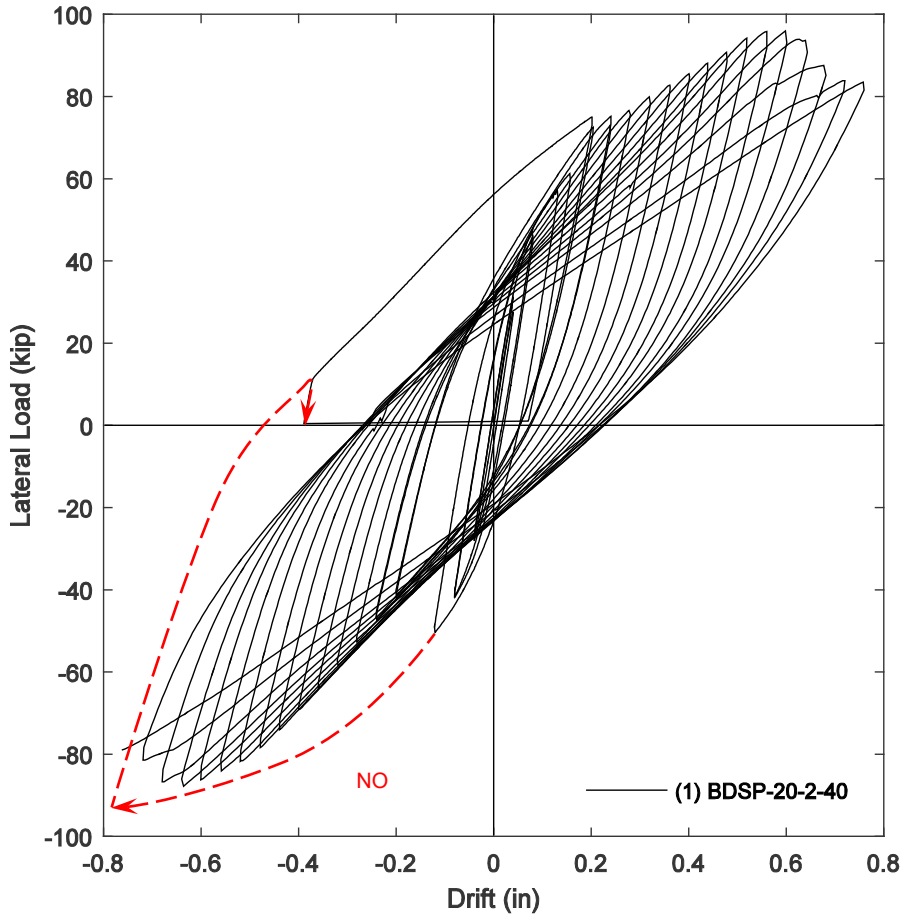

Figure 5-2: Test 1: Experimental lateral force-lateral drift response

5.5 Test 2 - Specimen BDSP-24-2-40

Test 2 on specimen BDSP-24-2-40 was completed over four days (June 11, 12, 15 and 16). The applied lateral drift history is shown in Figure 5-3 and the final lateral force-drift response is plotted in Figure 5-4. As it can be seen from the drift history plot, a mistake in the actuator control led to a small deviation from the design loading history during the negative excursion of cycle 24. However, the effect of this inaccuracy was deemed tolerable and its influence on the result was neglected.

5.5.1 Shear panel yielding observations

The panel first yielding occurred after the ninth loading cycle, when the lateral drift increased past the predicted yielding drift δ_y. Whitewash on the CT and CB subpanels started flaking during cycle 10, at a 45 degrees angle along the edges of the perforations. During the next cycle more whitewash detached in these subpanels and the CM subpanel. Some flaking also occurred at the transverse stiffener weld toe on the LM subpanel. Similar yielding regions, oriented at 45 degrees around the perforation edges, in the LM and RM subpanels were visible after cycle 13. At the beginning of cycle 18, the whitewash was also showing some yielding at the weld toe of all the four panel-to-flange welds. The yielding of the panel web progressed steadily during the next cycles in the five aforementioned subpanels, while no significant flaking was observed for the entire test in the corner subpanels (i.e. LT, RT, LB, RB). It should be noted that a precise estimate of the yielding areas boundaries was not possible at this time: the whitewash coating applied to this specimen turned out to be thicker than desired, leading to the layer flake in big chunks (roughly 0.5”). A series of pictures of the panel at different time intervals is presented in Figure 5-5. These pictures also highlight that the shear deformation in this panel is concentrated along the horizontal subpanels (LM, CM, RM), as it can be seen by looking at the relative rotation of the transverse stiffeners.

5.5.2 Total lateral force response summary

Visible stiffness degradation initiated after cycle 15, when the drift reached 4 times the yielding value. At this time, out-of-plane displacements of the panel web also became significant, as shown in Figure 5-6 and Figure 5-7 for the CT and CM subpanels. The decrease in lateral stiffness progressed slowly with each cycle, as indicated by the difference among the slopes of the hysteresis loops during the following cycles. The maximum total lateral force reached was 92.2 kips, and it was reached during the first excursion at 14 times the yielding drift (0.633 in) during cycle 36 (T=35.25). After this point, the stiffness started to rapidly decrease and the hysteresis loops became significantly narrower. The test was terminated after five more cycles. The maximum normalized drift reached during testing of this specimen was 16 times the yielding drift, equal to 0.720 in.

5.5.3 Damage initiation and evolution

Damage was first observed after cycle 29, as a ductile crack developed at the lower-right corner of the CT perforation, at a 45 degrees angle, perpendicular to the edge, Figure 5-8. A symmetric crack on the lower right corner developed two cycles later. Similar cracks at 45 degrees directions gradually developed in the following cycles in the LM, CB and RM subpanels. In the central subpanel cracks developed along the edge of the perforation at 90 and 270 degrees directions. By the end of cycle 40, cracks had formed and propagated in all four diagonal directions on subpanels LM and RM, almost reaching the weld access holes at the right and left side of the panel. In subpanels CT and CB cracks only formed on the two inner directions (225 and 315 degrees directions). The final shape of the damage in the panel web is visible in Figure 5-9, where two photographs taken at the maximum negative and positive drift are shown to clearly illustrate the length and opening of the cracks.

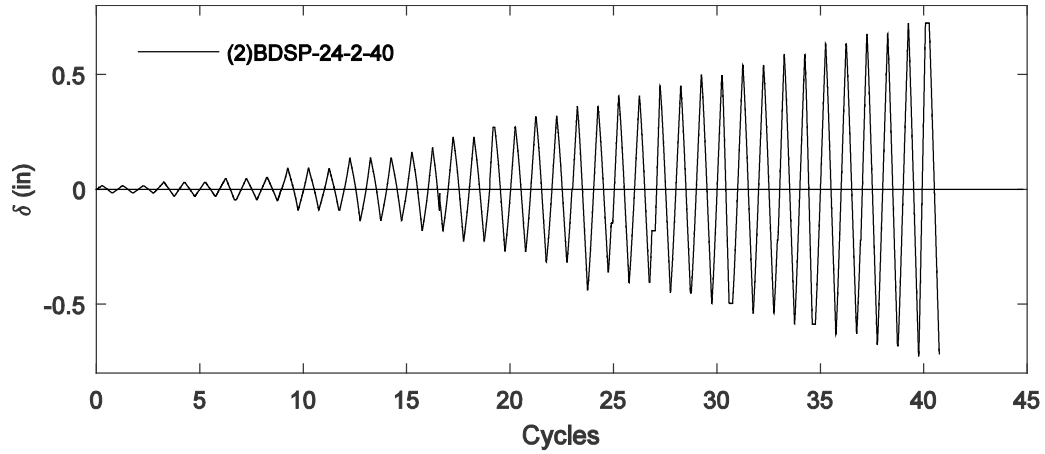

Figure 5-3: Test 2: Experimental lateral drift history

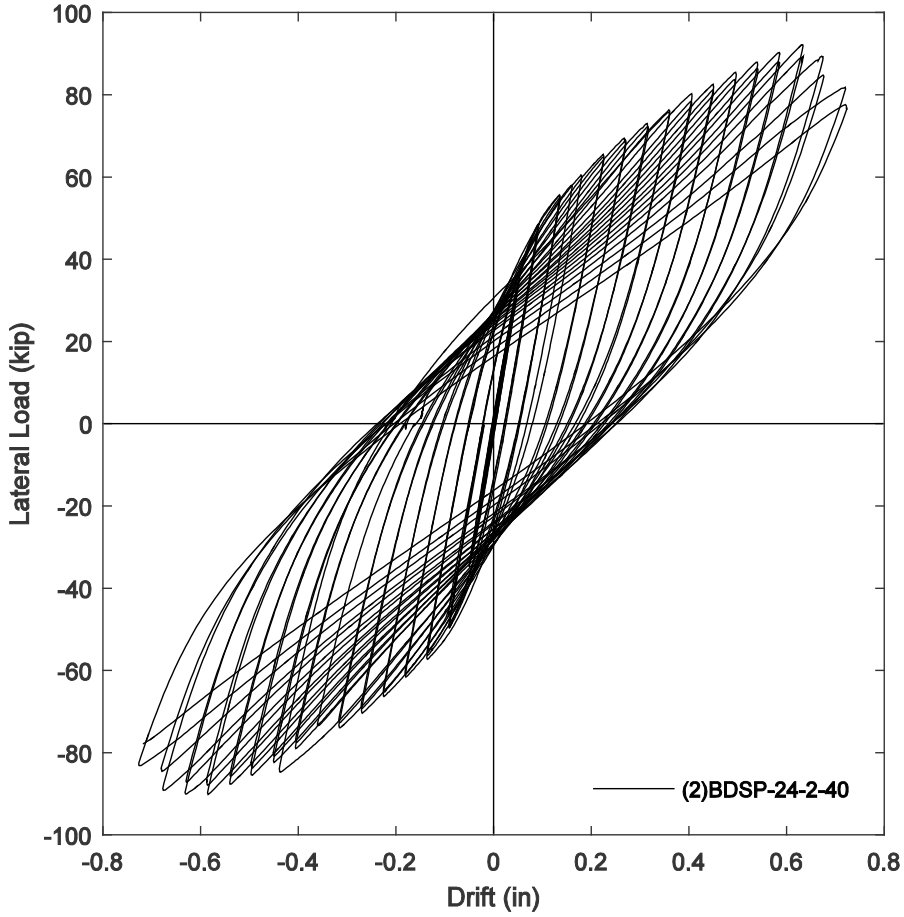

Figure 5-4: Test 2: Experimental lateral force-lateral drift response

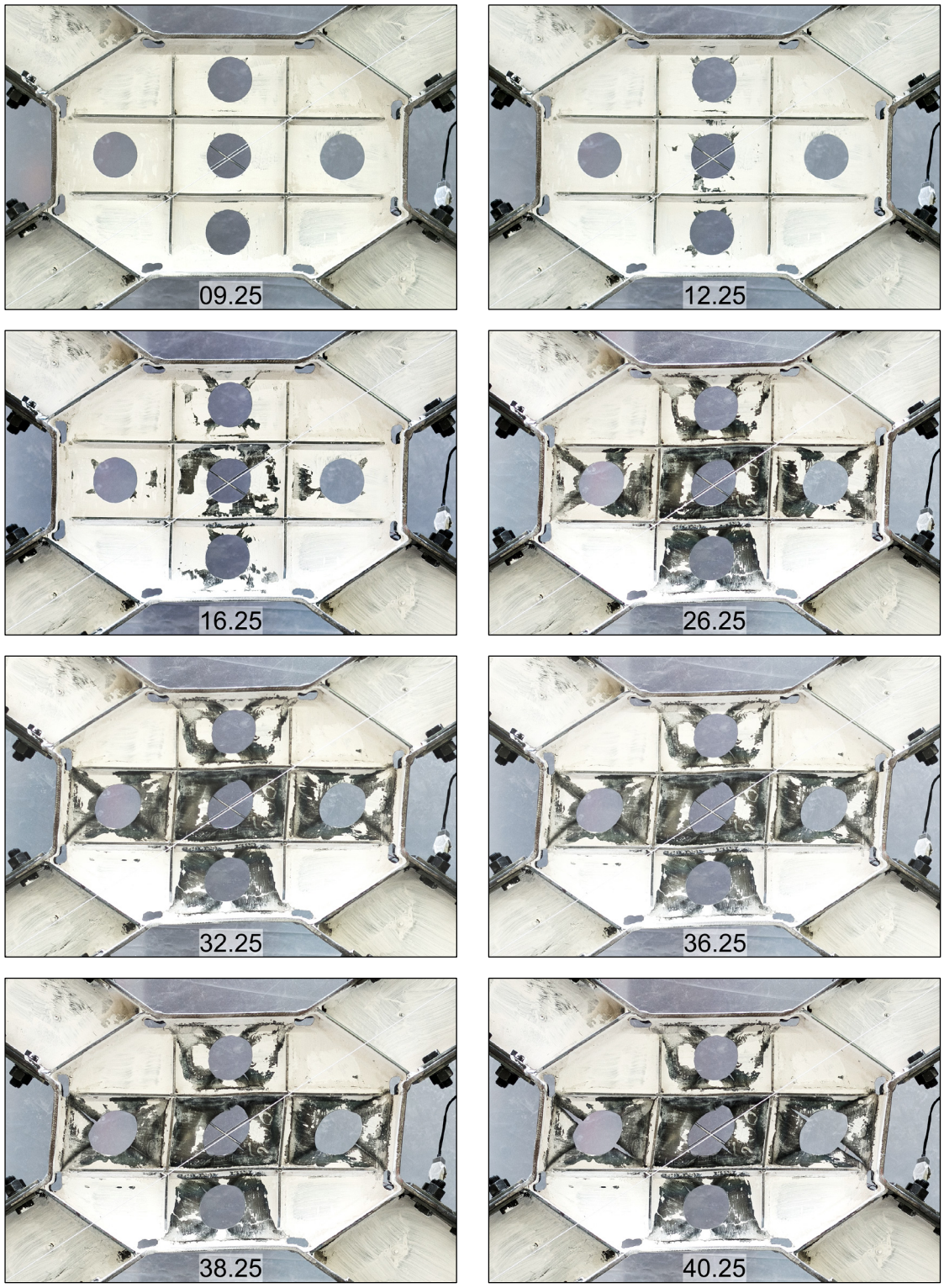

Figure 5-5: Test 2: Yielding and damage evolution

Figure 5-6: Test 2 – Out-of-plane displacements in CT subpanel

Figure 5-7: Test 2 – Out-of-plane displacements in CM subpanel

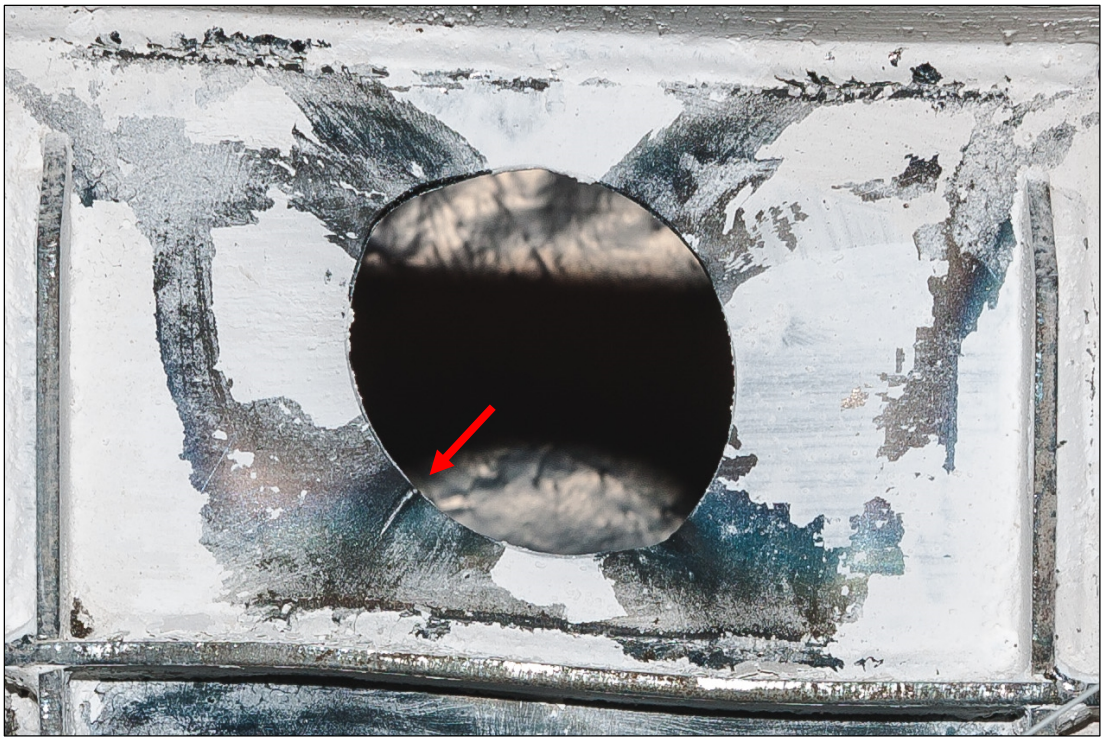

Figure 5-8: First observed damage in CT subpanel for Test 2

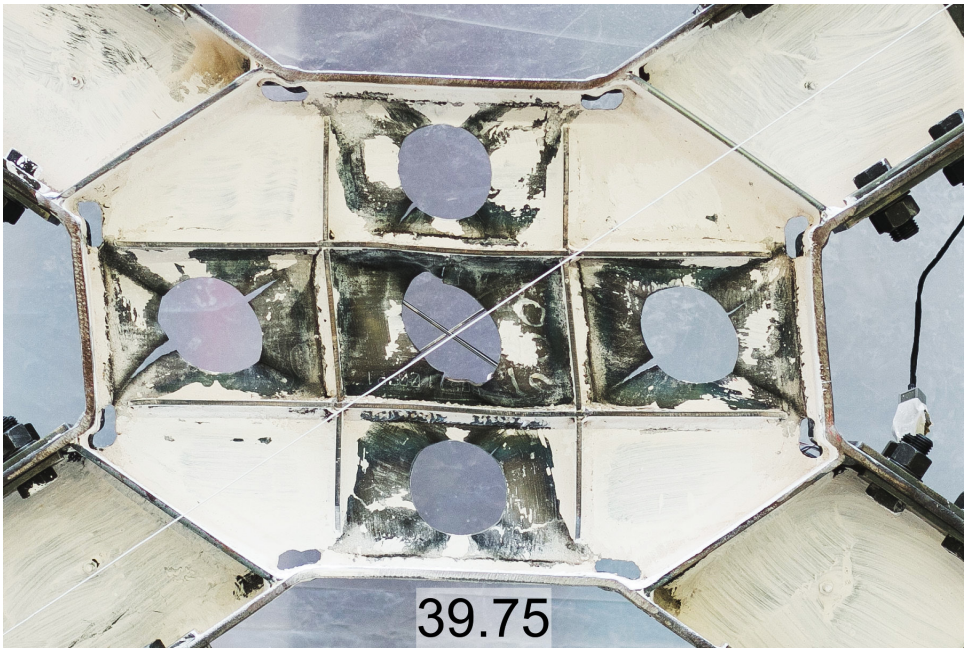

(a)

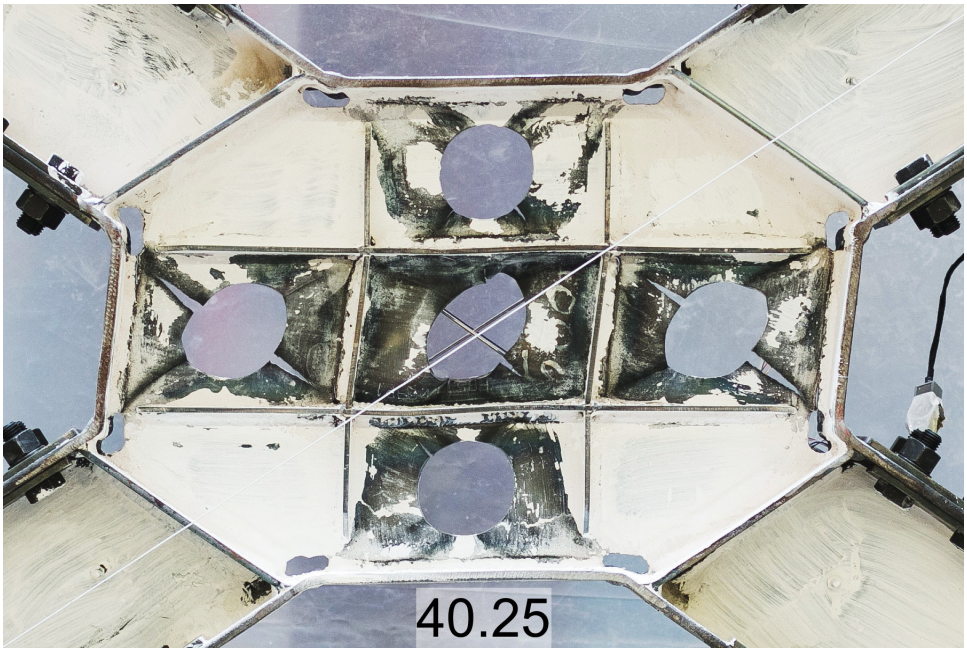

(b)

Figure 5-9: Damage of the specimen at the end of test 2
(a) max. negative drift; (b) max. positive drift

5.6 Test 3 - Specimen BDSP-20-2-25

Test 3 on specimen BDSP-20-2-25 was completed over four days (June 19, 22, 23 and 24). The applied lateral drift history is shown in Figure 5-10 and the final lateral force-drift response is plotted in Figure 5-11. The test was terminated after the negative excursion of the 39th cycle. The maximum lateral drift reached was 0.675 in, equal to 15 times the design yield drift $\delta_y = 0.045\ in$.

5.6.1 Shear panel yielding observations

The panel first yielding was observed during the 11th loading cycle. Some flaking of whitewash was visible on the CM subpanel, both around the perforation edge and in the middle of the web. Minor flaking also occurred at some of the toes of the stiffener welds. During cycle 14, more whitewash detached in the CM subpanel around the top and bottom edges. Yielding in the other subpanels was visible by the end of the 19th cycle; at this point, inelastic strain were also highlighted at the toes of the panel-flanges welds. At the end of the 30th cycle, most of the whitewash in the central subpanel had flaked. In the other subpanels, yielding was more pronounced along diagonal lines, with inclination parallel to the braces, that extended from points of maximum strain along the perforation edges. The yielding pattern remained mostly unaltered for the following cycles. A series of pictures of the panel at different time intervals is presented in Figure 5-12. Similarly to test 2, the shear deformation in this specimen was also concentrated along the horizontal subpanels (LM, CM, RM).

5.6.2 Total lateral force response summary

Stiffness degradation was noticeable after cycle 19, that is when the drift reached 6 times the yielding value. Out-of-plane displacements were observed at the same time, Figure 5-13 shows the amplitude of the out-of-plane displacements during the 21st cycle (t = 20.75). The maximum total lateral force reached was 95.1 *kips*, and it was reached at t = 31.25, peak of first excursion at 12 times the yielding drift, 0.538 in. The test was terminated after both, left and right panel-flange

weld fractured across the entire base metal length. The maximum normalized drift reached during testing of this specimen was 15 times the yielding drift.

5.6.3 Damage initiation and evolution

Damage was first observed during cycle 26, when two cracks developed at the lower-left and upper-right diagonals of the CM perforation perpendicular to the edge. Symmetric cracks developed two cycles later in the same subpanel. During the 30th cycle, a crack was observed at the top of the right panel-flange weld toe (RM subpanel). During cycle 33 a similar crack was observed in the symmetric weld on the left side. Between cycles 33 and 36, cracks at 45 degrees angle initiated at all perforations of the remaining subpanels, while the cracks in the panel-flange welds also initiated at the bottom and propagated from each end. In cycle 37 the cracks in the left weld met and the web was fractured along the entire length as shown in Figure 5-14. Similarly, the RM subpanel weld completely fractured during cycle 39. The final cracking pattern can be seen in Figure 5-15. The inspection of the specimen after the test had ended, revealed cracking at the termination of some of the stiffeners welds as shown in Figure 5-16. The crack developed because the area is a (welding produced) heat-affected zone and because of the concentration of strains at that corner due to the restraint of out-of-plane displacements.

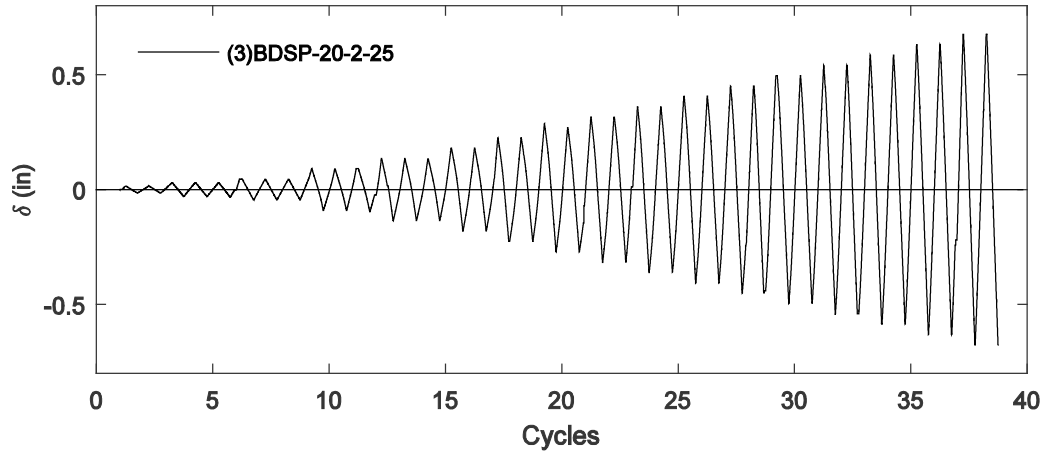

Figure 5-10: Test 3: Experimental lateral drift history

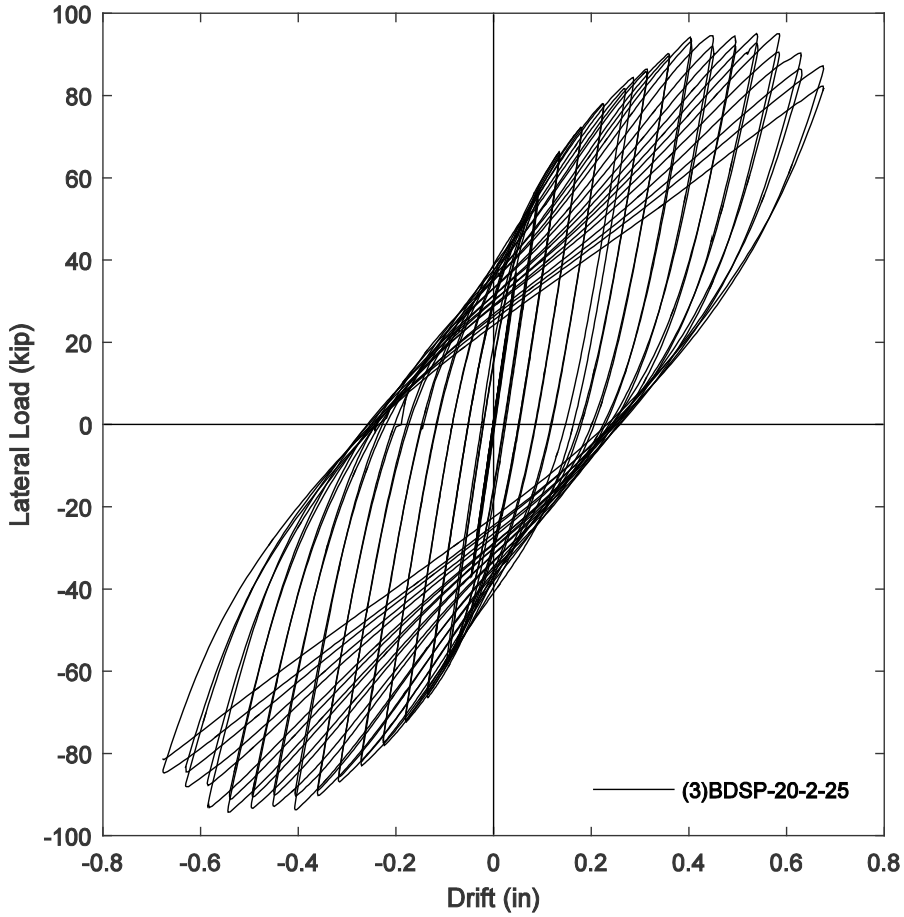

Figure 5-11: Test 3: Experimental lateral force-lateral drift response

Figure 5-12: Test 3: Yielding and damage evolution

Figure 5-13: Test 3 – Out-of-plane displacements in the web at t=20.75

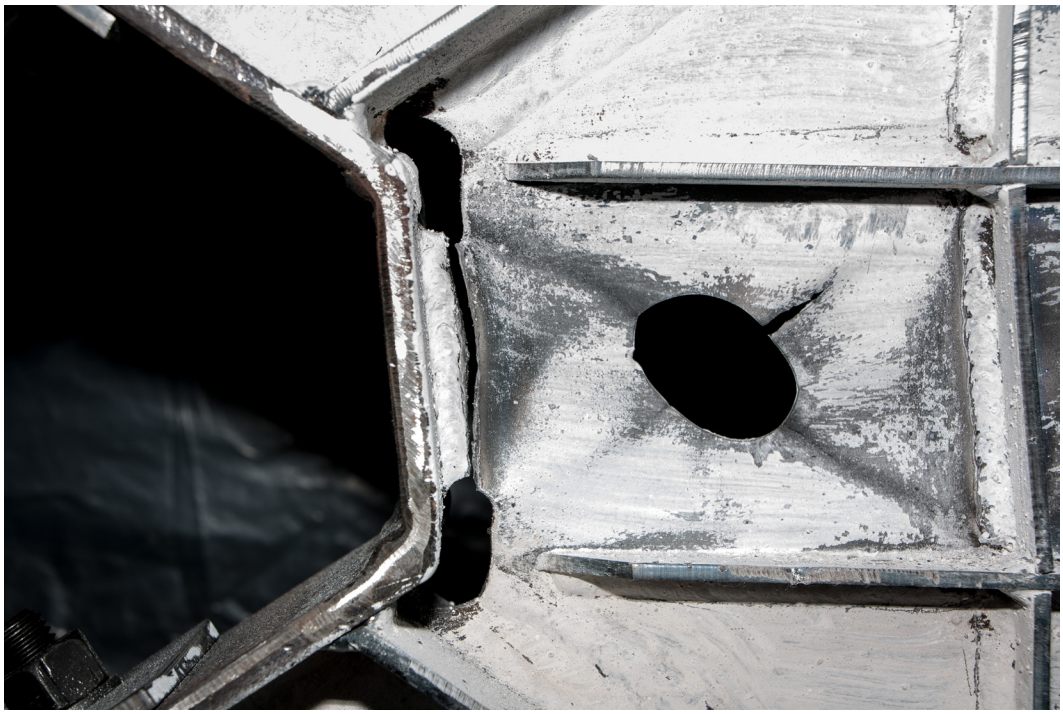

Figure 5-14: Test 3 – Fracture of the LM subpanel flange weld (t=36.75)

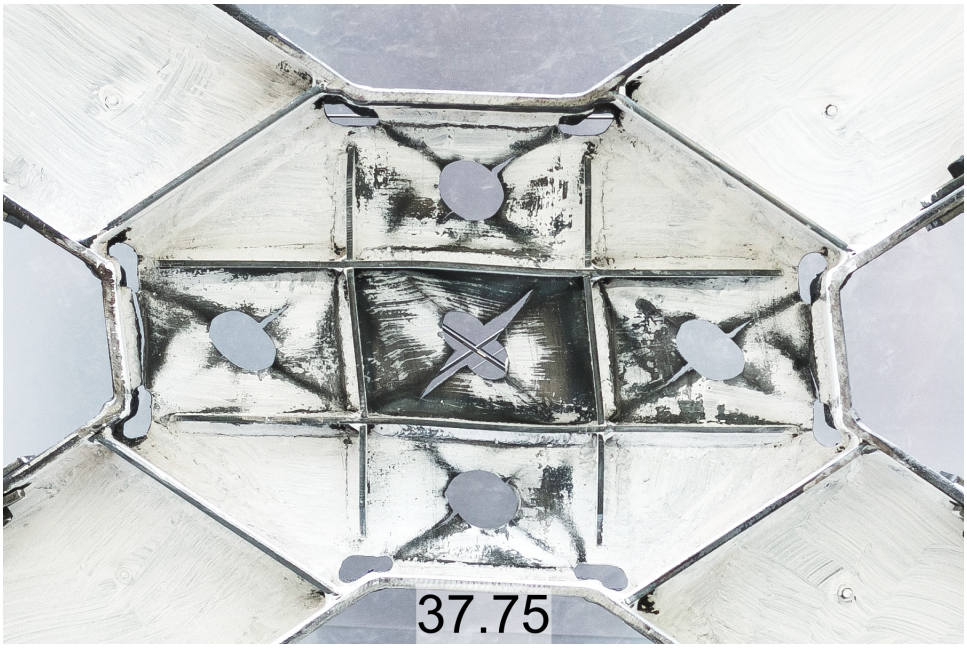

(a)

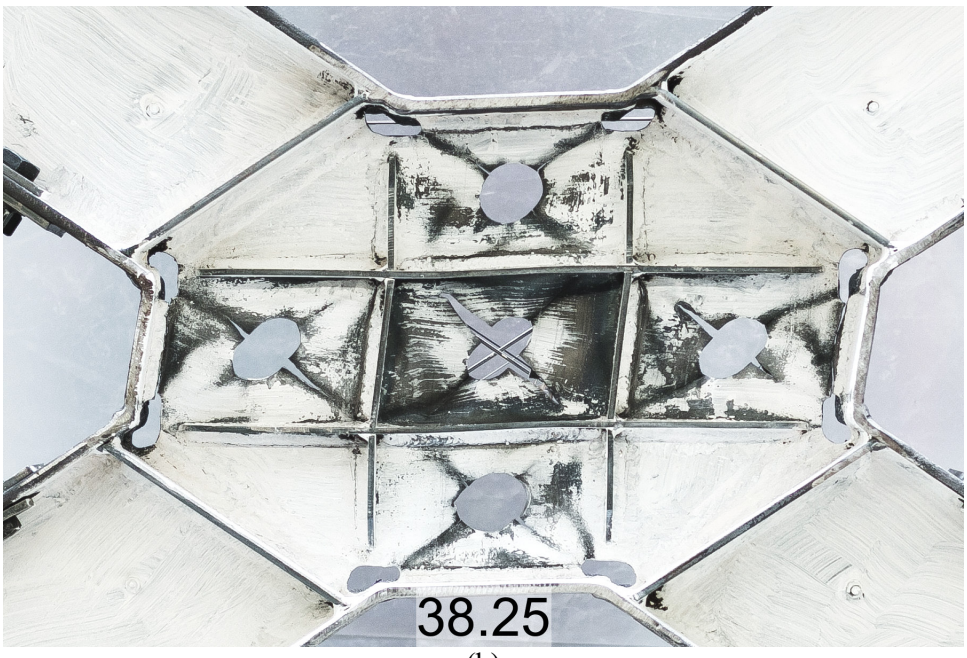

(b)

Figure 5-15: Damage of the specimen at the end of test 3
(a) max. negative drift; (b) max. positive drift

Figure 5-16: Test 3 – Cracking at stiffener weld termination

5.7 Test 4 - Specimen BDSP-24-2-25

Test 4 on specimen BDSP-24-2-25 was completed over two days (July 2 and 4). The applied lateral drift history is shown in Figure 5-17 and the final lateral force-drift response is plotted in Figure 5-18. The test was terminated after the positive excursion of the 38th cycle. The maximum lateral drift reached was 0.825 in, equal to 15 times the design yield drift $\delta_y = 0.055\ in$.

5.7.1 Shear panel yielding observations

The panel first yielding was observed during the 12th loading cycle at the toe of some transverse stiffeners welds. Yielding on the panel web was observed in the following cycles around the perforation edges at 45 degrees orientations, like in previous tests. These regions grew in length with subsequent cycles, tracing a pattern along which the panel will later fatigue and crack. The evolution of the yielding areas can be followed in Figure 5-19. After cycle 21, whitewash flaking was also observed at the end of the vertical transverse stiffeners, and at the toe of the web-to-flange welds. A series of pictures of the panel at different time intervals is presented in Figure 5-19.

Similarly to test 2 and 3, the shear deformation in this specimen was also concentrated along the horizontal subpanels (LM, CM, RM).

5.7.2 Total lateral force response summary

Stiffness degradation was noticeable after cycle 17, when the drift reached 5 times its yielding value. At this point, out-of-plane displacements were also significant in CM and CT subpanels. The maximum total lateral force reached was 102.9 *kips*, during the 34th cycle at t = 33.25, peak of first excursion at 13 times the yielding drift. The test was terminated at cycle 38, when the stiffness degraded significantly and the hysteresis cycles had narrowed. The maximum normalized drift reached during testing of this specimen was 15 times the yielding drift.

5.7.3 Damage initiation and evolution

Damage was first observed during cycle 26 as a crack opened at the upper-left diagonal around the RM subpanel perforation. A similar crack in the CM subpanel developed during the following cycle. After cycle 28 cracks had formed at 45 and 225 degrees around the hole in the CM subpanel and at 225 degrees in the CT subpanel. During the 29th and 30th cycle, cracks opened in subpanels CM at (315 deg, t=28.25), CT (45 deg, t=28.75) and RM (225 deg, 29.75). The CB subpanel developed cracks in all directions during cycles 31 and 32. At this time minor cracking was observed at the terminations of the vertical web-to-flange welds on the panel. At the end of the 36th cycle, new cracks had opened at all four diagonals around the LM and RM subpanels perforations, and at 315 degrees in the CT subpanel. During the 37th and last cycle, cracks opened in the LM subpanel away from the perforation edge due to the high strains caused by the out-of-plane bending of the plate. These cracks are shown and highlighted in Figure 5-20. The damage at the end of the loading history can be seen in Figure 5-21.

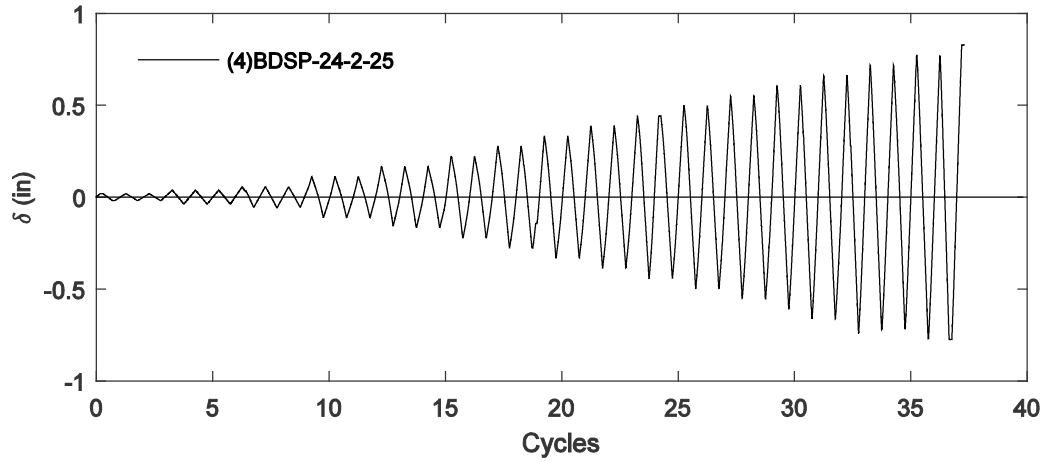

Figure 5-17: Test 4: Experimental lateral drift history

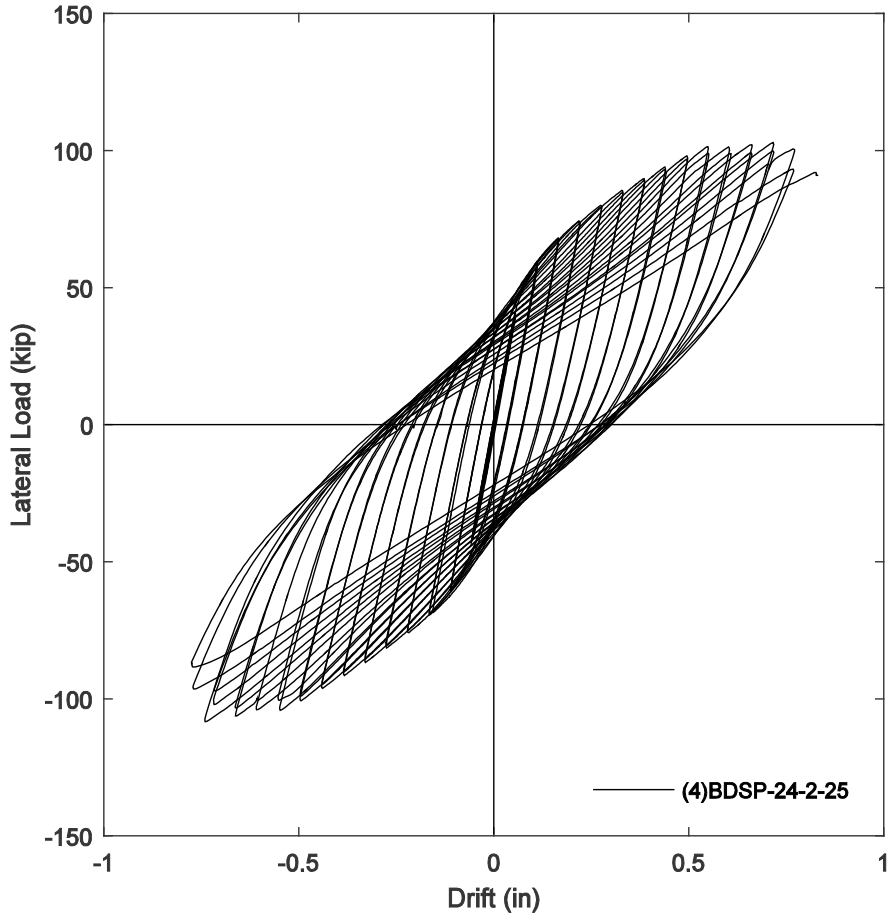

Figure 5-18: Test 4: Experimental lateral force-lateral drift response

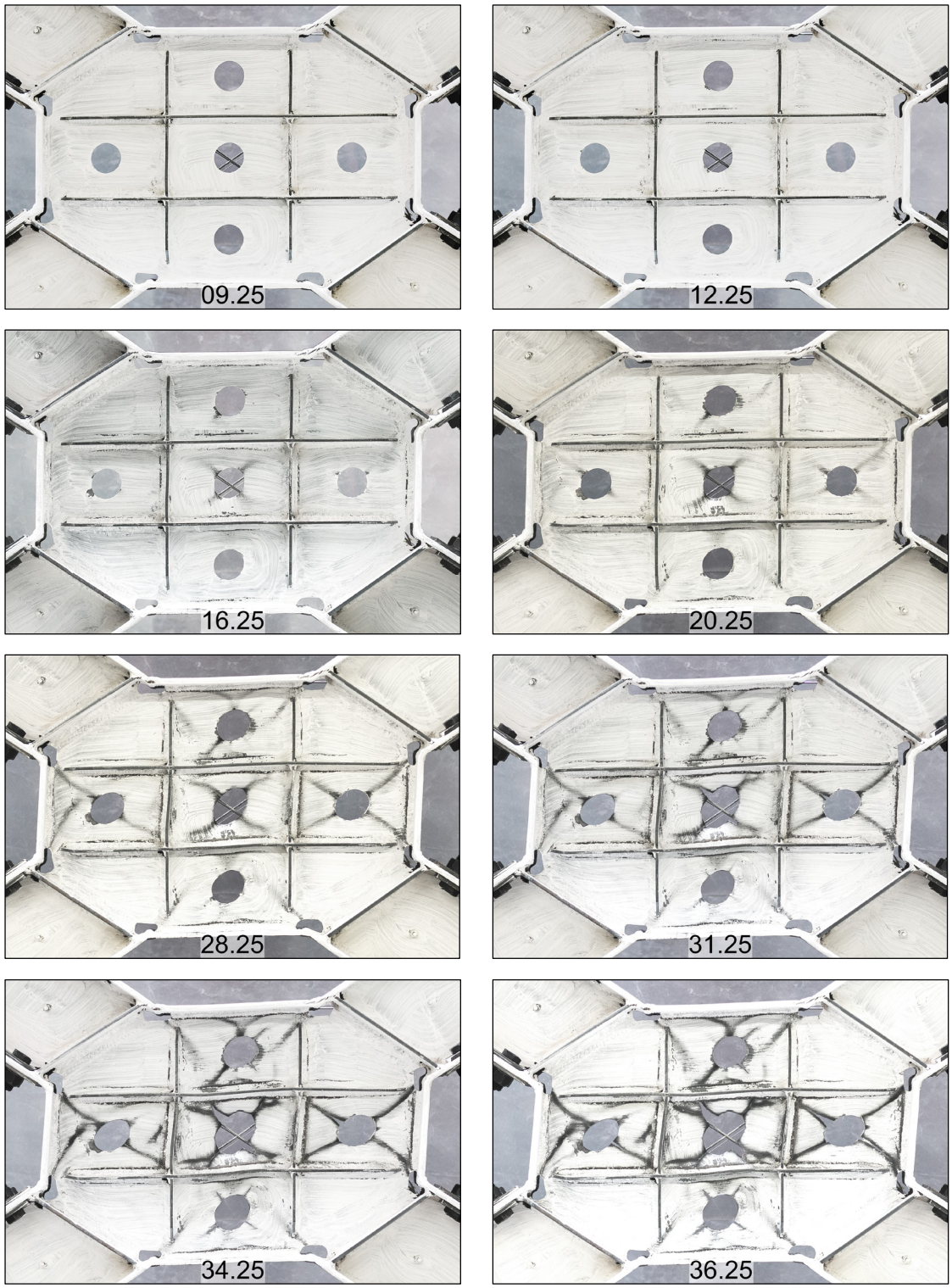

Figure 5-19: Test 4: Yielding and damage evolution

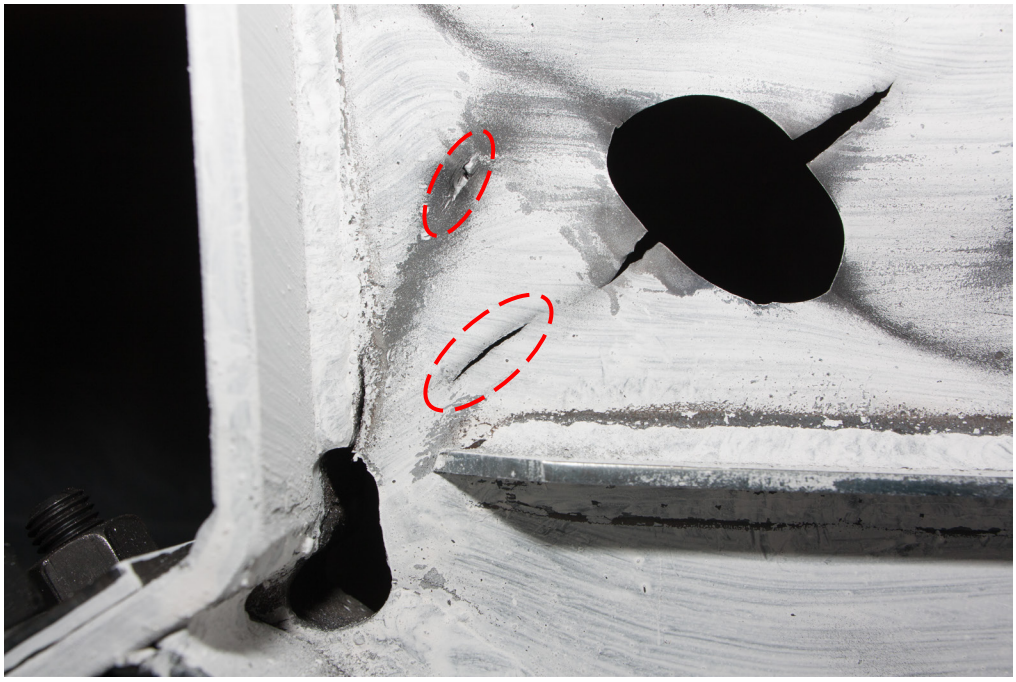

Figure 5-20: Damage in the LM subpanel during the last cycle of test 4 (t=36.75)

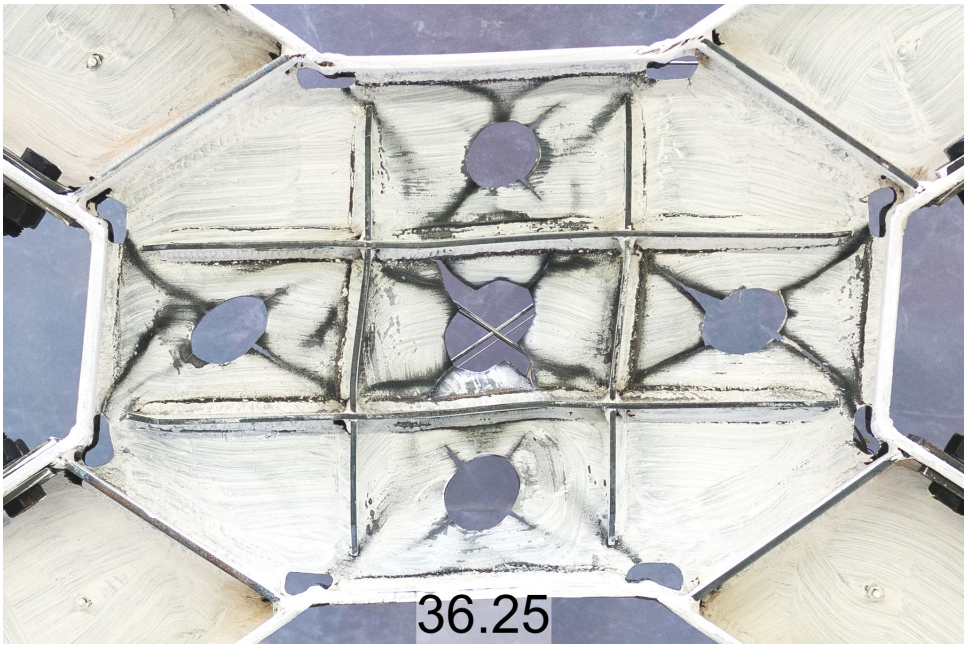

(a)

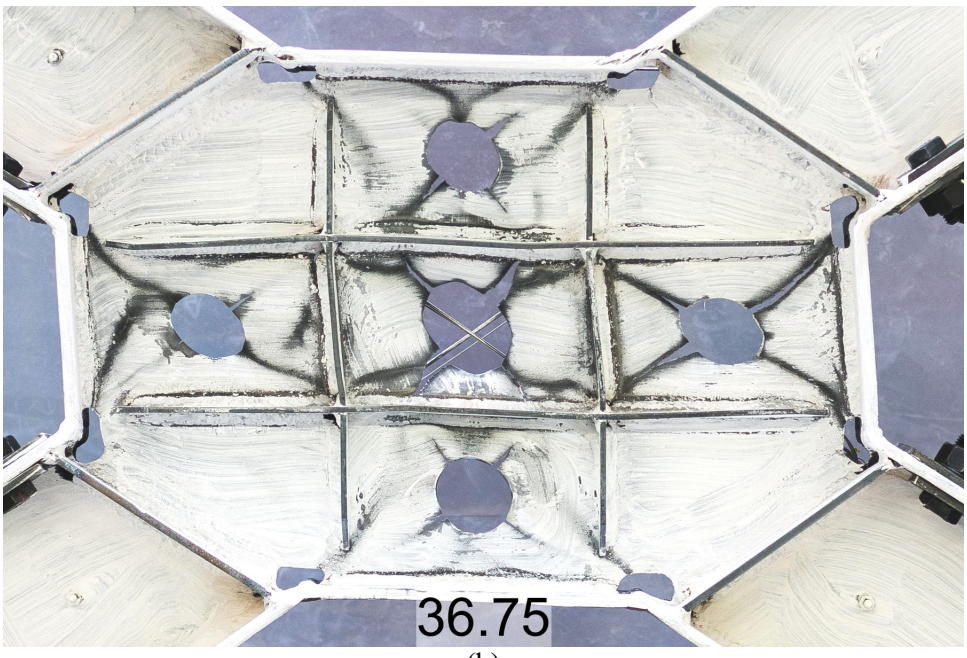

(b)

Figure 5-21: Damage of the specimen at the end of test 4
(a) max. positive drift; (b) max. negative drift

5.8 Test 5 - Specimen BDSP-20-3-40

Test 5 on specimen BDSP-20-3-40 was conducted on July 10th. The applied lateral drift history is shown in Figure 5-22 and the final lateral force-drift response is plotted in Figure 5-23. Note that a control mistake during cycle 15 led to an unplanned, large negative excursion, roughly twice the maximum drift at this point in the loading protocol. The normal loading protocol was resumed after this event. The test was terminated after cycle 31. At this point the stiffness of the system had rapidly degraded and the shape of the hysteresis cycle had narrowed.

5.8.1 Shear panel yielding observations

The panel first yielding occurred after the ninth loading cycle, when the lateral drift increased past the predicted yielding drift δ_y. Minor whitewash flaking was observed in CT, CM and CB subpanels in the form of lines at diagonal inclinations around the perforations. Some whitewash also detached at the toe of the stiffener welds. For the following four cycles, previously yielded regions expanded, and more yielding was observed at the toe of all welds on the web (stiffeners and flanges). Yielding of the LM and RM subpanels was also visible during cycle 16, located around the perforations and in the area between the perforations and the flanges. For the rest of the test, the overall distribution of yielding remained similar in shape but increased in area. As a result, the yielding lines around the perforations of the CT, CM and CB subpanels gradually coalesced into one inch wide regions around the perforations. A series of pictures of the panel at different time intervals is presented in Figure 5-24. The shear deformation in this specimen was concentrated along the vertical subpanels, CT, CM and CB.

5.8.2 Total lateral force response summary

No significant stiffness degradation was observed for test 5 up to cycle 25, or 8 times the yielding drift. However out-of-plane displacements in three of the subpanels (CT, CM and CB) were visible from cycle 22. In Figure 5-25 photographs of the three subpanels show the amplitude of the displacements during the 23rd cycle (t=22.25). This shows that for this specimen, the out-of-

plane displacements have a remarkably less significant effect on the overall stiffness than for the previous tests. The maximum total lateral force reached was 138.1 kips, during the second excursion at 8 times the yielding drift (0.040 in) during cycle 25 (t=24.25). The peak lateral force stayed mostly constant for the next cycles at 9 times yield drift, but dropped rapidly after cycle 27. In fact, as described in the next paragraph, during cycles 25, 26 and 27 diagonal cracks had initiated and propagated around the perforations in all three vertical subpanel (CT, CM and CB). The damage in the three panels soon created a weaker region in the shear panel, which concentrated shear deformations and reduced the panel shear stiffness. The test was terminated after cycle 31 when the cracks closer to the flanges in the CT and CB subpanels propagated along the weld up to the weld access holes, effectively detaching the web from the horizontal flanges. The maximum normalized drift reached during testing of this specimen was 11 times the yielding drift, equal to 0.550 in.

5.8.3 Damage initiation and evolution

Damage propagation in specimen BDSP-20-3-40 was faster than in the previous tests. However, cracks only opened in the three vertical subpanels, while the LM and RM subpanels only showed limited yielding. In three cycles, from 26 through 28, cracks in all diagonal directions opened in the CT, CM and CB subpanels. During cycle 30 and 31, the diagonal cracks closer to the flanges in CT and CB subpanels completely propagated along the web to flange weld toe and each reached the closest weld access hole, as shown in Figure 5-26 . This completely detached the web from the horizontal flanges, and created a softer region in the panel, where the shear deformations concentrated and the only resisting force was provided by the horizontal flanges. The effects of this behavior can be seen in Figure 5-27, in particular by looking at the deformation of the horizontal transverse stiffeners and comparing it to the relatively undeformed vertical stiffeners.

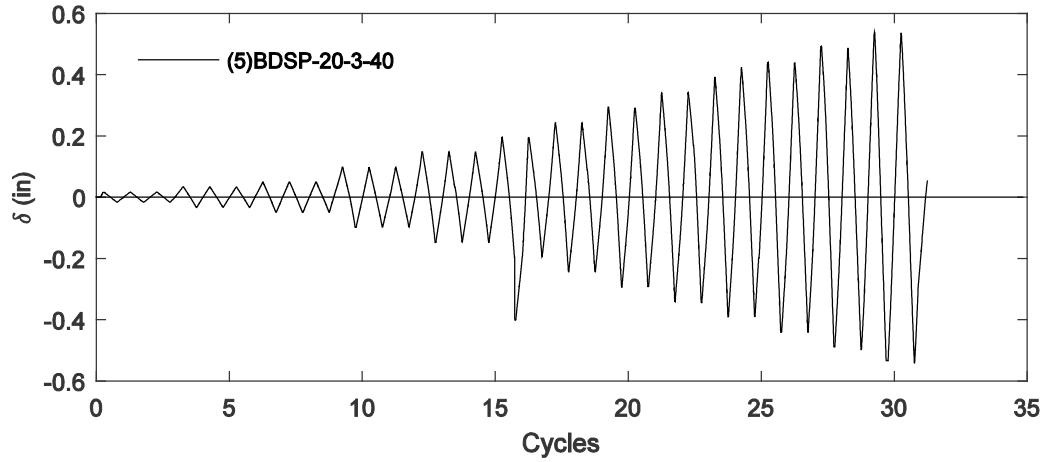

Figure 5-22: Test 5: Experimental lateral drift history

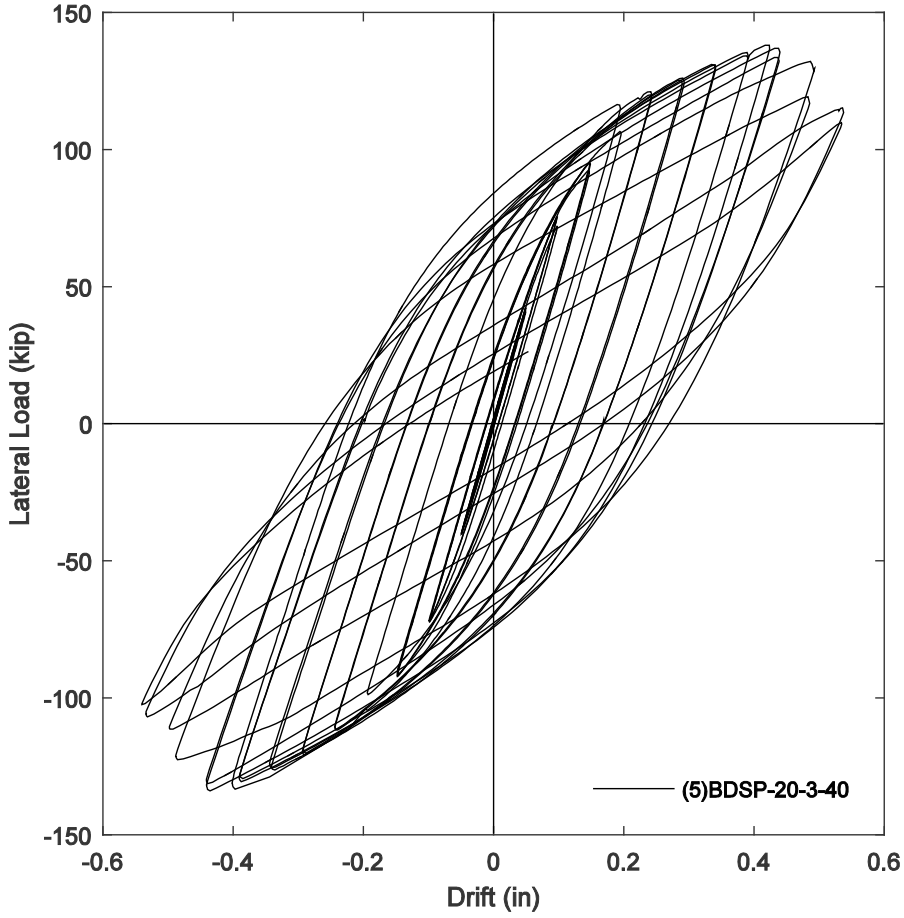

Figure 5-23: Test 5: Experimental lateral force-lateral drift response

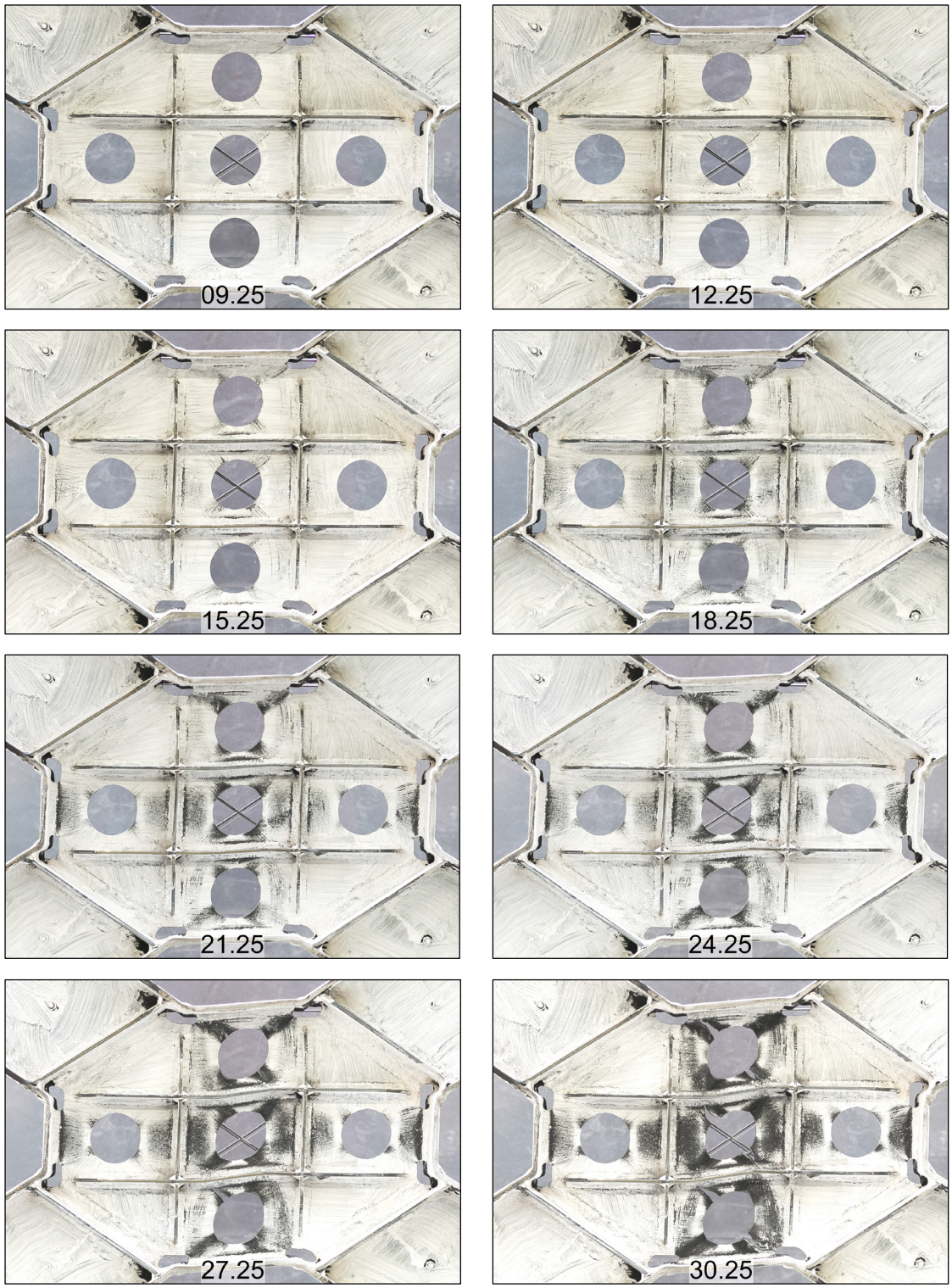

Figure 5-24: Test 5: Yielding and damage evolution

(a)

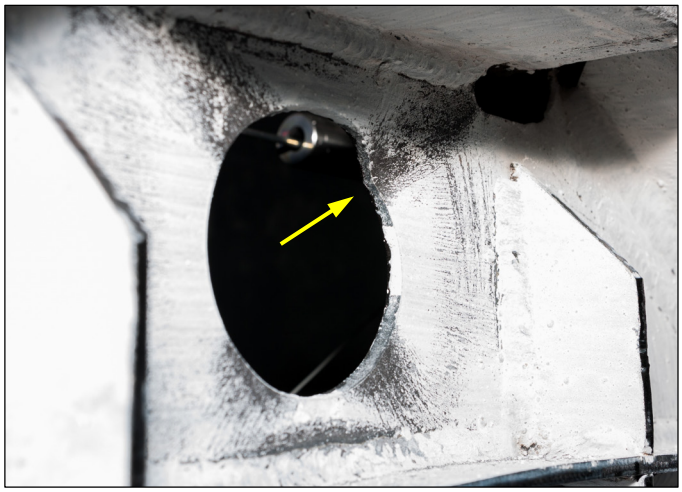

(b)

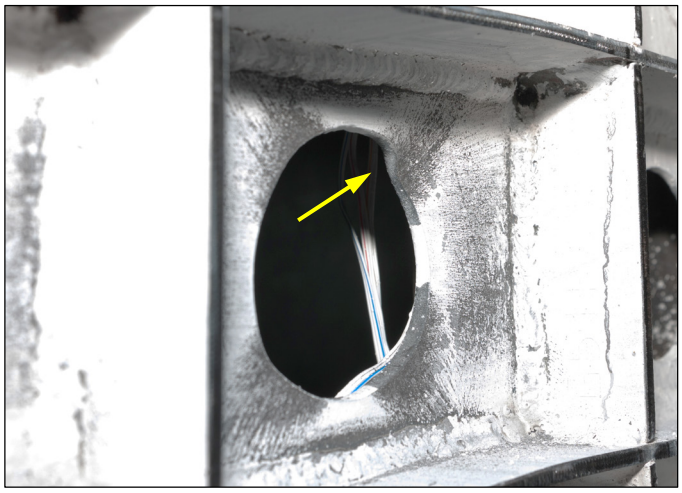

(c)

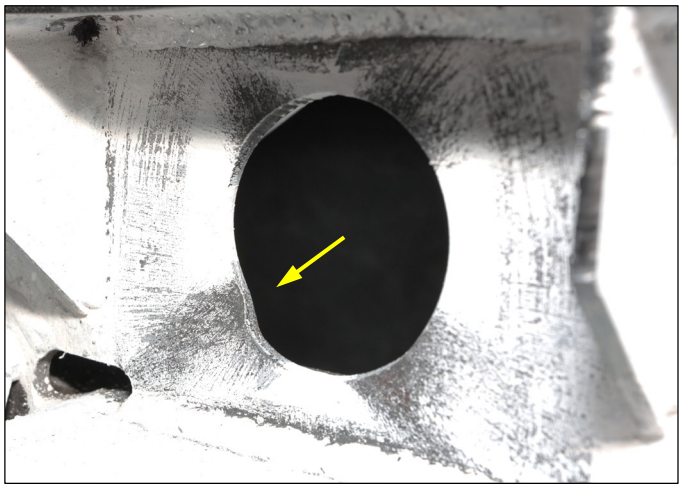

Figure 5-25: Out-of-plane displacements during cycle 23 of test 5 (t=22.25)
(a) CT subpanel; (b) CM subpanel; (c) CB subpanel

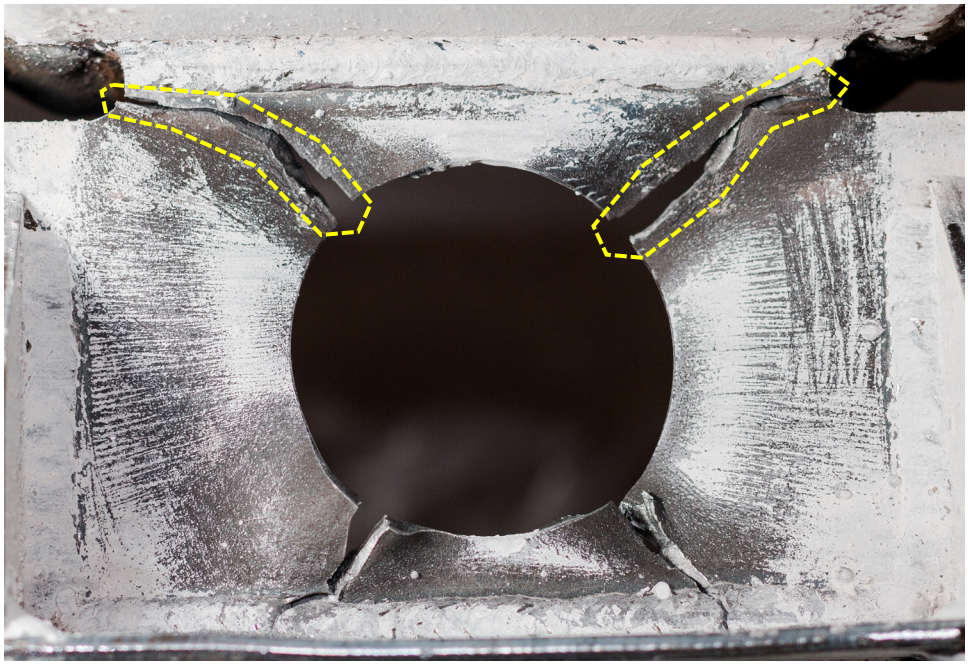

(a)

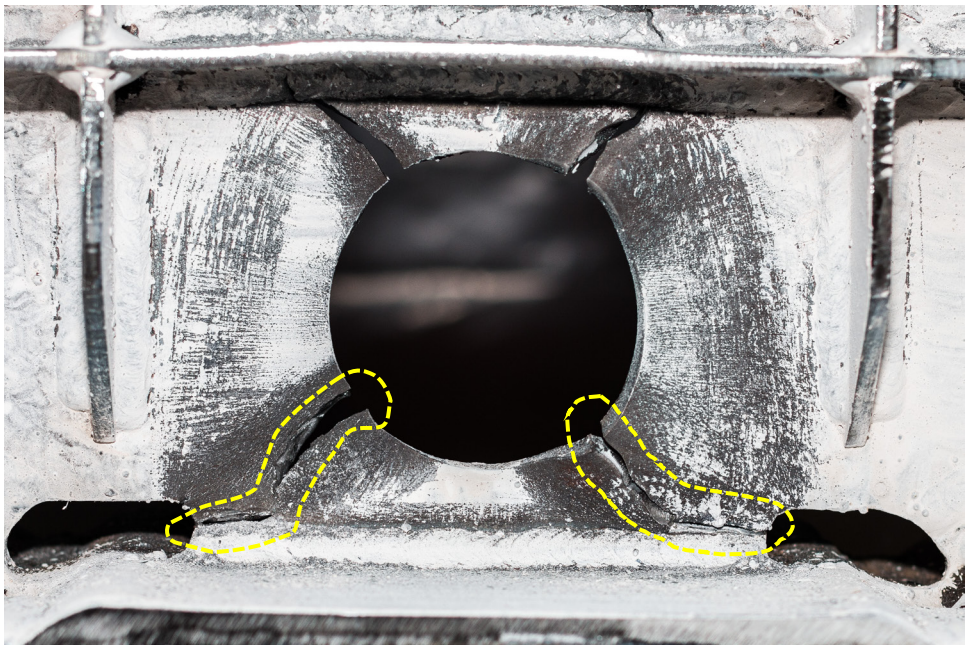

(b)

Figure 5-26: Test 5: Perforation cracks propagated through web to access holes (a) CT subpanel; (b) CB subpanel

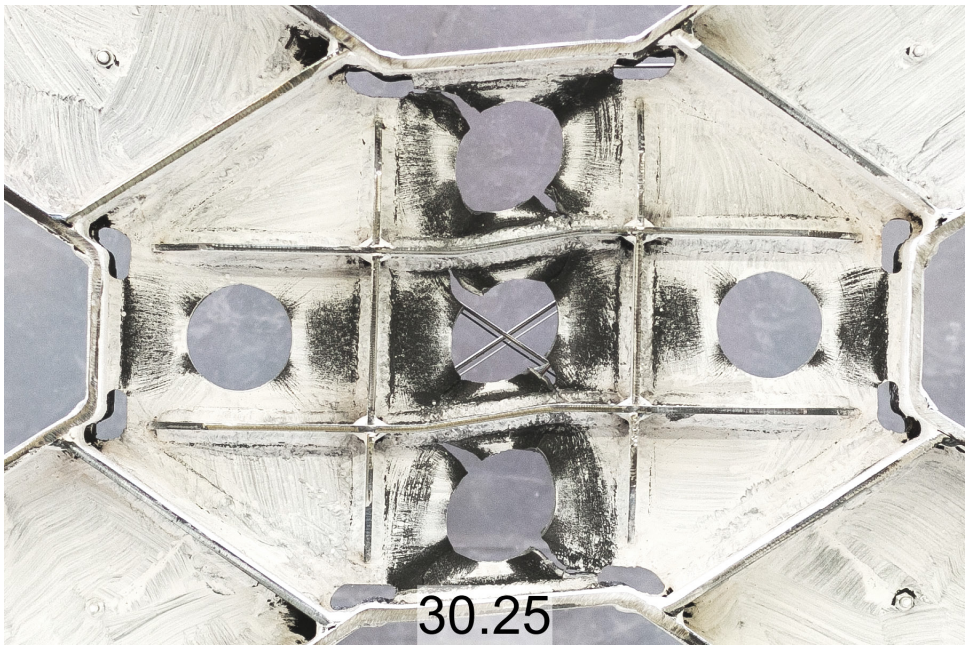

(a)

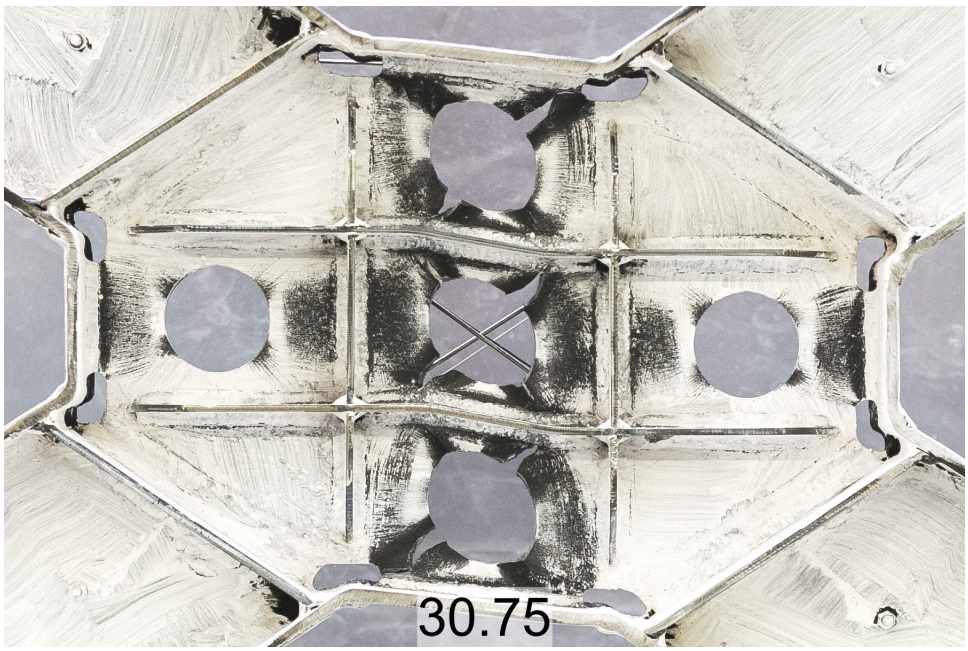

(b)

Figure 5-27: Damage of the specimen at the end of test 5
(a) max. positive drift; (b) max. negative drift

5.9 Test 6 - Specimen BDSP-20-2-00

Test 6 on specimen BDSP-20-2-00 was completed over two days (July 17 and 18). The applied lateral drift history is shown in Figure 5-28 and the final lateral force-drift response is plotted in Figure 5-29. The test was terminated after the negative excursion of the 38th cycle. The maximum lateral drift reached was 0.900 *in*, equal to 15 times the design yield drift $\delta_y = 0.060\ in$.

5.9.1 Shear panel yielding observations

The panel first yielding was observed during cycle 13, at the toe of some of the fillet welds on the web. First visible yielding on the web was observed during cycle 16 in the CM subpanel. The yielding in the central subpanel became more evident during the following cycles, and during cycle 20 similar yielding began to be visible also in the LM and RM subpanels. The yielding areas on each subpanel during the rest of the test localized along diagonal lines, as shown in Figure 5-30. The shear deformation in this specimen was concentrated along the horizontal subpanels (LM, CM, RM).

5.9.2 Total lateral force response summary

Stiffness degradation was noticeable after cycle 19, when the drift reached 6 times the yielding value. Out-of-plane displacements were observed starting from cycle 17 in the CM subpanel. The maximum total lateral force reached was 122.4 *kips*, and it was reached at t = 27.25, peak of first excursion at 10 times the yielding drift, 0.600 *in*. The test was terminated after cycle 38, 8 cycles after both left and right, panel-flange welds fractured across the entire web length. The maximum normalized drift reached during testing of this specimen was 15 times the yielding drift.

5.9.3 Damage initiation and evolution

Damage was first observed during cycle 25 as a crack opened in the CM subpanel, shown in Figure 5-31. The location and orientation of the crack relatively to the yielding pattern, suggested that the damage was caused by repeated curvature reversal due to the reversal of out-of-plane displacements under cyclic loading. Small cracks were also observed at this time at the lower end

of the left web-flange weld and at the termination of the panel-stub butt weld ending at the same access hole, as shown in Figure 5-32. A symmetric crack in the right web-flange weld was observed during the 26th cycle, while cracks at the upper end of the same welds initiated during cycle 27 and 28. These cracks propagated through the entire length during the next two cycles. At the beginning of cycle 31 the panel web was completely detached from the two vertical flanges, see Figure 5-33. More cracks developed during the same cycle in the LM and RM subpanels. By this point, it was clearly visible that shear deformations were localizing in the three horizontal subpanels. As a result of the large displacements, the weld between vertical and transverse stiffeners between the LM, CM and RM subpanels fractured during cycle 36. The final cracking pattern can be seen in Figure 5-34.

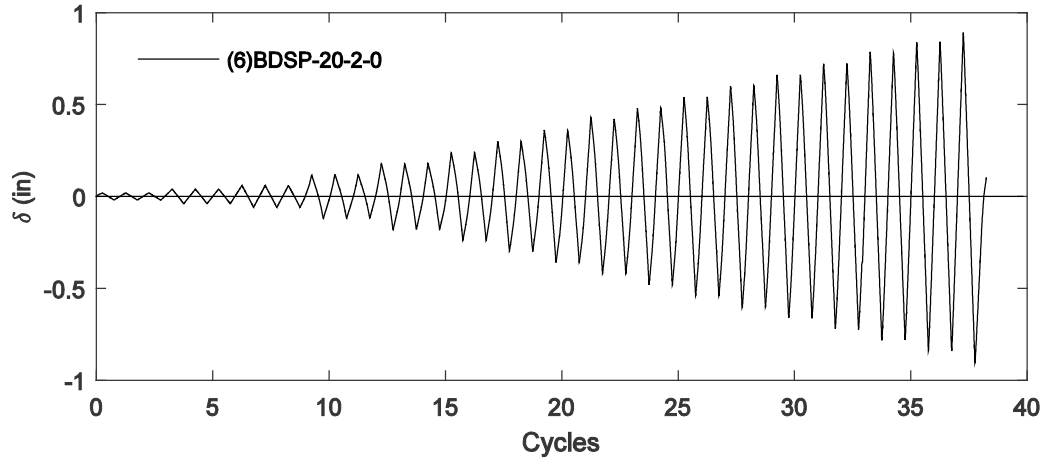

Figure 5-28: Test 6: Experimental lateral drift history

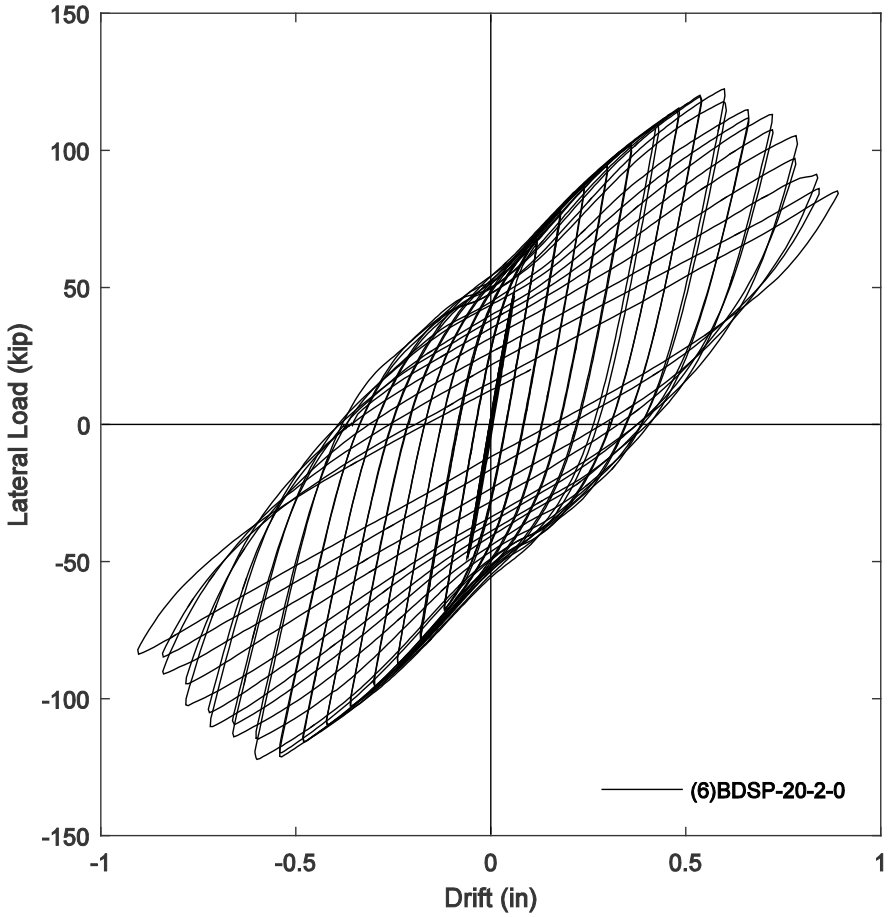

Figure 5-29: Test 6: Experimental lateral force-lateral drift response

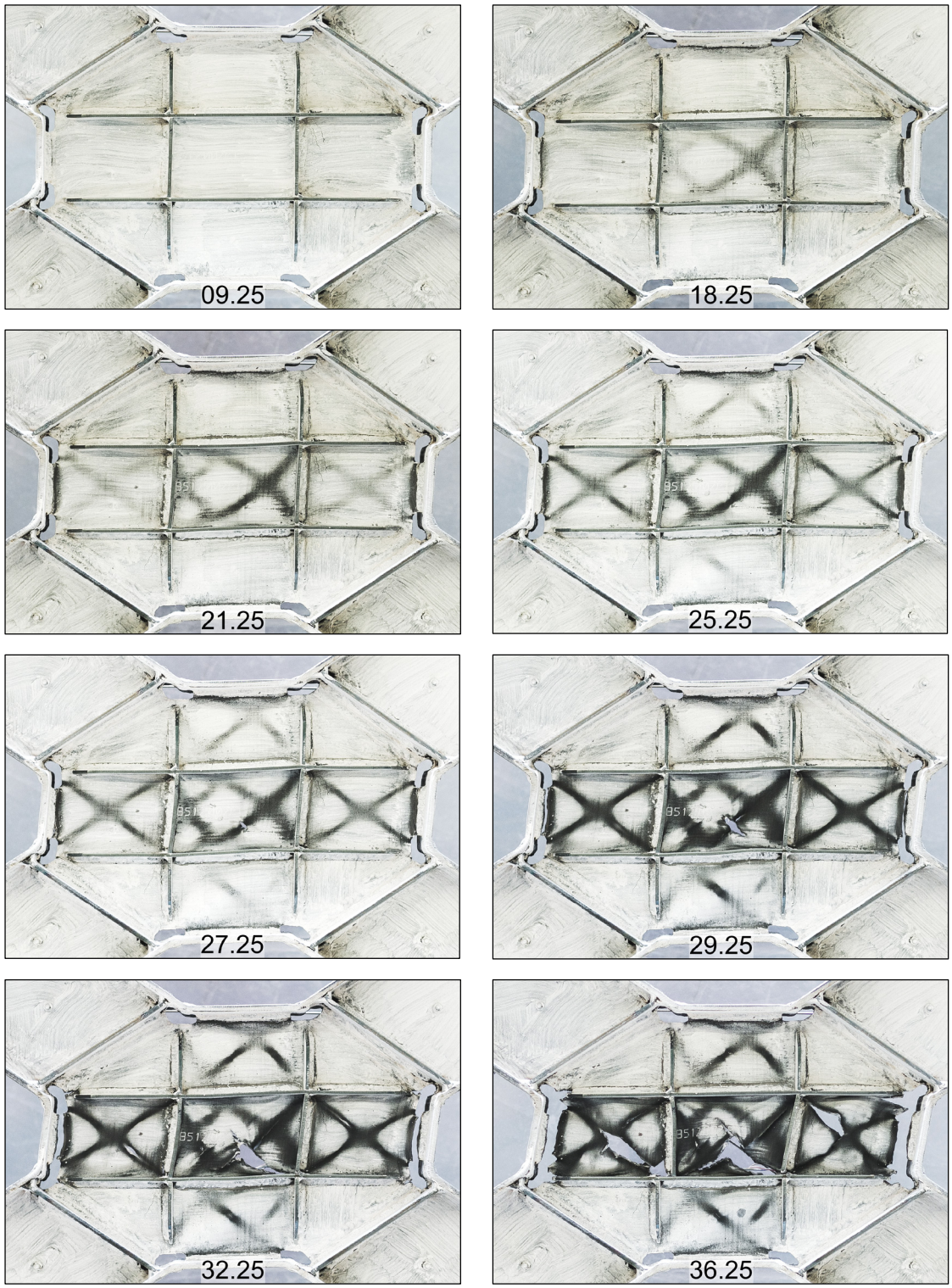

Figure 5-30: Test 6: Yielding and damage evolution

Figure 5-31: First crack in CM subpanel, test 6 (t=27.50)

Figure 5-32: Cracks at welds termination (t=24.50)

(a) (b)

Figure 5-33: Cracks in the panel web at flange weld, test 6 (t=29.25)
(a) LM subpanel: (b) RM subpanel

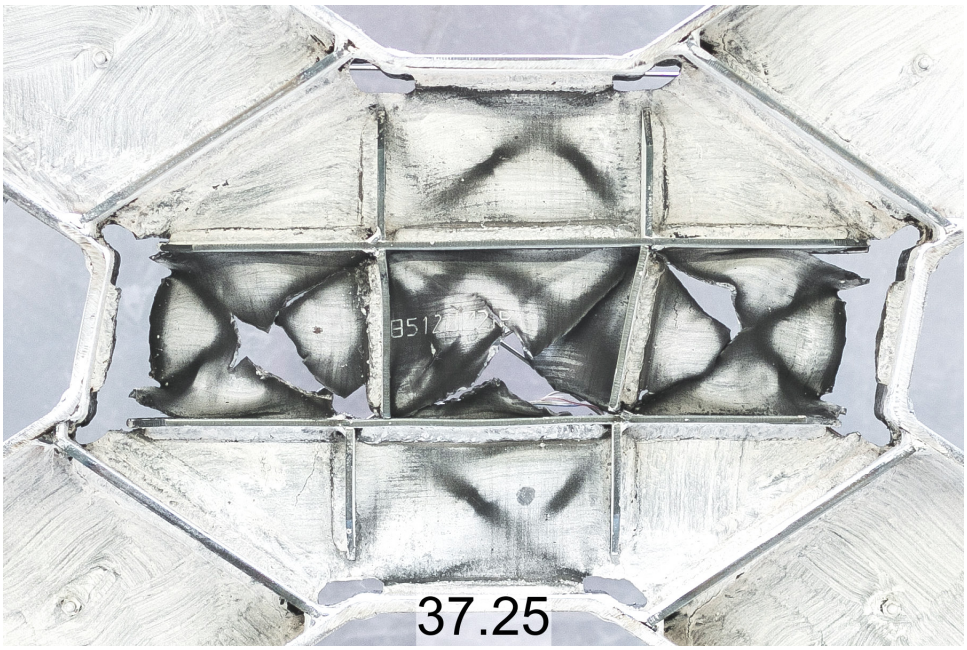

(a)

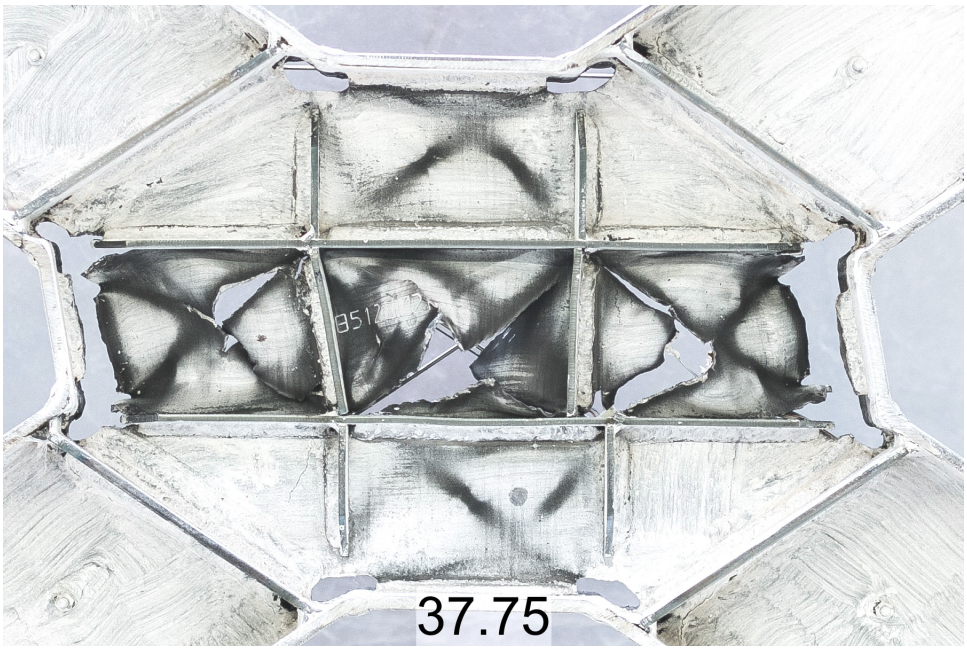

(b)

Figure 5-34: Damage of the specimen at the end of test 6
(a) max. positive drift; (b) max. negative drift

5.10 Test 7 - Specimen BDSP-24-3-40

Test 7 on specimen BDSP-24-3-40 was completed over two days, July 21st and 22nd. The applied lateral drift history is shown in Figure 5-35 and the final lateral force-drift response is plotted in Figure 5-36. The test was terminated after cycle 33. The stiffness of the bracing system at this point was significantly degraded, as the panel web was almost entirely detached from the top and bottom horizontal panel flanges.

5.10.1 Shear panel yielding observations

Minor flaking of whitewash was observed early in the 9th cycle in the shape of thin diagonal lines around some of the perforations. Larger areas around the perforations of the three vertical subpanel (CM, CT, CB) yielded starting from cycle 10. These areas were localized around the perforations and extended along the 45 degrees diagonals. From the 14th cycle yielding was visible at the weld toes of most of the stiffeners and flange welds. The LM and RM subpanels did not show significant yield until cycle 20, but never reached the same extent as in the other subpanels. The shape of the yielded areas remained mostly unchanged for the rest of the test. A series of pictures of the panel at different time intervals is presented in Figure 5-37. The shear deformation in this specimen was concentrated along the vertical subpanels CT, CM and CB, see Figure 5-38.

5.10.2 Total lateral force response summary

No significant stiffness degradation was observed for test 7 up to cycle 21, or 7 times the yielding drift. Out-of-plane displacements in three of the subpanels (CT, CM and CB) were visible from cycle 18. The maximum total lateral force reached was 149.0 kips, during the first excursion at 8 times the yielding drift during cycle 24 (t=23.25). The peak lateral force stayed mostly constant for the next cycles at 9 and 10 times yield drift, but dropped rapidly after cycle 29, after diagonal cracks had initiated and propagated around the perforations in all three vertical subpanel (CT, CM and CB). The damage in the three panels soon created a weaker region in the shear panel, which concentrated shear deformations and reduced the panel shear stiffness. The test was terminated

after cycle 33 when the cracks closer to the flanges in the CT and CB subpanels propagated along the weld up to the weld access holes. The maximum drift reached during testing of this specimen was 12 times the yielding drift, or 0.696 in.

5.10.3 Damage initiation and evolution

The pattern and propagation speed of damage in specimen 7 were similar to the ones of specimen 5. The first crack was observed during the negative excursion of cycle 24 in the CM subpanel. As shown in Figure 5-39, this crack formed along an indentation in the web (part of the fabricator's impressed part number) which promoted the initiation of the same crack. Between cycles 25 and 29, cracks at the perforations formed in all three vertical subpanels (CM, CB, CT). No cracks formed in the LM and RM subpanels. By the end of the test at cycle 33, the diagonal cracks closer to the flanges in CT and CB subpanels completely propagated along the web-flange weld toe and each reached the closest weld access hole. The damage at the end of the test is shown in Figure 5-38.

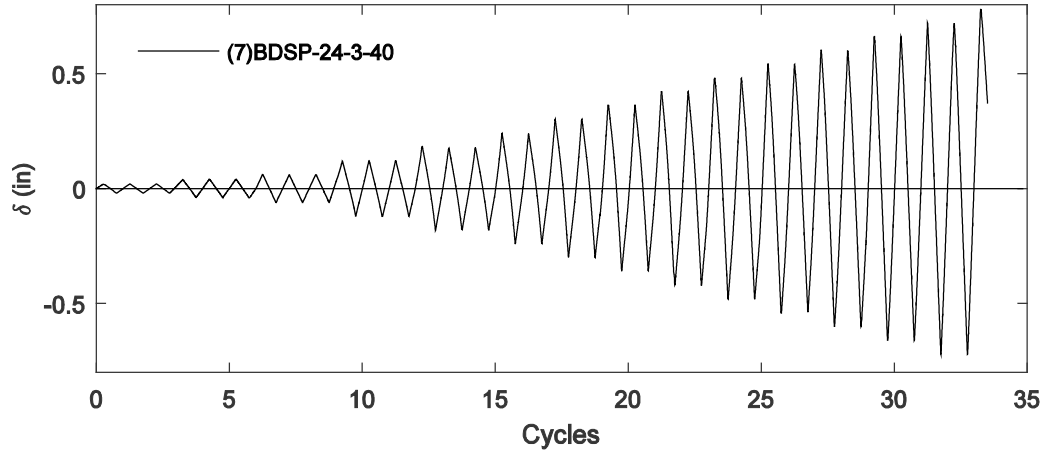

Figure 5-35: Test 7: Experimental lateral drift history

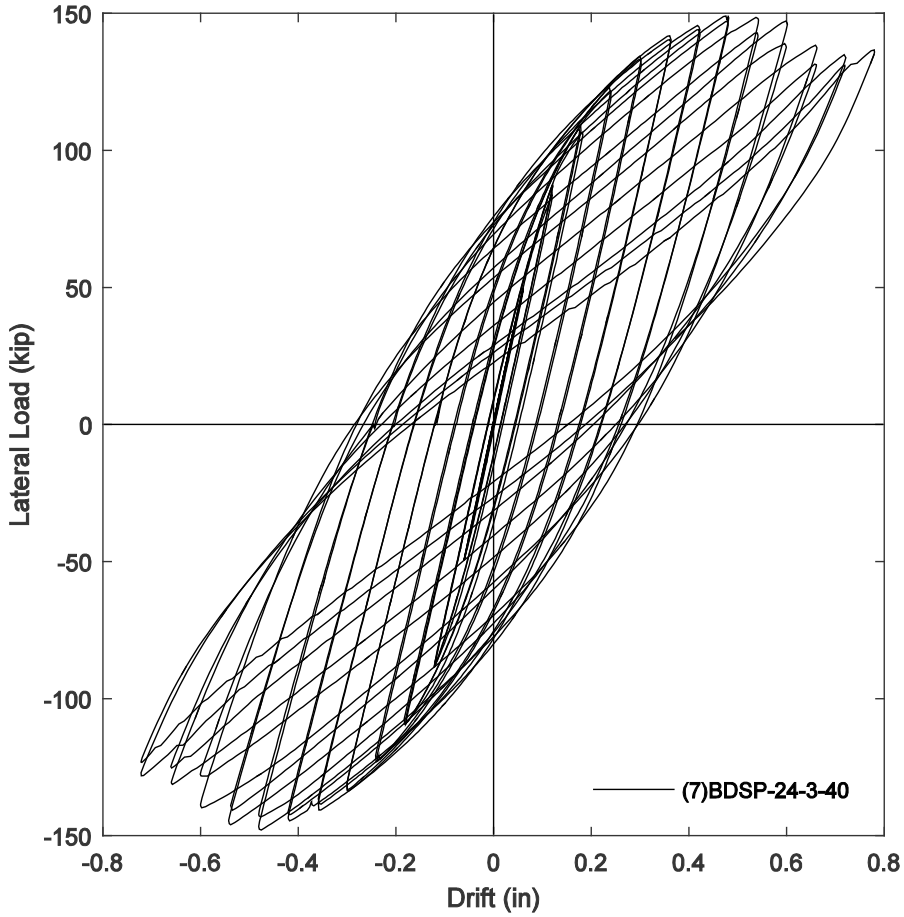

Figure 5-36: Test 7: Experimental lateral force-lateral drift response

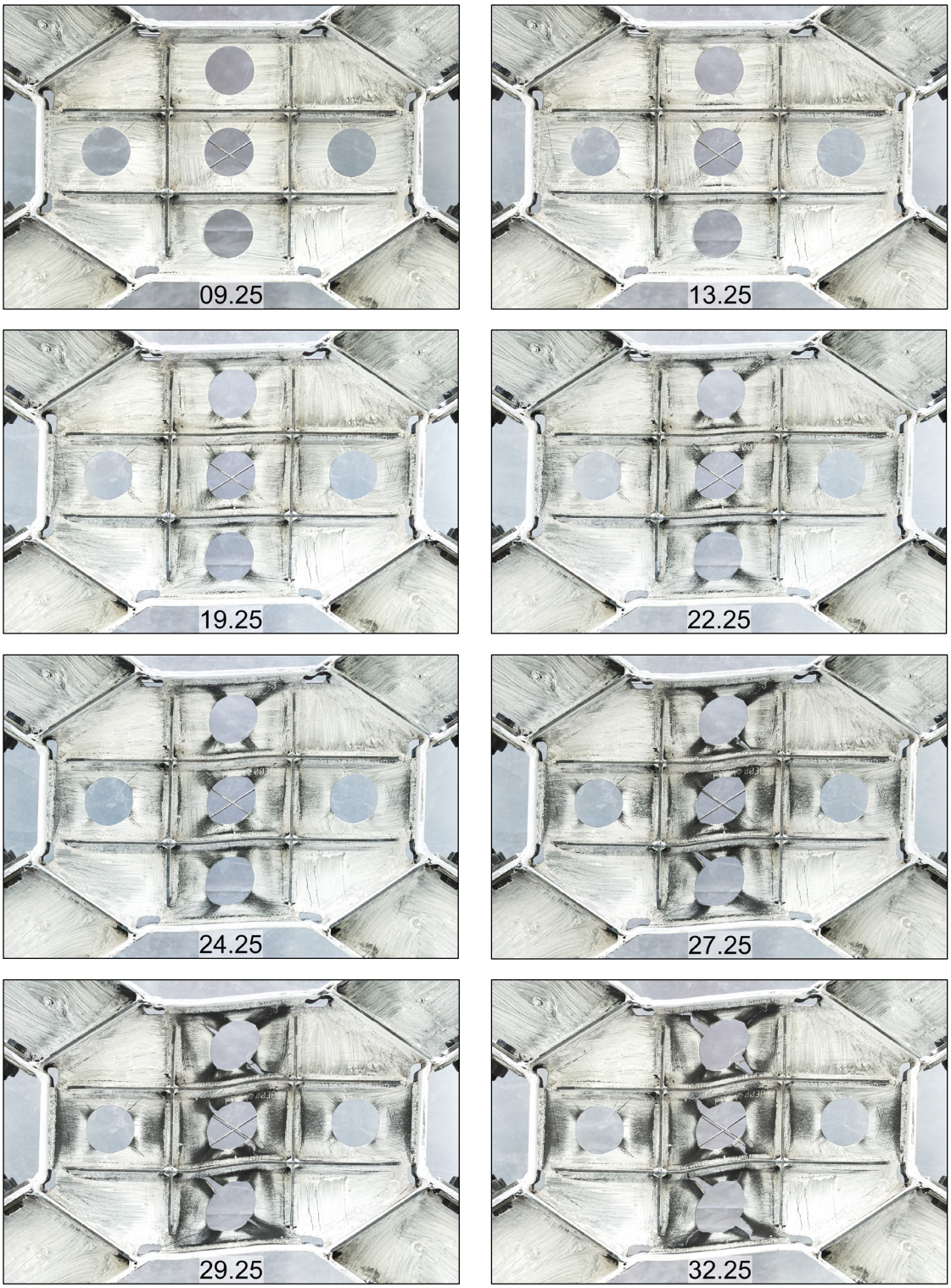

Figure 5-37: Test 7: Yielding and damage evolution

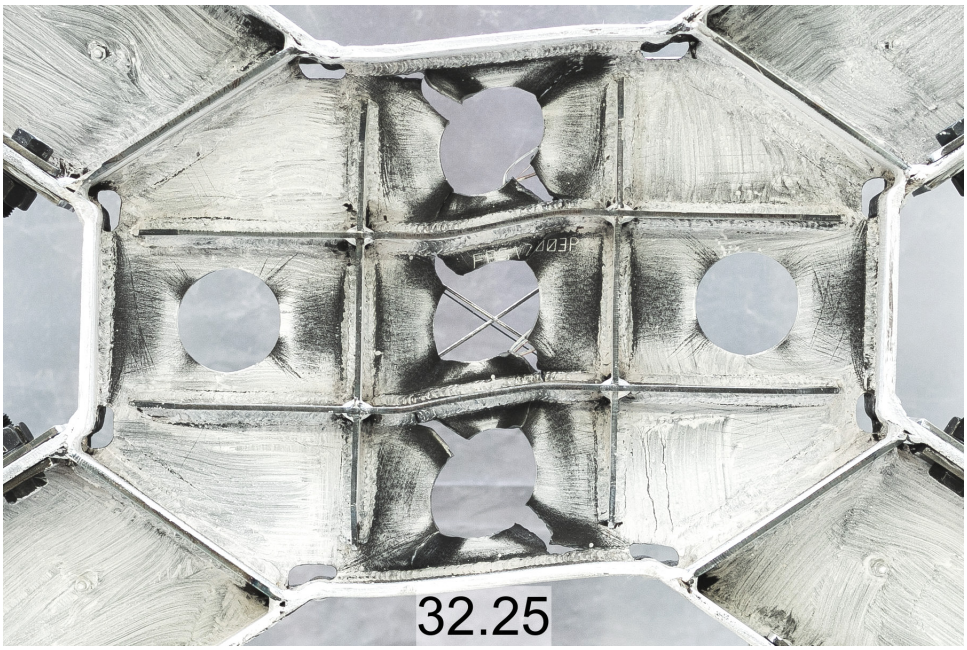

(a)

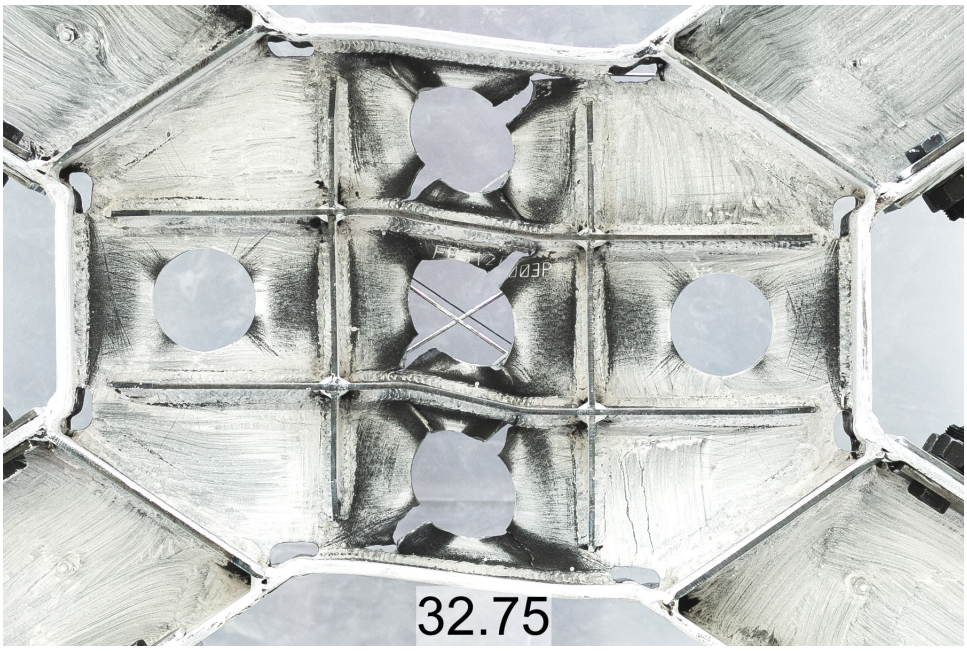

(b)

Figure 5-38: Damage of the specimen at the end of test 7
(a) max. positive drift; (b) max. negative drift

Figure 5-39: Test 7: Crack formed at the indented part number defect (t=25.00)

5.11 Test 8 - Specimen BDSP-20-3-25

Test 8 on specimen BDSP-20-3-25 was completed over two days, July 27th and 228th. The applied lateral drift history is shown in Figure 5-40 and the final lateral force-drift response is plotted in Figure 5-41. The test was terminated after cycle 33. The stiffness of the bracing system at this point was significantly degraded, as the panel web was entirely detached from the top and bottom horizontal panel flanges.

5.11.1 Shear panel yielding observations

Minor flaking of whitewash was observed during the 10th cycle, in the shape of thin diagonal lines around some of the perforations. More diffused whitewash flaking was observed starting from cycle 16 in the three vertical subpanel (CM, CT, CB). These areas were localized around the perforations and extended along the 45 degrees diagonals. By the end of cycle 18 most of the central subpanel was yielded, while the remaining ones showed concentrated yielded around the perforations. Yielding at this time was also noticeable at most weld toes. The LM and RM subpanels

yielded horizontally, on the left and right sides of the perforations. Yielded regions continued growing in this pattern until cycle 31, when damage became extensive and no new regions yielded. Pictures of the panel at different time intervals is presented in Figure 5-42. The shear deformation in this specimen was concentrated along the vertical subpanels as in tests 5 and 7, see Figure 5-43.

5.11.2 Total lateral force response summary

No significant stiffness degradation was observed for test 8 until cycle 23, or 8 times the yielding drift. Out-of-plane displacements in three of the subpanels (CT, CM and CB) were visible from cycle 18. The maximum total lateral force reached was 171.5 kips, during the first excursion at 8 times the yielding drift during cycle 24 (t=23.25). The peak lateral force began slowly decreasing after this point, but the degradation accelerated after cycle 29 after the two cycles at 10 times the yielding drift. The damage in the CT, CB and CM subpanels soon created a weaker region in the shear panel, which concentrated shear deformations and reduced the panel shear stiffness. The test was terminated after cycle 33 when the cracks closer to the flanges in the CT and CB subpanels propagated along the weld up to the weld access holes. The maximum drift reached during testing of this specimen was 12 times the yielding drift, or 0.720 in.

5.11.3 Damage initiation and evolution

The pattern and propagation speed of damage in specimen 8 were similar to the ones of specimens 7 and 5. The first crack was observed during the positive excursion of cycle 24 in the CM subpanel. Between cycles 26 and 29, cracks at the perforations formed in all three vertical subpanels (CM, CB, CT). No cracks formed in the LM and RM subpanels. By the end of the test at cycle 33, the diagonal cracks closer to the flanges in CT and CB subpanels completely propagated along the web-flange weld toe and each reached the closest weld access hole. The damage at the end of the test is shown in Figure 5-43.

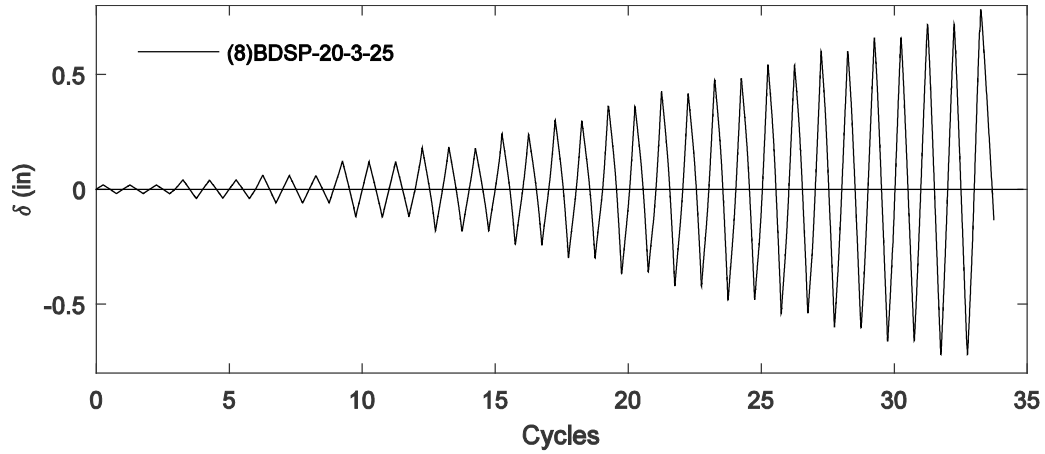

Figure 5-40: Test 8: Experimental lateral drift history

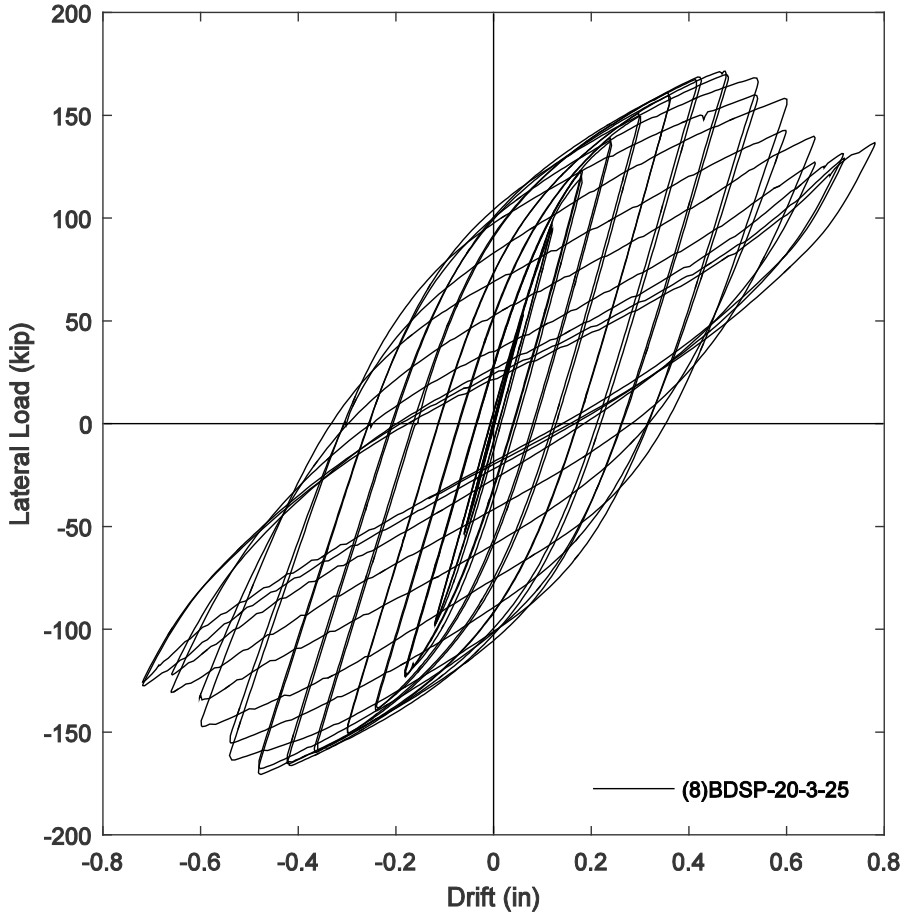

Figure 5-41: Test 8: Experimental lateral force-lateral drift response

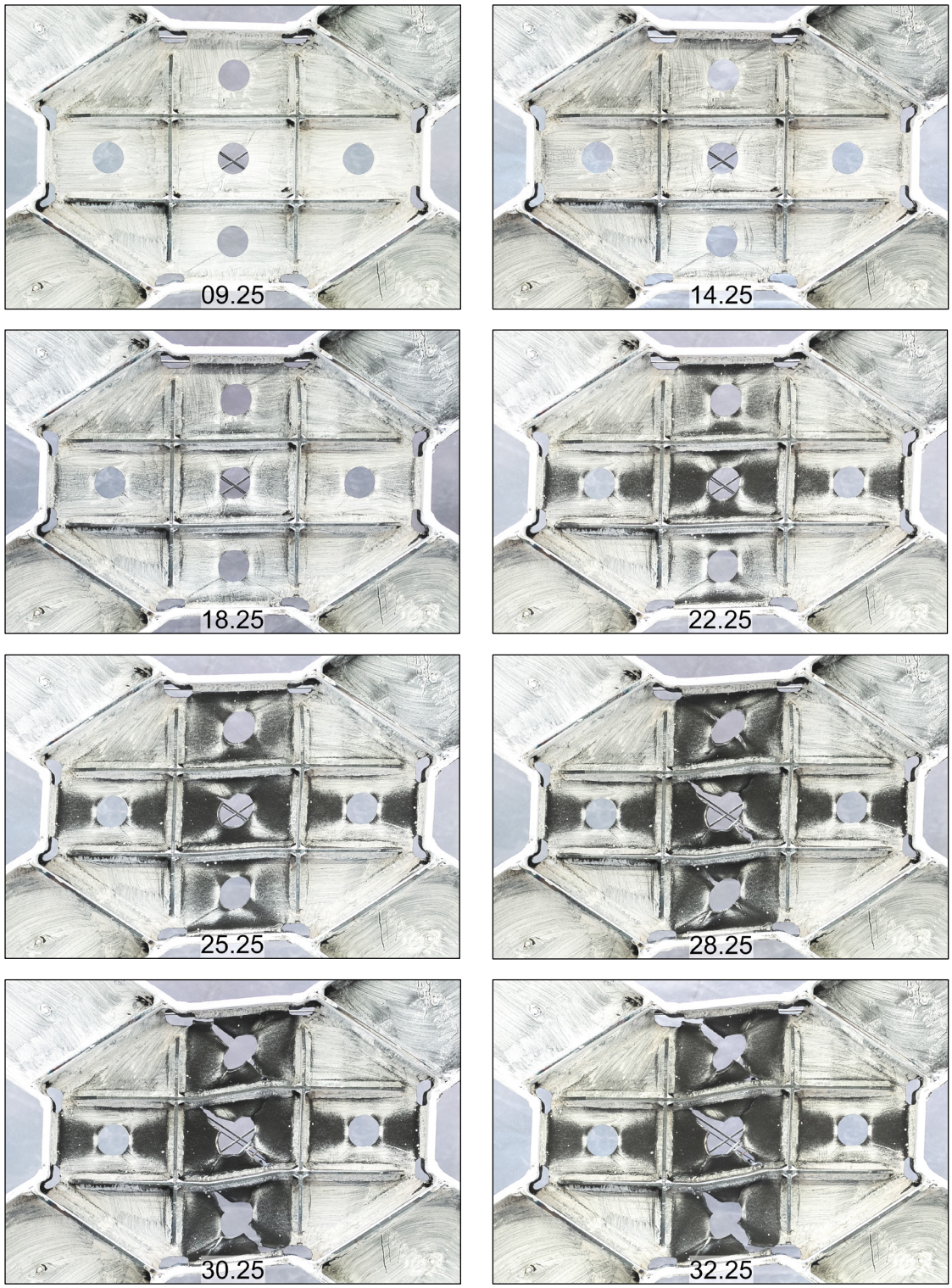

Figure 5-42: Test 8: Yielding and damage evolution

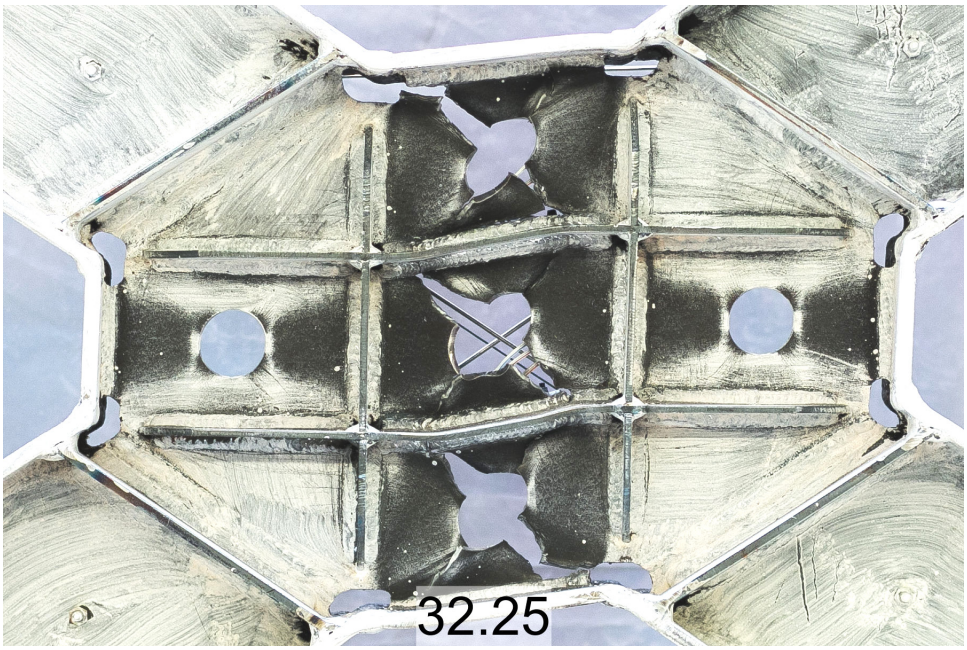

(a)

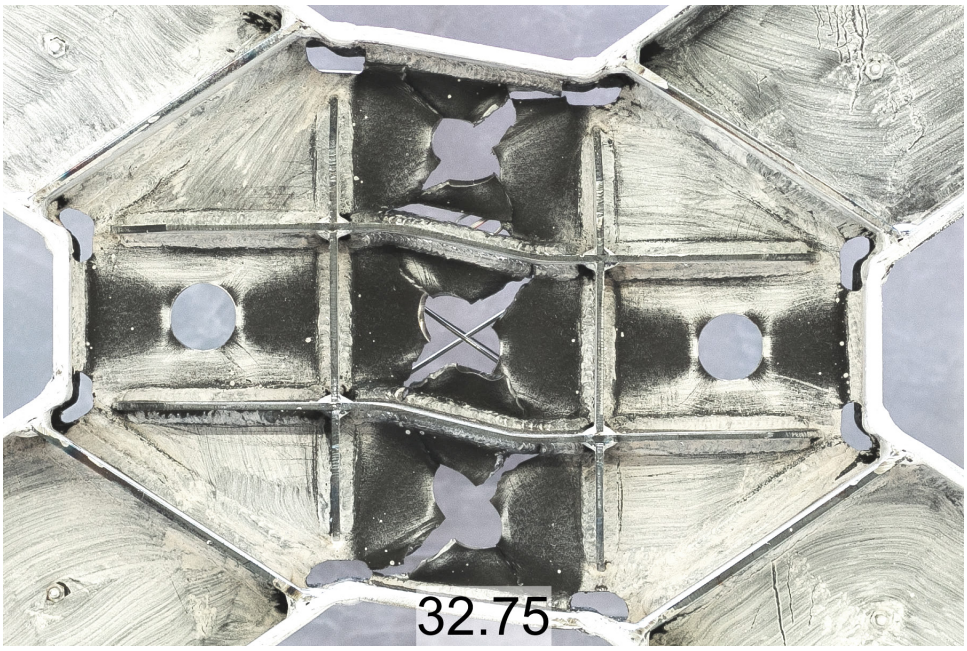

(b)

Figure 5-43: Damage of the specimen at the end of test 8
(a) max. positive drift; (b) max. negative drift

5.12 Test 9 - Specimen BDSP-20-4-40

Test 9 on specimen BDSP-20-4-40 was completed over two days, July 31st and August 1st. The applied lateral drift history is shown in Figure 5-44 and the final lateral force-drift response is plotted in Figure 5-45. The test was terminated after cycle 39. The stiffness of the bracing system at this point was significantly degraded, as the panel web was entirely detached from the top and bottom horizontal panel flanges.

5.12.1 Shear panel yielding observations

Flaking of whitewash was first observed in the CT subpanel, at the top of the perforation, during cycle 15. The CM and CB subpanels showed similar yielding after cycle 18. These areas, localized around the perforations at 45 degrees angles, were the most significant yielding regions on the panel. For the remaining cycles these areas kept increasing in size until cracks formed at the most strained locations. A series of pictures of the panel at different time intervals is presented in Figure 5-46. The shear deformation in this specimen was concentrated along the vertical subpanels as in tests 5 and 7, see Figure 5-47.

5.12.2 Total lateral force response summary

No significant stiffness degradation was observed for test 9 up to cycle 25, or 9 times the yielding drift. Out-of-plane displacements were not visible before test 25 in any of the subpanels before cracking. The maximum total lateral force reached was 171.8 kips, during the first excursion at 9 times the yielding drift during cycle 26 (t=25.25). The peak lateral force began decreasing rapidly after this point for the following four cycles, that is until the web detached from the top and bottom flanges. However, after cycle 30 the peak lateral force increased again. This behavior had been found to be caused by the contribution to the system stiffness of panel flanges and transverse stiffeners, which become more significant when the panel is subject to large shear deformations. The test was terminated after cycle 39 and the maximum drift reached during testing of this specimen was 15 times the yielding drift, or 0.900 in.

5.12.3 Damage initiation and evolution

The pattern and propagation speed of damage in specimen 9 was similar to the ones of specimens 8 and 7. The first crack was observed during the positive excursion of cycle 23 in the CT subpanel, at the perforation. More cracks around the perforations opened in the CT, CB and CM subpanels in the following cycles. During cycle 27, the first crack propagated across the web, close to the web-flange weld, and reached the weld access hole. The other three cracks close to the flanges all did the same during the 30th cycle. No cracks formed in the LM and RM subpanels. The damage at the end of the test is shown in Figure 5-47.

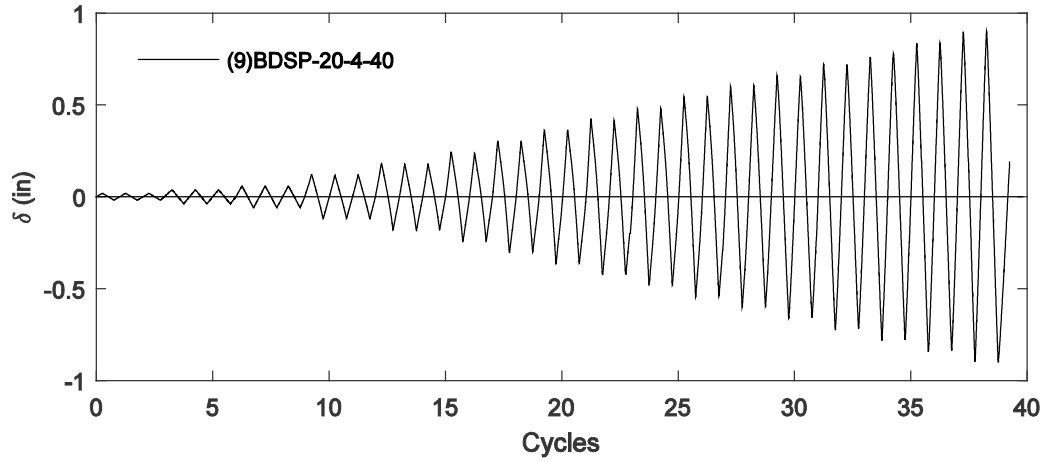

Figure 5-44: Test 9: Experimental lateral drift history

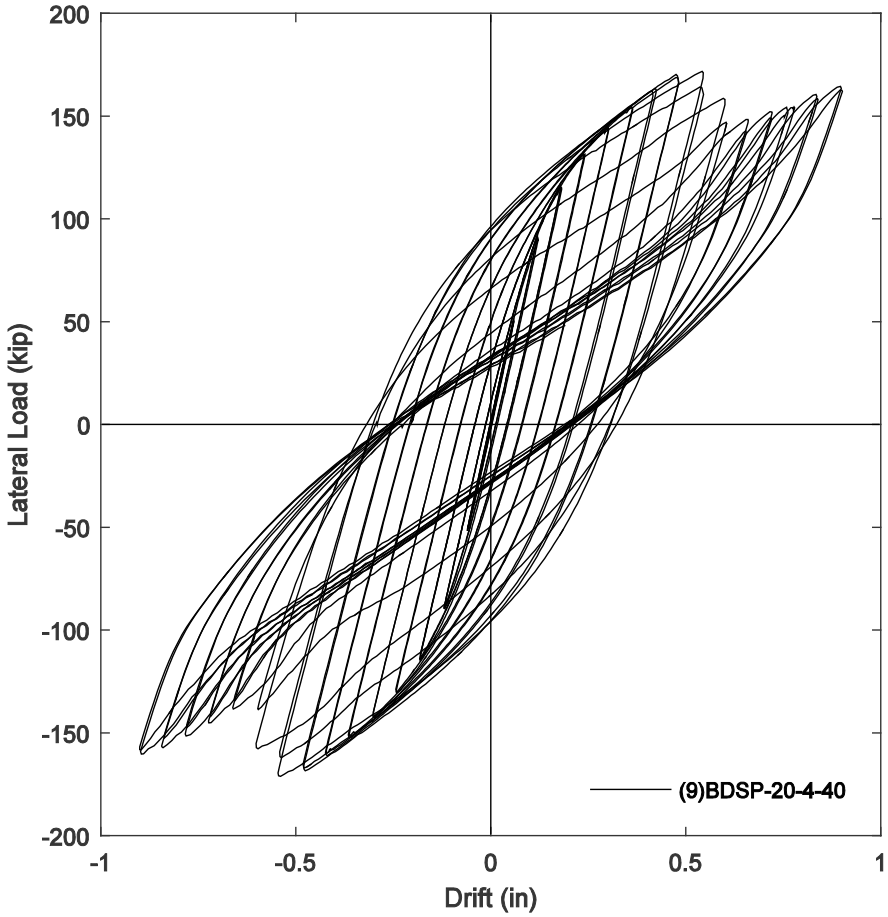

Figure 5-45: Test 9: Experimental lateral force-lateral drift response

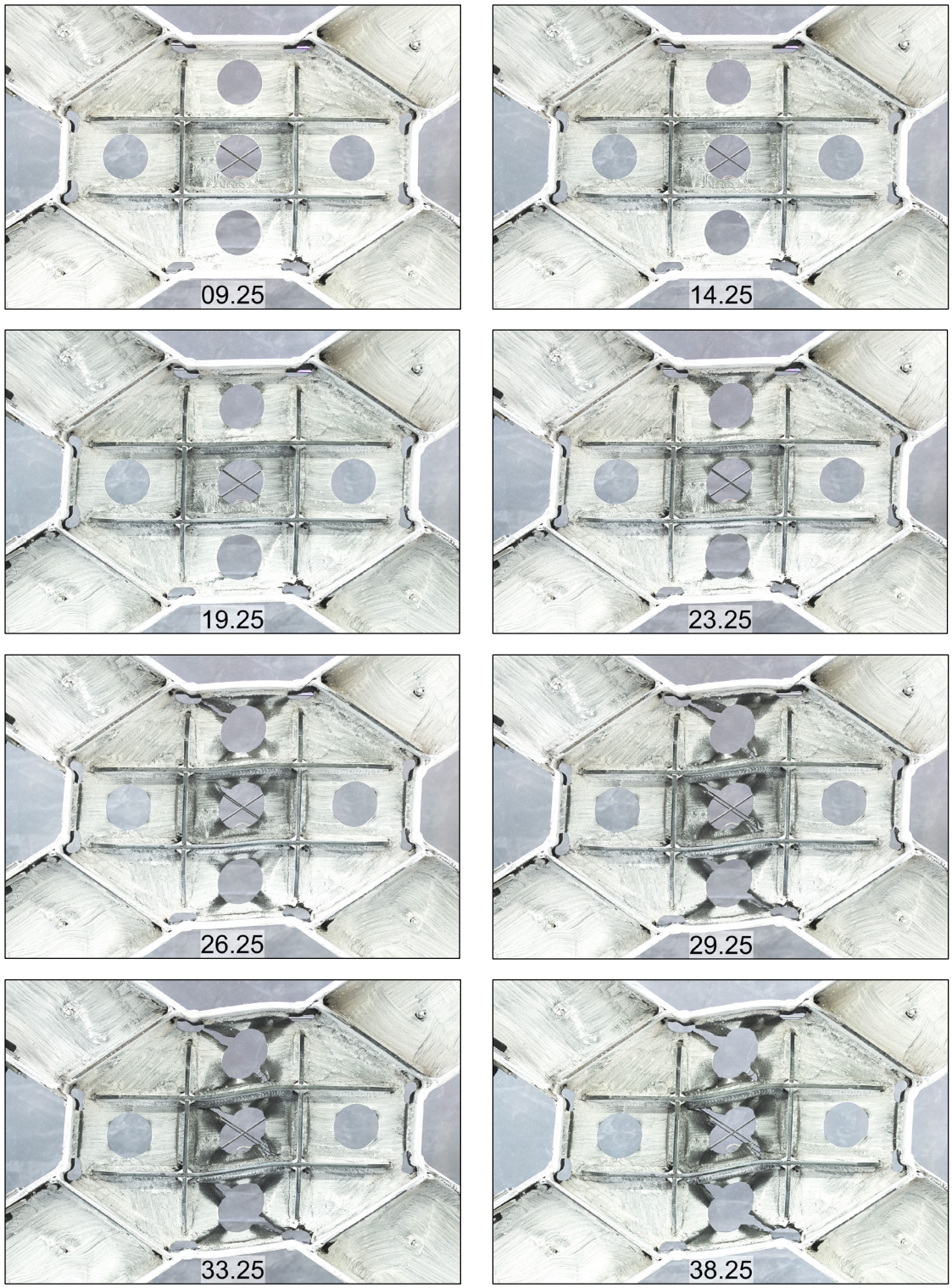

Figure 5-46: Test 9: Yielding and damage evolution

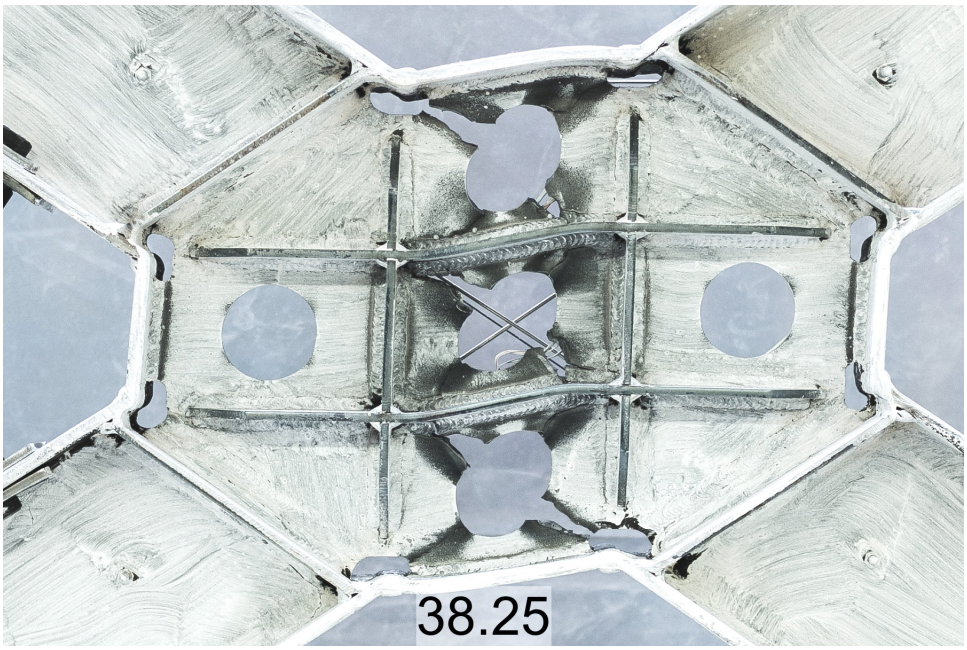

(a)

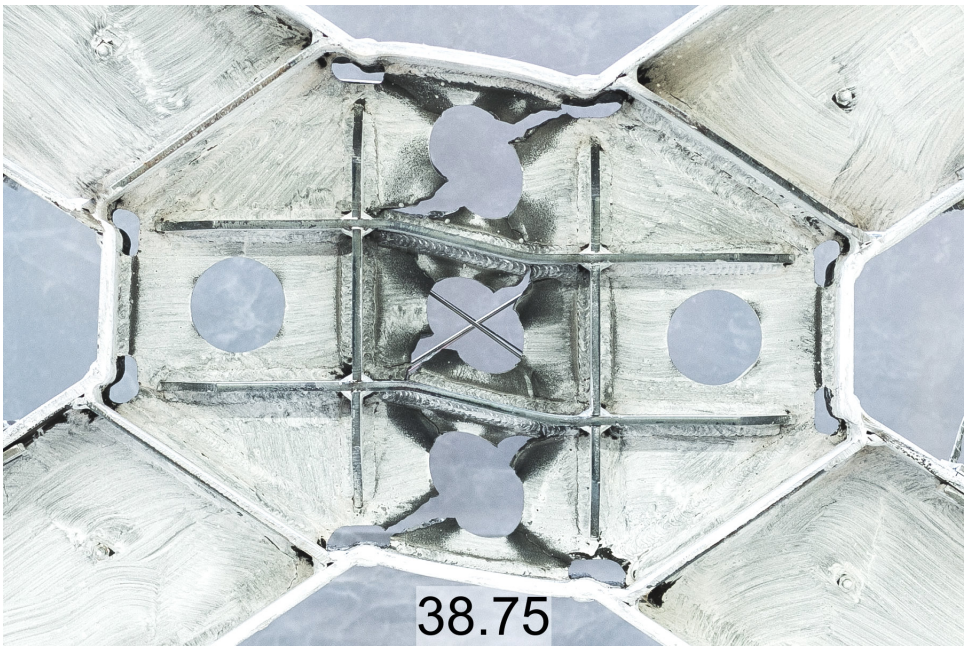

(b)

Figure 5-47: Damage of the specimen at the end of test 9
(a) max. positive drift; (b) max. negative drift

5.13 Test 10 - Specimen BDSP-24-2-00

Test 10 on specimen BDSP-24-2-00 was the last test of the series and second test without perforations in the web. It was completed over two days (August 4th and 5th). The applied lateral drift history is shown in Figure 5-48 and the final lateral force-drift response is plotted in Figure 5-49. The test was terminated after the positive excursion of the 38th cycle. The maximum lateral drift reached was 1.08 *in*, equal to 15 times the design yield drift $\delta_y = 0.072$ *in*.

5.13.1 Shear panel yielding observations

The panel first yielding was observed during cycle 11, at the toe of some of the fillet welds on the web. First visible yielding on the web was observed during cycle 14 in the CM subpanel, in the center, along one of the diagonals. The yielding in the central subpanel became more evident during the following cycles, and during cycle 20 similar yielding began to be visible also in the LM and RM subpanels. At the end of cycle 24, a similar yielding pattern could be seen on the CT and CB subpanels. The yielding areas on each subpanel during the rest of the test localized along diagonal lines and at around the weld access holes in sections LM and RM, as shown in Figure 5-46 (t=31.25). The shear deformation in this specimen was concentrated along the horizontal subpanels (LM, CM, RM).

5.13.2 Total lateral force response summary

Stiffness degradation was noticeable after cycle 17, when the drift reached 5 times the yielding value. Out-of-plane displacements were observed starting from cycle 17 in the CM subpanel. The maximum total lateral force reached was 135.6 *kips*, and it was reached at t = 27.25, peak of first excursion at 10 times the yielding drift, 0.720 *in*. The test was terminated after one excursion of cycle 38, 4 cycles after the web was detached from the flanges. The maximum normalized drift reached during testing of this specimen was 15 times the yielding drift.

5.13.3 Damage initiation and evolution

Damage was first observed during cycle 26 as a crack opened in the CM subpanel, shown in Figure 5-51 before it propagated through the thickness. The crack location and orientation are similar to the first crack observed for test 6. The next crack opened during cycle 28 in the CM subpanel, mirroring the previous one. During the next four cycles similar cracks opened in the LM and RM subpanels, while previous cracks grew and, in some cases, branched out. During cycles 32 and 33 cracks were observed at the terminations of the web-flange welds in the LM and RM subpanels. At the end of cycle 34 the diagonal cracks in the LM and RM subpanels had propagated to the weld access holes and joined with the weld cracks, detaching the web from the vertical flanges. At this point the web was heavily damaged and the vertical flanges and stiffeners were providing most of the stiffness to the system, as it can be seen by the shape of the load-drift curve during the last 5 cycles. The final cracking pattern can be seen in Figure 5-52.

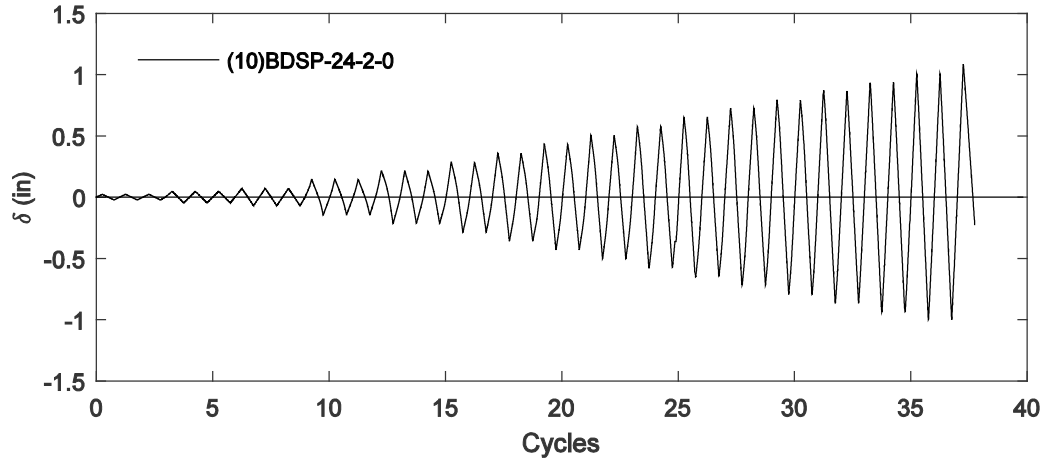

Figure 5-48: Test 10: Experimental lateral drift history

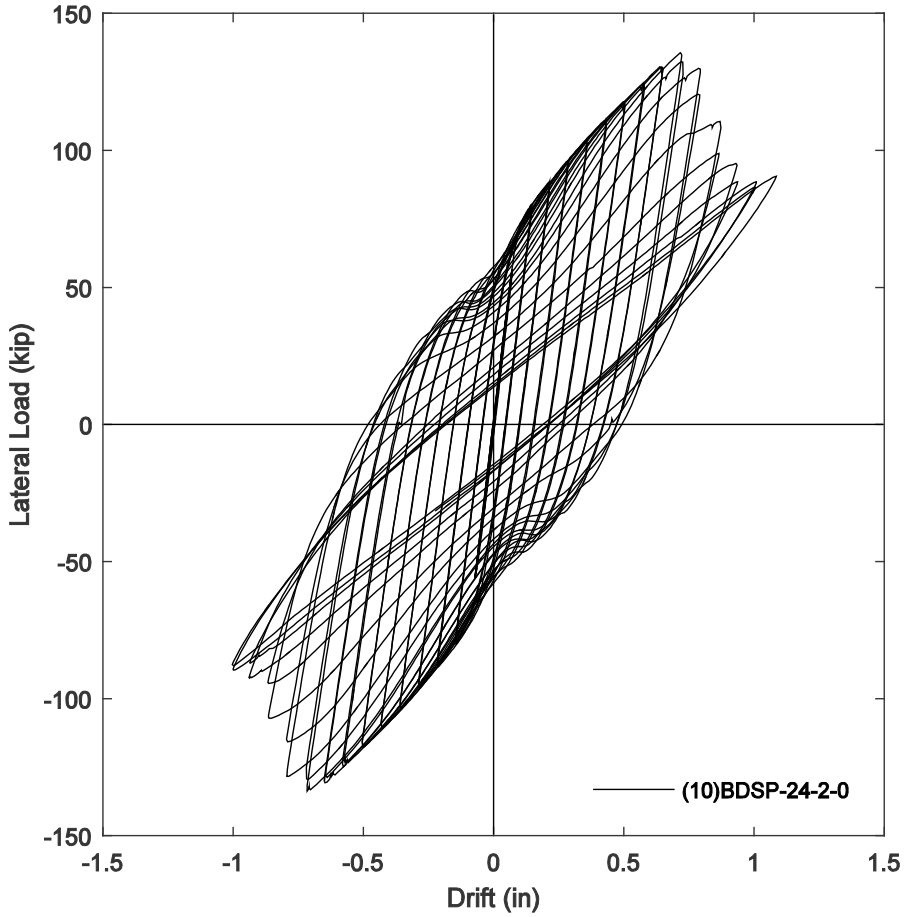

Figure 5-49: Test 10: Experimental lateral force-lateral drift response

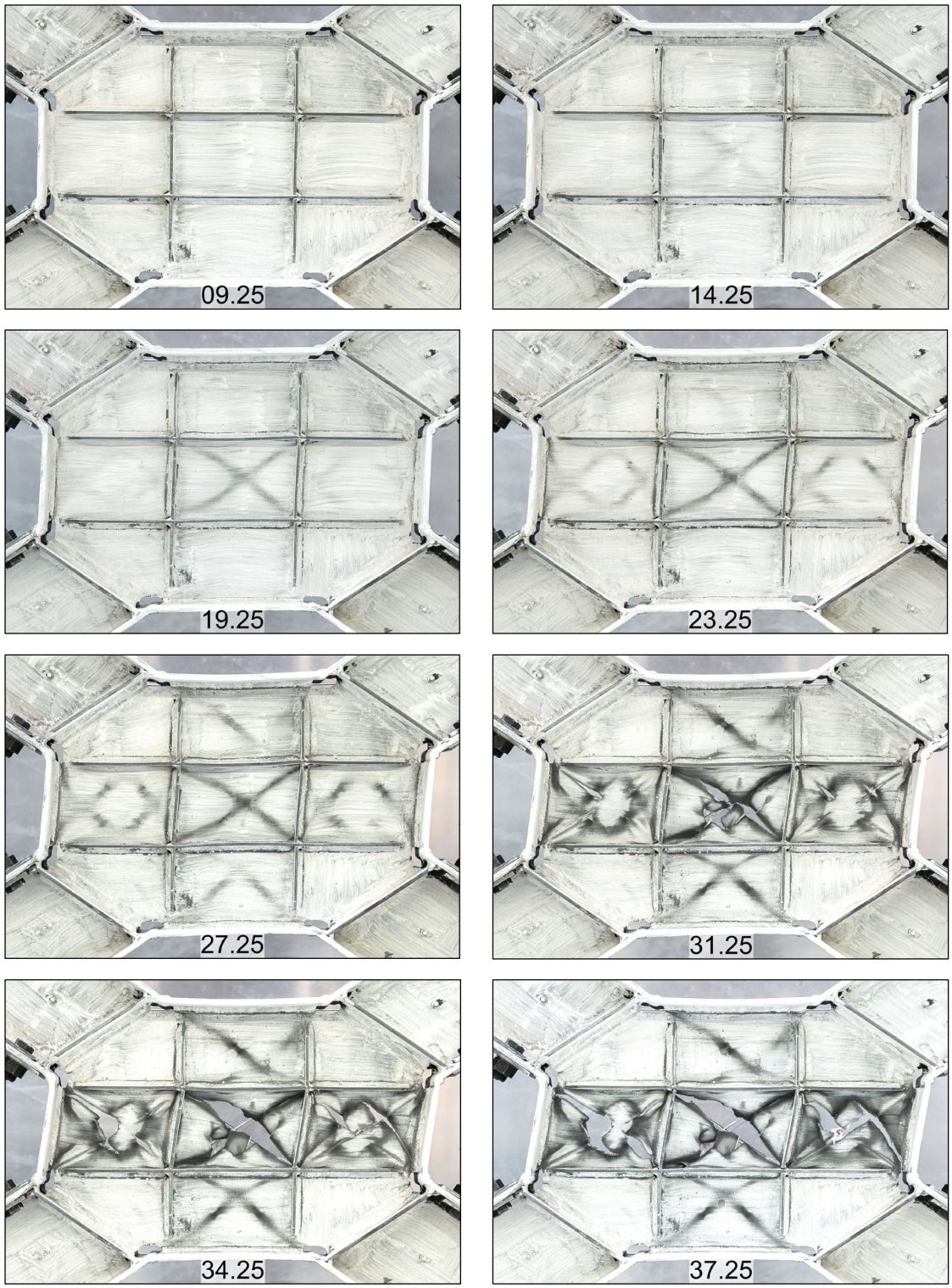

Figure 5-50: Test 9: Yielding and damage evolution

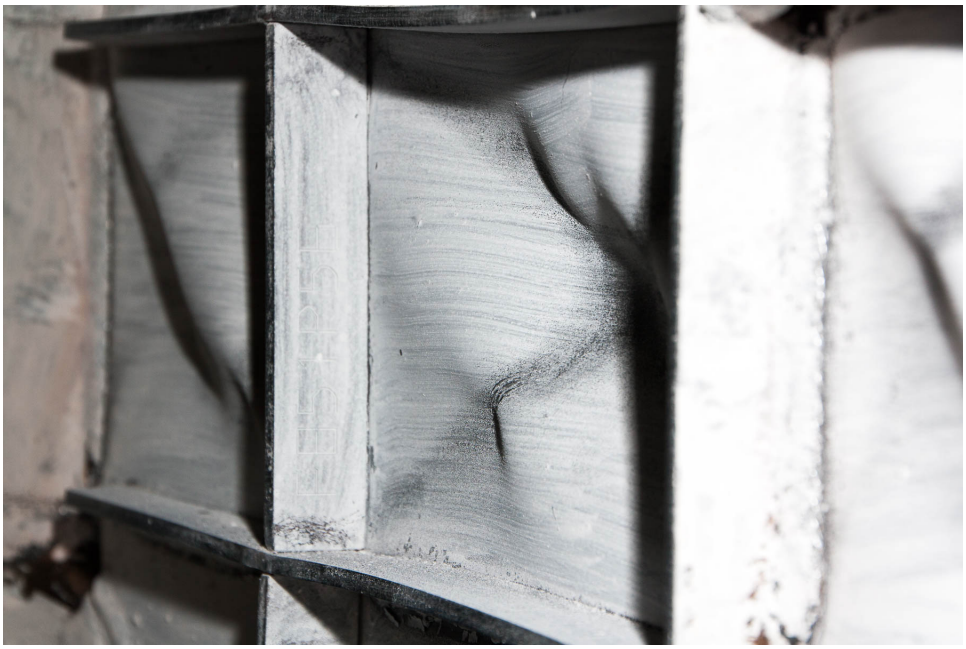

Figure 5-51: First crack forming on CM subpanel in test 10

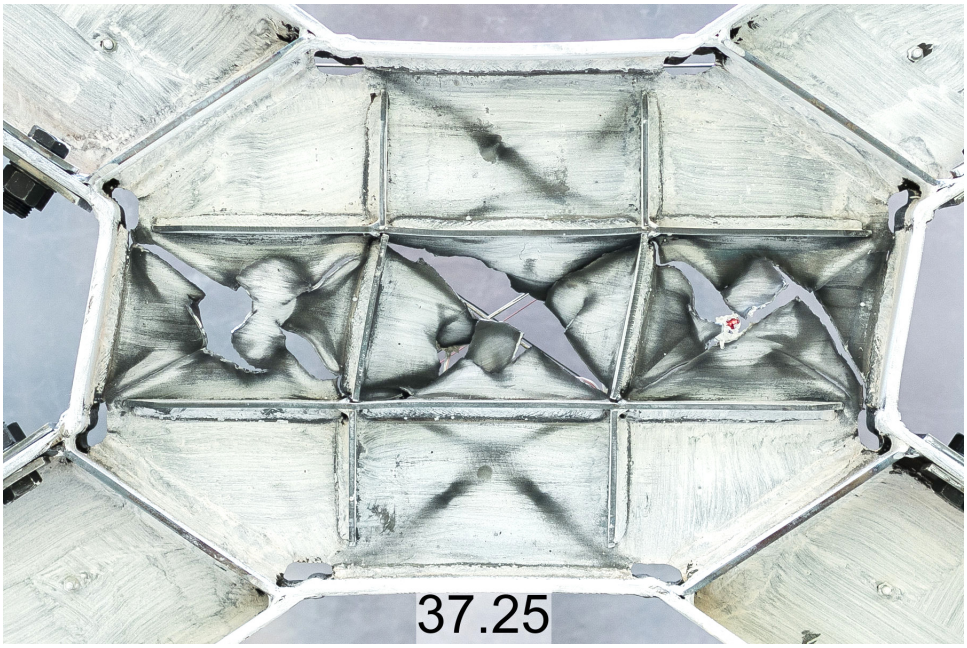

(a)

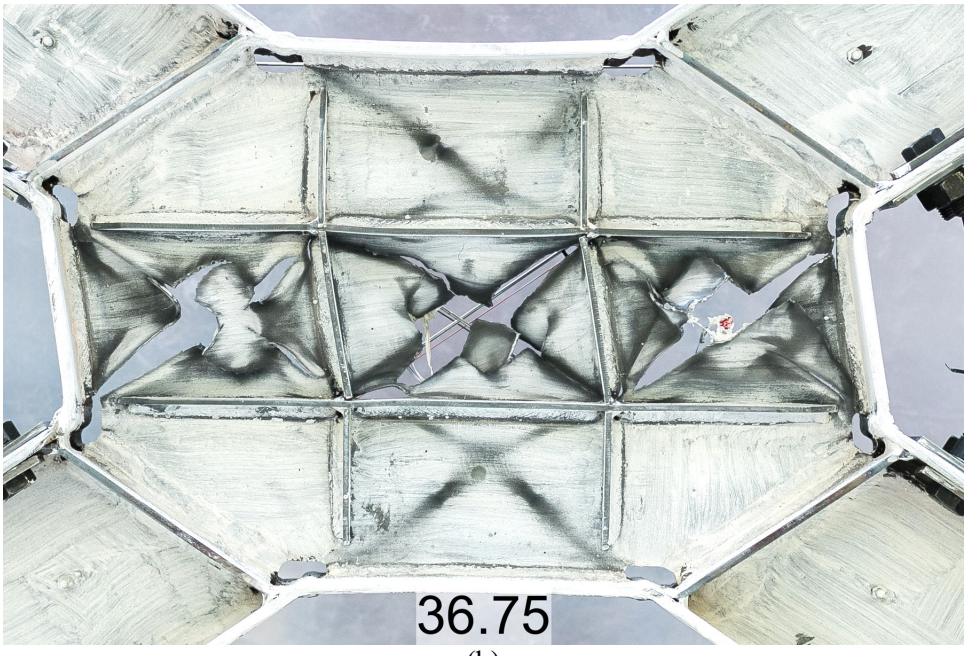

(b)

Figure 5-52: Damage of the specimen at the end of test 10
(a) max. positive drift; (b) max. negative drift

5.14 Experimental results summary

5.14.1 Overview

All the tested specimens exhibited satisfactory performance in terms of cyclic response and energy dissipation. The observed yield drifts and lateral forces were predicted with a good degree of accuracy by the equations introduced in 3.2. The failure modes for all the specimens were similar, with cracks originating at points of maximum strain and then propagating through the web, until a weaker region was created and later detached from the panel flanges, which then became the last source of lateral stiffness. However, by looking at the lateral force-drift curves, displacement fields and damage features, the specimens can be divided into two groups with very similar behavior and response characteristics. The first set includes tests numbered 1 through 4, 6 and 10, while specimens 5, 7, 8 and 9 are part of the second set. In the following paragraphs, the observed response of each set of specimens will be described in greater detail, and compared with the other set.

5.14.2 Response description and comparison

The response of all the panels in the first group showed a sharper transition between the elastic and plastic region than the ones in the second group, when the drift increased past the predicted yield drift δ_y. In fact, past the yield point the tangent stiffness of the force-drift curve decreased more rapidly for the first set than the second. The ratio of maximum lateral force over predicted yield force, V_{max}/V_y, is also found to be larger for the panels in the second set. On the other hand, the panels in the first group achieved much larger ductility than the other panels. In fact, the former showed slower stiffness degradations throughout the loading protocol and ductility ratios μ between 15 and 16, while the latter displayed a rapid stiffness loss after peak and ductility in the 10-11 range. These and other response parameters are listed in Table 5-1.

Another major difference in the behavior of the specimens in the two groups, highlighted by the tests, is the magnitude of the out-of-plane displacements observed during loading. During the

testing of the panels in the first set, out-of-plane displacements of the panel webs were visible at drift levels five or six times the yield drift, while in the other panels, the same displacements were not observed until after cracks developed in the webs. The reason for this difference is attributed to the disparity in slenderness of the specimens due to the different web thickness. In fact, all the specimens in the first set have webs 1/8" thick and slenderness R_w between 0.56 and 0.67, while the panels in the second set have webs with thicknesses of 3/16" and 1/4", and slenderness between 0.28 and 0.44. It can be deduced that, after yielding, inelastic buckling controlled the response of the slender webs of the first panels, while the thicker, less slender panels of the second group were not significantly affected by the same instability. As a consequence, the yielding and damage patterns for the two groups were also different.

The webs of the slender specimen, group one, yielded mostly along diagonal lines that experienced the largest out-of-plane displacements, and therefore the maximum curvatures and strains. In tests 1 through 4, these regions were mainly located at four points at 45 degrees angles along the edges of the perforations. In specimens 6 and 10, which did not have perforations, the yielding areas were oriented diagonally across each subpanel. Under cyclic loading, cracks developed in these areas starting from the points that experienced the largest curvature reversal. Thus, cracks for this set of specimens were driven mostly by flexural strains caused by the out-of-plane deflection and the onset of a tension field action on each subpanel. In contrast, in the less slender specimens of the second set, out-of-plane displacements had little to no effect.

The second group of panels yielded mostly around the perforations similarly to the other panels, but in this case yielding was caused by the higher strains around the perforations caused by stress concentration along the curved edge. Damage still developed along the yield regions, at similar drift levels to the first set, but in these specimens the cracks, originated around the perforations, propagated faster through the web, therefore limiting the ductility of the whole bracing system.

Another macroscopic difference in behavior, between the two sets, is the distribution of yielding and damage in the subpanels. All the specimens in the first group began yielding uniformly in all the subpanels and, if perforated, later developed cracks around most or all of the perforations. As loading continued, the damage eventually localized along the three horizontal subpanels (LM, CM and RM). This created a weaker region which attracted displacements and further localized damage. As discussed in the previous sections, this effect was highlighted by the different deflections of vertical and horizontal transverse stiffeners. On the other hand, yielding regions in the panels of the second group were mostly confined to the three vertical subpanels CT, CM and CB. Yielding in the other two subpanels was limited to small areas around the perforations and at weld toes. Therefore, damage in the second group localized in the vertical subpanels, which combined together constituted the weakest region in these specimens. As a result, the displacement field in these panels was characterized by large vertical displacements.

Table 5-1: Test results summary

Test No	Specimen ID	V_y (kip)	δ_y (in)	V_{max} (kip)	$\frac{V_{max}}{V_y}$	$\frac{\delta_u}{\delta_y}$	Damage initiation (δ/δ_y)	Failure (cycle)	Shear deform.
1	BDSP-20-2-40	33.3	0.038	95.9*	2.88*	n/a	n/a	n/a	H
2	BDSP-24-2-40	39.8	0.045	92.2	2.32	16	29	40	H
3	BDSP-20-2-25	41.3	0.046	95.2	2.30	15	26	39	H
4	BDSP-24-2-25	49.6	0.055	102.9	2.18	15	26	38	H
5	BDSP-20-3-40	53.3	0.049	138.1	2.59	11	26	31	V
6	BDSP-20-2-0	59.8	0.060	122.4	2.05	15	25	30	H
7	BDSP-24-3-40	59.0	0.058	149.0	2.53	12	24	33	V
8	BDSP-20-3-25	59.0	0.059	171.5	2.90	12	24	33	V
9	BDSP-20-4-40	65.0	0.059	171.8	2.64	15	23	30	V
10	BDSP-24-2-0	66.0	0.072	135.6	2.05	15	26	34	H

*Test 1 data from a different, unknown loading history

Chapter 6
Data Analysis

6.1 Introduction

This chapter provides a detailed analysis of the test results, including global response characteristics, local behavior of the components and energy dissipation performance. The data used for this analysis consists of the recorded sensor data – from LVDTs, string-pots and strain gauges – and the additional quantities derived from it by data reduction, as detailed in Appendix B. The main focus of the analysis will be on the response parameters which are necessary to define an accurate analytical model of the system, and for which analytical expression will be proposed.

For clarity in the presentation of some results, a classification of the specimens based on their response characteristics will be used in the following analysis. The classification, similar to the one described at the end of the previous chapter, divides the specimens into three sets. The first group includes tests 2, 3 and 4, the second group includes tests 6 and 10, and the third group includes tests 5, 7, 8 and 9.

6.2 BDSP System Lateral Response

This section presents the analysis of the lateral response of the BDSP specimens as measured during the tests. The analysis includes a discussion of the elastic response of the system, and a discussion of the post-yield and cyclic behavior of the bracing system. In order to study the force-displacement response of the bracing system, the two contributions to the global measured response, of the bracing system and the braced frame, need to be separated. The portion of lateral force resisted by the panel is calculated for each data point as the difference between the total measured lateral force in the actuator and the shear force in the frame. This last term is calculated as the drift

δ multiplied by the frame elastic stiffness K_f, under the assumption that the frame stays elastic for the duration of loading, see Equation (6-1).

$$V_f = K_f\,\delta \tag{6-1}$$

The elastic stiffness of the frame in the equation above, is estimated using the data from small loading cycles performed on the frame without the shear panel, and it was found to be equal to $K_f = 70.5\ kip/in$. Therefore the shear in the panel V_{sp} at each data point is calculated using Equation (6-2). The assumption of the frame being elastic throughout the tests is justified by the experimental observations.

$$V_{sp} = V_{tot} - K_f\,\delta \tag{6-2}$$

6.2.1 Initial Elastic Stiffness of BDSP Specimens

The experimental horizontal elastic stiffness of each specimen is calculated by dividing the panel shear V_{sp} by the estimated local panel displacement u_{sp}. The local panel displacement is defined as the average shear angle in the panel γ_{sp} (see Appendix B.4) times the panel height a. The values of the experimental panel stiffness $K_{BDSP,exp}$ are shown in Table 6-1, along with the panel stiffness calculated using Equation (3-5), where b is replaced by $(1-\rho)b$ for perforated panels. By comparing the two values, it can be seen that Equation (3-5) systematically underestimates the actual panel stiffness, providing values that are 15-40% lower than the experimental ones. In other words, the data suggests that the specimens are much stiffer than what is predicted by the equation, which assumes a uniform distribution of shear strains. The main reason for this difference can be identified in the restraining, stiffening effect that the braces have on the panel. This idea is supported by the experimental observations of the yielding and damage patterns on the specimens. In fact, as discussed in the previous chapter, yielding and damage were only observed in the five central subpanels, while no yielding was observed in the corner regions of the panel. This proves that the deformations in these areas were consistently much smaller than in the rest of the web. Thus, these portions of the web could be seen as effectively being constrained by

the I-beam stubs and by the diagonal stiffeners, making them more rigid than the rest of the panel; as a result, the overall stiffness of the panels increases.

In order to obtain an estimate of the panel stiffness with adequate accuracy for design purposes which doesn't require complex finite element simulations, an equation is proposed which approximates the stiffness of shear panels with similar geometries. The equation is obtained from a numerical study on octagonal web plates subject to shearing diagonal displacements. The elastic stiffness of octagonal plates, with and without perforations, is evaluated by solving the plane stress boundary value problem shown in Figure 6-1, where the boundary conditions are chosen to mirror the interaction of the panel with the braces. The chamfered edges are assigned displacements along the diagonals as shown in Figure 6-1 (Dirichlet b.c.), while the horizontal, vertical and perforation edges are tractions free (Neumann b.c.). The parameters considered for this study are the bracing angle α, the perforation ratio ρ, and the sectional depth of the attaching braces d_X. For each set of parameters, the displacements solution is computed and the total horizontal force is calculated by integrating shear stresses. To maximize the accuracy of the approximating equation, the range of values for each parameter was restricted to practically meaningful values. Therefore, the proposed Equation (6-3) is valid for the following parameters range: $\alpha = [0.45, 0.85]$, $d_X/c = [0.15, 0.40]$ and $\rho = [0.0, 0.4]$. This equation neglects the contribution of the transverse web stiffeners and boundary flanges to the stiffness of the panel; this contribution is in fact negligible for the displacements resulting from the small shear angles produced during the elastic deformation of the panel. A comparison between the panel stiffness calculated using Equations (6-3) and (3-5) and the experimental stiffness is shown in Figure 6-2 for the first 6 cycles ($\delta < \delta_y$). In the figure the horizontal axis is the measured average shear deformation in the panel γ_{avg} (see definition in B.4), and the vertical axis is the measured horizontal shear in the panel shear V_{sp}; for comparison the panel shear predicted by the stiffness equations was calculated as $V = K \cdot \gamma_{avg} \cdot a$, where K is the stiffness given by each equation. A summary of the comparison is presented in Table 6-1. As it can

be seen in the table, the difference between the predicted stiffness and the experimental stiffness is of the order of ±10%.

$$K^{*}_{BDSP} = \frac{5}{6}\frac{G\,t\,b}{a}\,k_s\,k_p \tag{6-3}$$

$$k_s = 0.77 - 2.395\left(\alpha - \frac{\pi}{4}\right)^2 + \left(2.88\frac{d_X}{c}\right)^2 \quad \text{with} \quad \begin{cases} \alpha = [0.45, 0.85] \\ \dfrac{d_X}{c} = [0.15, 0.4] \end{cases} \tag{6-4}$$

$$k_p = 1 - \rho\left(\frac{\rho}{\tan^2\alpha} - 1\right) \quad \text{with} \quad \rho = [0.1, 0.4] \tag{6-5}$$

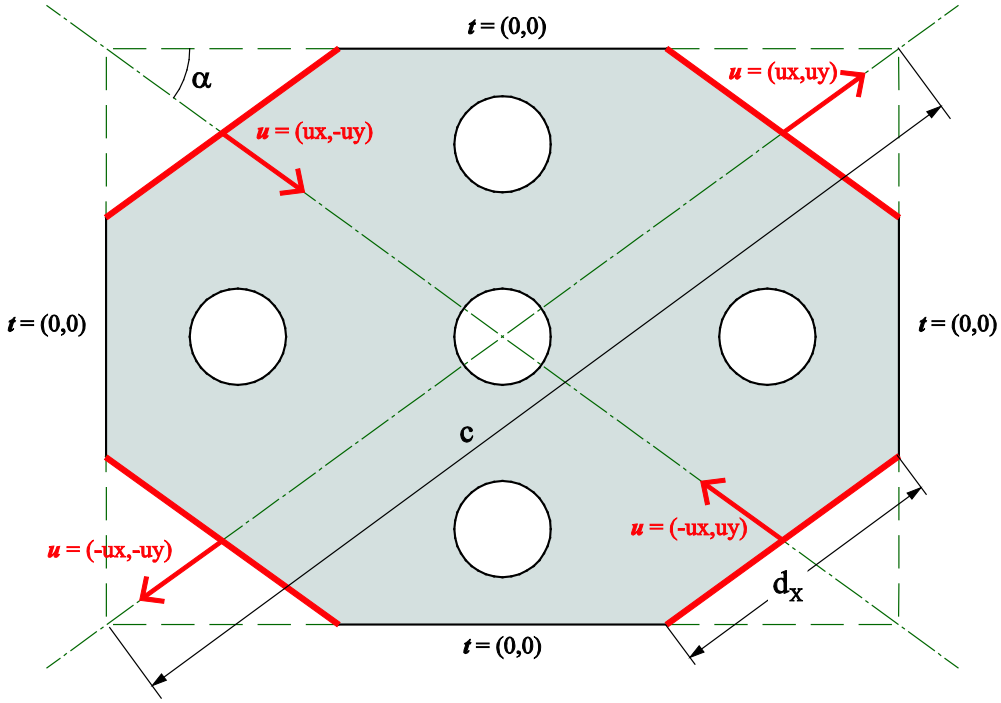

Figure 6-1: Boundary value problem for parametric study of web stiffness

Table 6-1: Panels initial elastic stiffness

Test	Eq. (3-5)	Eq. (6-3)	Experimental	% Error Eq. (6-3)
1	1255	1796	1728	4.0%
2	1255	1472	1565	-6.0%
3	1569	2395	2377	0.8%
4	1569	1963	2040	-3.7%
5	1882	2695	2695	-0.0%
6	2091	2879	2867	0.4%
7	1882	2208	2467	-10.5%
8	2353	3593	3951	-9.1%
9	2510	3593	3345	7.4%
10	2091	2359	2452	-3.8%

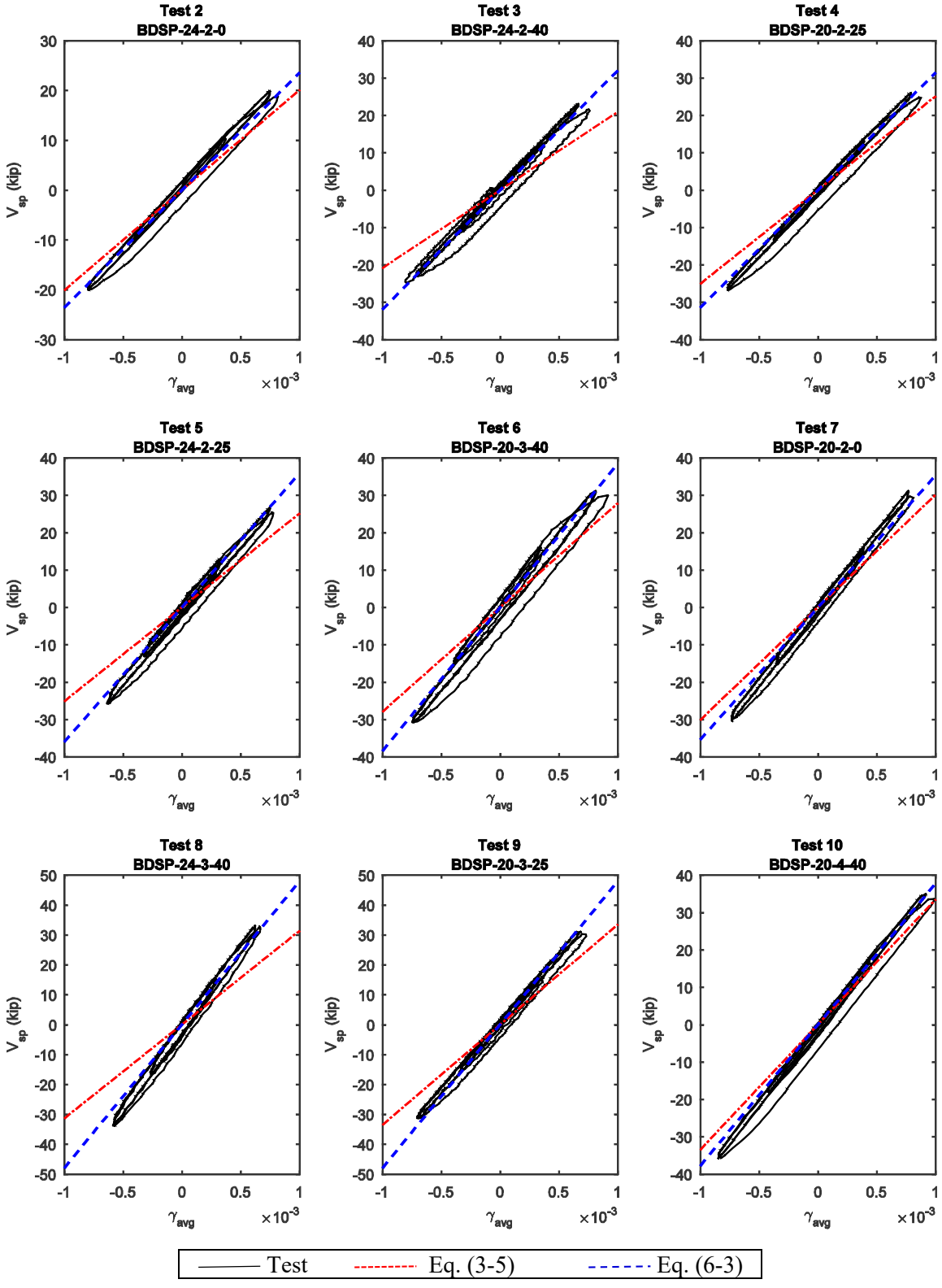

Figure 6-2: Initial BDSP elastic stiffness comparison

6.2.2 BDSP Shear Strength Envelopes

In this section, the lateral response of the test specimens will be analyzed and compared to analytical expressions for the prediction of yielding and maximum horizontal shear. The plots in Figure 6-3 show the response of the shear panels during each test. The vertical axes are the horizontal shear force in the panel V_{sp} normalized by the yielding shear force calculated using Equation (3-2), while the horizontal axes are the lateral drift normalized by the yielding drift. The resulting lateral response envelope is also superimposed on each plot. It can be seen from the figures that Equation (3-2) gives a good estimate of the yielding load for tests 2-4, 6 and 10, while it seems to underestimate the yielding load for the remaining specimens (5, 7-9). This difference is likely due to the variability in the yield stress of the web plates, as suggested by the finite element simulations that will be presented in Chapter 7. In fact, since the steel fabricator was not able to provide samples of the sheets used for the web specimens, a uniaxial yield stress equal to 36 ksi (minimum required yield stress for A36 grade steel) was assumed for use in Equation (3-2). However, it is well known that, in practice, it is not uncommon for this grade of steel to achieve higher yield stress than the specified minimum. This hypothesis is corroborated both by the numerical simulations presented in the next chapter, and by the fact that all the specimens with same web plate thickness also appear to have a similar yield stress. Moreover, the shop drawings for the panel specimens indicate that actual A36 grade steel sheet was used for the 3/16" and 1/4" thick web plates (specimens 5, 7, 8 and 9), while A1011 Gr36 steel was used for the 1/8" web plates in the other specimens. In Table 6-2 the experimental yielding load is compared to the one predicted by Equation (3-2) for each test. For the specimens with 1/8" webs the difference between the prediction and the measured lateral force varies between 3% and -8%. On the other hand, for the specimens made with thicker plates (and different steel grade) the error is between -45% and -69% when the yield stress is set to 36 ksi. However when a yield stress of 55 ksi is used (obtained from comparison of numerical simulations, see Chapter 7) a better estimate of the yielding load can be obtained and errors range between -10% and 6%; the values relative to the 55 ksi yield stress are

shown in parentheses in Table 6-2 for tests 5, 7, 8 and 9. Therefore, Equation (3-2) can be used to predict the horizontal force V_{ysp} to cause first yielding in the shear panel, once the yield stress of the panel web is known. This fundamental parameter of the bracing system can then be used to design the bracing system, either by linear analysis (response spectrum or linear time-history) or nonlinear dynamic analysis.

The maximum horizontal shear in each panel V_{max} is also determined from the envelopes in Figure 6-3, and the values obtained are listed in Table 6-3. However, in contrast to what has been assumed for the study of the elastic behavior in the previous section, the contribution of the boundary flanges and transverse stiffeners to the total lateral shear can no longer be neglected at the point of peak load – due to the large displacements and rotations to which the device is subjected. As a consequence, when the maximum strength is reached, the deformations in the panel are large enough to yield the boundary flanges at their extremities. The same is true for the transverse stiffeners, especially when displacements localize along the clear height of the panel as observed during tests. Therefore, with reference to Equation (6-6), the maximum lateral force V_{max} is expressed as the sum of two distinct contributions: the horizontal force resulting from shear in the panel web ($V_{max,web}$), and the shear in the flanges and stiffeners with fully developed plastic hinges ($V_{max,pl}$). The last quantity is calculated using Equation (6-7), where h_{fl} is the clear height of the vertical flanges, and the sections plastic moments are taken as shown in (6-8).

$$V_{max} = V_{max,web} + V_{max,pl} \tag{6-6}$$

$$V_{max,pl} = \frac{\left(2\, M_{pl,fl} + 2\, M_{pl,s}\right)}{h_{fl}} \tag{6-7}$$

$$M_{pl,fl} = \frac{b_{fl}\, t_{fl}^2}{4}\, f_y \qquad\qquad M_{pl,s} = \frac{2\, d_s\, t_s^2}{4}\, f_y \tag{6-8}$$

In the last equation, b_{fl} and t_{fl} are the width and thickness of the boundary flanges, d_s and t_s are the depth and thickness of the transverse stiffeners on each side of the panel, and f_y is the yield stress. The maximum horizontal force in the web $V_{max,web}$ for each test is then calculated using Equation (6-6), and the values are listed in Table 6-3. These values are compared to the nominal

ultimate shear strength of the web $V_{u,web}$, calculated assuming a uniform shear stress along the panel width equal to the ultimate shear stress $\tau_u = f_u/\sqrt{3}$, see Equation (6-9) below, where f_u is the maximum shear stress reached in the panel web. Here a value of 58 ksi –the minimum specified strength for ASTM A1011 Gr36 steel – is used for specimens 1/8" thick web plates, while a value of 70 ksi is used for the thicker plates, consistent with the assumption of a higher yield stress previously discussed.

The ratio $V_{max,web}/V_{u,web}$ is plotted in Figure 6-4 for each specimen against the respective slenderness parameter R_w. It can be seen that for specimens with thick web plates the ratio is between 1.0 and 1.1, while for specimens with more slender webs (higher R_w) the ratio decreases indicating that Equation (6-9) overestimates the ultimate strength for these panels. The main cause of this difference is the inelastic buckling of the webs, which was observed during tests for all of these specimens as detailed in the previous chapter. To account for this reduction, a coefficient C_v is introduced to model the effect of plate slenderness on the ultimate shear strength of the panel. Since this coefficient is conceptually equivalent to the coefficient C_v used in Section G of the *Specification* (AISC 2010b), a similar expression is used, where the coefficient decreases proportionally to the inverse of a slenderness parameter when the latter is greater than a threshold value which indicates the point at which inelastic instability can occur. Thus, the value of this coefficient is set to 1.0 for webs having $R_w \leq R_{w0}$, and decreases when $R_w > R_{w0}$ as defined in Equation (6-10). The function $C_v(R_w)$ is superimposed in Figure 6-4 to the experimental values, where it can be seen that Equation (6-10) is a good predictor of the strength reduction due to instability. The experimental values of $V_{max,web}$ are then compared with the values obtained using Equation (6-11), see Table 6-3. The difference between the strength predicted by this equation and the experimental results is found to be within -5% and 3% for all tests except test 8 for which the predicted value is 10% lower than the experimental one.

$$V_{u,web} = \tau_u \, b_e \, t_w \tag{6-9}$$

$$C_v(R_w) = \begin{cases} 1 & if \; R_w \leq R_{w0} \\ 1 - \dfrac{R_w - R_{w0}}{R_w} & if \; R_w > R_{w0} \end{cases} \tag{6-10}$$

$$V_{max,web} = C_v \, V_{u,web} \tag{6-11}$$

From the data analysis presented above, it can be seen that Equations (3-2) and (6-11), respectively, give a reasonable estimate of the yielding and maximum horizontal force in the bracing system. Therefore, these two equations are proposed as design equations to calculate the yielding and ultimate strength of the BDSP system for use in common finite element analysis software.

In order to completely define the lateral response of the bracing system, the drifts at which the panel reaches yielding, maximum lateral force and damage initiation need also to be defined. Given the overall better performances in terms of ductility and energy dissipation observed in the panels without perforations, the development of the proposed envelope model is limited to the case of panels with solid webs. Figure 6-5 shows the experimental envelopes of the lateral force in the bracing system V_{sp} on the vertical axis, against the average shear deformation γ_{avg} on the horizontal axis for tests 6 and 10. The proposed model is shown with a thicker line in the same figure. The proposed envelope is a bilinear model, followed by a softening region and a residual strength plateau. The first segment corresponds to the elastic region, and it extends from the origin to the yield point—defined by the lateral yielding force $V_{sp,y}$ and the quantity $\gamma_{avg,y}$—calculated as shown in Equation (6-13). The second segment then connects to the point defined by Equation (6-14), and it captures the post-yield strain hardening response of the web and the formation of the plastic hinges in the vertical boundary flanges. For the calculation of $\gamma_{avg,1}$—and the other post-yield deformation quantity $\gamma_{avg,2}$—the height of the panel a is replaced by the clear height a_c, defined as the length across which displacements and shear strains are expected to localize. As observed during the tests, this length is equal to the nominal height of the panel minus the portion that is restrained by the braces, thus:

$$a_c = a - 2\, d_X \sin\alpha \tag{6-12}$$

The shear strain at the end of the strain hardening region γ_1 is fitted to the data, and set to 0.10, which is consistent with the range of shear strains obtained in previous studies for low-yield steel panels (Zhang et al. 2013). The third segment of the envelope, which corresponds to the softening

in the response due to propagation of damage in the web, extends to the point defined by Equation (6-15), where $\gamma_2 = 0.15$ and the lateral force $V_{sp,2}$ only includes the contribution of the vertical boundary flanges, since the web is assumed to have exhausted its strength at this point. The envelope is completed by a horizontal segment at constant force.

$$\gamma_{avg,y} = \frac{1}{a}\frac{V_{sp,y}}{K^*_{BDSP}} \qquad V_{sp,y} = \tau_y \cdot b_e \cdot t_w \tag{6-13}$$

$$\gamma_{avg,1} = \gamma_1 \cdot \frac{a_c}{a} \qquad V_{sp,1} = V_{max,web} + V_{max,pl} = V_{max} \tag{6-14}$$

$$\gamma_{avg,2} = \gamma_2 \cdot \frac{a_c}{a} \qquad V_{sp,2} = V_{max,pl} \tag{6-15}$$

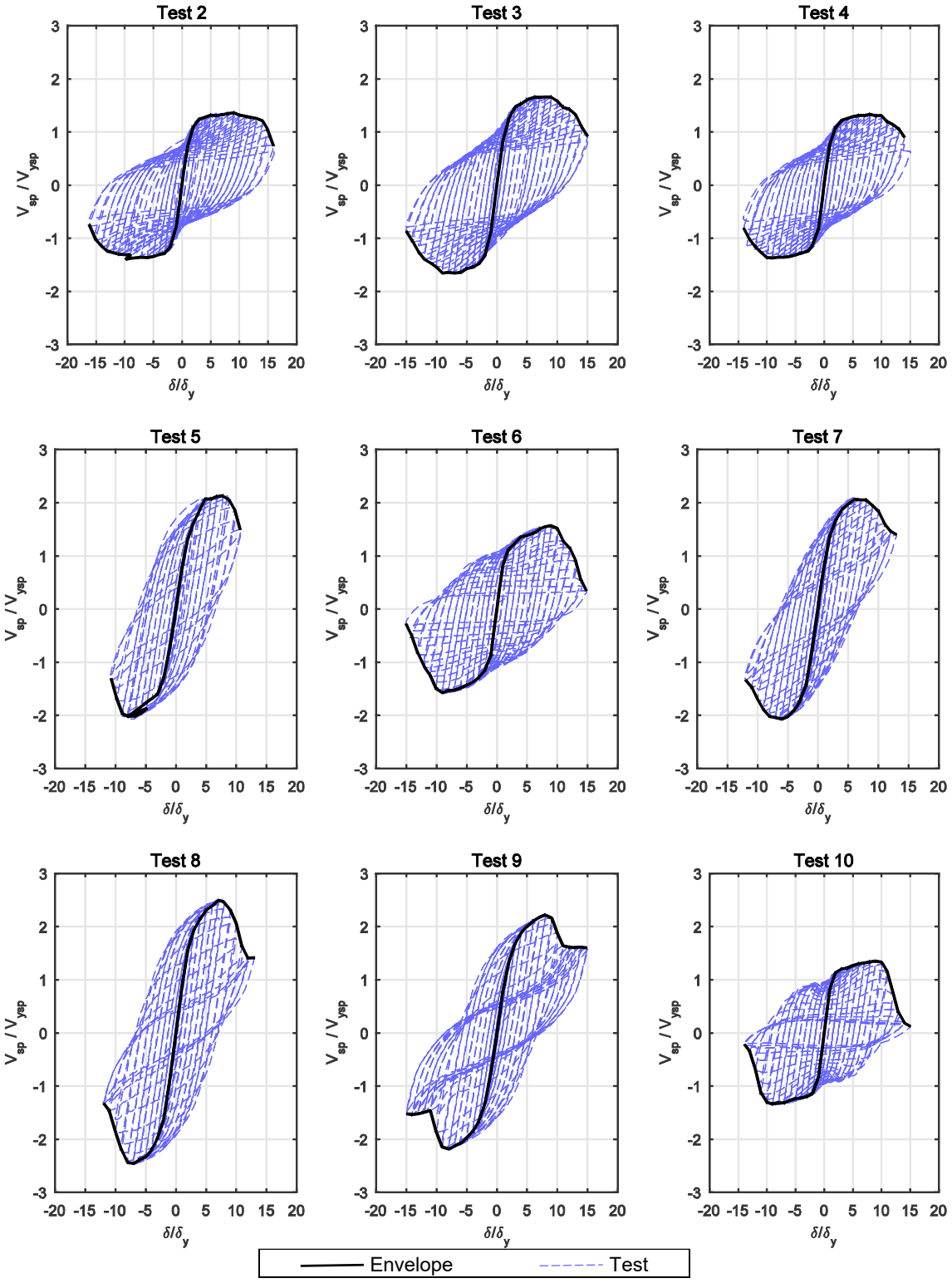

Figure 6-3: Normalized panel shear envelopes

Table 6-2: BDSP experimental and predicted yield lateral force

Test	V_{ysp} [kip]		
	Eq. (3-2)	**Test**	**Error %**
1	31.2	32.5	-4.2
2	37.4	38.5	-2.7
3	39.0	42.2	-8.2
4	46.8	45.3	3.3
5	46.8* (71.5)	75.6	-61.5* (5.7)
6	52.0	51.7	0.6
7	56.2* (85.8)	85.9	-52.9* (0.1)
8	58.5* (89.4)	98.8	-68.8* (-10.5)
9	62.4* (95.3)	90.6	-45.2* (4.9)
10	62.4	66.5	-6.6

+ Data from Test 1 obtained with non-standard loading history
* Shaded rows indicate specimens with higher yield stress, f_y = 55 *ksi* used for values in parentheses

Table 6-3: BDSP experimental and estimated maximum shear strength

Test	$V_{u,web}$ [kip]	R_w	C_v	V_{max} [kip]	$V_{max,web}$ [kip]		
	Eq. (6-9)		Eq. (6-10)	Test	Eq. (6-11)	Test	Error
1	50.2	0.55	0.85	58.1	42.9	45.1	-5.1%
2	60.3	0.67	0.75	53.2	44.9	46.2	-2.8%
3	62.8	0.55	0.85	65.2	53.7	52.2	2.7%
4	75.3	0.67	0.75	65.6	56.2	58.6	-4.4%
5	90.9	0.37	1.00	108.0	90.9	94.5	-3.9%
6	83.7	0.55	0.85	82.9	71.5	69.9	2.3%
7	109.1	0.44	1.00	115.4	109.1	108.4	0.7%
8	113.7	0.37	1.00	138.7	113.7	125.2	-10.1%
9	121.2	0.28	1.00	135.9	121.2	120.5	0.6%
10	100.5	0.67	0.75	84.7	74.9	77.7	-3.8%

* Shaded rows indicate $f_u = 70\ ksi$ was used for Equation (6-9)

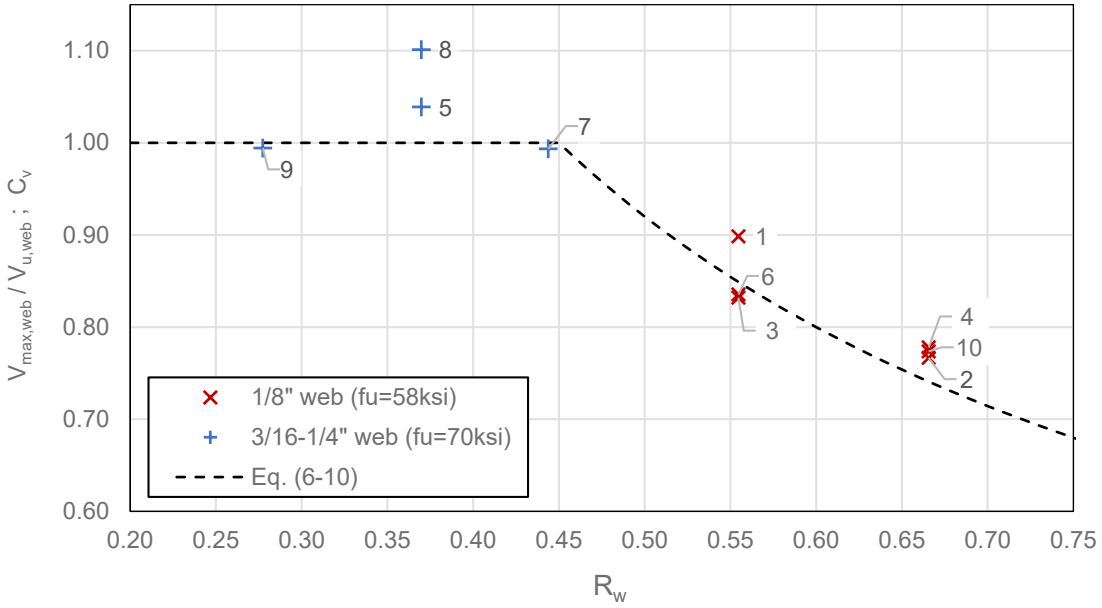

Figure 6-4: Panel slenderness and maximum shear strength

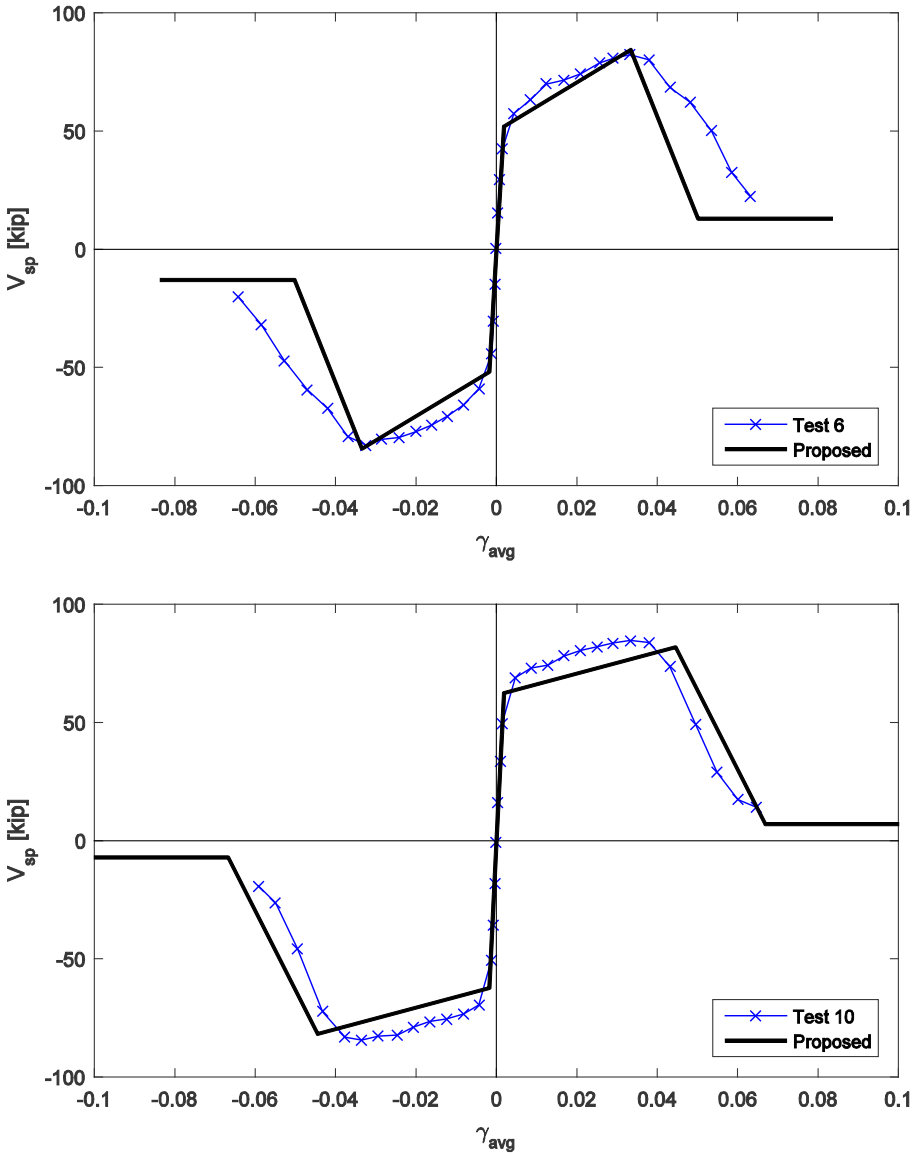

Figure 6-5: Proposed envelope for shear panels with solid webs

6.2.3 Cyclic Performance and Energy Dissipation

The cyclic performance of the BDSP specimens and their energy dissipation capacity is investigated in the following section. In figures 6-6 to 6-10, the hysteretic response of the specimens at various drift levels is presented, where the normalized horizontal shear force is plotted on the vertical axis, against the average panel shear angle γ_{avg}. In the following discussion, the average

shear angle is used as an independent variable because it allows to more accurately capture the local behavior of the panel, as opposed to the lateral drift quantity which includes the effects of the compliance of the other components in the structure; a more detailed discussion of the relationship between these two quantities is presented at the end of this section in 6.2.3.1.

Figure 6-6 shows the force–shear angle plot for each specimen during cycles from 6 to 15, which correspond to the nine cycles at one, two and three times the design yield drift δ_y. From the plots it can be seen that tests 2, 3 and 4—panels with 1/8" perforated webs—have very similar hysteresis cycles. The same can be said for tests 6 and 10 (the two panels with 1/8" thick web and no perforations), and test 5, 7, 8 and 9 all of which have webs thicker than 1/8". Note that this pattern matches the observations made during testing, described in Chapter 5, regarding the amplitude of out-of-plane displacements and stability of the panel webs. At this drift levels none of the panels display a reduction in stiffness or in the area of the hysteresis cycles.

In Figure 6-7 the data from the next six cycles (15 to 21) at four, five and six times the reference yielding drift is plotted for each test. The plots show that the hysteresis cycles are still similar among panels with similar characteristic. However, at this drift level, a minor loss in stiffness can be noticed in the slenderest specimens with 1/8" thick webs. In particular, tests 2, 3 and 4 show a small loss in stiffness as the peak load stays virtually constant with the increasing drift; likewise, specimens 6 and 10 exhibits a slight pinching of the hysteresis curve, which is caused by the inelastic buckling of the panel web, and the consequent need to straighten the web when the load is reversed—in order to recover load bearing capacity in the new direction. The effect is more pronounced in the last specimen, as it would be expected because of its larger slenderness due to the wider subpanel.

The response of the bracing system during the cycles from 21 to 27—drifts between seven and nine times the yielding value—are shown in Figure 6-8. During these cycles, damage initiation was observed in all the panels except specimen 2 (see Chapter 5). The onset of damage, and the resulting loss in stiffness, are easily discernible in the plots of the stockier panels (tests 5, 7, 8 and 9); in the

other specimens, the decrease in stiffness due to the opening of cracks in the web is less evident at this drift level. It is the author's opinion that the effects of damage are not immediately visible for the slender panels due to the earlier inelastic buckling: at this point in the loading the web plates had already experienced out-of-plane displacements for several cycles, the stiffness of the web has already been affected, and the stresses are now redistributed away from the location of damage. On the other hand, in these panels the larger drift causes an increase in the amplitude of the out-of-plane displacements, which results in a more significant pinching of the hysteresis curves—especially in specimens 6 and 10.

The next set of plots in Figure 6-9 shows the response of the specimens during the following 8 cycles—from cycle 27 to 35 at drift levels from ten to thirteen times δ_y. It should be noted that tests 5, 7 and 8 were terminated within this loading range, therefore the plots only include the response up to the last complete cycle (refer to Chapter 5 for details on last cycle and test termination). The decrease in strength is evident in the response for all the specimens which experienced damage in the previous cycles; for specimen 2, in which damage was first observed during cycle 29, the decrease in maximum strength is less marked. From the plots it can be seen that as drift increases and damage propagates, the hysteresis cycle of each specimen gets progressively narrower. Moreover, as the panels ultimately approach their failure point, the responses can be seen shifting gradually towards differently shaped hysteresis cycles; this behavior is particularly evident in the response of tests 5-10, as it unfolds at a faster rate than for tests 2-4. Failure of the specimens was identified during the tests when the damage in the panel web had propagated through the web, which resulted in the creation of a continuous, heavily damaged region that was visibly unable to carry any lateral load. This observation, together with the markedly changed shape of the hysteresis cycles, suggests that a different mechanism is responsible for the residual lateral stiffness and energy dissipation after the web had failed, see Figure 6-10. By observing the displacement field of the panels after the web exhausted its capacity, the source of the residual resistance can be recognized in the boundary flanges and the transverse stiffeners. In

fact, under large drifts, plastic hinges form at the end of the boundary flanges and along the transverse stiffeners subject to the maximum relative displacement. For tests 2-4, 6 and 10 this mechanism involves the vertical flanges and stiffeners—since the displacements localize along the three horizontal subpanels—while the horizontal flanges and stiffeners are the resisting elements for tests 5, 7-9 (see Chapter 5). A major difference between the two group of specimens is the shape and stiffness of the residual mechanism. In fact, for tests 6 and 10, the final hysteresis cycles are characterized by a short elastic response—at load reversal—followed by an extended region at constant force, which closely matches the expected response of a beam (i.e. boundary flanges) with fully formed plastic hinges. On the other hand, the hysteresis cycles after failure of the stocky specimens (5, 7, 8 and 9)—which experienced a vertical localization of relative displacements—are characterized by a comparatively large tangent stiffness at all time, and more importantly they display a significant stiffening when the value of the average panel strain approaches 0.025-0.030. This stiffening effect is attributed to nonlinear geometry effects caused by the large displacements field in the panel; the vertical type of deformation in these panels generates significant bending moment in the panel and braces, as described below in 6.3.

The normalized plastic energy dissipation $\overline{E_p}$ is plotted against the loading cycles in Figure 6-11 for each test. The dissipated energy is calculated from the area inside the load-displacement curves, and then normalized by the experimental values of V_{max} and δ_y to obtain a non-dimensional measure. In the same figure, the histories of half the Cumulative Inelastic Displacement (CID) are shown; the value of CID is calculated at each data point by subtracting the elastic displacement obtained using the initial stiffness from the total displacement and then normalized by the yield displacement. From the plots it can be seen that the two quantities are in good agreement up prior to damage initiation (marked by a vertical dashed line), except for test 5 where the normalized energy is larger than the displacement quantity. The difference observed in this last test is due to the accidental deviation from the prescribed loading protocol, which caused an overly large drift (as mentioned in 5.8) and the resulting increase in lateral force due to the isotropic component of

the hardening behavior of steel. The correlation between the energy and the inelastic displacement shows that an estimate of the energy dissipated by the bracing system can be obtained by multiplying the expected inelastic displacement by the quantity $V_{max}/2$.

In Figure 6-11, the amount of energy dissipated in each panel at damage initiation and at failure are highlighted—which corresponds respectively to the point where the solid line crosses the damage initiation threshold, dashed line, and the failure threshold, dot-dashed line. For the tests with thin web plates—and $R_w > R_{w0}$—the value at onset of damage range from 130 to 170, which denote a good energy dissipation capacity of the specimens. In contrast, the perforated panels with thicker webs achieved lower plastic dissipation before damage, with values less than 50% of the other tests: test 9 had the lowest dissipation with a value of 44, while the maximum value of 79 was reached by test 5. However, if the CID/2 quantity is considered, instead, the maximum value before damage for test 5 falls to about 60 which is closer to the values for tests 7 and 8. The total energy dissipated before failure for the first group of specimens ranges between 299 (test 10) and 383 (test 2), while for the specimens with $R_w < R_{w0}$ the total dissipation ranges from 112 (test 9) to 135 (test 7). The values of the normalized energy and the cumulative inelastic displacement are summarized in Table 6-4.

Table 6-4: Energy dissipation and CID for specimens at damage initiation and failure

Test	Damage Initiation			Failure		
	E_p (kip-in)	$\overline{E_p}$	CID	E_p (kip-in)	$\overline{E_p}$	CID
2	406	170	340	918	383	767
3	390	130	260	1055	352	704
4	491	136	272	1185	329	657
5	637	79	241	966	119	365
6	662	133	266	1687	339	678
7	620	61	185	1383	135	413
8	723	58	177	1650	132	403
9	538	44	134	1368	112	341
10	978	160	321	1824	299	598

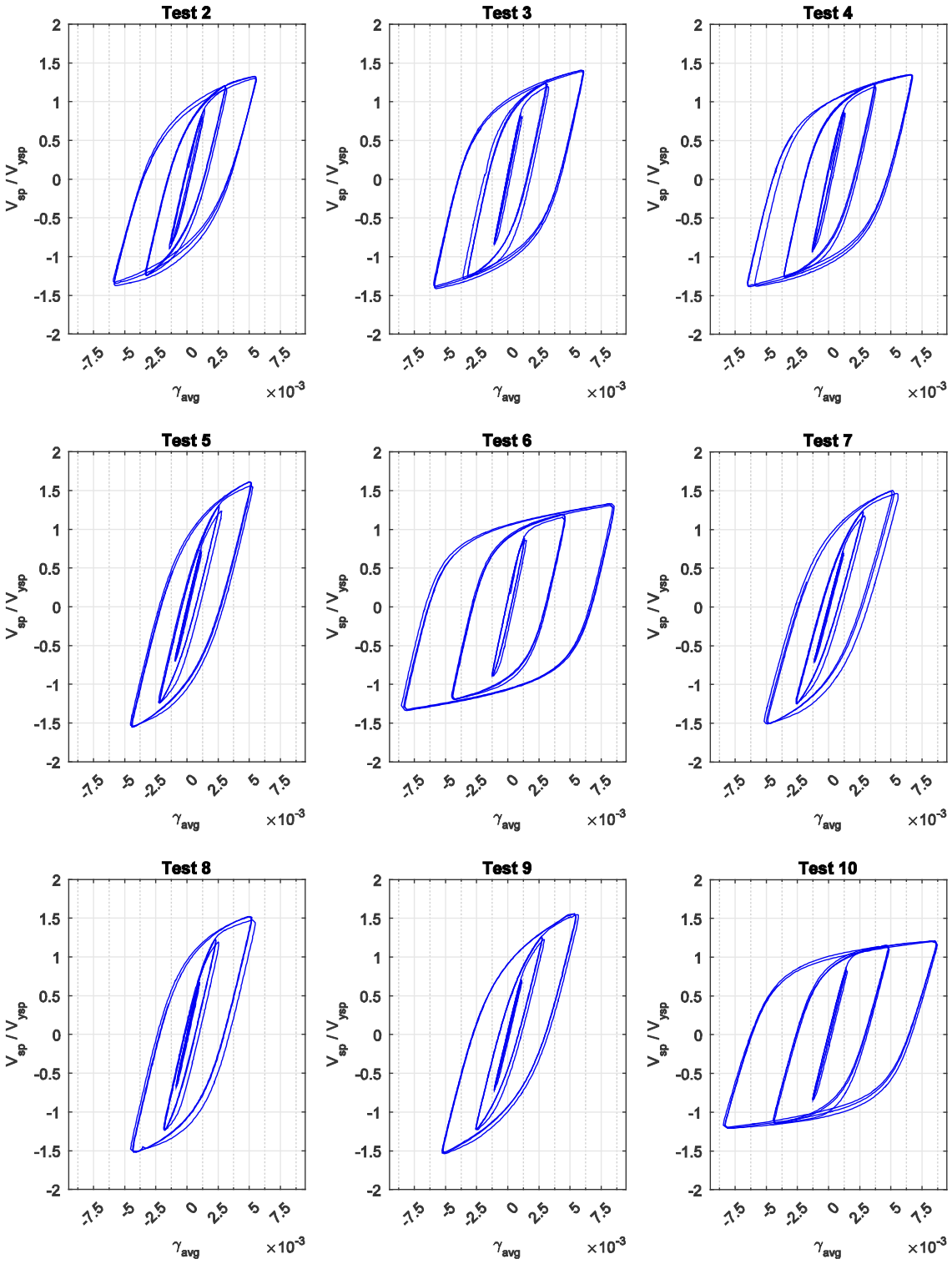

Figure 6-6: Specimens hysteresis cycles, cycles 6-15

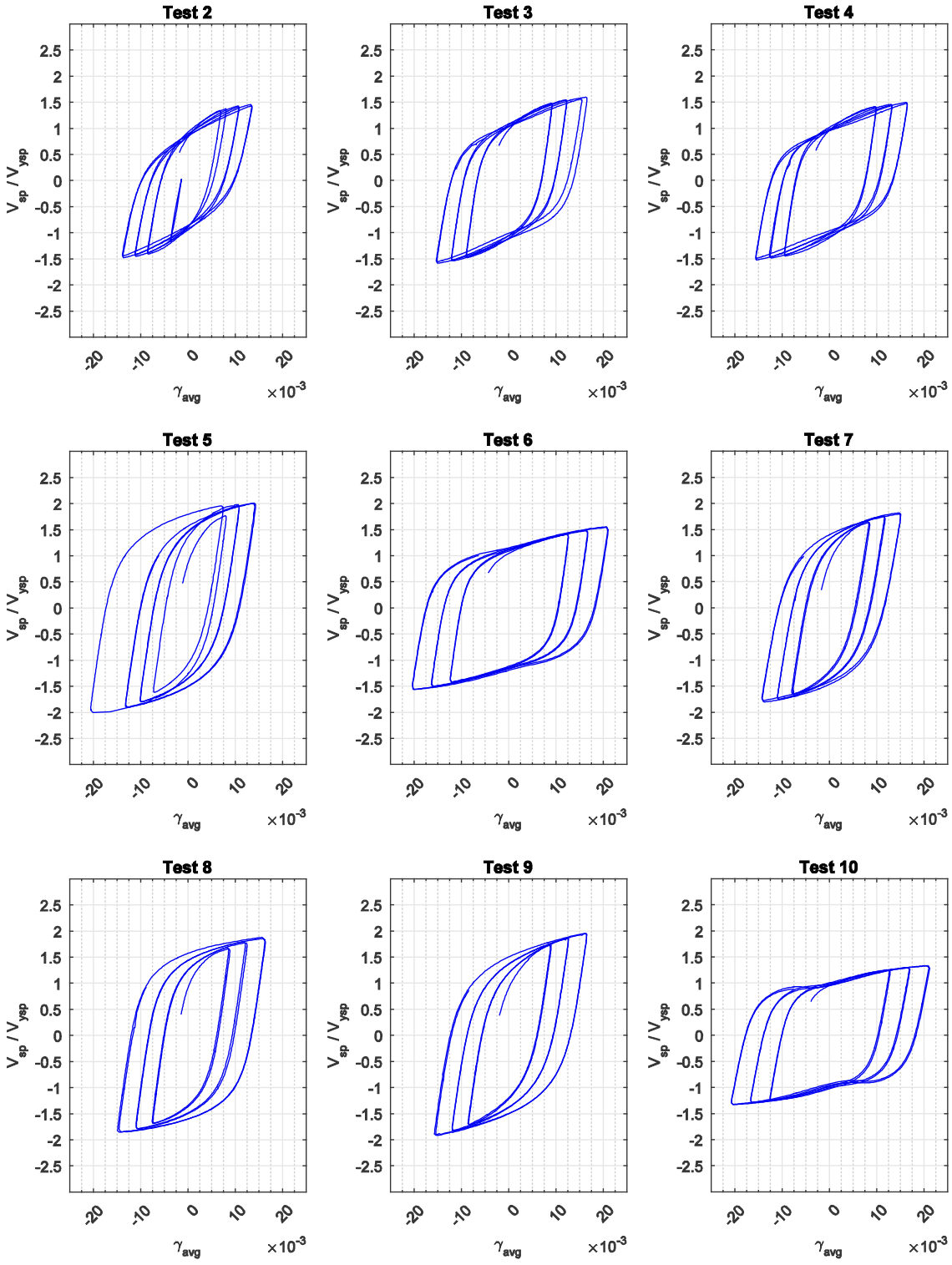

Figure 6-7: Specimens hysteresis cycles, cycles 15-21

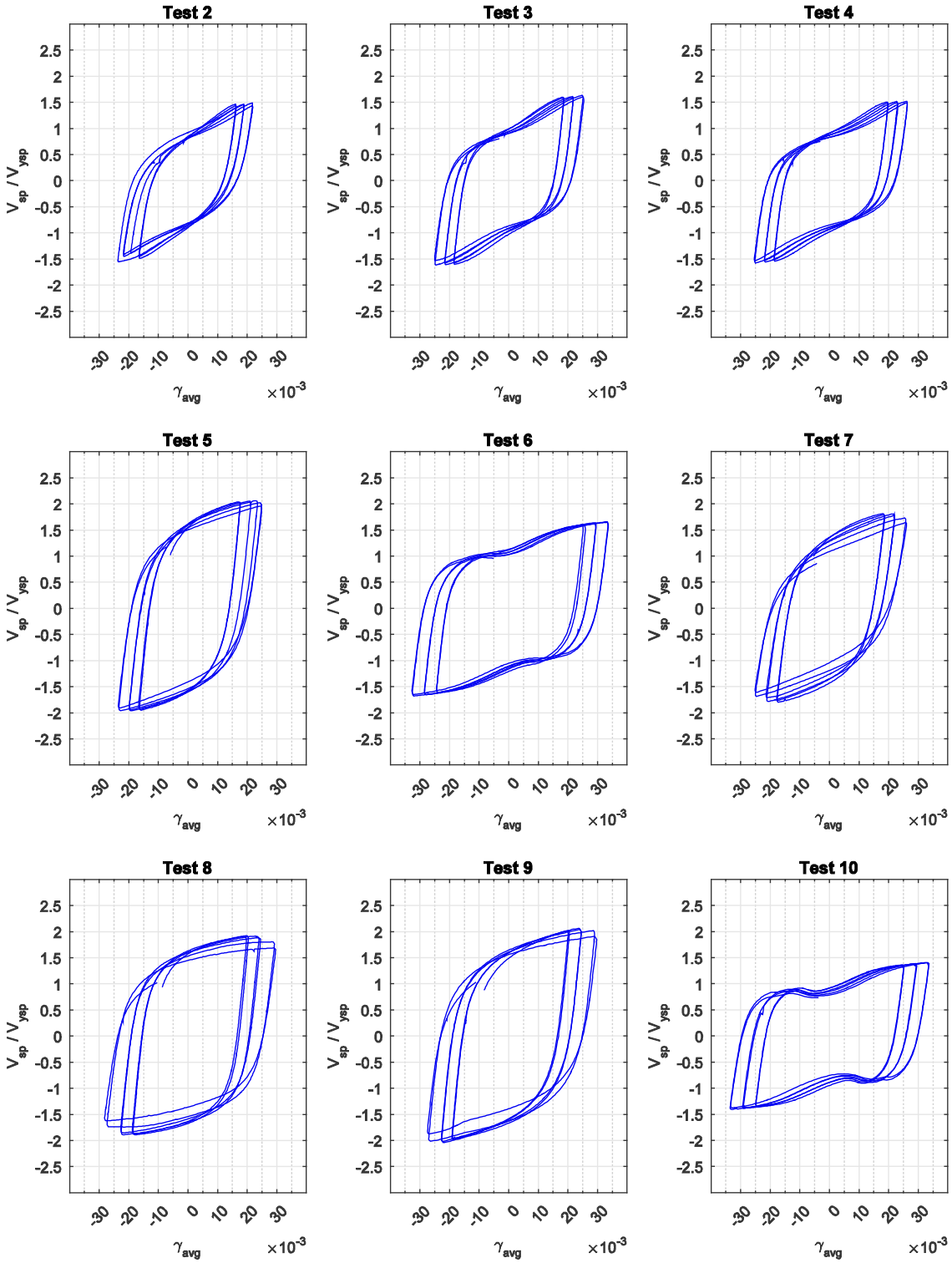

Figure 6-8: Specimens hysteresis cycles, cycles 21-27

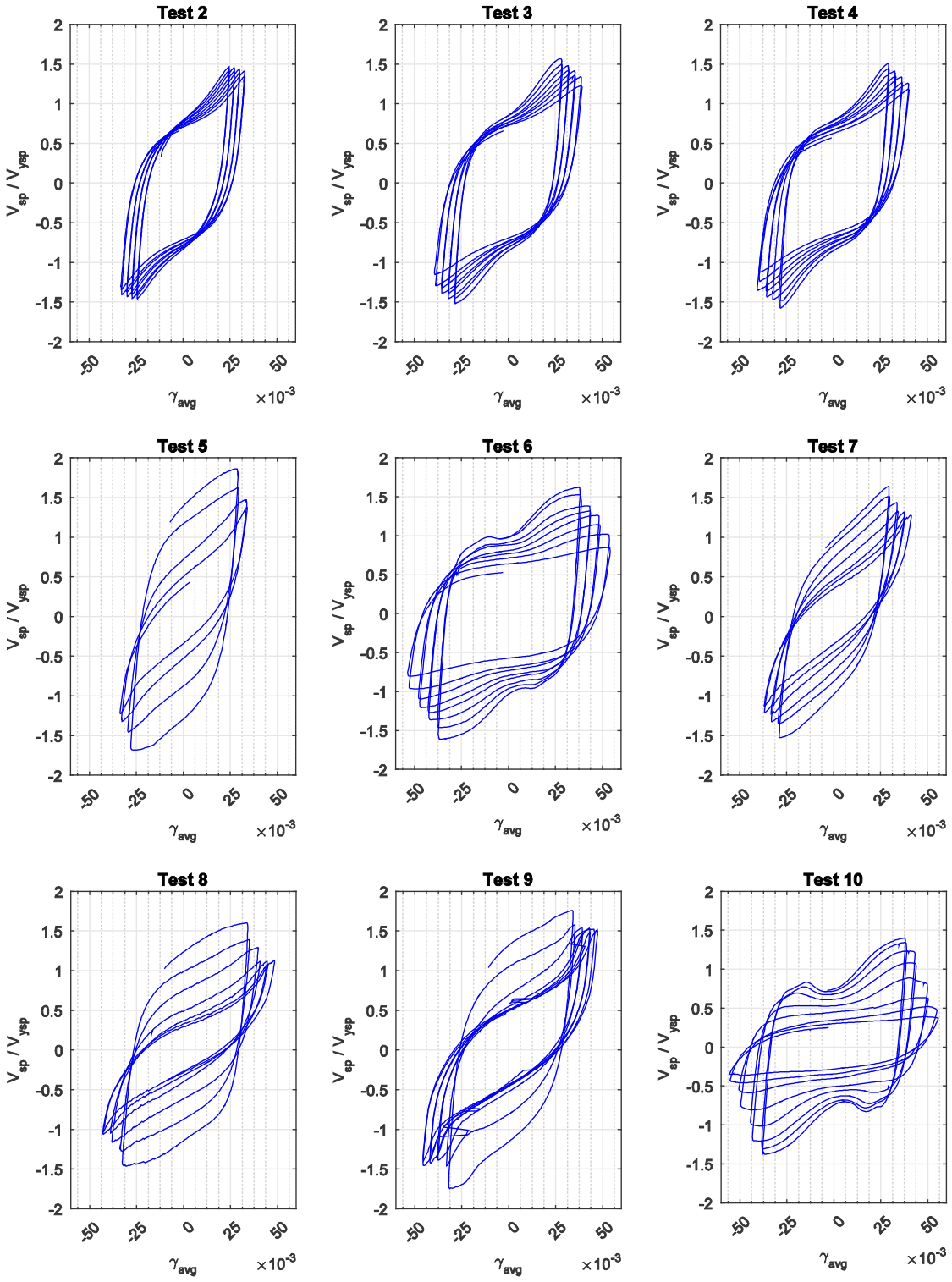

Figure 6-9: Specimens hysteresis cycles, cycles 27-35

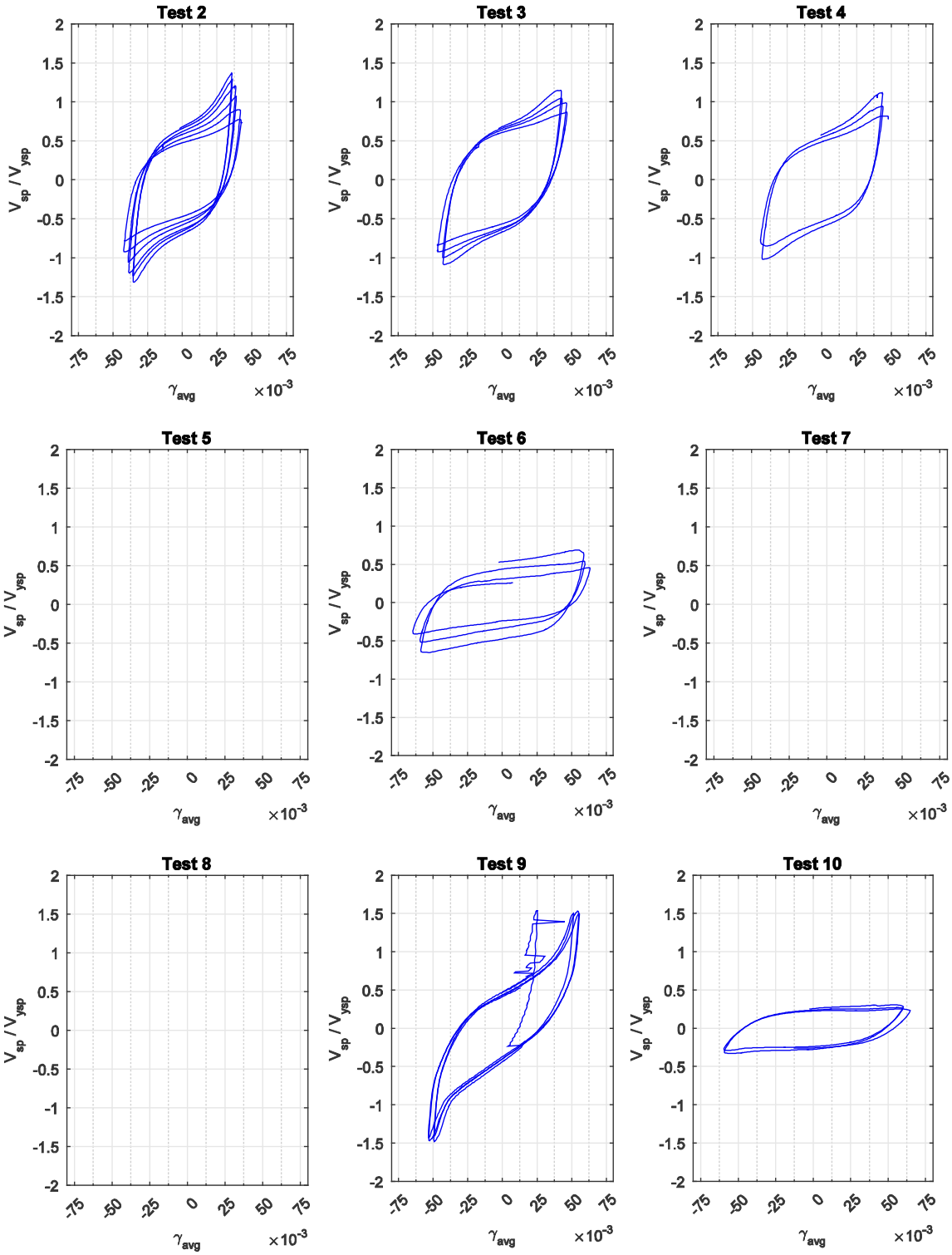

Figure 6-10: Specimens hysteresis cycles, cycles 35 and up

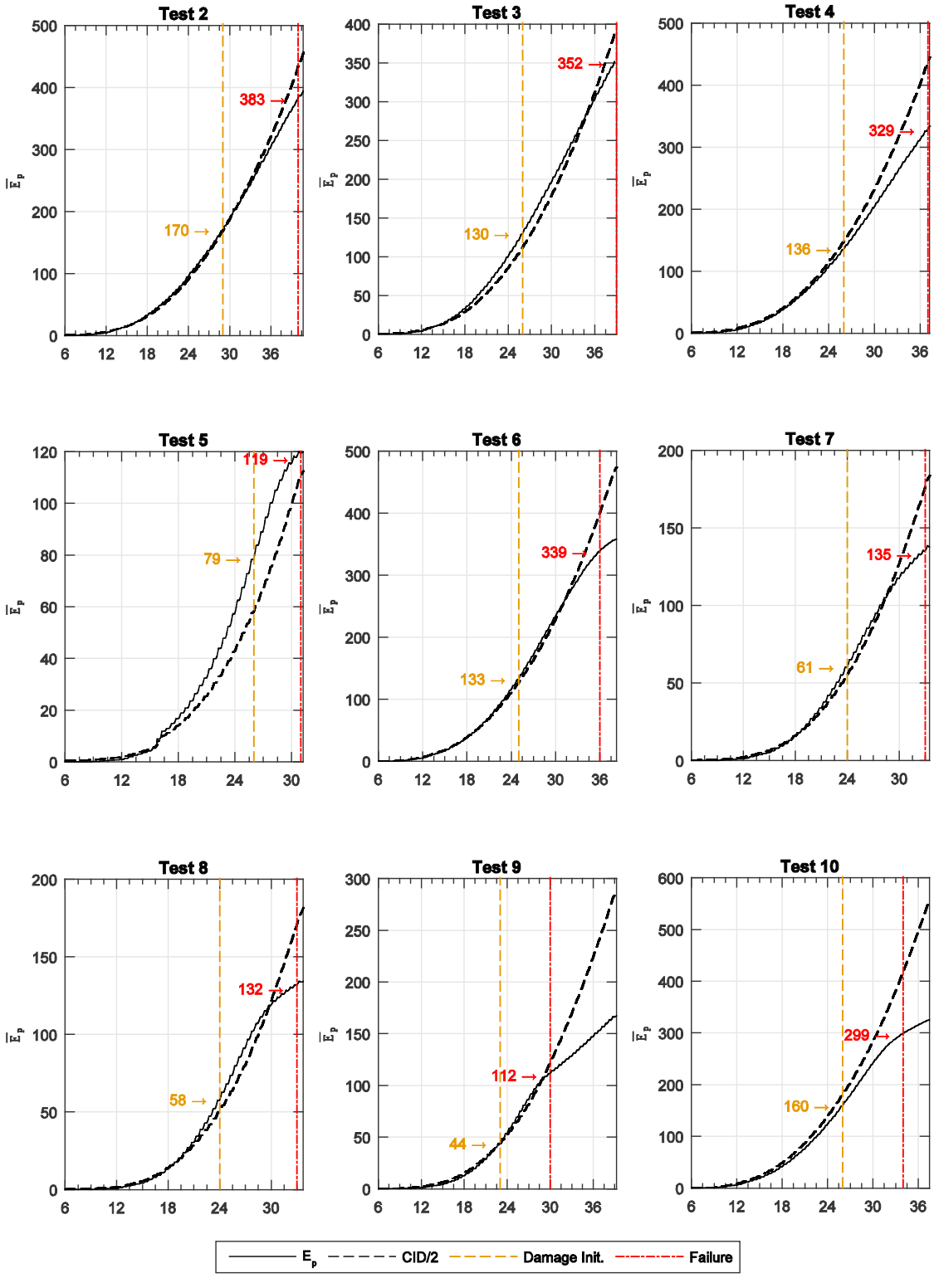

Figure 6-11: Plastic energy dissipation histories

6.2.3.1 Average Shear Angle and Drift Relationship

The relationship between the average shear angle in the panel γ_{avg} and the inter-story drift index θ is illustrated in this paragraph. When the panel is in the elastic region, the relationship is linear and it can be written using the equations developed to this point. In fact, For a given bracing horizontal force $V < V_{ysp}$, the lateral drift can be calculated as

$$\delta = \frac{V}{K_X}$$

where K_X is the total stiffness of the bracing system, see Equation (3-4. Dividing the lateral drift by the story height h gives the inter-story drift index θ. Similarly, the relative horizontal displacement in the panel can be calculated using the following expression

$$u_{sp} = \frac{V}{K_{panel}}$$

where K_{panel} is the horizontal stiffness of the panel. Once more, the average shear strain can be calculated by dividing this displacement by the panel height a. The ratio γ_{avg}/θ can now be written as

$$\frac{\gamma_{avg}}{\theta} = \frac{K_X}{K_{panel}} \frac{h}{a} \tag{6-16}$$

This equation holds while the panel is elastic, and it results in a ratio always less than h/a (since K_X is always greater than K_{panel}). When the horizontal force V is greather than V_y and the panel yields, the relationship between the shear angle and the lateral drift is no longer linear, due to the localization of displacements in the specimen. An estimate of the ratio between the two angles when $\theta > \theta_y$ is given by Equation (6-17).

$$\frac{\gamma_{avg}}{\theta} = \frac{h}{a} \tag{6-17}$$

This equation provides a good approximation of the ratio γ_{avg}/θ for drift levels greater than 4 times the yielding drift, and the error decreases as the secant stiffness of the panel becomes

negligible with respect to the stiffness of the braces (in fact, when $K_{panel} \to 0, K_X/K_{panel} \to 1$). Thus, Equation (6-17) implies that, as the drift increases, the relative horizontal displacement of the panel u_{sp} approaches the total lateral drift δ.

The relationship between the panel displacement u_{sp} and the lateral drift δ is shown in Figure 6-12 for all specimens; both variables are normalized by δ_y. It can be seen that the slope of the curve is, in fact, lower before yielding (i.e. $K_{panel} > K_X$ and $u_{sp} < \delta$), while the data points approach the line $u_{sp} = \delta$ for drifts past the yield point.

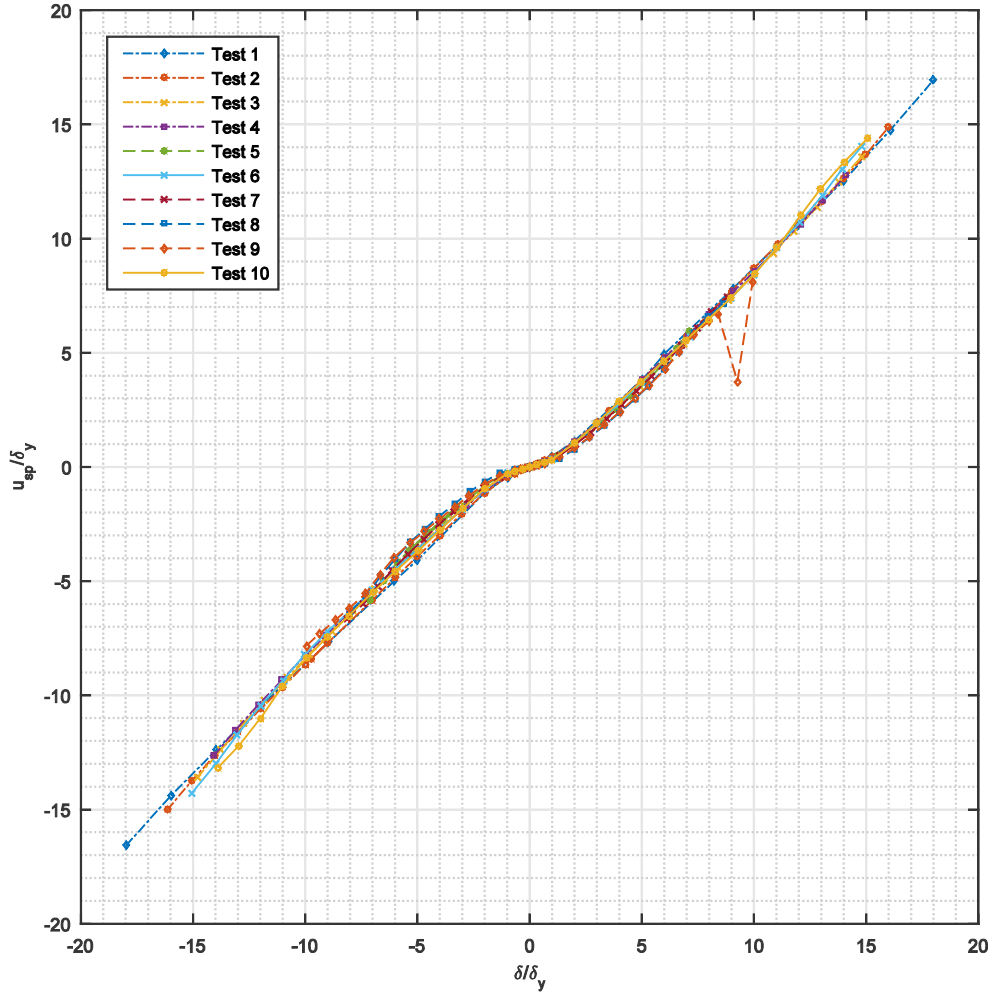

Figure 6-12: Normalized horizontal panel displacement and lateral drift relationship

6.3 Braces Demands

In the following section the data from the strain gauges on the braces is used to evaluate the demands on the connecting members in terms of axial force, major- and minor-axis shear, bending moment, and twisting moment. An accurate or otherwise conservative estimate of these effects is necessary to conduct the capacity design of the connecting elements of the BDSP, which are expected to have enough strength to remain in the elastic range, thus allowing to fully develop the ductility capacity of the sacrificial shear panel.

The configuration of the sensors on the braces cross-section is illustrated in 4.6.3, and the data reduction models used to obtain the internal actions from the strain readings are described in Appendix B.3. The redundancy in the collected data warrants a higher degree of confidence in the forces and moments obtained by data reduction. Specifically, the comparison of the data from braces on the same diagonal (i.e. 1 with 3, and 2 with 4) was used to confirm the accuracy of the axial force and bending moments estimates; inversely, by comparing the data of opposing diagonal braces 3 and 4 during each cycle, the twisting moment and major and minor shears were also checked for consistency—assuming anti-symmetry in the response. Therefore, for the purpose of determining and describing the demands in the braces, the measurements from only one of the braces are used for the analysis, with the understanding that the results can be extended to the other members.

6.3.1 Braces Axial Demands

As described in Chapter 3, the particular geometry of the shear panel is expected to result only in compressive and tensile axial forces in the braces, when a first-order analysis is considered. Therefore, this is the most critical action that the braces are designed to resist in a capacity design approach. Figure 6-13 shows the envelope of the horizontal component of the axial force in brace 4 during each test—normalized by the maximum horizontal force in the panel V_{max}—with the normalized lateral drift δ/δ_y on the horizontal axis.

From the plots, it can be seen that for all tests the axial stiffness of the braces is symmetric for $\delta \leq \delta_y$, resulting in an equal distribution of the lateral force between the compression and tension diagonals. After yielding, the stiffness of the compressive diagonals begins to deteriorate, due to the inelastic buckling of the web plates; as predictable, this behavior is much more significant in the panels with thinner webs than in the other specimens.

Overall, the values for all the tests are consistent with the two limiting cases of stiffness distributions: symmetric response of the compression and tension diagonals, and tension only response with no force along the compression diagonal. Under the first assumption, an upper bound of $-1/2$ for the horizontal component of the maximum compressive force is obtained. In opposition, by considering the second case, the total lateral force is expected to be resisted by the tension diagonal alone, resulting in a limit of +1 on the vertical axes of Figure 6-13. Therefore, to ensure that the objective capacity hierarchy is obtained, the braces sections have to be chosen to ensure that the compression strength P_{nc} and tension strength P_{nt} are greater than the values predicted by the two limiting cases, as shown in Equation (6-18).

$$P_{nc} \geq \frac{1}{2}\frac{V_{max}}{\cos\alpha} \quad ; \quad P_{nt} \geq \frac{V_{max}}{\cos\alpha} \tag{6-18}$$

Under large displacements, the response of specimens that exhibited a vertical localization of shear strains—namely tests 5, 7, 8 and 9—showed a second-order stiffening. The mechanism responsible for this behavior is believed to be the tensioning of the boundary flanges, due to the large rotations which gradually straighten the flanges and align them with the tension diagonal. A quantitative measure of this effect is not proposed, since its effects are significant only at very large drifts: at this point the device is considered to have failed and the presence of this effects is conservatively neglected.

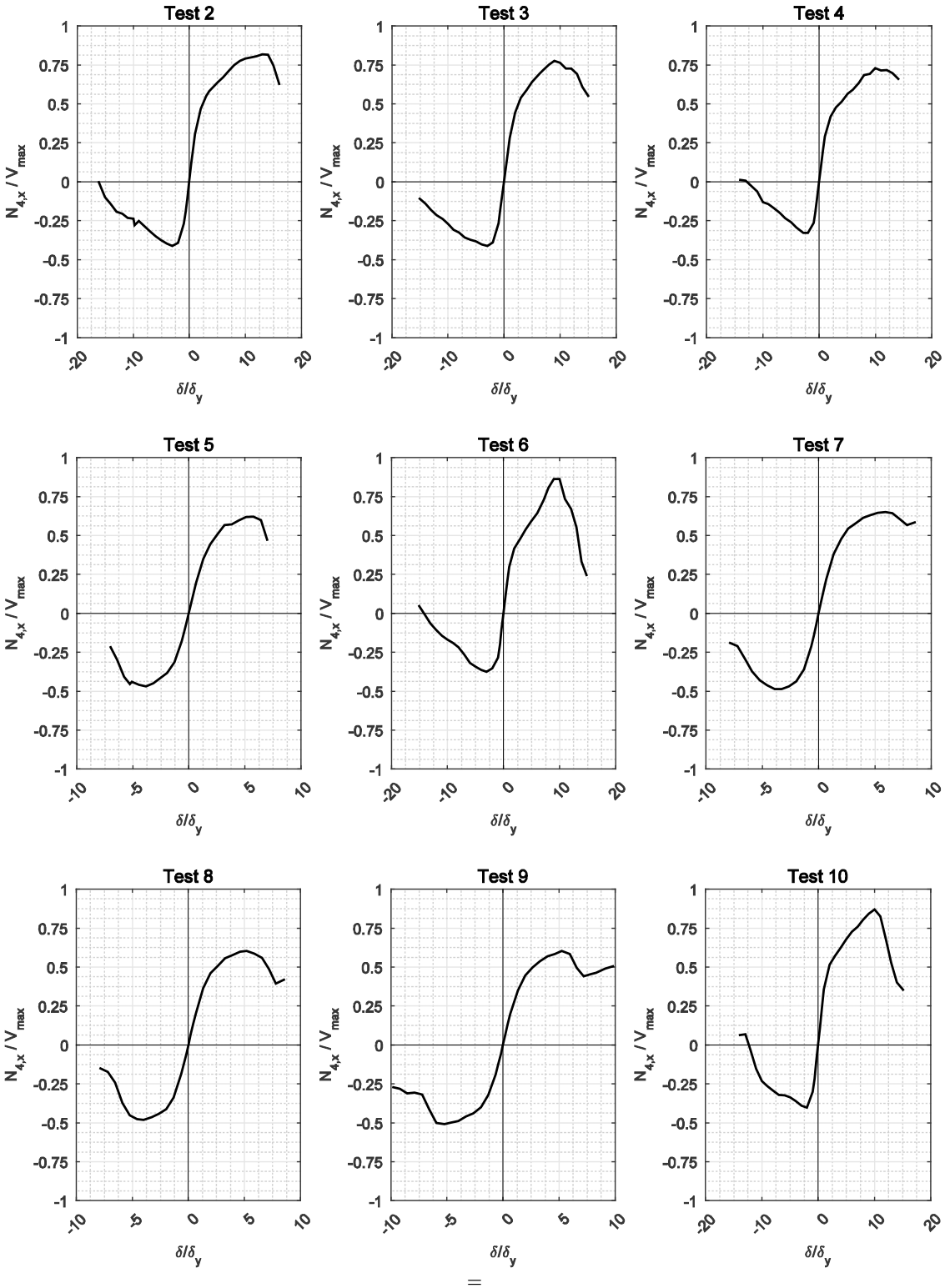

Figure 6-13: Ratio of horizontal component of brace axial force to maximum horizontal force

6.3.2 Braces Major-Axis Demands

Figure 6-14 shows the envelope of the calculated strong-axis shear V_x for braces 3 and 4. The absolute value of the maximum shear recorded is less than 5 kip for all the panels with slender webs—and horizontal displacement localization—while it approaches 10 kip at larger drifts for the panels with thicker webs. The shear force in the braces is the result of accidental eccentricities and second-order effect, therefore an accurate prediction would require a separate analysis. However, when compared to the design axial force and the shear capacity of the I-beams, its magnitude is small enough that its effects can be neglected. For simplicity, a conservative value equal to 10% of the design axial force can be used the design of the bolted connections to ensure that enough capacity is provided to transfer the shear force from the panel to the connecting elements.

The major-axis bending moment in the braces 3 and 4 at the sensors location (midpoint of the braces) is shown in Figure 6-15. It can be seen that the bending moment is close to null before yielding, $\delta < \delta_y$, while it increases as displacements localize in the panel. A difference can also be noted between the panels with horizontally localized displacements—tests 2-4, 6 and 10—and the other panels where displacements localized in the vertical subpanels. In fact, for the first group, the bending moment increases mostly linearly until it reaches a peak; it then starts decreasing, and eventually changes sign for very large lateral drifts (tests 6 and 10). The point of maximum bending moment—and inversion—coincides with the failure point of the panel, when the panel has lost most of its post-buckling stiffness. Conversely, in the panels with vertically localized displacements, the bending moment increases at a similar rate for smaller inelastic drifts, but as the panel nears its failure point, the moment in subsequent cycles increases at a faster rate.

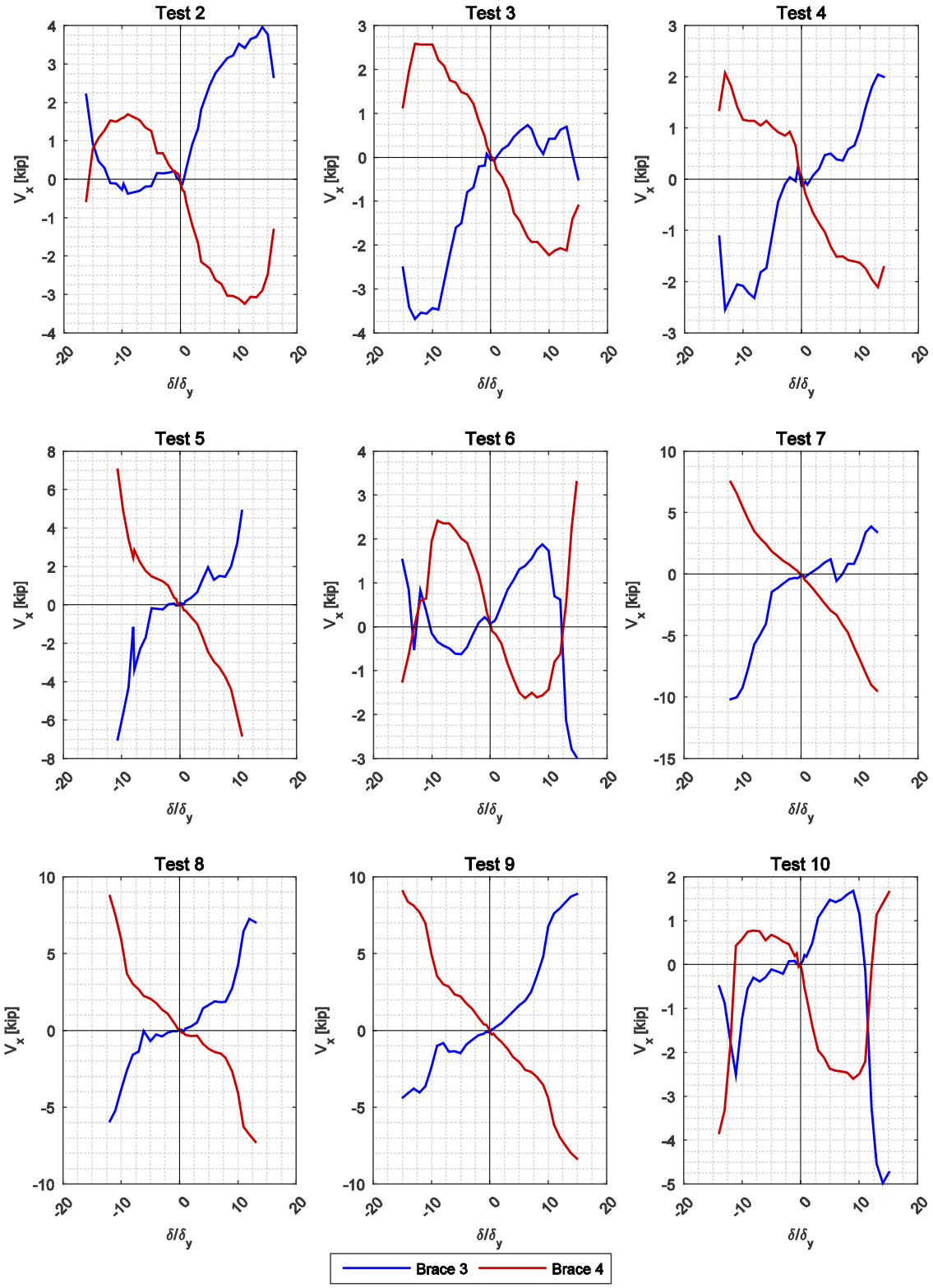

Figure 6-14: Strong axis shear for tests 2-9

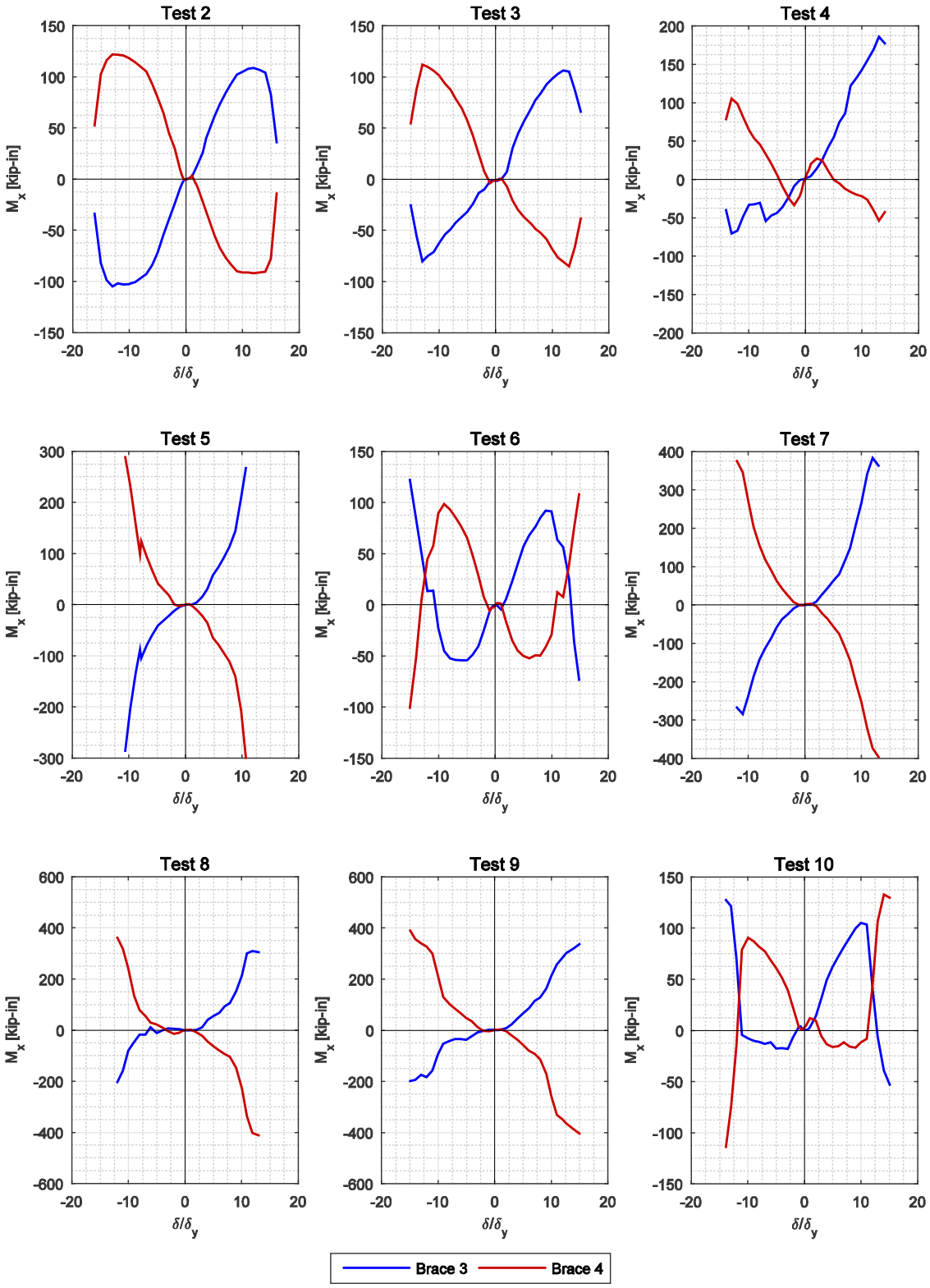

Figure 6-15: Brace #1 strong axis moment

6.3.3 Braces Minor-Axis and Torsional Demands

The envelopes of the minor-axis shear in brace 3 is shown in Figure 6-16, while the envelopes of the minor-axis bending moment in braces 3 and 4 are shown in Figure 6-17. The minor-axis shear force for brace 4 was not available due to a malfunction of the instrumentation. From these plots it can be seen that the magnitude of the minor-shear demand in the braces is small enough that it can be neglected for design purposes. In fact, if the system possesses adequate out-of-plane stability, minor-axis shear and bending moments are solely due to intrinsic imperfections in the alignment of the members. In fact, as the drift increases the value of the minor-axis shear and moment remains constant, and it is linearly related to the horizontal force in the bracing system.

Similarly, the magnitude of the torsional moment calculated as described in Appendix B, was negligible when compared to the other demands, or the torsional capacity of the braces sections. A plot of this quantity is not shown because the signal-to-noise ratio of the calculated value was very low and would not provide any relevant additional information.

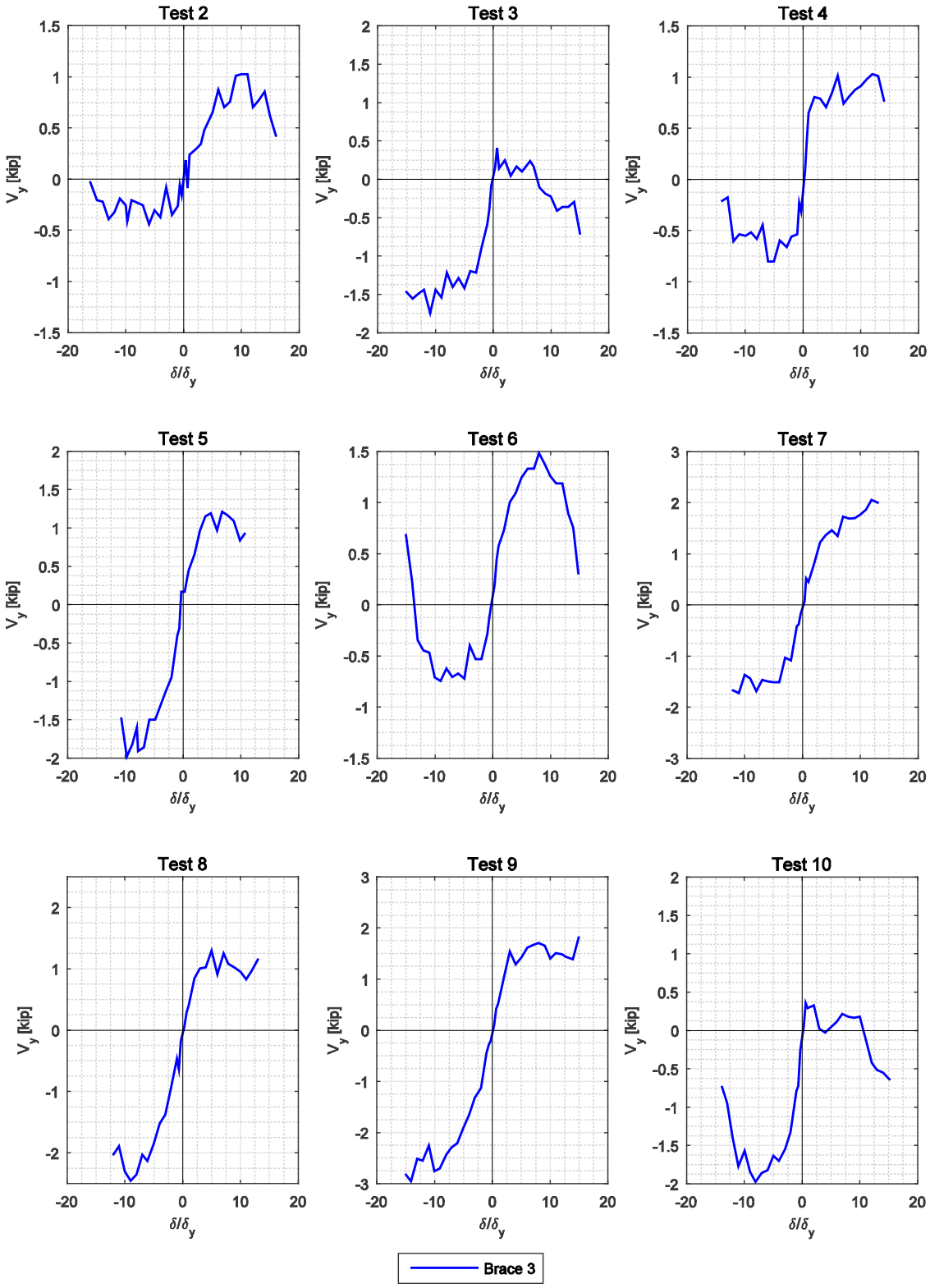

Figure 6-16: Weak axis shear in brace #3 for tests 2 to 9

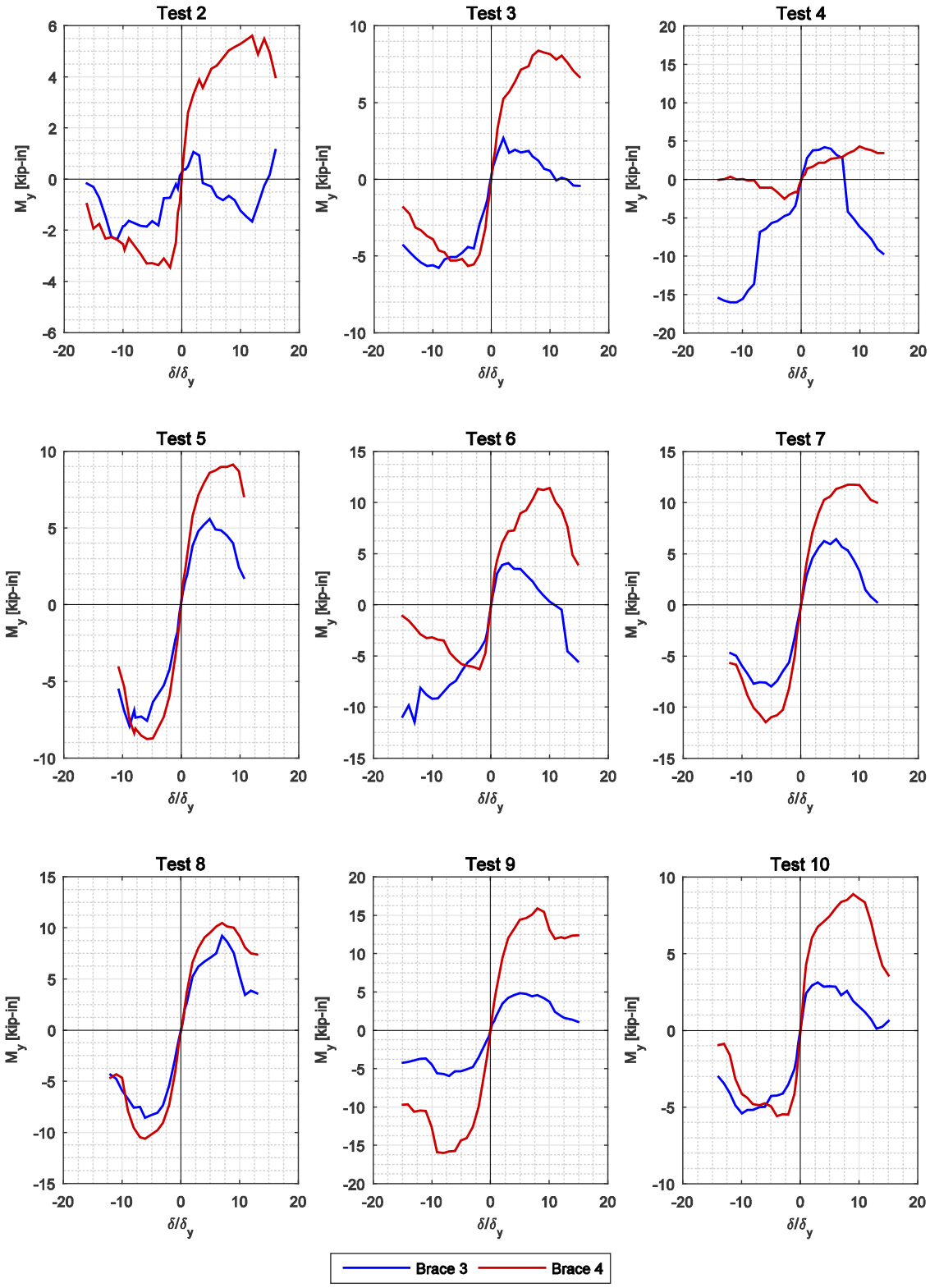

Figure 6-17: Brace #1 weak axis moment

6.4 Data Analysis Summary

The data analysis presented in this chapter allowed to quantify the response of the bracing system in terms of static, kinematic and energy dissipation quantities. From the analysis of the elastic behavior prior to yielding, a more accurate expression for the calculation of the panel stiffness was obtained. The new expression—shown in Equation (6-3)—uses two coefficients k_s and k_p to modify the nominal stiffness K_{BDSP}, and is shown to be able to capture the effects that the I-beam stubs and the perforations have on the elastic stiffness of the shear panel. An equation was also developed to predict the maximum lateral strength of the system as a function of the web slenderness as measured by parameter R_w, and a slenderness threshold value R_{w0} was defined. Finally, a model is proposed to approximate the lateral response of panels with solid webs, which were found to be able to achieve the highest levels of ductility. In fact, the analysis of the hysteresis cycles proved that perforations in non-slender webs significantly reduce the ductility and energy dissipation capacity of the system—due to the high stress concentration generated by the openings. The reduction in performance was also noticeable in non-stocky perforated webs, however the effect was mitigated due to the softening of the high strain regions caused by inelastic buckling.

The data from the braces instrumentation was used to determine the demands on the braces and the other connecting members. In particular, the effective distribution of axial forces between the tension and compression diagonal was investigated. It was shown that, to ensure that the braces and connections have enough capacity to develop the full ductility of the shear panel, after yielding the compression diagonal should conservatively be neglected. Therefore, the braces, connections and gusset plates shall be designed to carry the maximum lateral force expected in the panel through tension only.

Chapter 7
Finite Elements Model Validation

7.1 Introduction

In this chapter the data from the experimental program is compared to the results of finite element simulations performed on a model of the experimental frame, as constructed, and the different tested specimens. Through this comparison, the finite element model of the shear panel, braces and connections is validated. The objective of these simulations is to assess the ability of existing simulation methods to accurately replicate and predict the nonlinear behavior of the Braced Ductile Shear panel bracing system. Once the fitness of these numerical experiments is evaluated, the finite element analyses can be used to investigate the response of full-scale BDSP systems with different geometries and design details, without the need for extensive experimental testing. The commercial finite element software ABAQUS is used to perform the numerical simulations. In the following sections, the model will be compared to the experimental data in terms of lateral force-drift response of the bracing system, energy dissipation and damage initiation.

7.2 Model description

7.2.1 Geometry and Analytical Idealization

The numerical models used for the simulations replicated the geometry of the entire testing frame, which consists of the bracing system, the gusset plates, the brace-to-gusset bolted connections, beams and columns. The column base plates were not included in the model and were assumed to be rigid, therefore the lower edges of the columns and column stiffeners were fully restrained. All the elements were modeled using S3 and S4R elements (trilateral and quadrilateral shell elements with one integration point). The resulting analytical model of the testing frame is shown in Figure 7-1, and the typical finite element discretization is shown in Figure 7-2. The

connection between the braces and the shear panel is realized by rigidly tying together the nodes on the edges of the braces ends to the facing nodes on the shear panel stubs. The angles between the braces and gusset plates are tied to the member flanges and gusset plate web by distributing the kinematic constraints on the areas interested by the bolted slip-critical connections.

Imperfections are also included in the geometry by seeding the first four, unique buckling modes obtained applying a unit lateral force at the load reference point. The amplitude of the imperfections—defined as the value of the largest displacement—was set to 0.04 inches. An example of the buckled shapes used to define imperfections is shown in Figure 7-3 for specimen 10, where the contour plot indicates the amplitude of the displacements normalized to the maximum displacement.

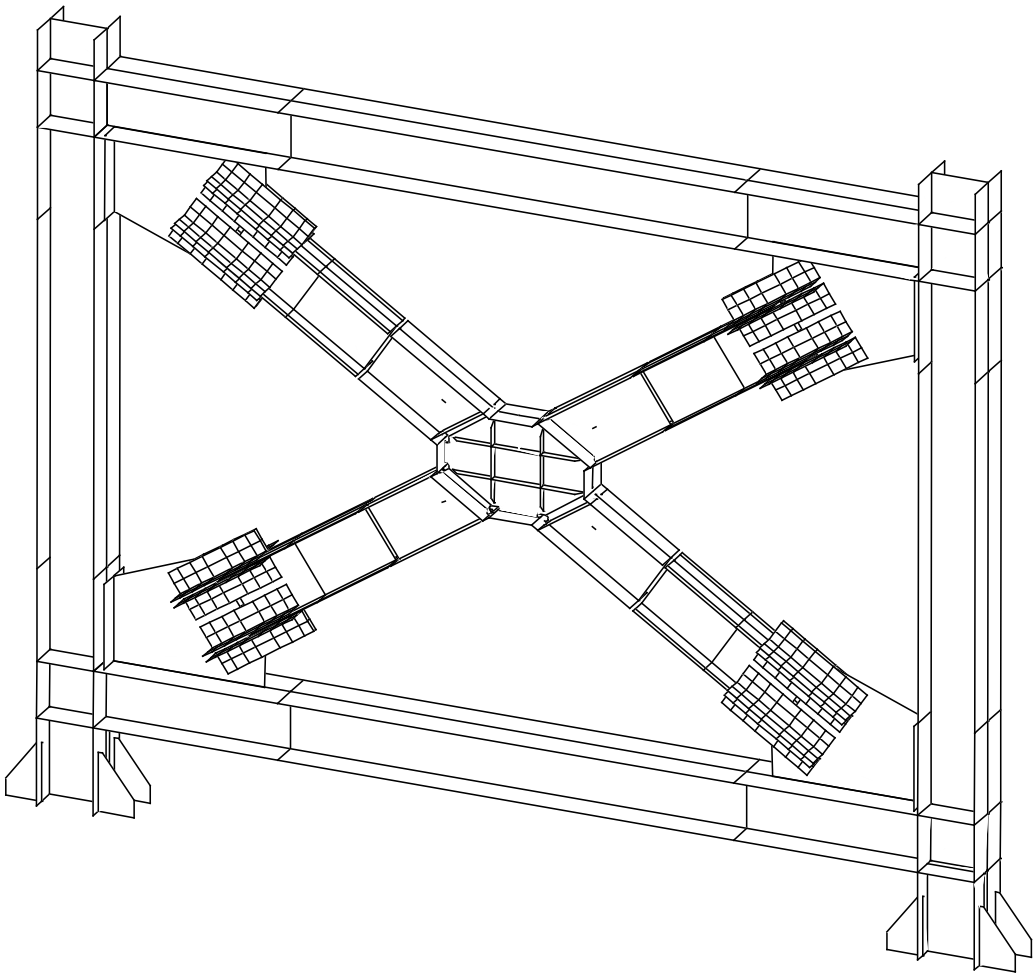

Figure 7-1: Analytical model of the experimental frame

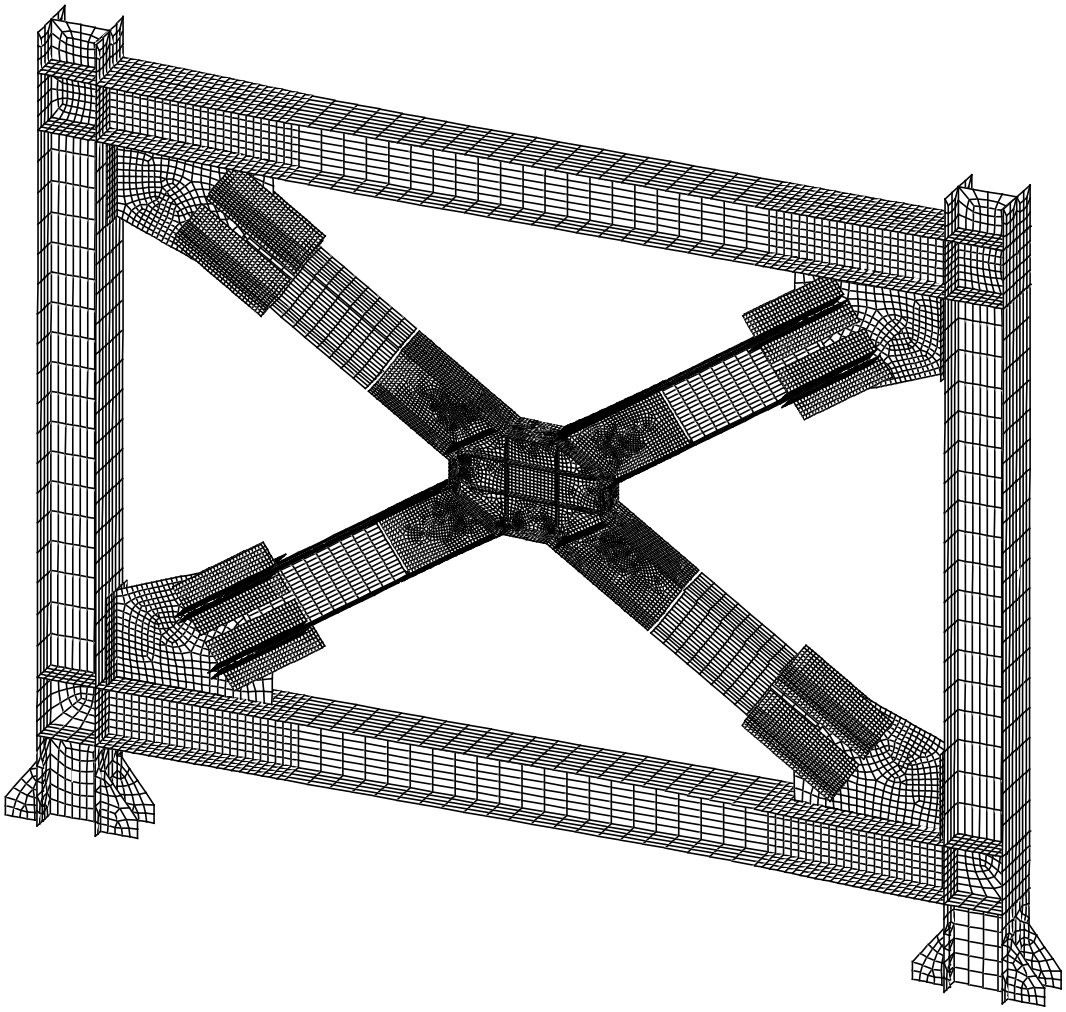

Figure 7-2: Finite elements discretization of the shell geometry

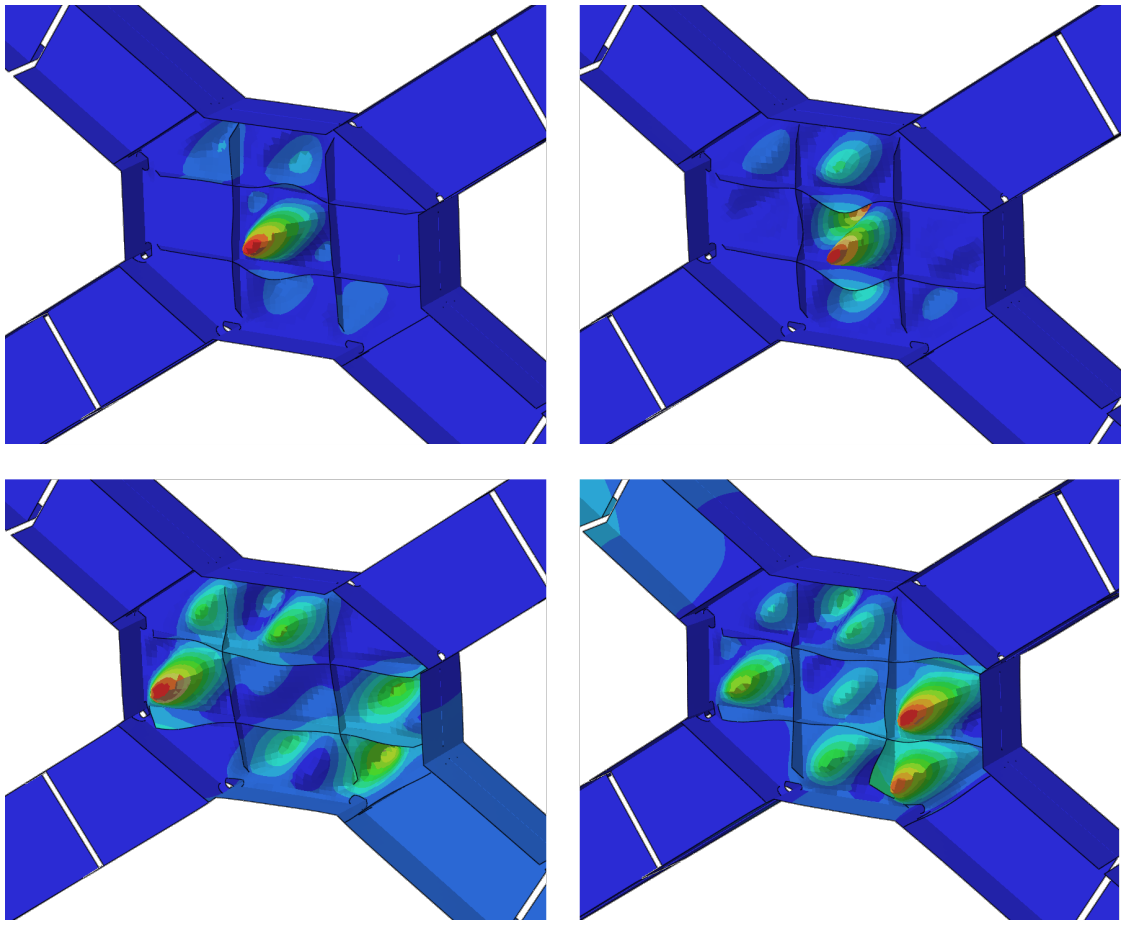

Figure 7-3: Example of buckled shapes used to model imperfections

7.2.2 Displacement-based Loading

The actual lateral drift history obtained from each test is applied as imposed lateral displacement on the frame; therefore the resulting loading includes any accidental deviation from the prescribed loading protocol defined in 4.7. The first six cycles of the loading protocol with $\delta < \delta_y$ are not included in the simulation to reduce the computational time, since the numerical model would remain elastic during these cycles and therefore the solution in subsequent steps would not be affected. Therefore, the simulation pseudo-time and cycle numbers are reduced by 6 when compared to the experimental ones ($T_{sim} = T_{exp} - 6$). In order to replicate the experimental loading conditions—deriving from the presence of the load-transfer plate—to an adequate level of precision, the lateral displacements were applied uniformly over a rectangular loading area on the outer

surface of the West column. This area included all the nodes in the region between the two column transverse stiffeners, as shown in Figure 7-4. The nodes in these region were kinematically coupled together and a reference point at the centroid of the region was used to apply the lateral load; this method allows to distribute the force on multiple nodes without introducing an artificial bending moment.

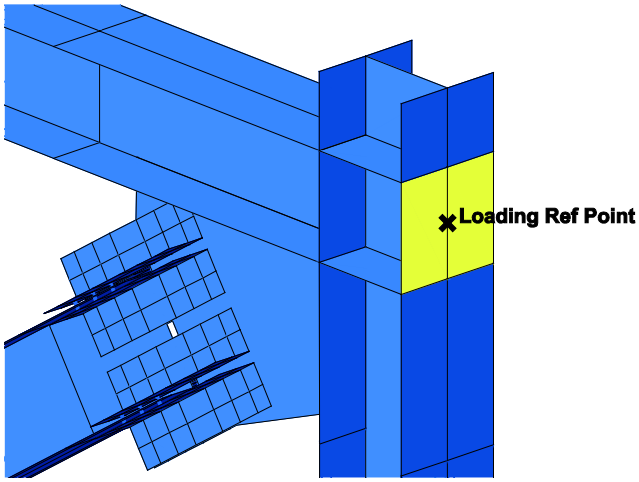

Figure 7-4: Imposed lateral displacement and load application region and reference point

7.2.3 Material models

The material models used for the model are similar to the ones used during the preliminary parametric analyses described in 3.3.2. An elastic-plastic model with mixed nonlinear isotropic and kinematic hardening is assigned to the shear panel web, flanges and stiffeners; an elastic-perfectly plastic material is used for the other elements—fabricated with A992 and A572 Gr50 steel. Since no coupon specimens of the web plates were made available by the steel fabricator, uniaxial monotonic and cyclic tests could not be performed to properly calibrate the material stress-strain response. Therefore, the model had to be indirectly calibrated by comparing the global response of the system. For the calibration, it was assumed that webs with the same thickness were fabricated from the same steel plate, thus their uniaxial stress-strain relationship would also be the same. Initially, the model used for the parametric investigation—calibrated to the test data of A36 steel (Cofie and Krawinkler 1985) and described in 3.3.2—was used for all the shear panel specimens.

The hardening behavior of the model was then calibrated to replicate accurately the response of the specimens with 1/8" web plates—fabricated with ASTM A1011 Grade 36 (equivalent to ASTM A36). The resulting uniaxial stress-strain relationship for this model is shown in Figure 7-5. However, this model was shown to be unsuitable to replicate the response of the thicker web plates, which were fabricated of actual ASTM A36 steel (see Appendix A) and exhibited a higher yield stress than the Standard prescribed minimum. A second model was defined by increasing the yield stress to 50 ksi, and reducing the amount of kinematic strain hardening (C_1, C_2), the uniaxial response of this material is shown in Figure 7-6. This model matched the response of specimen 9, with 1/4" thick web. A third model to replicate the response of the panel specimens with 3/16" thick web plates (specimens 5, 7 and 8) was defined by further increasing the yield stress (55 ksi) and the hardening parameters (C_1, C_2, Q_∞), see Figure 7-7. The values of the final parameters of all three models are listed in Table 7-1.

The relatively large difference between the stress-strain relationship of the different plates is attributed to the use of different ASTM Standards used for fabrication of the plates and the common variability in the yield strength of lower yield structural steel. In fact, the variability of yield stress of A36 steel grade is well known and acknowledged in the literature as well as in building codes. As an example, the *AISC Seismic Provisions* (AISC 2010a) in Table A3.1 prescribe a higher overstrength factor (R_y = 1.3 ÷ 1.5) for A36 than for A572 or A992 steel grades (R_y = 1.1).

Table 7-1: Material models parameters

Web plate thickness (in)	F_y (ksi)	C_1 (ksi)	γ_1	C_2 (ksi)	γ_2	Q_∞ (ksi)	κ
1/8	35	2500	600	450	35	4	10
1/4	50	2000	350	200	35	5	10
3/16	55	2500	350	250	35	7	10

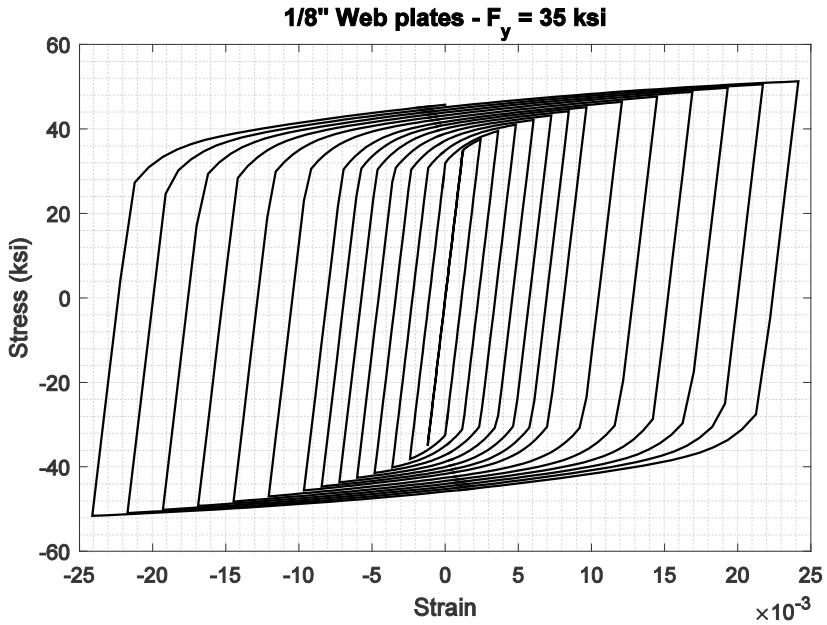

Figure 7-5: Uniaxial response of material model used for 1/8" thick web plates

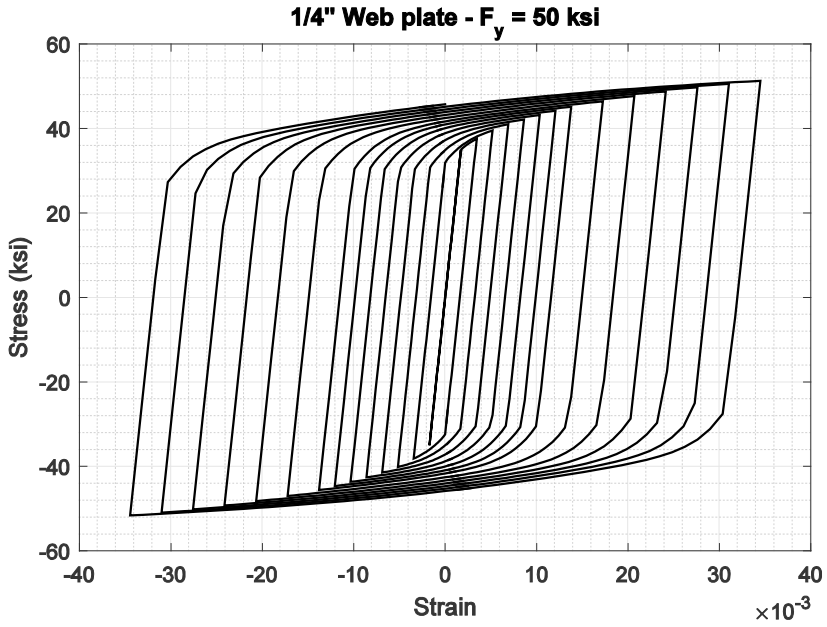

Figure 7-6: Uniaxial response of material model used for 1/4" thick web plate

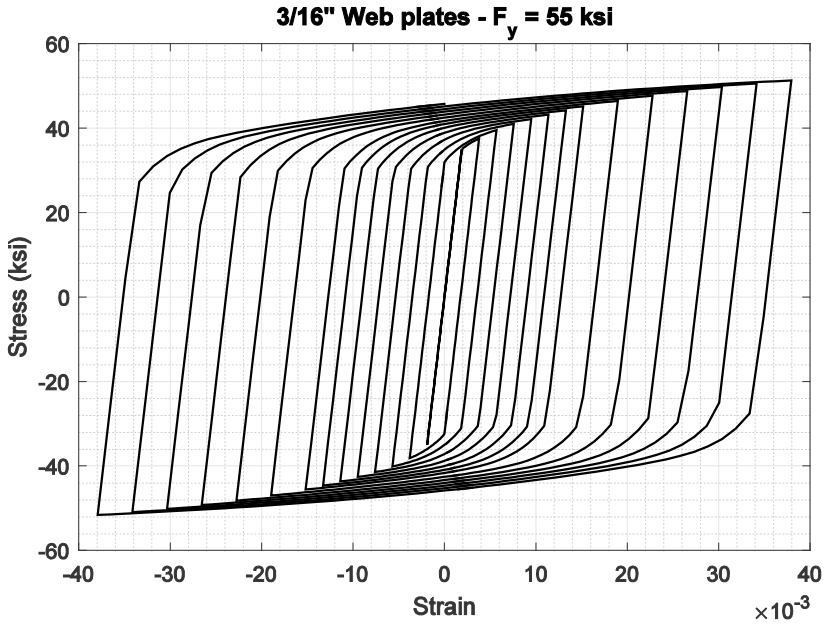

Figure 7-7: Uniaxial response of material model used for 3/16" thick web plates

7.3 Force-Displacement Response

Figures 7-8 through 7-16 show the comparison between the experimental and the numerical lateral force-drift response of the braced frame; the horizontal axis is the absolute drift as measured by the external LVDT (and applied as displacement history to the numerical model), the vertical axis is the total lateral force. The curves are divided in two parts, plotted with different line styles. The first part—solid line—shows the response of the experimental frame and numerical model up to the first cycle during which damage was first observed. The remaining cycles are plotted with a dashed line. This distinction is made to properly compare the results of the tests and the finite element simulations. Since the material used in the simulations does not include a damage model, the results from the analyses are expected to be accurate only up to the cycle of damage initiation. It can be seen that the finite element analyses are able to accurately replicate the behavior of the bracing system for all the specimens prior to damage. In particular, the results show that the yielding force, nonlinear response and cyclic strength degradation—due to out-of-plane buckling—are all captured by the numerical model. The only major differences observed between the two responses are in the initial slope of the unloading path, and in the curvature after yielding in the opposite direction of the same portion of the curve. The first difference causes the numerical model to overestimates the stiffness of the bracing system on unloading; this is most evident in tests 8 and 9 at larger drifts. Multiple reasons could account for this discrepancy; however, the author believes it is most likely due to the presence of ductile voids in the web plate, and the loss of stiffness caused by the closing of the voids. The difference in the curvature at the onset yielding after load reversal is caused by inaccuracies in the inelastic response of the material, due to the lack of data from material test coupons. A more precise calibration of the material model would address this issue. However, without the data from monotonic and cyclic uniaxial tests, an accurate calibration would not be practical. Another factor that contributes to the mismatch between the responses is likely the difference between the values of the monotonic and cyclic yield stresses: for common structural steel grades, in fact, the yield stress on load reversal after first yield is less than the monotonic yield

stress (Cofie and Krawinkler 1985). Although these issues could be addressed as described—mainly by refining the constitutive relationship for the material—they are outside the scope of the current study. In addition, as demonstrated below, the effect on the global response of the system are minimal.

A global measure of the difference between the lateral force-drift behavior predicted by the numerical models and the experiments can be obtained calculating the total plastically dissipated energy. The energy dissipation during the tests is found by computing the area enclosed within the lateral force-drift curve; the same method can be used to calculate the plastic dissipation in the finite element model. By comparing the energy histories, a global measure of the difference between the numerical and experimental response can be calculated. In fact, since the lateral drift history from each test is imposed as a displacement at the load reference point (see 7.2.2), the difference between the numerical and experimental plastic energy is equal to the sum of the differences in lateral force. The time-histories of the plastically dissipated energy from the tests and the simulations are shown in Figure 7-17, while the values at the end of the first cycle after damage initiation was observed are shown in Table 7-2. It can be seen that the total difference between the analyses and the experimental data is less than 6% for seven of the nine tests, with larger errors obtained for test 8 and 9.

Table 7-2: Experimental and numerical energy dissipation at damage initiation

Test	$E_{p,exp}$ (kip-in)	$E_{p,FEA}$ (kip-in)	Error
2	406.4	408.7	-0.57%
3	389.7	394.3	-1.18%
4	490.8	487.7	0.63%
5	636.7	639.2	-0.39%
6	661.3	693.1	-4.81%
7	619.4	584.0	5.72%
8	722.7	809.2	-11.97%
9	537.7	636.4	-18.36%
10	977.2	1003.5	-2.69%

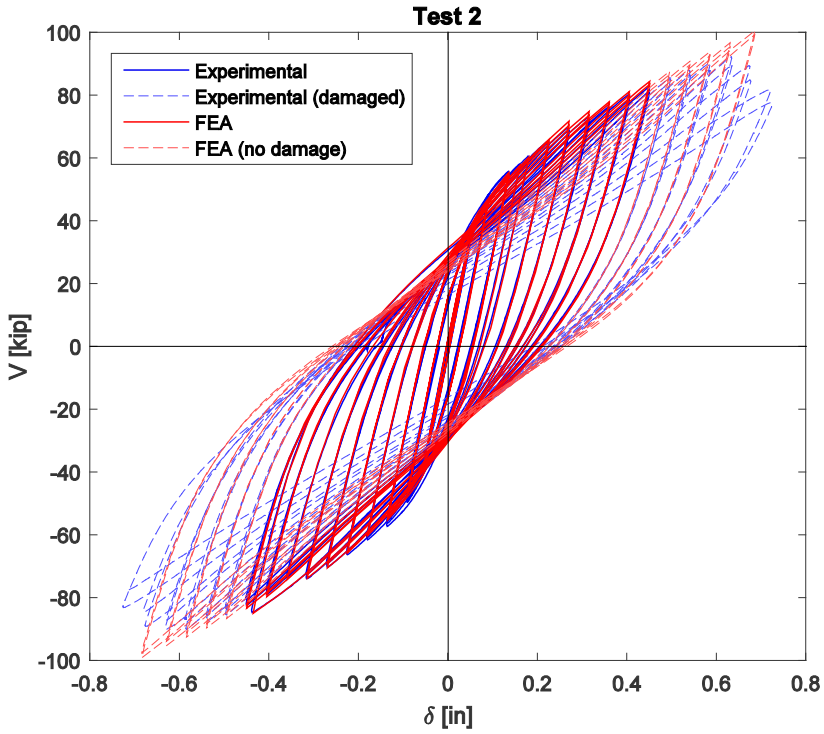

Figure 7-8: Test 2 – FEA and Experimental lateral response comparison

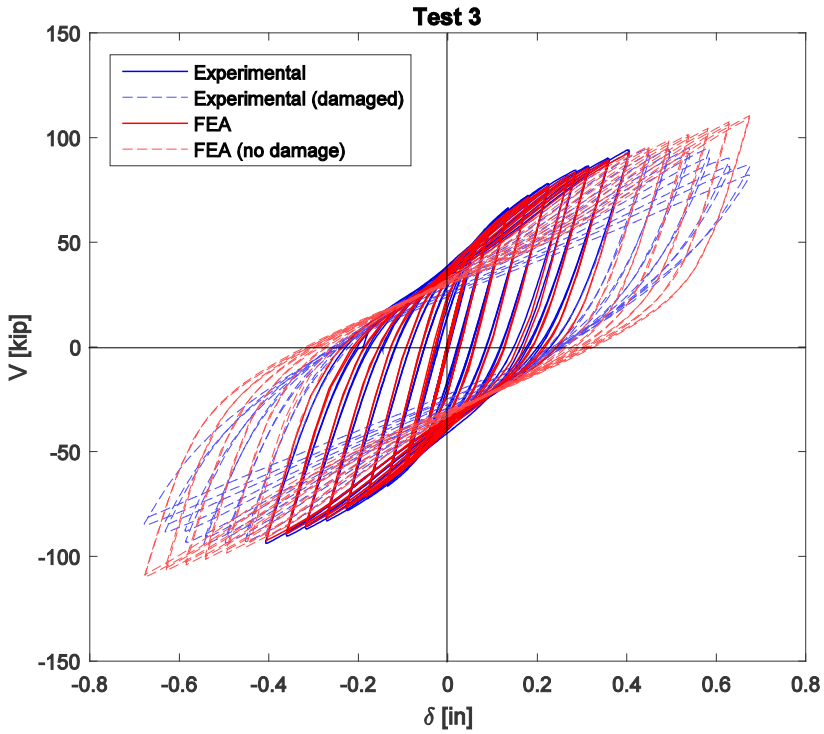

Figure 7-9: Test 3 – FEA and Experimental lateral response comparison

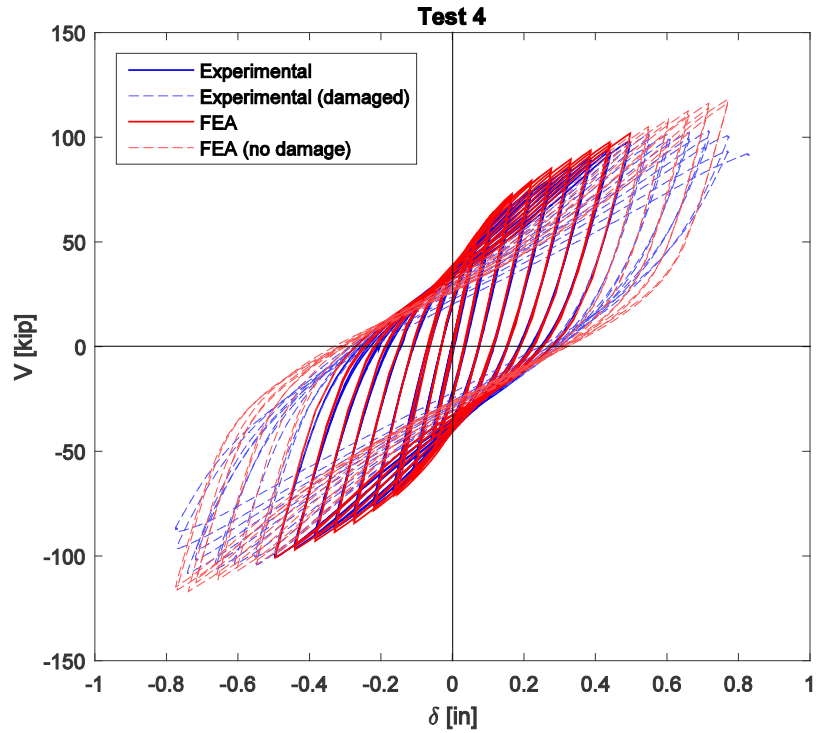

Figure 7-10: Test 4 – FEA and Experimental lateral response comparison

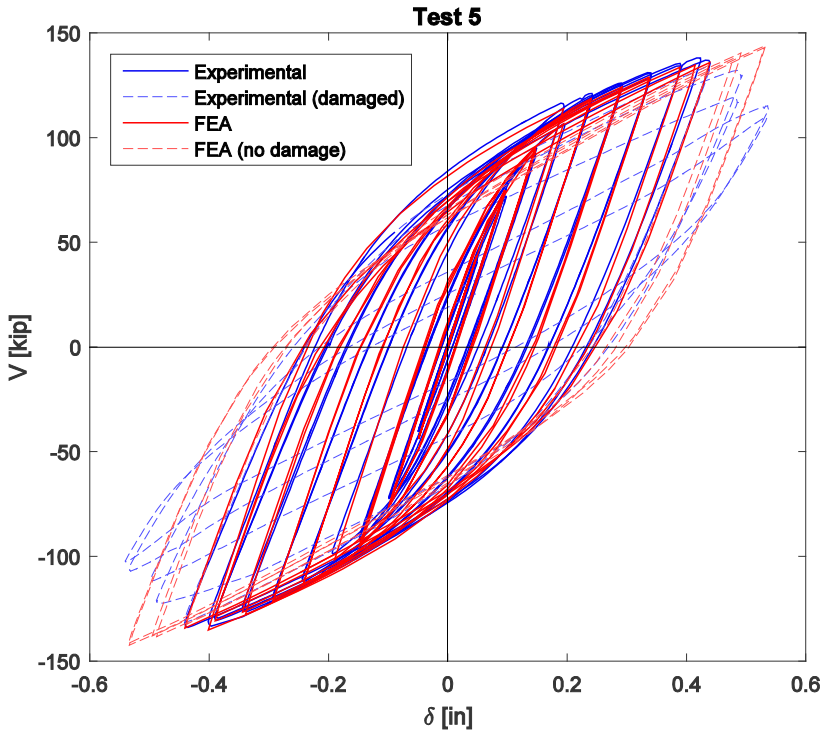

Figure 7-11: Test 5 – FEA and Experimental lateral response comparison

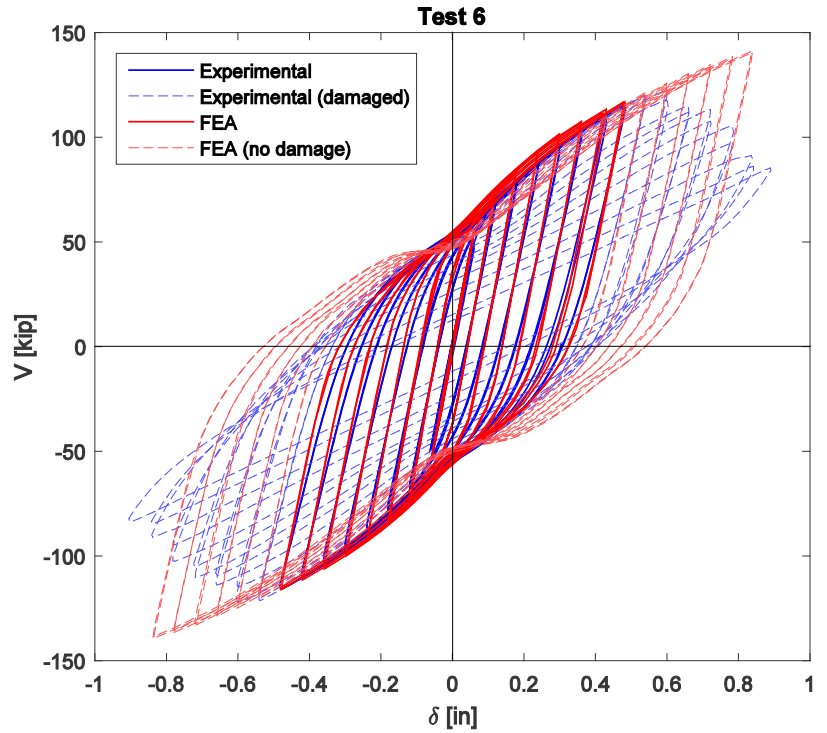

Figure 7-12: Test 6 – FEA and Experimental lateral response comparison

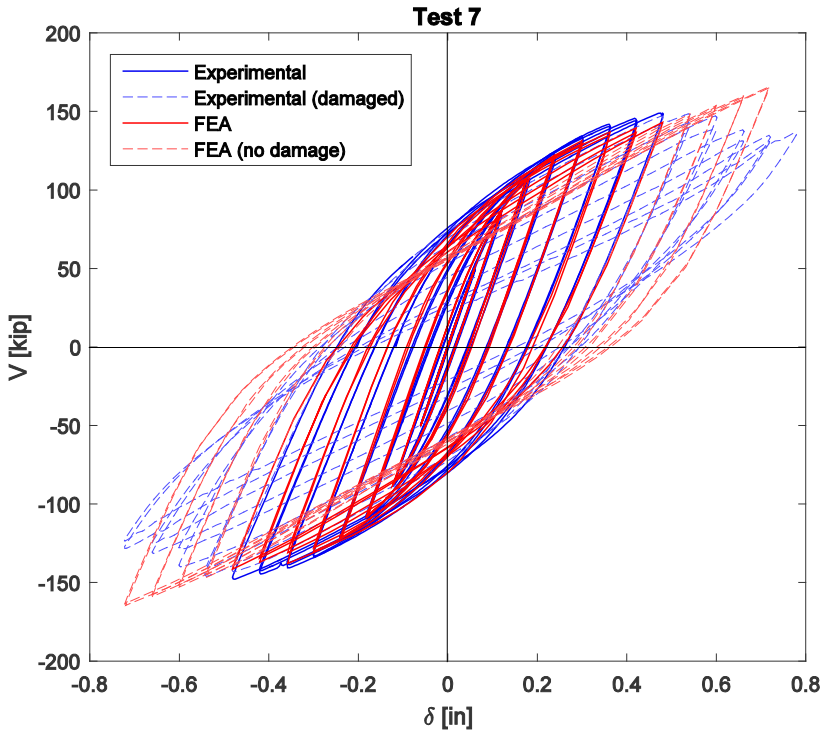

Figure 7-13: Test 7 – FEA and Experimental lateral response comparison

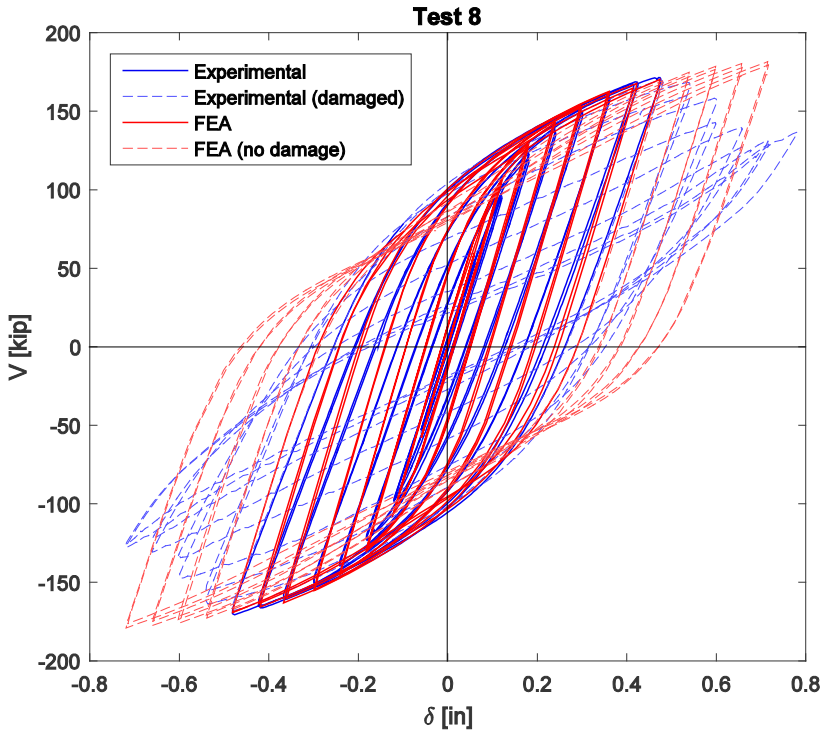

Figure 7-14: Test 8 – FEA and Experimental lateral response comparison

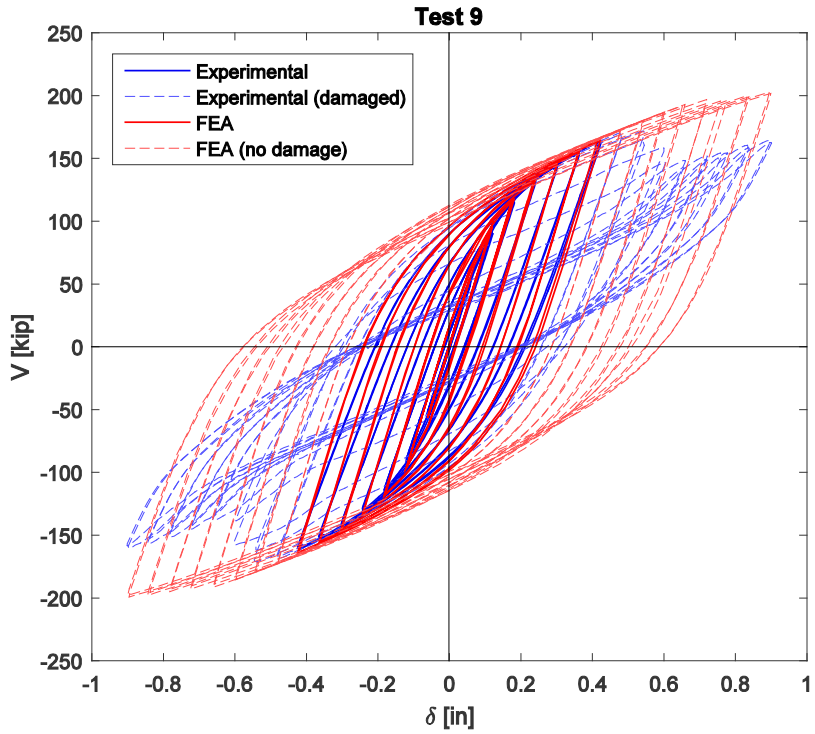

Figure 7-15: Test 9 – FEA and Experimental lateral response comparison

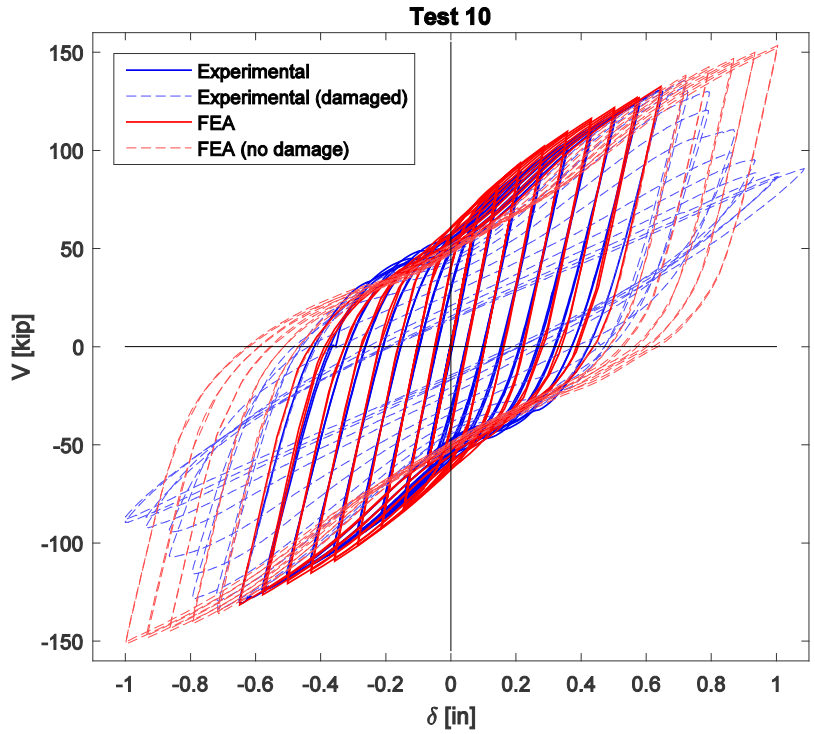

Figure 7-16: Test 10 – FEA and Experimental lateral response comparison

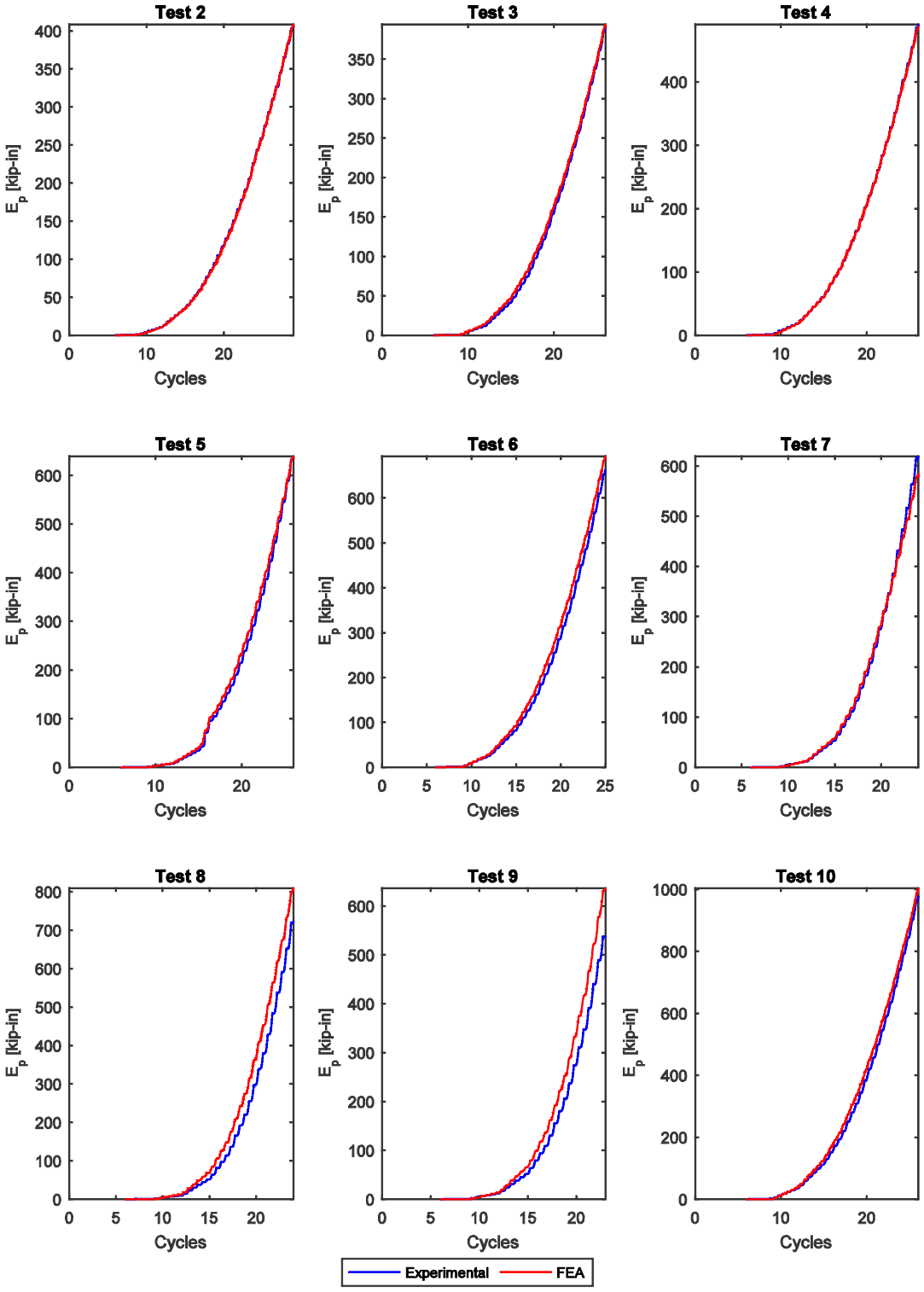

Figure 7-17: Plastic energy dissipation comparison (cycles before damage)

7.4 Damage Initiation

In this paragraph, the location and time of damage initiation observed during the tests is compared to the results from the numerical simulations. Even if a damage model was not included in the material response to capture failure of the material, the results from the simulations can still be used to identify the locations where damage is expected to initiate. The type of damage observed in the specimens during the tests was a ductile failure caused by low-cycle fatigue. This type of failure is directly related to the total plastic strain accumulated in the steel. For a material following a Mises plasticity, the measure of the total plastic strain is given by the Cumulative Equivalent Plastic Strain (PEEQ). The PEEQ index is calculated by integrating the effective plastic strain over time, where the effective plastic strain $\bar{\epsilon}_{pl}$ is defined by Equation (7-1).

$$\bar{\epsilon}_{pl} = \sqrt{\frac{2}{3}\,\boldsymbol{\epsilon}_{pl} \cdot \boldsymbol{\epsilon}_{pl}} \tag{7-1}$$

In Figures 7-18 through 7-20, shows a side-by-side comparison of the PEEQ index from the finite element analyses and the damage location in the test specimens. For each test, a close-up picture of the shear panel at the end of the first damage cycle is shown in the right column; an arrow indicates the location of the damage. The contour plot of the maximum PEEQ index (maximum of all the thickness integration points) at the corresponding instant in the simulation is shown on the left. By qualitatively comparing the images, it can be seen that the intensity of the PEEQ index closely matches the yielding areas in the specimens. In particular, for all the models, the locations of maximum PEEQ reflect the locations where damage was observed in the specimen. Therefore, the location of damage initiation could be predicted using the PEEQ index alone. However, the time of damage initiation is not captured. The values of the maximum cumulative plastic strain at these locations ranges from 4.3 to 5.9 for the 1/8” plates, from 3.6 to 4.9 for the 3/16” plates, and is equal to 2.9 for specimen 9 (1/4” plate). While some variability in the results is to be expected, the large scatter of these values demonstrates the need for a more refined damage index parameter. In fact, while the cumulative plastic strain is the plays a fundamental role in several damage models

in literature, see (Johnson and Cook 1985) and (Bai and Wierzbicki 2008), it is not sufficient to capture damage initiation. However, the application and calibration of a damage model was not possible without data from coupon tests of the material—which was not available for the tested specimens: an indirect calibration of any of these models—which all require the calibration of multiple parameters—would not be practical nor meaningful.

7.5 Conclusions

The applicability of the current finite element model to simulate the response of the BDSP bracing system has been demonstrated. The numerical model is able to predict the lateral force-drift behavior of the specimens with a high level of precision, as shown by the magnitude of the global error in the amount of energy dissipated for most of the simulations. It is worth noting that, while imperfections were included in the model, they were not matched to the actual shape or amplitude of the imperfections in the test specimen. However, the model was still able to replicate the response of the experiments. This confirms that the size of the imperfections is not significant in modelling the response of the system, as observed during the conceptual design of the system. The PEEQ index is shown to be an excellent indicator of the location of the most critical regions for damage initiation. While this parameter cannot to predict the actual moment of damage initiation, it can be used to guide improvements to the design and detailing of the BDSP system.

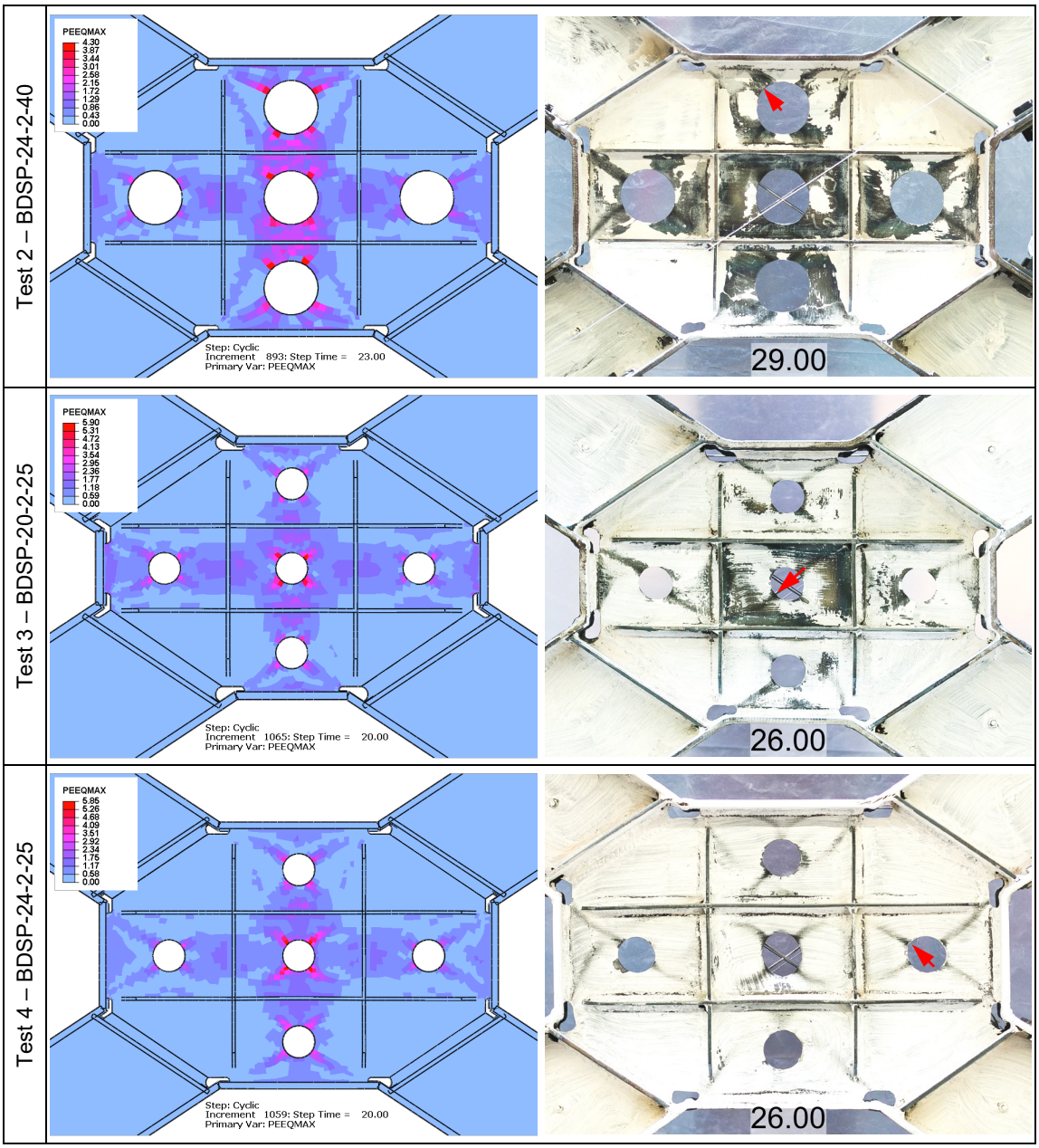

Figure 7-18: Cumulative Equiv. Plastic Strain (PEEQ) and specimens damage comparison (tests 2-4)

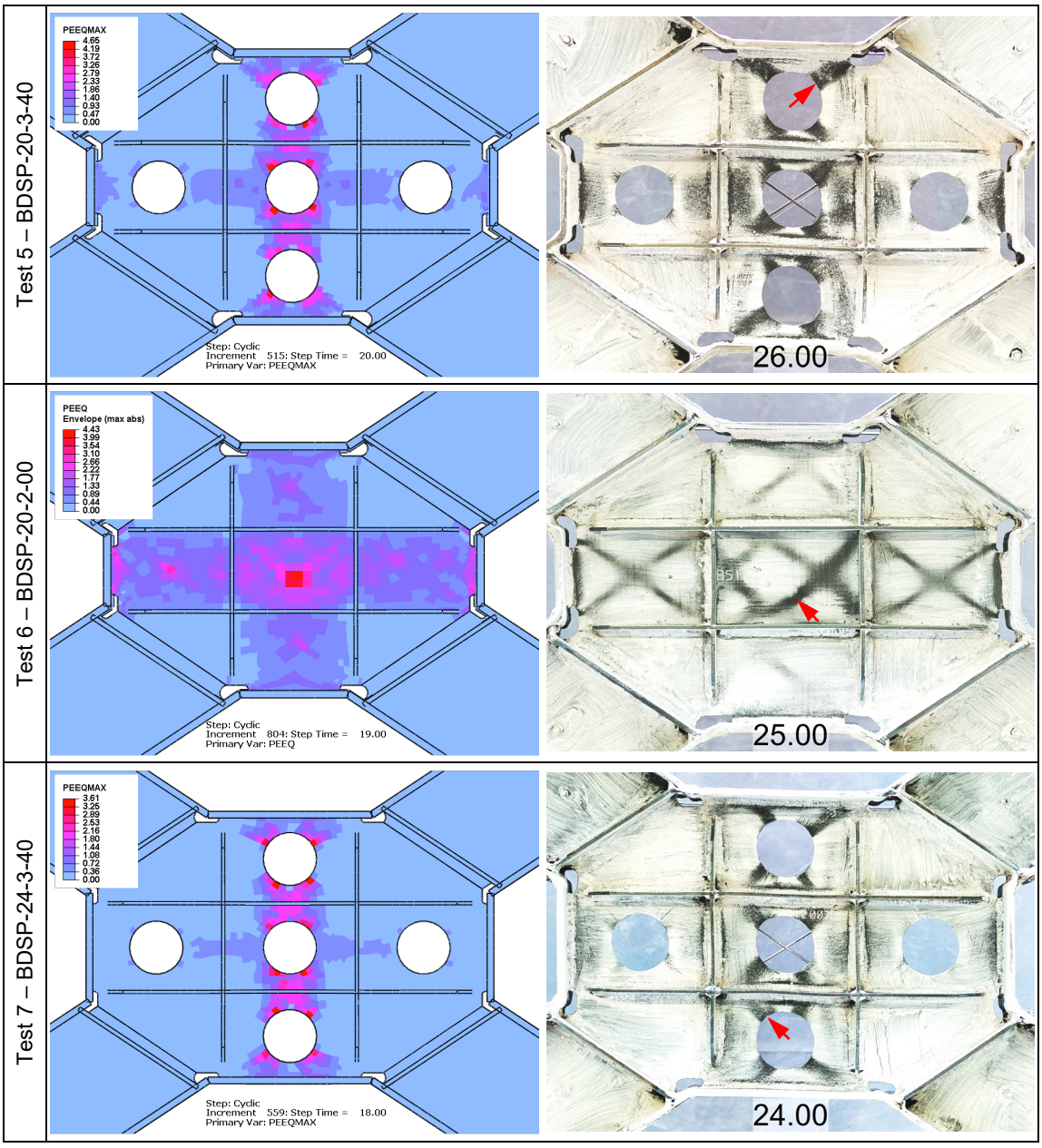

Figure 7-19: Cumulative Equiv. Plastic Strain (PEEQ) and specimens damage comparison (tests 5-7)

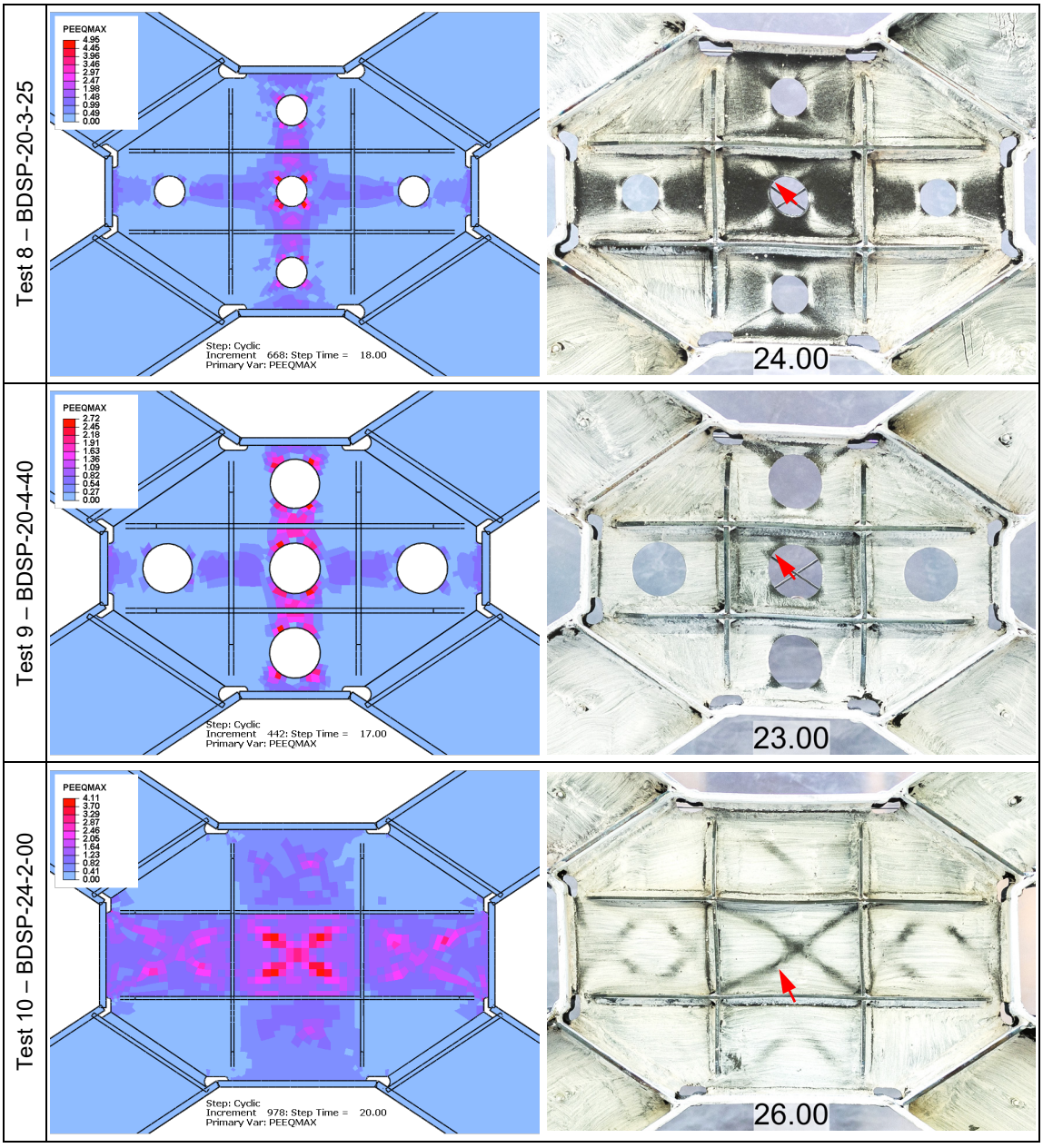

Figure 7-20: Cumulative Equiv. Plastic Strain (PEEQ) and specimens damage comparison (tests 8-10)

Chapter 8
Design and Performance Evaluation of the BDSP system

8.1 Introduction

In the previous chapters the results from experimental and numerical investigations of the response of the Braced Ductile Shear Panel were presented. In this final chapter, the performance of the bracing system as a LFRS in a multi-story sample building is evaluated.

In order to assess the performance at system level of the proposed system, the design of a sample building is conducted using seismic performance factors similar to the ones provided in ASCE/SEI 7-10 for buckling restrained braced frames (BRBFs). This assumption is justified by the general similarity in the lateral response of the BDSP to the BRB. The BRB system is identified as the one codified system with the most similar hysteretic response to the BDSP, therefore its response parameters were used as initial values for the design of the BDSP. The sample building is then analyzed using the procedure described in FEMA P-695 (FEMA 2009), which defines a methodology to quantify the seismic performance parameters of new lateral force resisting systems. This chapter first illustrates the design procedure used to calculate the necessary lateral force resisting system strengths. Once the demands have been determined, a series of shear panels are designed using the analytical expression that have been developed and validated in the previous chapters. The lateral response of each geometry is then calculated using finite element analyses similar to the ones carried out in Chapter 7. The characteristics of the response are then included in a reduced order model in SAP2000. The response of the building is simulated with nonlinear dynamic time-history analyses—following the methodology in FEMA P-695—and the performance factors are evaluated.

8.2 Sample Building Design

8.2.1 Building Description

The building used for this example was selected to have an identical geometry and loading as a BRBF archetype that was studied using the same methodology in a project of the National Institute of Standards and Technology (NIST 2010). The use of the same building allows for a direct comparison between the BRBF and the BDSP systems.

The sample building is a 12 story office structure, with a regular plan and elevation. Plan and elevation views, and dimensions are shown in Figure 8-1. For a more direct comparison of the results of the present study and the NIST project, the building was designed using the same codes and assumptions. The unfactored dead and live loads acting on the structure, in addition to self-weight, are listed in Table 8-1.

The seismic design parameters used for the design are the same as the one used in the NIST study. An exception is the Response Modification Factor, *R*, which was set to 7 instead of 8 to offset the effect of the slightly larger uncertainty in the model on the Adjusted Collapse Margin Ratio. Fixed beam-to-column connections and fixed column bases were used to replicate the analysis conditions for the BRBF. The value of the Deflection Amplification Factor C_d is set equal to *R*, per FEMA P-695. All the parameters are listed in Table 8-2.

Table 8-1: Dead and Live Loads for Design of Sample Building

Roof Level		**Interior Levels**	
Superimposed Dead	67 psf	Superimposed Dead	85 psf
Roof Live	20 psf	Live	50 psf

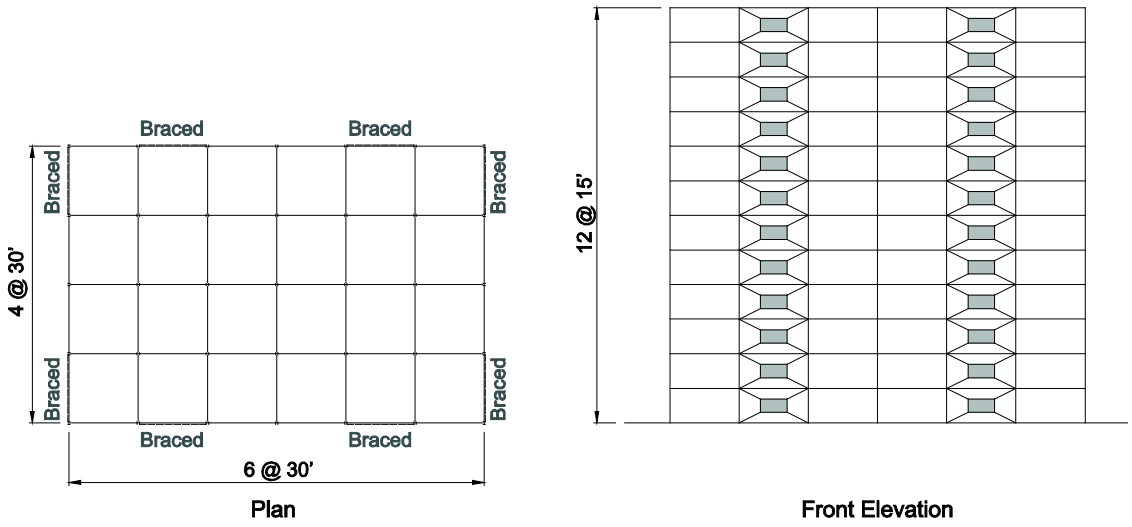

Figure 8-1: Sample building geometry and bracing

Table 8-2: Seismic Design Parameters

Parameter	Value
Occupancy Category	II (Office)
Importance Factor I_e	1.0
Design Spectral Acceleration at short period S_{DS}	1.0g
Design Spectral Acceleration at 1-second period S_{D1}	0.6g
F_a	1.0
F_v	1.5
R	7
C_d	7
Ω_0	2.5

8.2.2 ELF Procedure and BDSP System Design

The first step in the design is to determine the minimum base shear using the Equivalent Lateral Force (ELF) procedure. The maximum allowable fundamental period of the structure is computed according to clause 12.8.2 of ASCE/SEI 7-10, using the coefficient for upper limit C_u = 1.4 and the approximate fundamental period T_a from (12.8-7) of ASCE/SEI 7-10. Thus:

$$T = C_u T_a = C_u\,(C_t\,h_n^x) = 1.4\left[0.03\,(180\;ft)^{0.75}\right] = 2.06\;s \tag{8-1}$$

where C_t and x are the approximate period parameters from Table 12.8-2 of the code, and h_n is the building height in feet. The seismic base shear is calculated from Equation (12.8-1) of ASCE/SEI 7-10 multiplying the effective seismic weight W by the seismic response coefficient C_s. With the chosen seismic parameters, the controlling value for C_s according to clause 12.8.1.1 is given by equation (12.8-6) of ASCE/SEI 7-10, thus:

$$C_s = 0.5\,S_1\frac{I_e}{R} = 0.5 \cdot 0.6 \cdot \frac{1}{7} = 0.047 \tag{8-2}$$

$$V_{base} = C_s W = 0.047\,(11525\;kip) = 543\;kip \tag{8-3}$$

Where S_1 is mapped maximum considered earthquake spectral response acceleration parameter, R is the Response Modification Factor, and I_e is the Importance Factor. The vertical distribution of the base shear at each level is determined following clause 12.8.3. At any level x, the portion of the seismic shear acting at that level is calculated using Equations (12.8-11) and (12.8-12) of ASCE/SEI 7-10, shown here in (8-4) and (8-5):

$$F_x = C_{vx} V_{base} \tag{8-4}$$

$$C_{vx} = \frac{w_x h_x^k}{\sum_{i=1}^{n} w_i h_i^k} \tag{8-5}$$

Where k is an exponent related to the structure period, equal to 1.78, w_i is the portion of the total effective seismic weight at level i, and h_i is the height in feet from the base to level i. The coefficients and seismic forces calculated are listed in Table 8-3.

After the story shear demands V_i have been calculated, the lateral force resisting system can be designed. The strength requirement for the design is that the factored strength (nominal strength V_n reduced by $\phi = 0.9$) of the BDSP system at each level must be larger than the seismic force V_i.

Since two bays are braced at each story, the total shear strength of the LFRS at each level, V_{ni}, is the sum of the shear strengths of the two BDSP. The shear strength of each braced frame is the yielding strength of the panel, V_{ysp}, calculated using Equation (3-2). The other objectives and constraints that guided the design were: (1) to minimize the width of each panel while ensuring (2) that the panel had adequate drift capacity; (3) keep the slenderness parameter R_w below 0.55; (4) minimize the number of unique panels required. A minimum thickness of 1/8" was used. The final design includes four unique BDSP configurations. The geometric and mechanical properties of the BDSPs at each level are listed in Table 8-4. The same brace section W10X49 was used for all the braced frames.

These dimensions will be used to calculate the elastic properties of the equivalent bracing system for the response spectrum analysis.

Table 8-3: Vertical distribution of seismic forces

Story	w_i (kip)	h_i (ft)	C_v	F_i (kip)	V_i (kip)
12	757	15.0	0.1701	92.4	92.4
11	951	13.8	0.1831	99.5	191.9
10	960	12.5	0.1560	84.7	276.7
9	960	11.3	0.1293	70.2	346.9
8	969	10.0	0.1058	57.5	404.4
7	969	8.8	0.0834	45.3	449.7
6	979	7.5	0.0640	34.8	484.5
5	979	6.3	0.0462	25.1	509.6
4	987	5.0	0.0313	17.0	526.6
3	987	3.8	0.0188	10.2	536.8
2	1015	2.5	0.0094	5.1	541.9
1	1015	1.3	0.0027	1.5	543.4
Total	**11526**		**1**	**543.4**	

Table 8-4: BDSP System Selection

Story	Panel Dimensions				R_w	V_{ysp} (kip)	V_{ni} (kip)	$0.9\ V_{ni}$ (kip)
	b	a	t_w	n_s				
12	66	33	1/8	5	0.53	167	333	300
11	66	33	1/8	5	0.53	167	333	300
10	66	33	1/8	5	0.53	167	333	300
9	66	33	3/16	4	0.42	250	500	450
8	66	33	3/16	4	0.42	250	500	450
7	72	36	3/16	4	0.46	274	547	492
6	72	36	3/16	4	0.46	274	547	492
5	84	42	3/16	4	0.54	318	637	573
4	84	42	3/16	4	0.54	318	637	573
3	84	42	3/16	4	0.54	318	637	573
2	84	42	3/16	4	0.54	318	637	573
1	84	42	3/16	4	0.54	318	637	573

8.2.3 Response Spectrum Analysis and Frame Design

The design of the gravity frame members was conducted using response spectrum analysis. The analysis was performed with the commercial software SAP2000 on a two-dimensional model of a single BDSP braced frame. The geometry of the model was defined using the centerline dimensions of the frame. Beams and columns were modeled as elastic elements, with rigid offsets at beam-column joints—defined using half-depth of the connecting member. The BDSP bracing system was modeled using two concentric, force-displacement based, link elements. The elastic properties of each element were defined to provide an elastic response equivalent to the BDSP system. Thus, the equivalent stiffness of each element was calculated as:

$$K_{eq} = \frac{K_X}{2\cos^2\alpha} \tag{8-6}$$

Where K_X is the total horizontal stiffness of the bracing system from Equation (3-4), and α is the angle of the bracing with the horizontal.

The analysis was conducted using the design response spectrum defined by the seismic parameters in Table 8-2. The mass assigned at each level was determined from the dead load at the story and the tributary area of the lateral force resisting system—that is half the floor area. The base shear from the response spectrum analysis was 488 kip. The minimum allowable base shear for scaling of the response spectrum analysis is calculated as per clause 12.9.4.1 of ASCE/SEI 7-10, and is equal to:

$$V_{allow} = 0.85\ V_{base} = 462\ kip \tag{8-7}$$

Since the base shear from the analysis was larger than the minimum allowed, the spectrum did not need to be rescaled.

Beams and columns were designed using the factored load combinations from the code, and the overstrength factor of Ω_0. For consistency with the NIST study, the design of the frame was conducted using the minimum design combinations from the code, rather than a capacity design approach.

Beams were assumed to be braced at quarter points along the span, and designed for the combined effects of gravity loads and the axial and bending force from the seismic load case. Since the factored design forces were very similar for all the levels, the same section was designed for all the beams, and a W18X50 was selected. The columns were spliced every two floors, and designed using the same load combinations. The sections selected for the columns are listed in Table 8-5.

The first mode period computed in SAP2000 for the frame model was found to be 2.55 s. The maximum allowable period calculate above was 2.06 s. Therefore, the choice of using the fundamental period is correct. For comparison, the period of the BRBF frame in the NIST study was lower at 2.26 s.

Table 8-5: Column Sections

Story	Column Section
12-11	W12X87
10-9	W12X96
8-7	W12X106
6-5	W14X145
4-3	W14X176
2-1	W14X283

8.3 Nonlinear BDSP Response Calculation

The lateral response of each BDSP geometry was determined using finite element analyses on a model of the bracing system. The model has the same features of the model used in Chapter 7 and validated against experimental results. However, the outer frame was not included in this model and the displacement was applied to the welded edges of the gusset plates. The response was calculate using a simulated monotonic displacement-based loading protocol, with a maximum drift of 5 inches. A sketch of each model and its lateral force-drift response are shown in Figure 8-2.

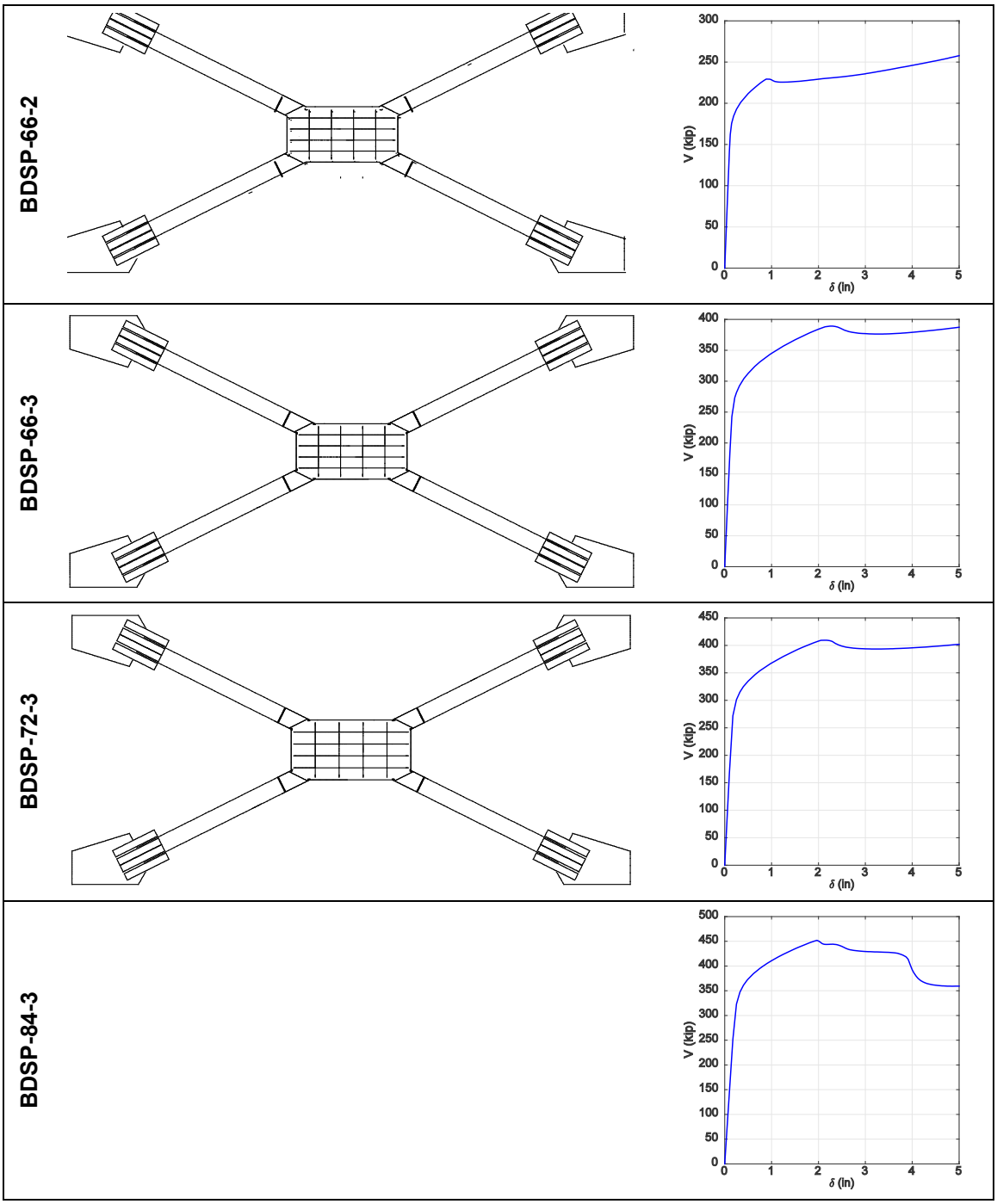

Figure 8-2: Geometry and computed lateral response of the BDSP systems

8.4 Nonlinear Analyses and Performance Evaluation

8.4.1 Model Description

The same building model used in the previous section is used to conduct nonlinear analyses in SAP2000. This section describes the nonlinear features that are included in the model for this part of the study.

The nonlinear behavior of the BDSPs is included in the SAP2000 building model using two concentric nonlinear link elements. The elements are assigned an axial force-displacement response defined using a Multilinear Plastic model in SAP2000. For each link, the equivalent axial force-displacement relationship is calculated using the response obtained from the detailed finite element analyses. The response curves are first approximated by five straight segments. The values of the horizontal force are then rotated into the link reference system, and symmetrically distributed to the two links. Thus, the equivalent force at each point is:

$$F_{eq}^{i} = \frac{V_{FEA}^{i}}{2\cos\alpha} \tag{8-8}$$

Similarly, the horizontal inter-story drift at each data point is transformed into its link equivalent displacement:

$$\Delta_{eq}^{i} = \delta_{FEA}^{i}\cos\alpha \tag{8-9}$$

The resulting model of the braced frame is shown in Figure 8-3.

The beams and columns are modeled with elastic elements. A rigid offset from the centerline node is included, equal to half the column depth for beam elements, and vice versa. Plastic hinges are included at the end of the beam and column elements to capture the nonlinear moment-rotation response.

The gravity loads acting on the structure were determined following the requirements of FEMA P-695, which result in 1.05 times the dead loads and 0.25 times the live load.

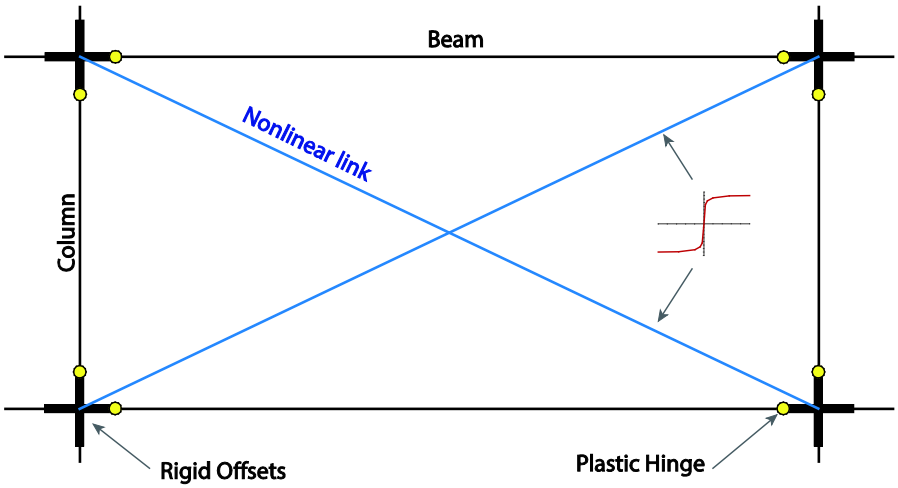

Figure 8-3: BDSP bracing system two-links model

8.4.2 Pushover Analysis

The methodology requires a nonlinear static pushover analysis to evaluate the assumed over-strength factor Ω_0, and to calculate the spectral shape factor (SSF). The SSF is used to calculate the adjusted collapse margin ratio (ACMR). The lateral load distribution for the pushover is proportional to the product of the seismic weight at each story and the story's ordinate of the fundamental mode. The resulting curve from the pushover analysis on the building model is shown in Figure 8-4, along with the parameters defined in FEMA P-695.

The overstrength factor is calculated as shown in Equation (8-10):

$$\Omega = \frac{V_{base,max}}{V_{base,design}} = \frac{1263\ kip}{543\ kip} = 2.33 \tag{8-10}$$

where $V_{base,max}$ is the peak base shear and $V_{base,design}$ the design base shear from the ELF analysis. This result confirms the initial design selection of $\Omega_0 = 2.5$. Failure was associated with the formation of a soft story mechanism at the fourth level.

The system collapse ductility μ_c is calculated using the effective yield displacement per FEMA P-695. The effective yield displacement Δ_{yeff} is computed using Equation (8-11).

$$\Delta_{yeff} = C_o \frac{V_{base,max}}{W_{tot}} \left(\frac{g}{4\pi^2}\right) \cdot \max(T, T_1) \tag{8-11}$$

Where W_{tot} is the total seismic weight for the frame, T is the fundamental period per code, T_1 is the period of the first mode determined by eigenvalue analysis. C_o is a factor calculated from the mode shape as shown in Equation (8-12):

$$C_o = \phi_{1r} \left[\frac{\sum_1^N W_i \, \phi_{1i}}{\sum_1^N W_i \, (\phi_{1i})^2} \right] \tag{8-12}$$

Where W_i is the seismic weight at level i, ϕ_{1i} and ϕ_{1r} are respectively the values of the first mode shape in the horizontal direction at level i, and at roof level, and N is the number of stories. The value calculated for C_0 is 1.50. The resulting effective yield displacement is equal to 10.55 in. The system collapse ductility μ_c, calculated as the ratio of the ultimate displacement Δ_u to Δ_{yeff}, was calculated to be 3.19. This parameter is used to obtain the spectral shape factor from Table 7-1b of FEMA P-695. The SSF determined for this structure is 1.336.

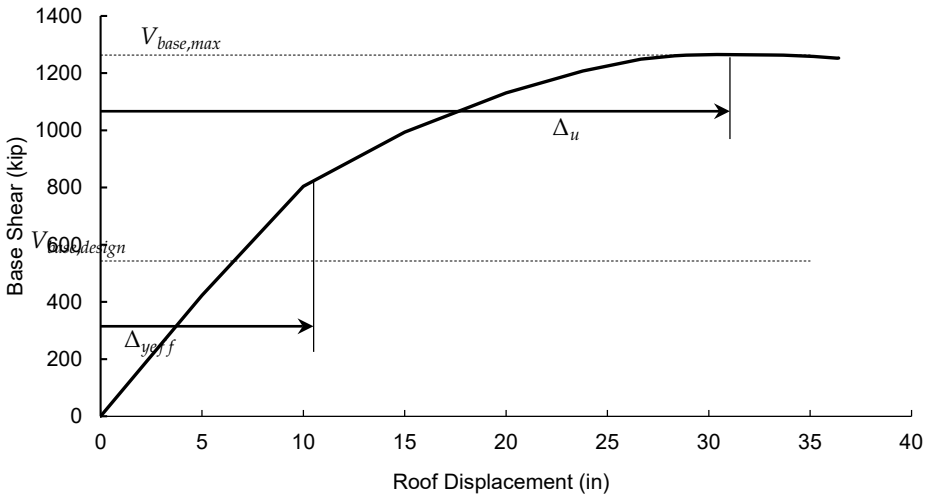

Figure 8-4: Pushover curve of the sample building and FEMA P-695 parameters

8.4.3 Nonlinear Incremental Dynamic Analysis

An Incremental Dynamic Analysis (IDA) was carried out on the 12-story BDSP frame building—according to the requirements of FEMA P-695. This type of analysis requires the model to be subjected to a pre-selected suite of far-field ground motions. The suite intensity is scaled incrementally until half of the scaled ground motions cause collapse of the structure, as defined by one or more indexes. The lowest scale factor to cause "collapse" in at least 50% of the analyses is then used to compute the Collapse Margin Ratio (CMR): the CMR is the ratio of the median spectral intensity of the whole set, as measured at the fundamental period of the structure, and the MCE design spectrum at the same period. For this study, collapse will be defined in terms of maximum inter-story drift and plastic hinges rotation. The maximum inter-story drift at each level is compared to a limit value of 3%, and the structure is considered collapsed if the value is exceeded at any level. Similarly, if a plastic hinge in any element of the frame reached the maximum rotation, the structure will be considered collapsed. Therefore, collapse of the BDSP system due to low-cycle fatigue is not directly captured by this definition. However, the model is considered still valuable to explore the system level performance of the BDSP. In fact, the experimental results have shown that the system can dissipate a significant amount of energy before failure.

The suite of ground motion records is defined by the methodology in FEMA P-695 and includes 22 far-field records with components in two orthogonal directions. For a two-dimensional frame analysis like the one in this study, the document suggests that both components be applied independently on the structure, for a total of 44 analyses at each intensity level. The ground motions are scaled in two steps. The first step consists in normalizing the ground motions by their peak ground velocities. This normalization did not need to be performed since FEMA P-695 provides the corresponding scale factors for each pair of ground motion records. The second step is to scale the ground motions to the MCE spectrum. This is done by anchoring the mean spectrum to the MCE spectrum at the fundamental period of the structure. The scale factors for this operation are

available in FEMA P-695. For the building object of this study, with a fundamental period of 2.06 s, the MCE scale factor is 3.08.

Results from the incremental dynamic analysis are shown in Figure 8-5. Each line in the plot corresponds to one ground motion record. In the plot the median spectral intensity of the ground motion set is plotted against the maximum inter-story drift in the analysis. The two horizontal lines indicate the spectral intensity of the MCE spectrum at the fundamental period, S_{MT}, and the median collapse intensity, $\hat{S}_{CT}$. Using these two values, the CMR was calculated and found to be equal to 1.363. The ACMR can now be calculated as the CMR times the SSF calculated previously in the pushover analysis and equal to 1.336: the resulting ACMR is 1.821. This value is less than the ACMR of 3.18 which is reported in the NIST project for the BRBF.

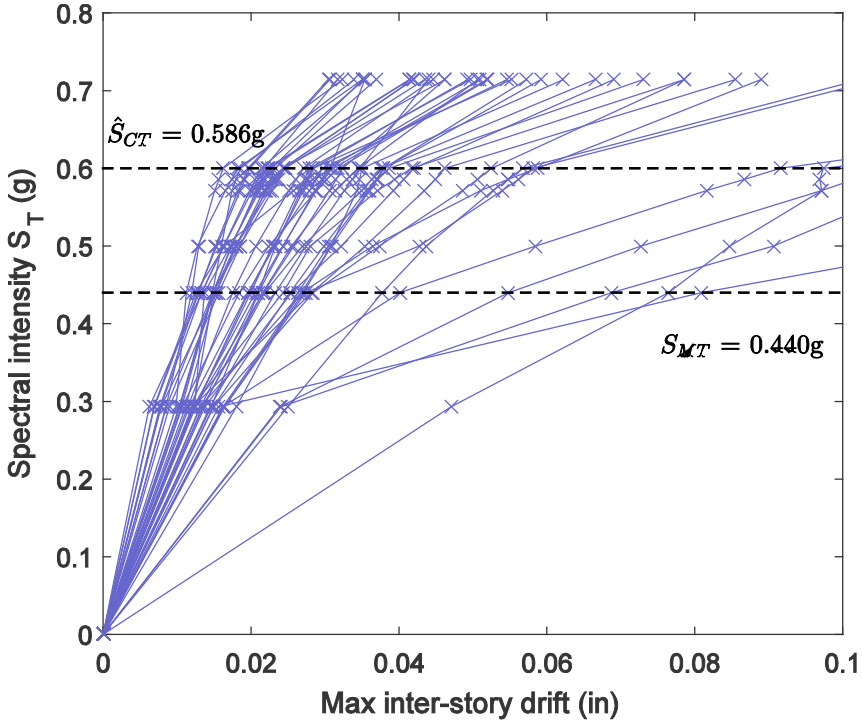

Figure 8-5: Incremental dynamic analysis of the FEMA P-695 far-field record set

FEMA P-695 defines the acceptable value of the ACMR as a function of a series of uncertainty factors which when combined give the total system collapse uncertainty β_{TOT}. The factors quantify

the uncertainty of the design requirements β_{DR}, the uncertainty in the available test data β_{TR}, the uncertainty in collapse modelling β_{MDL}, and the record-to-record uncertainty β_{RTR}.

The uncertainty in the design requirements is evaluated taking into account the robustness and completeness of the requirements. Since it is a unique and new system, the design requirements for the BDSP system are not yet codified. However, since the experimental and numerical studies have shown that there are relatively few design requirements, which significantly affect the response, for the purpose of this evaluation the BDSP requirements were assumed to have a rating of (B)-Good.

The test data uncertainty is evaluated considering the completeness of the parameters that have been investigated, and the confidence in the test data quality. The quality of the data used for this study from the experimental program is deemed highly reliable. On the other hand, since physical tests were conducted only on half-scale specimen, and not all the parameters that affect the response have been investigated (e.g. boundary flange thickness, size effects, stocky webs without perforations), a higher level of reliability in the test data can be achieved. At this time, the data uncertainty is set to a rating of (C)-Fair.

The uncertainty in the analytical model used to predict collapse is judged based on the quality of the model, and the distinct collapse mechanisms that are included. The model used for this study only considered collapse using a general approach, taking into account the maximum inter-story drift. However, plastic hinges were included in the model and allowed to model the resulting decrease in story stiffness. Second order P-Delta effects were also included in the model. As previously mentioned, a model that would allow to calculate a more robust collapse index could be developed, if failure due to cyclic loading is incorporated in the model. For these reasons, the model is conservatively assigned a rating of (C)-Fair.

The record-to-record uncertainty is defined according to FEMA P-695 instructions, that is using β_{RTR} equal to 0.4 for systems with a collapse ductility greater than 3.0, and evaluated using the full suite of 22 far-field records.

When all the uncertainties listed above are considered, the total system collapse uncertainty is equal to $\beta_{TOT} = 0.675$. From Table 7-3 of FEMA P-695 the acceptable values of the ACMR are: 2.38 for a 10% collapse probability, $ACMR_{10\%}$; 1.76 for a 20% collapse probability, $ACMR_{20\%}$. This methodology requires that all the archetype buildings considered in the study must exceed $ACMR_{20\%}$, while the average value for each performance group must exceed $ACMR_{10\%}$. Since a reduced methodology has been used in this study—for the purpose of illustrating the performance of a one sample building—only the first condition can be evaluated. The system is therefore considered acceptable, as the calculated $ACMR$ of 1.821 is larger than the value of 1.76 of $ACMR_{20\%}$. To confirm this result, a full FEMA P-695 study would need to be carried out. The use of a more detailed model would also be beneficial to the study, since it would decrease the model uncertainty factor, and therefore decrease the collapse probability threshold.

8.5 Conclusions

In this chapter an example of the design process for a frame braced with the BDSP system has been presented. The performance of the designed LRFS, which was conducted using Equivalent Lateral Force procedure from ASCE/SEI 7-10, was then evaluated using the sample building as an archetype to carry out one of the analysis required by the methodology in FEMA P-695. The response of the BDSP system was modelled in SAP2000 using two nonlinear elements for each braced frame. The force-displacement of these elements was obtained from the response of the modelled braced frame—calculated using three-dimensional finite elements analyses on a model similar to the one validated against the experimental program. The results of the performance evaluation showed that the assumed seismic performance factors would likely be found acceptable if the full methodology was used.

Chapter 9
Summary, Conclusion and Recommendations

9.1 Summary

The objective of this research was to investigate the performance of a new seismic lateral force resisting system for steel frames, the Braced Ductile Shear Panel, or BDSP. The proposed system can be an economical alternative to commonly used proprietary designs, in providing the necessary lateral strength to a building—while still offering similar levels of energy dissipation and drift control. The BDSP is envisioned as a sacrificial structural element, that could be replaced, if needed, after a major seismic event. Unlike the off-the-shelf systems like the BRB, the shear panel could be sized by the designer to provide the necessary strength, following existing design equations and requirements.

This research expands upon the preliminary results of the conceptual design that was conducted as part of a previous work (Giannuzzi 2011). The results of the previous study indicated that the system could be designed to achieve the necessary stiffness, strength and ductility capacity; they also provided more information about the parameters that affect the system behavior. However, since the data in the study was purely numerical, the results needed confirmation from experimental data. The first part of this research was aimed at collecting this data to validate the numerical model, and quantify its ability to capture the real behavior of the system. Once the model was verified, the second portion of the study focused on assessing the system level performance of the BDSP system.

An experimental program was designed to investigate the real behavior of the proposed system, including the energy dissipation capacity and failure modes, the demands on the braces and the design of the connections. A half-scale frame was designed, and used for testing of ten panel specimens, which allowed to study the response of devices with different geometry. Eight of the ten specimens had perforations in the web, with two diameters to width ratios of 0.40 and 0.25.

Three web thicknesses (1/8”, 3/16”, and 1/4”) and two panel widths (20” and 24”) were the other varying parameters.

All the tested specimens exhibited a lateral response consistent with the expected behavior, as all the panels displayed a stable response and ample hysteretic dissipation, before the onset of damage. The testing frame was successfully reused throughout the entire program, and no signs of yielding or damage were observed in its members. The gusset plates—by design attached only to the beam and stiffened on the free edge—did not present any damage or sign of instability. The slip critical connections, designed for the capacity of the panel, performed as expected; minor slippage—less than 0.25 inches—occurred only during tests 8 and 9, but did not affect the response of the system. The long-slotted holes on the panel stubs greatly facilitated the installation of the panel in the braces, and were also necessary for an easy removal of the specimens. As a result of the experimental program, the analytical expression for the calculation of initial elastic stiffness, yield force and maximum lateral load were also improved.

The experiments also highlighted the tendency of displacements in the shear panel to localize along the clear distance between the braces flanges. In the panels with thicker webs, this localization took place along the vertical direction, while a horizontally dominated displacement field was observed in the slender panels.

The tests proved that a major parameter that affects the response of the shear panels is the slenderness of the web plate. The slenderness parameter R_w was considered in this study. It was shown that plates with $R_w<0.40$ did not display significant out-of-plane displacements, as a consequence of inelastic buckling. Instead, web plates with $R_w>0.50$ buckled inelastically after the drift was increased past three times the yielding drift. However, the energy dissipation capacity was excellent in both cases. The negative effect of the perforations on the system ductility was significant in the perforated webs with $R_w<0.40$. In fact, the slender webs buckled inelastically early in the loading, and ultimately initiated damage at the edge of the perforations due to repeated reversal of the out-of-plane displacements. The thicker web plates, on the other hand, did not

deform out-of-plane: the damage was driven by the stress concentration around the perforation edges, which in turn led to a less ductile fracture. The damage in the two panels with solid webs was initiated at points which experienced the largest curvature reversals due to the alternation of the out of plane displacements.

The data from the experimental program was used to validate the results of finite element analyses. A three dimensional, shell elements model of the experimental setup was created, and the experimental drift histories of each test were used as imposed displacements to replicate the experimental loading protocol. The material models used for the web plate in each specimen included a model for mixed kinematic and isotropic hardening. The models were calibrated for each plate thickness using the global response of the system. Calibration of a damage model could not be conducted due to the lack of coupon test data.

The numerical model was shown to be able to accurately replicate the lateral response of the system and the experimental frame. This includes the inelastic buckling of the slender web plates—and the following gradual loss of stiffness—and pinching of the hysteresis curve. The overall difference between the two response—which is believed to be mostly due to inaccuracies in the stress strain curve—was evaluated by comparing the total energy dissipation. Since a damage model was not included, the comparison between the experimental and numerical response was limited to the loading cycles prior to damage initiation. However, it was shown that the areas of the specimen panels where damage initiated, corresponded to points in the model associated with peak cumulative equivalent plastic strain.

The design of the BDSP system for a 12-story sample office building was conducted to illustrate a viable design methodology. The BDSP at each level was designed according to the story shear obtained from the Equivalent Lateral Force procedure in ASCE/SEI 7-10. The seismic response parameters assumed for the design were R=7, C_d=5 and Ω_0=2.5. For the design of the BDSP system, the initial panel width and thickness were chosen based on the story shear requirement and the yielding strength of each panel. The number of stiffeners was then chosen

based on the slenderness parameter R_w. The gravity frame was designed using the Response Spectrum Analysis and the applicable load combinations.

Afterwards, the performance of the system in the sample building was evaluated using nonlinear analyses of the structure. The nonlinear lateral force-drift response of each BDSP geometry chosen in design was calculated using the finite element model previously validated. The force-displacement relationship obtained, was included in the nonlinear SAP2000 model of the building as a pair of concentric link elements. The two link model of the shear panel system performed as expected during the nonlinear time history analyses, when compared to the detailed finite element simulations.

The methodology used to quantify the performance of the system was taken from FEMA P 695. The previously designed sample building was used as one of the different archetypes required by the methodology. First, a pushover analysis of the building was conducted and the base shear-roof drift curve was used to determine the overstrength factor, Ω_0, the ductility, μ, and the spectral shape factor, SSF—as required by the methodology. To calculate the collapse margin ratio, CMR, an incremental dynamic analysis (IDA) was carried out, following the requirements in FEMA P 695. A maximum inter-story drift of 3% at any level of the structure was used to determine if the structure collapsed under each scaled ground motion. The BDSP system was deemed acceptable according to the result from the IDA on the archetype building. The adjusted collapse margin ratio—calculated by taking into account the different uncertainties described in FEMA P-695—was larger than the acceptance threshold. Thus, the validity of the seismic response coefficients assumed at the beginning of the study was confirmed.

9.2 Conclusions and Recommendations

The results of the present study have shown that the BDSP system possesses the required stiffness, strength and ductility to be used as a dissipative bracing system for seismic protection of buildings structures. Moreover, there is reason to believe that the performance levels that can be

achieved with the proposed system, are similar to those of BRBF. Among the bracing systems currently allowed in design by ASCE/SEI 7-10, the BRBF is the one that offers the best performance, when the seismic response factor is considered. According to the performance evaluation analysis, the response of the BDSP system can be compared to the one of the BRB.

In the analysis, a seismic response coefficient of 7.0 was assumed, which is lower than 8.0, the value currently provided by the code for BRBFs. This choice was made to offset the effects of the larger uncertainties, in the model and the data, on the value of the ACMR. However, if these uncertainties are reduced, the system would likely pass the full methodology from FEMA P 695 with higher values of R. The uncertainty in the model could be reduced by implementing a more complete and less conservative collapse criteria, such as energy dissipation or cumulative displacement of the link elements. The uncertainty in the data could be reduced with more research into the system behavior, and especially from experiments on full scale specimens.

More data on the behavior of the system could also be obtained from additional finite element simulations. The finite element model validation proved that the numerical model can be used to predict the nonlinear behavior of the system—prior to damage initiation—including inelastic buckling of the plate, cyclic stiffness degradation and energy dissipation. The behavior after damage was not captured by the current simulations, since a damage model could not be calibrated. However, the strong correlation between the PEEQ values—from the finite element simulations—and the damage pattern observed in the specimens, suggests that a ductile damage criterion could be implemented to estimate the point of damage initiation, and possibly follow the evolution of the damage if convergence of the solution allows it.

A viable design approach for the selection of the shear panel properties, was illustrated during the design of the sample building. From the example, some fundamental controlling parameters and constraints for the design of the system have been found. The first, and most restricting, constraint concerns the maximum drift that can be sustained by the system. Due to the localization of displacements in the panel, the average shear strain in the web is linearly related to the story

shear, by a factor equal to the ratio between the story height and the panel height. To ensure that the system has sufficient drift capacity, the clear height of the shear panel should be selected based on the maximum shear strain that the panel is expected to experience when the displacements have localized—at the maximum design story drift. During the design of the sample building, this was the controlling factor for the selection of the panel sizes. Once the minimum panel width and height were selected, the thickness of the web plate was chosen to satisfy the strength and stiffness requirements. Transverse stiffeners were then added to control the slenderness of the plate.

The need to accommodate the amplified design story shear in the panel, translates in a constraint on the minimum width, and height, of the panel. The finite element simulations carried out to calculate the response envelope of the BDSPs in the sample building, have shown that as the panels get larger, displacements can localize across a single subpanel height. This behavior would greatly reduce the ductility of the device, since it would result in a gross magnification of shear strains after localization. In order to avoid this possibility, the boundary flanges have to provide adequate stiffness to allow for stress redistribution. More research on the effect of the flanges is warranted, in order to develop an explicit requirement on the minimum value of the boundary flange thickness for a given panel geometry.

References

AISC. (2010a). *Seismic Provisions for Structural Steel Buildings*. ANSI/AISC 341-10, Chicago, IL.

AISC. (2010b). *Specification for Structural Steel Buildings*. ANSI/AISC 360-10, Chicago, IL.

ATC. (1992). *Guidelines for cyclic seismic testing of components of steel structures*. *ATC-24*, Redwood City, CA.

Bai, Y., and Wierzbicki, T. (2008). "A new model of metal plasticity and fracture with pressure and Lode dependence." *International Journal of Plasticity*, 24(6), 1071–1096.

Bergman, D. M., and Goel, S. C. (1987). *Evaluation of cyclic testing of steel-plate devices for added damping and stiffness*. UMCE, Ann Arbor, MI.

Berman, J. W., and Bruneau, M. (2009). "Cyclic Testing of a Buckling Restrained Braced Frame with Unconstrained Gusset Connections." *Journal of Structural Engineering*, 135(12), 1499–1510.

Chen, Z., Ge, H., and Usami, T. (2006). "Hysteretic Model of Stiffened Shear Panel Dampers." *Journal of Structural Engineering*, ASCE, 132(3), 478–483.

Chusilp, P., and Usami, T. (2002). "New Elastic Stability Formulas for Multiple-Stiffened Shear Panels." *Journal of Structural Engineering*, ASCE, 128(6), 833–836.

Cofie, N. G., and Krawinkler, H. (1985). "Uniaxial Cyclic Stress-Strain Behavior of Structural Steel." *Journal of Engineering Mechanics*, 111(9), 1105–1120.

FEMA. (2009). *Quantification of Building Seismic Performance Factors*. *FEMA P-695*, Washington, D.C.

Giannuzzi, D. (2011). "Braced Ductile Shear Panel: a new dissipative seismic resistant framing system." Politecnico di Milano.

Giannuzzi, D., Ballarini, R., Huckelbridge, A., Pollino, M., and Valente, M. (2014). "Braced Ductile Shear Panel: New Seismic-Resistant Framing System." *Journal of Structural Engineering*, American Society of Civil Engineers, 140(2).

Gupta, A., and Krawinkler, H. (1999). *Seismic Demands for Performance Evaluation of Steel Moment Resisting Frame Structures*. Stanford.

Hjelmstad, K. D., and Popov, E. P. (1983). "Cyclic Behavior and Design of Link Beams." *Journal of Structural Engineering*, 109(10), 2387–2403.

Hjelmstad, K. D., and Popov, E. P. (1984). "Characteristics of Eccentrically Braced Frames." *Journal of Structural Engineering*, American Society of Civil Engineers, 110(2), 340–353.

Johnson, G. R., and Cook, W. a. (1985). "Fracture characteristic of three metals subjected to various strains, strain rates, temperatures and pressures." *Engineering Fracture Mechanics*, 21(1), 31–48.

Lumpkin, E. J., Hsiao, P.-C., Roeder, C. W., Lehman, D. E., Tsai, C.-Y., Wu, A.-C., Wei, C.-Y., and Tsai, K.-C. (2012). "Investigation of the seismic response of three-story special concentrically braced frames." *Journal of Constructional Steel Research*, 77, 131–144.

McDaniel, C. C., Uang, C.-M., and Seible, F. (2003). "Cyclic Testing of Built-Up Steel Shear Links for the New Bay Bridge." *Journal of Structural Engineering*, American Society of Civil Engineers, 129(6), 801–809.

Merritt, S., Uang, C., and Benzoni, G. (2003). *Subassemblage Testing of Star Seismic Buckling-Restrained Braces*. Structural Systems Research Project, La Jolla, CA.

Nakashima, M. (1995). "Strain-Hardening Behavior of Shear Panels Made of Low-Yield Steel. I: Test." *Journal of Structural Engineering*, American Society of Civil Engineers, 121(12), 1742–1749.

NIST. (2010). *Evaluation of the FEMA P-695 Methodology for Quantification of Building Seismic Performance Factors (NIST GCR 10-917-8)*. Gaithersburg, MD.

Rai, D. C., and Wallace, B. J. (1998). "Aluminium Shear-Links For Enhanced Seismic Resistance." *Earthquake Engineering and Structural Dynamics*, 27, 315–342.

Saeki, E., Sugisawa, M., Yamaguchi, T., and Wada, A. (1998). "Mechanical Properties of Low Yield Point Steels." *Journal of Materials in Civil Engineering*, 10(3), 143–152.

Tanaka, K., and Sasaki, Y. (2000). "Hysteretic Performance of Shear Panel Dampers of Ulta Low-Yield-Strength Steel for Seismic Response Control of Buildings." 1–8.

Thornton, W. A. (1984). "Bracing Connections for Heavy Construction." *Engineering Journal*, AISC, 21(3), 139–148.

Tsai, K.-C., Chen, H.-W., Hong, C.-P., and Su, Y.-F. (1993). "Design of Steel Triangular Plate Energy Absorbers for Seismic-Resistant Construction." *Earthquake Spectra*, 9(3), 505–528.

Whittaker, A. S., Bertero, V. V., Thompson, C. L., and Alonso, L. J. (1991). "Seismic Testing of Steel Plate Energy Dissipation Devices." *Earthquake Spectra*, 7(4), 563–604.

Zhang, C., Aoki, T., Zhang, Q., and Wu, M. (2013). "Experimental investigation on the low-yield-strength steel shear panel damper under different loading." *Journal of Constructional Steel Research*, Elsevier Ltd, 84, 105–113.

Appendix A Drawings

Figure A-1: Assembled Testing Frame

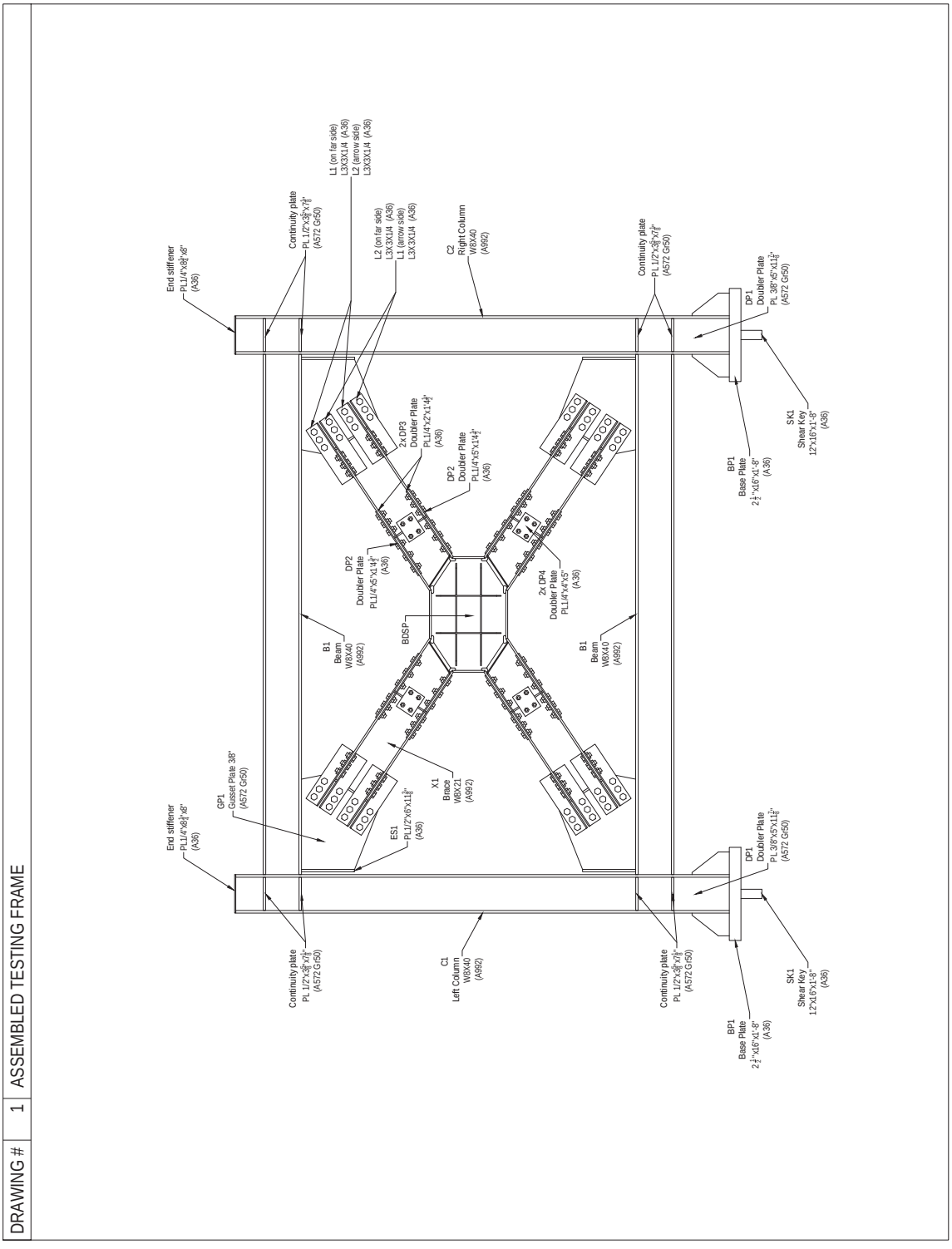

Figure A-2: Testing Frame

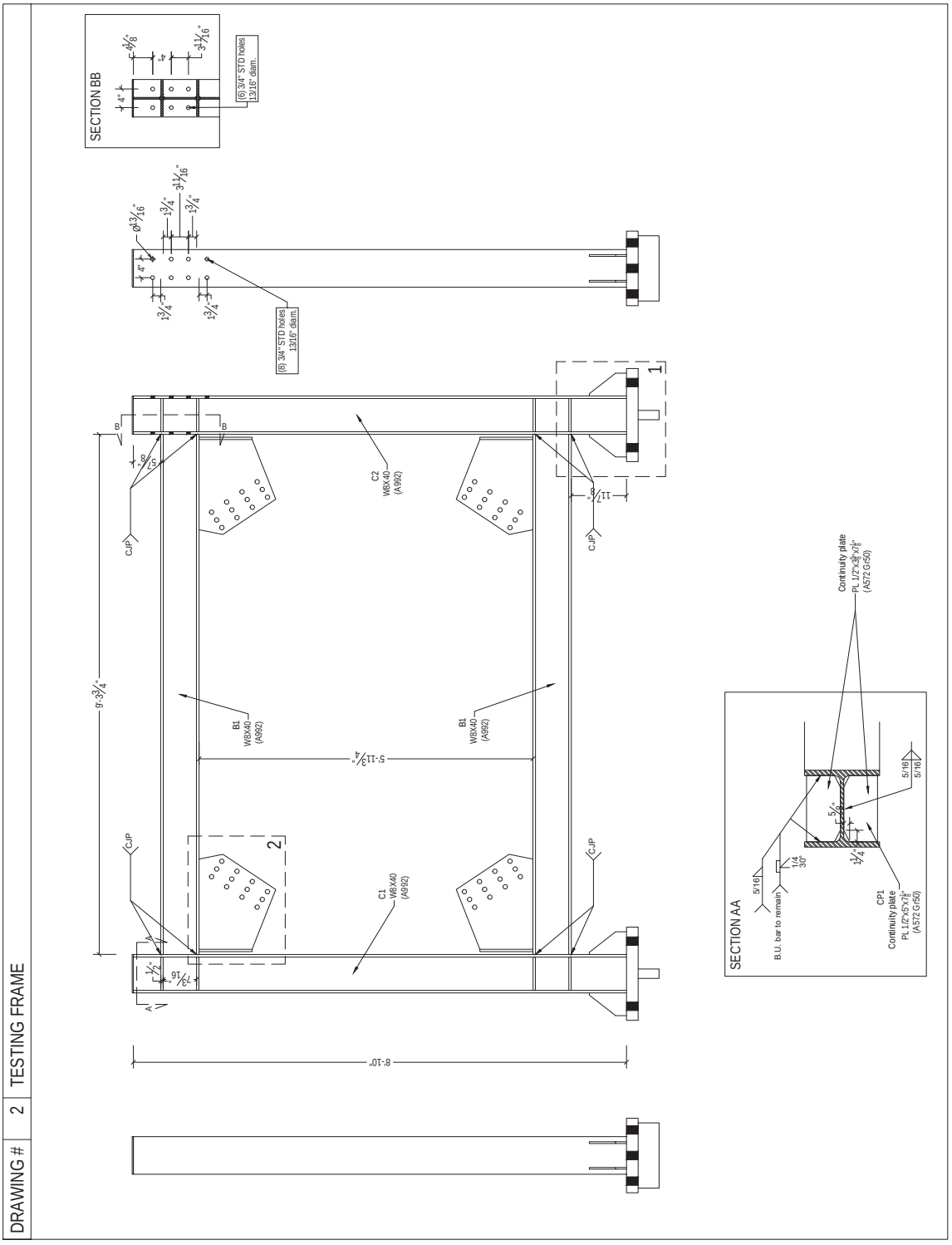

Figure A-3: Testing Frame Details

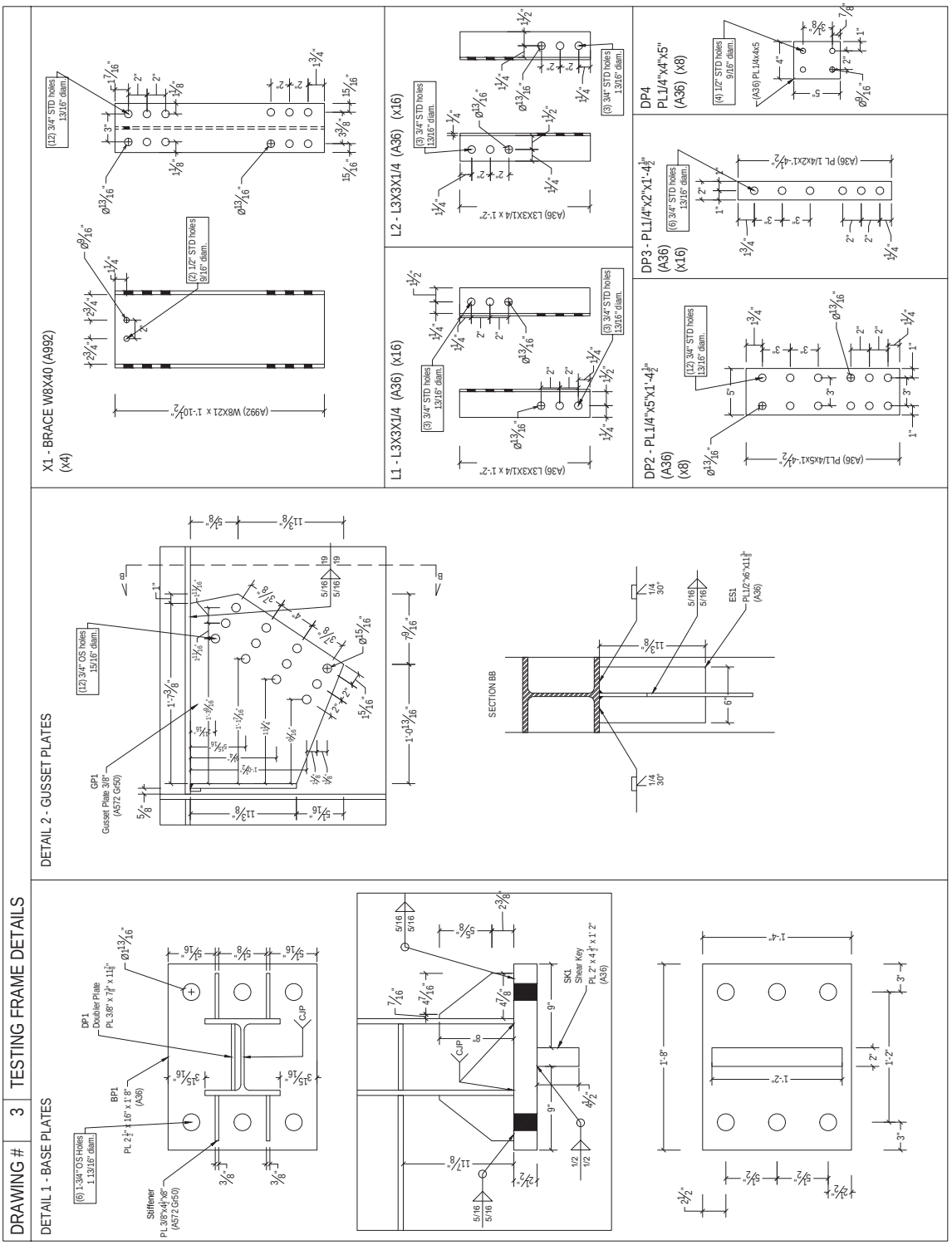

Figure A-4: Lateral Bracing

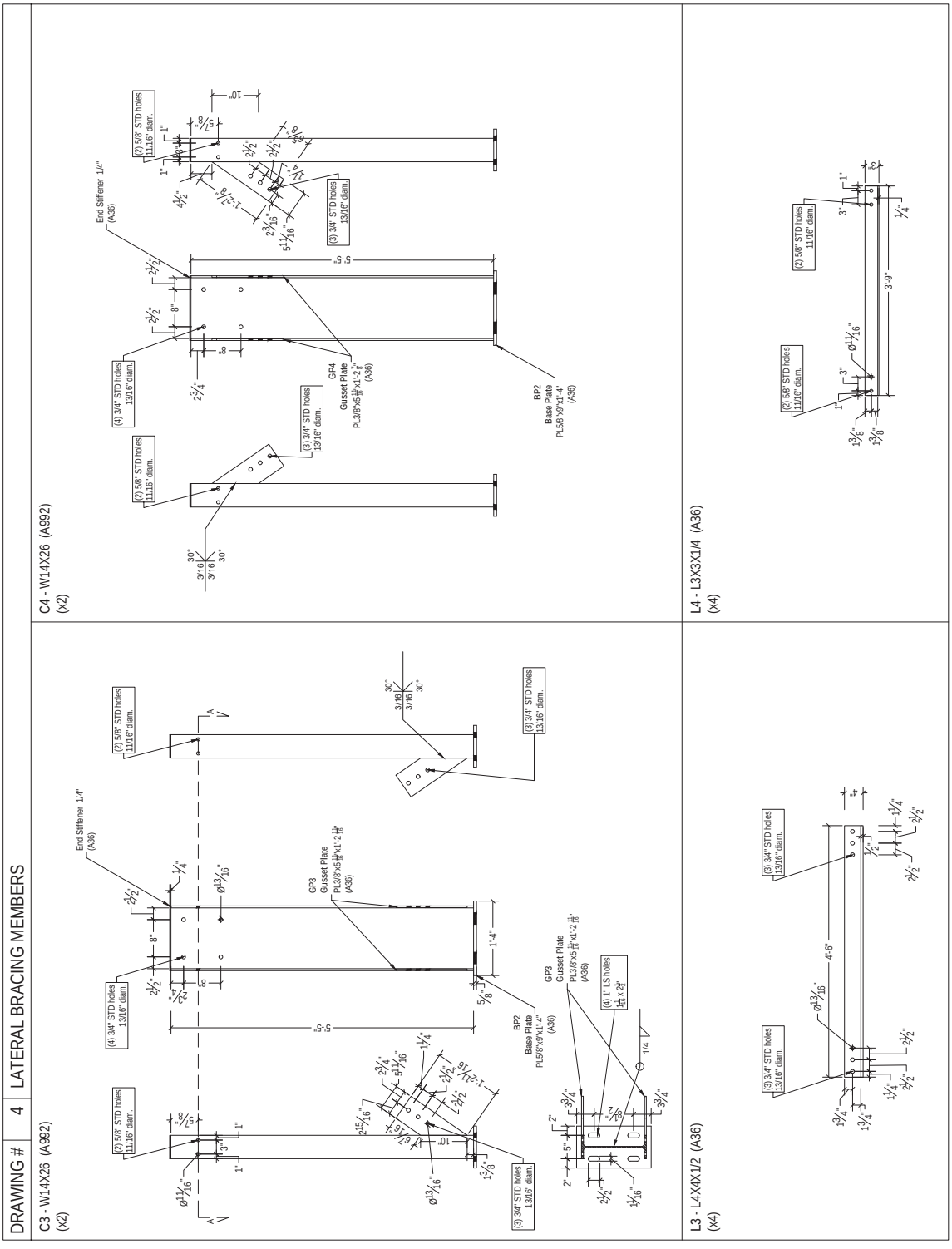

Figure A-5: Floor Beam

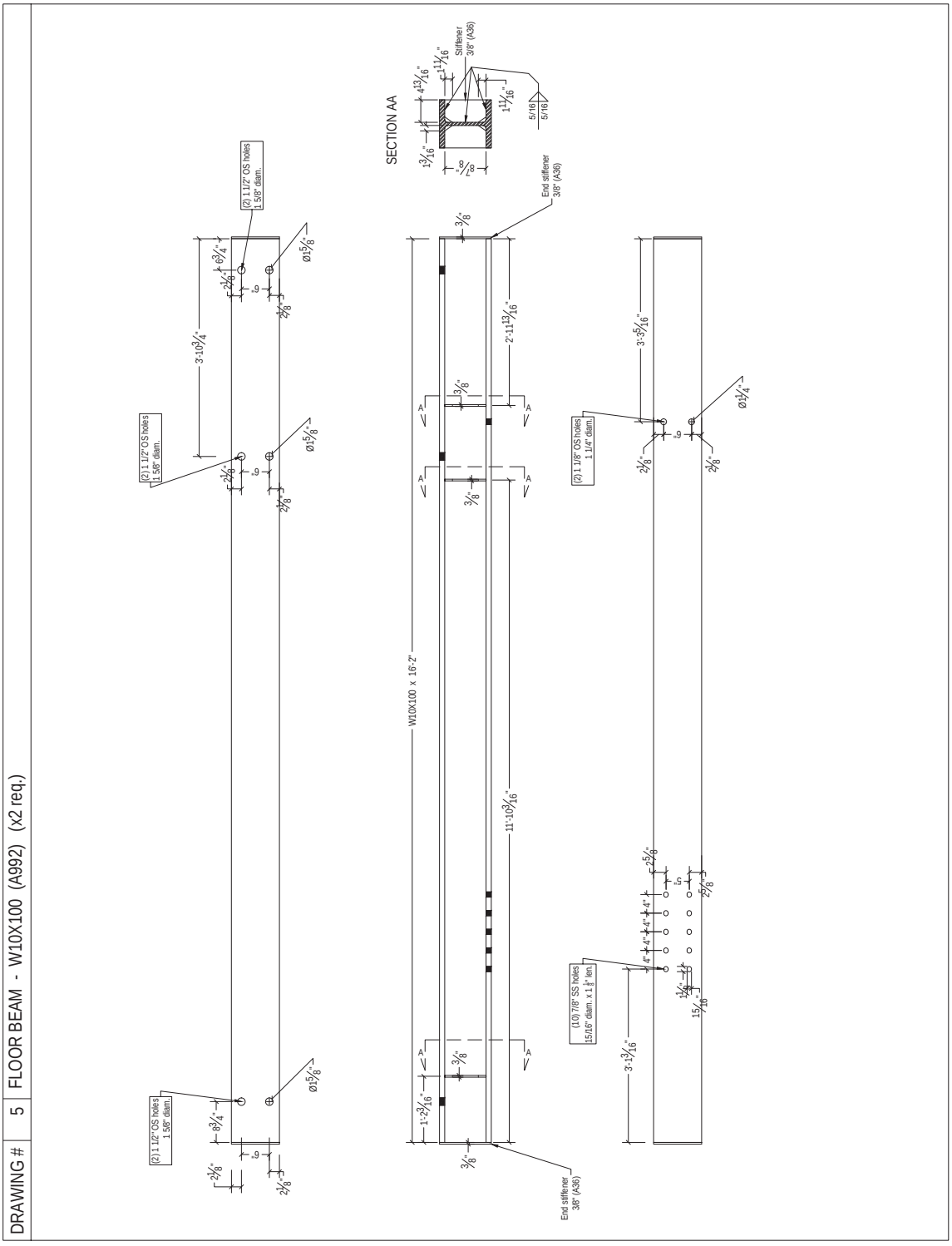

Figure A-6: Transfer Beam

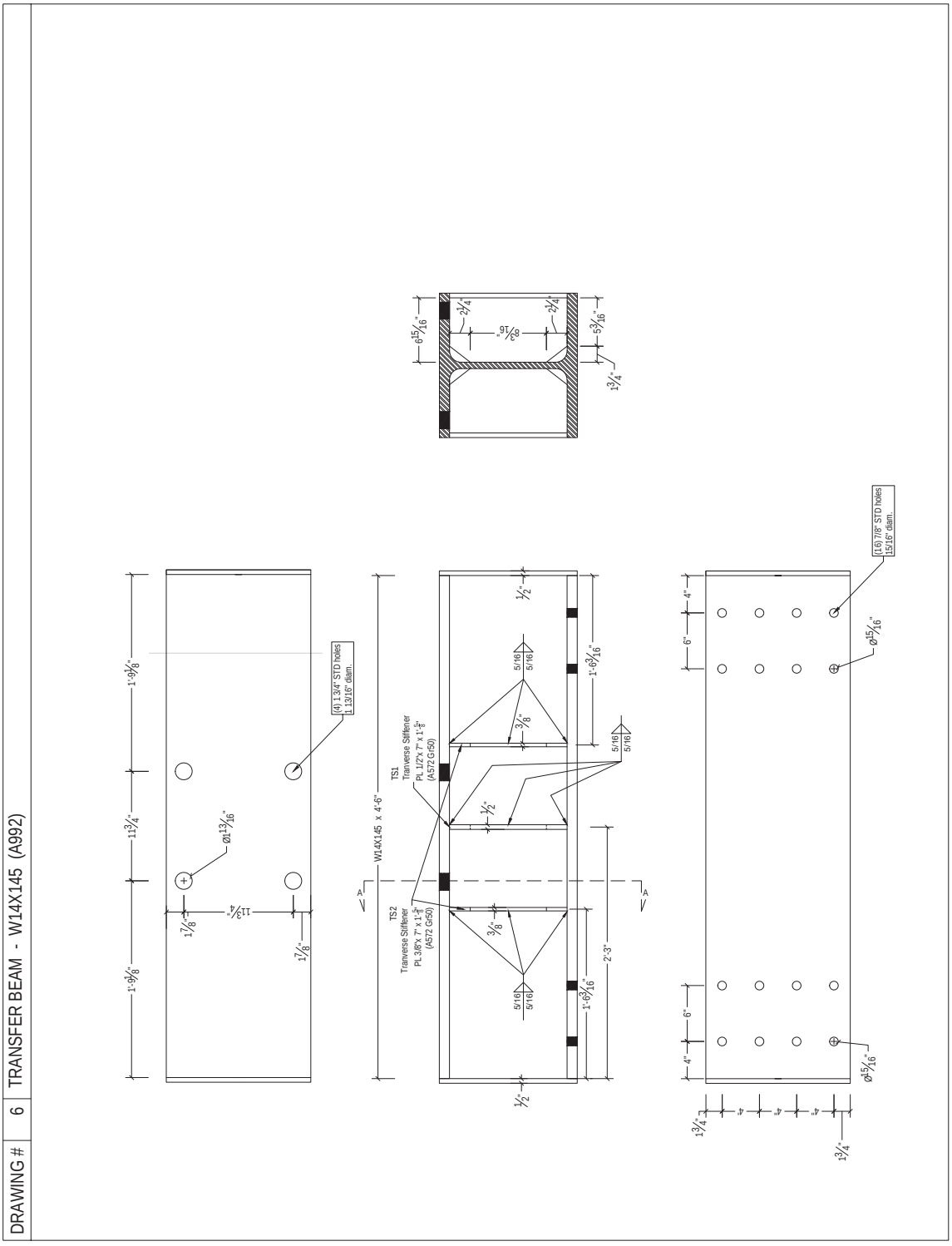

Figure A-7: Transfer Plate

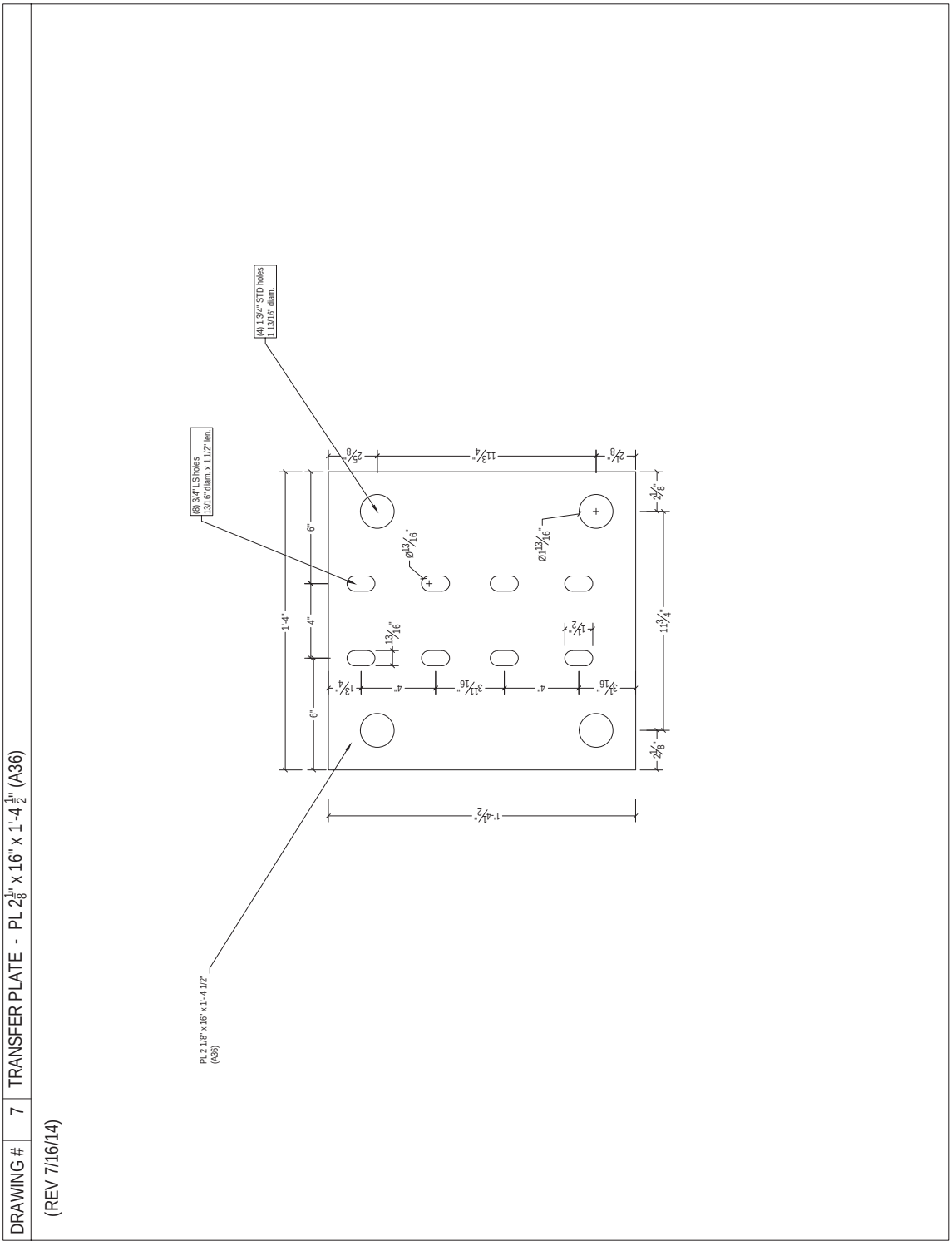

Figure A-8: Bearing Plate

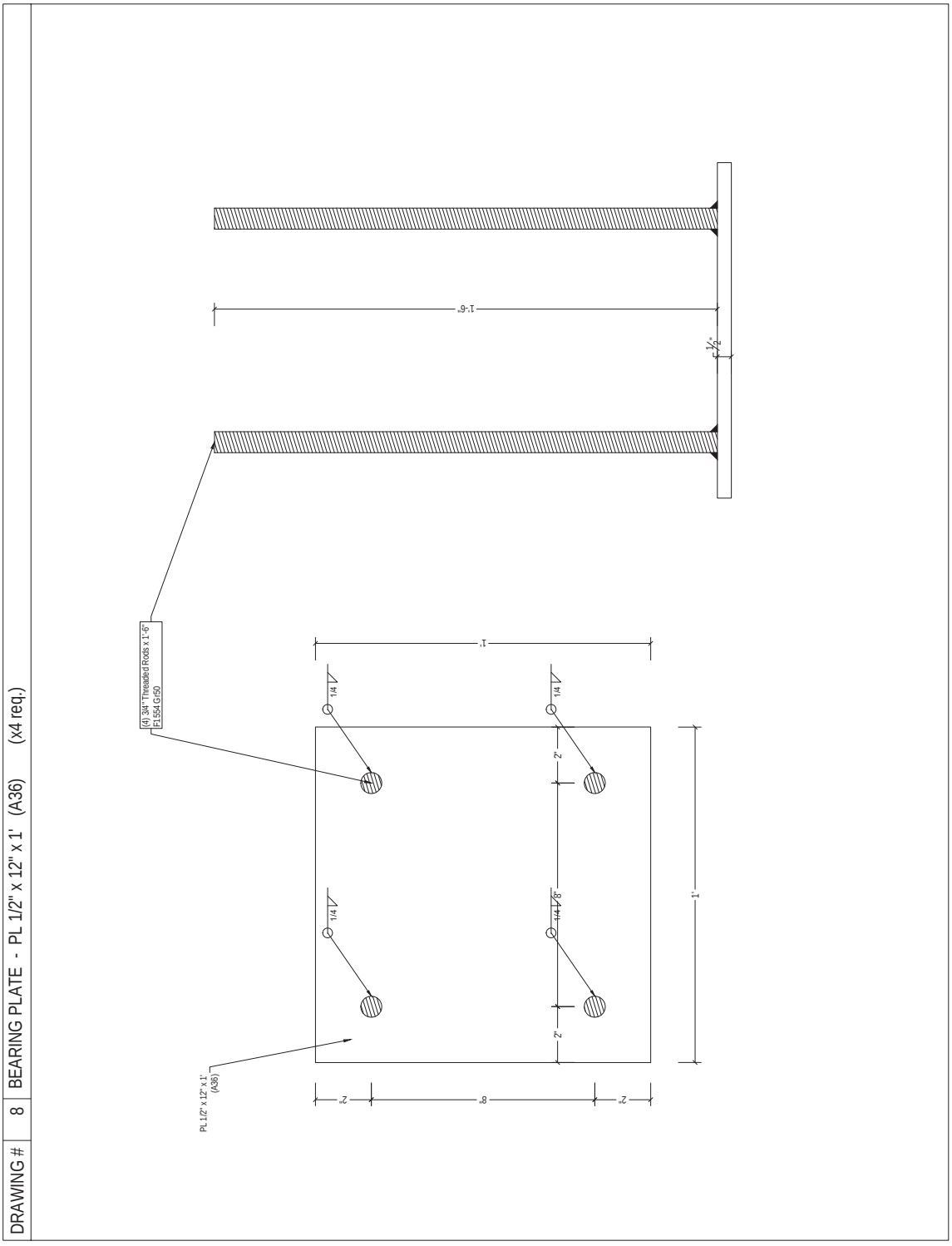

Figure A-9: Specimen BDSP20-2-00

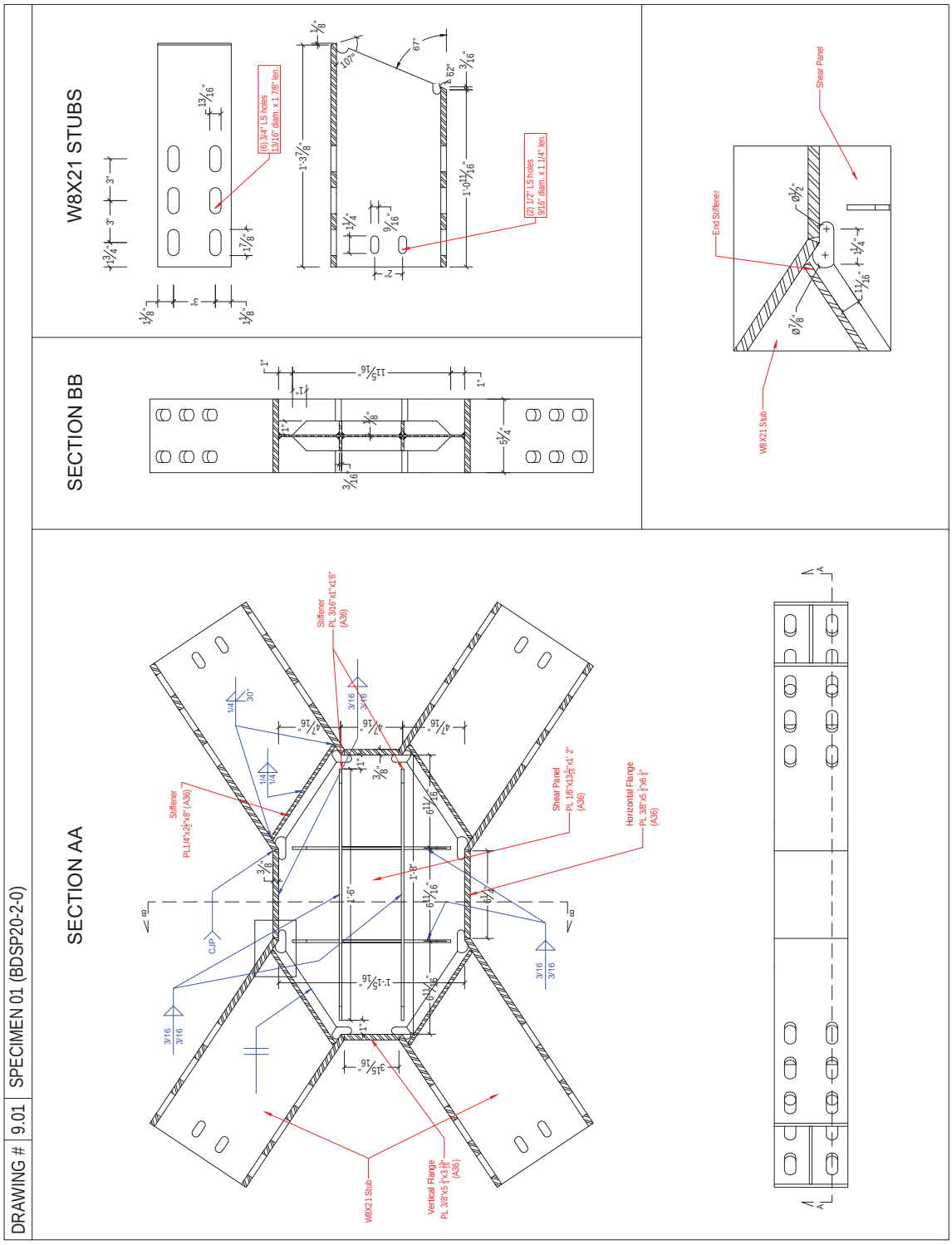

Figure A-10: Specimen BDSP20-2-25

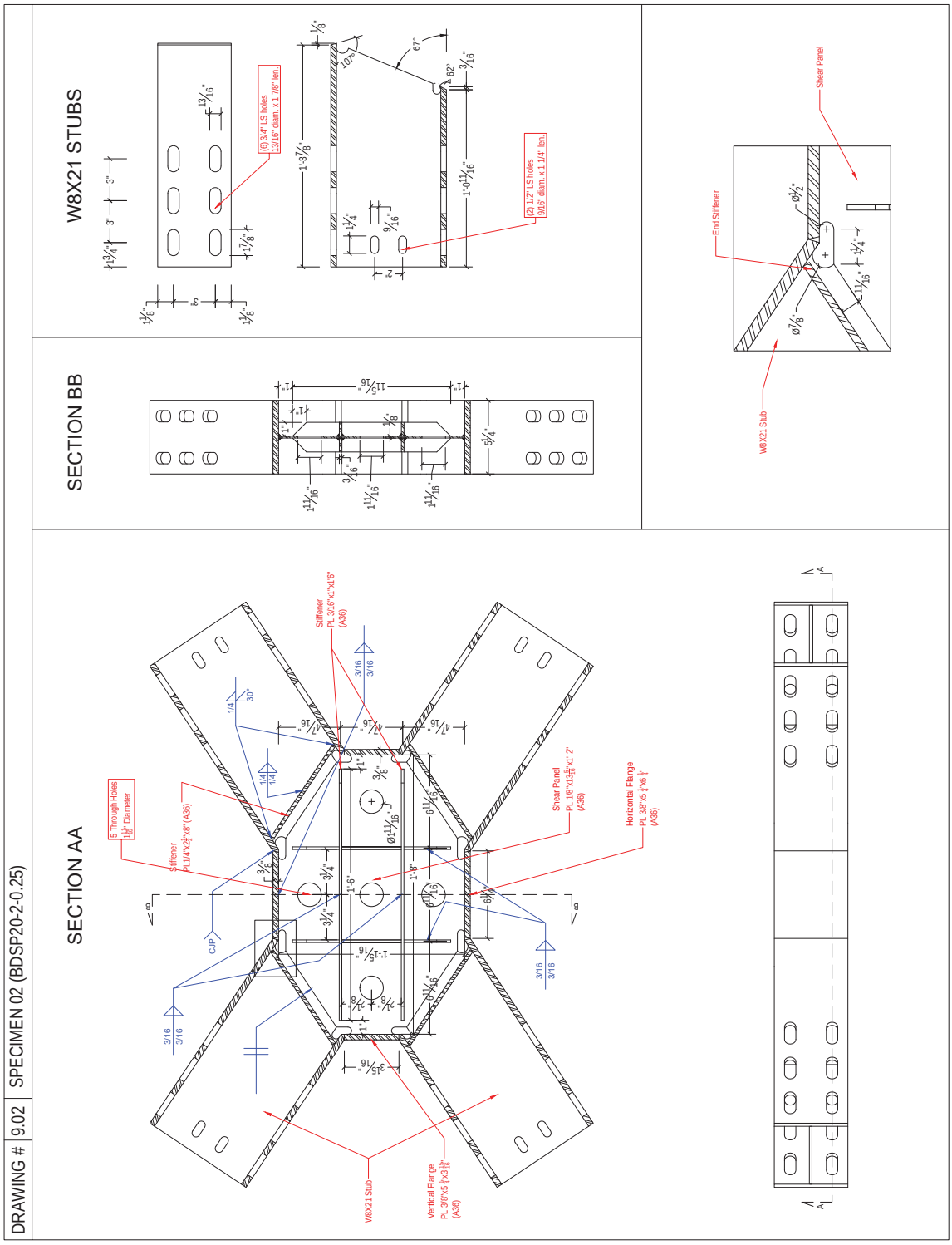

Figure A-11: Specimen BDSP20-2-40

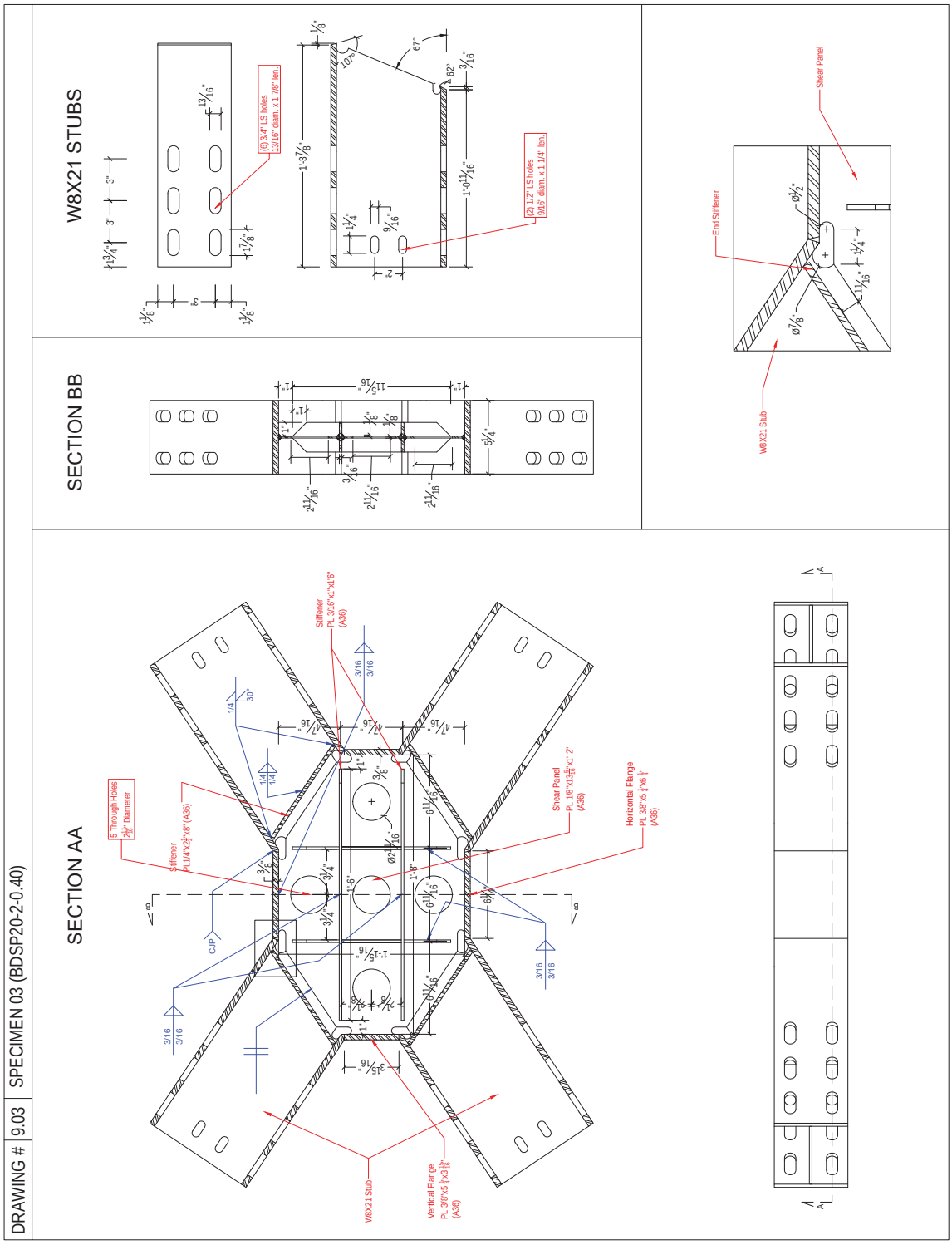

Figure A-12: Specimen BDSP20-3-25

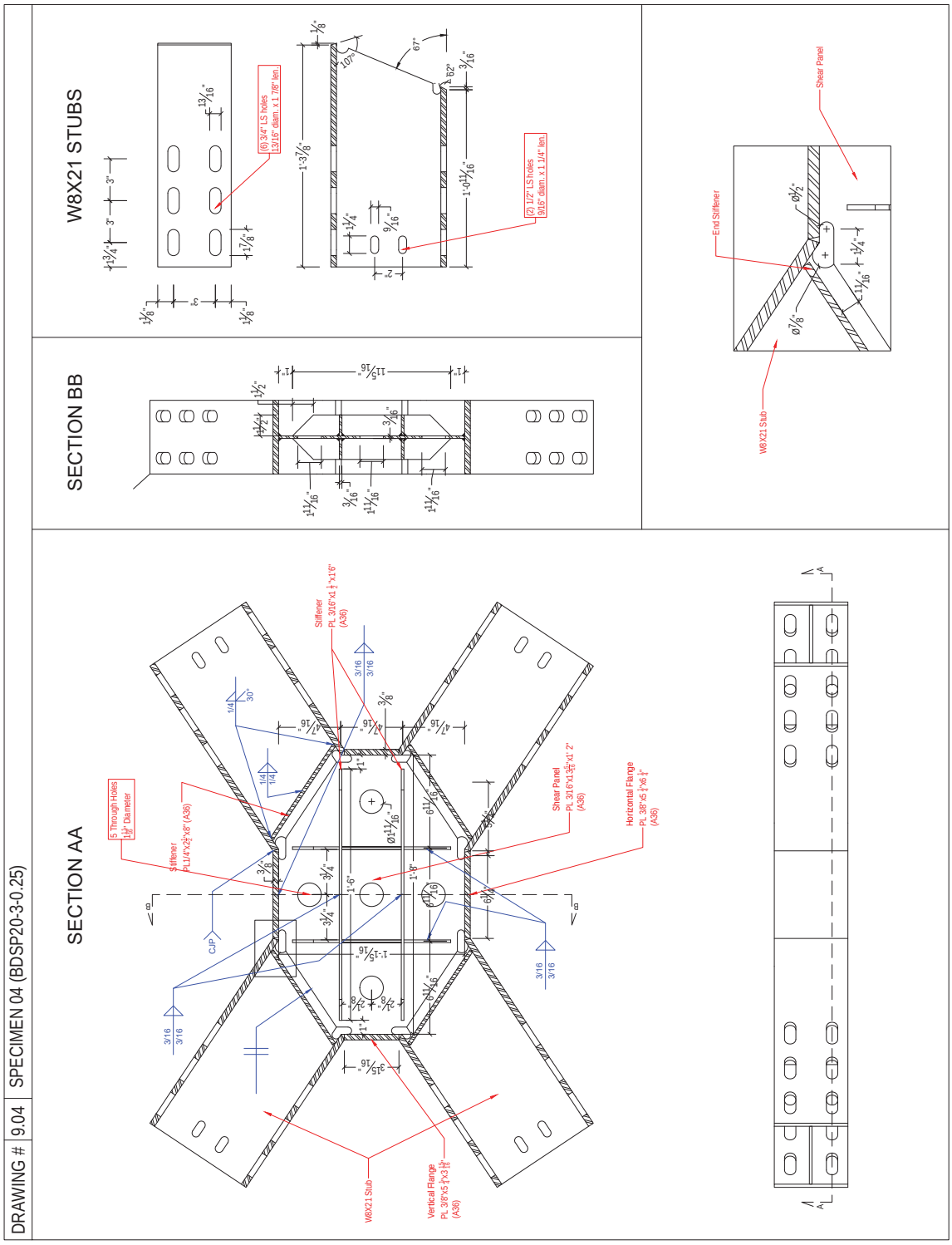

Figure A-13: Specimen BDSP20-3-40

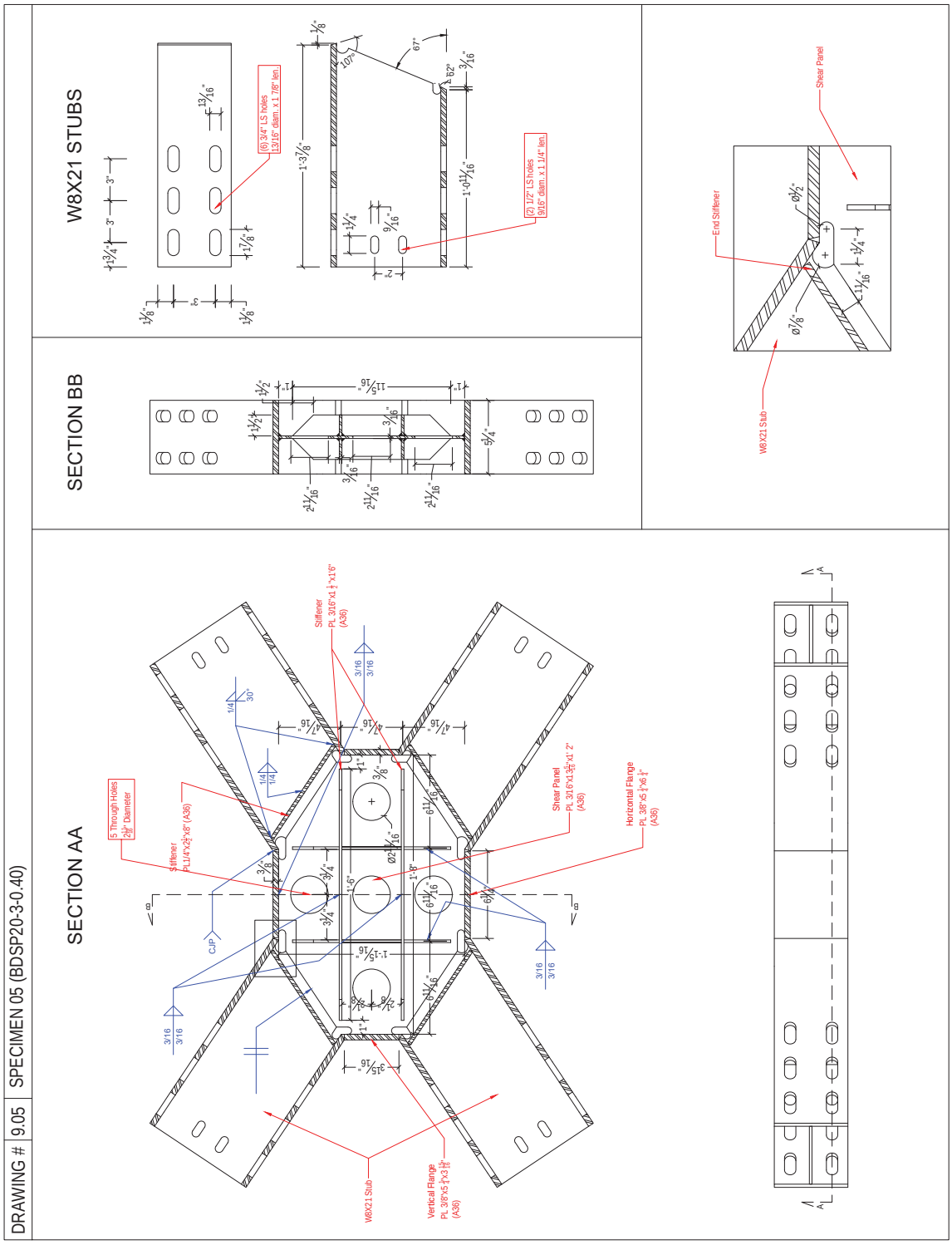

Figure A-14: Specimen BDSP20-4-40

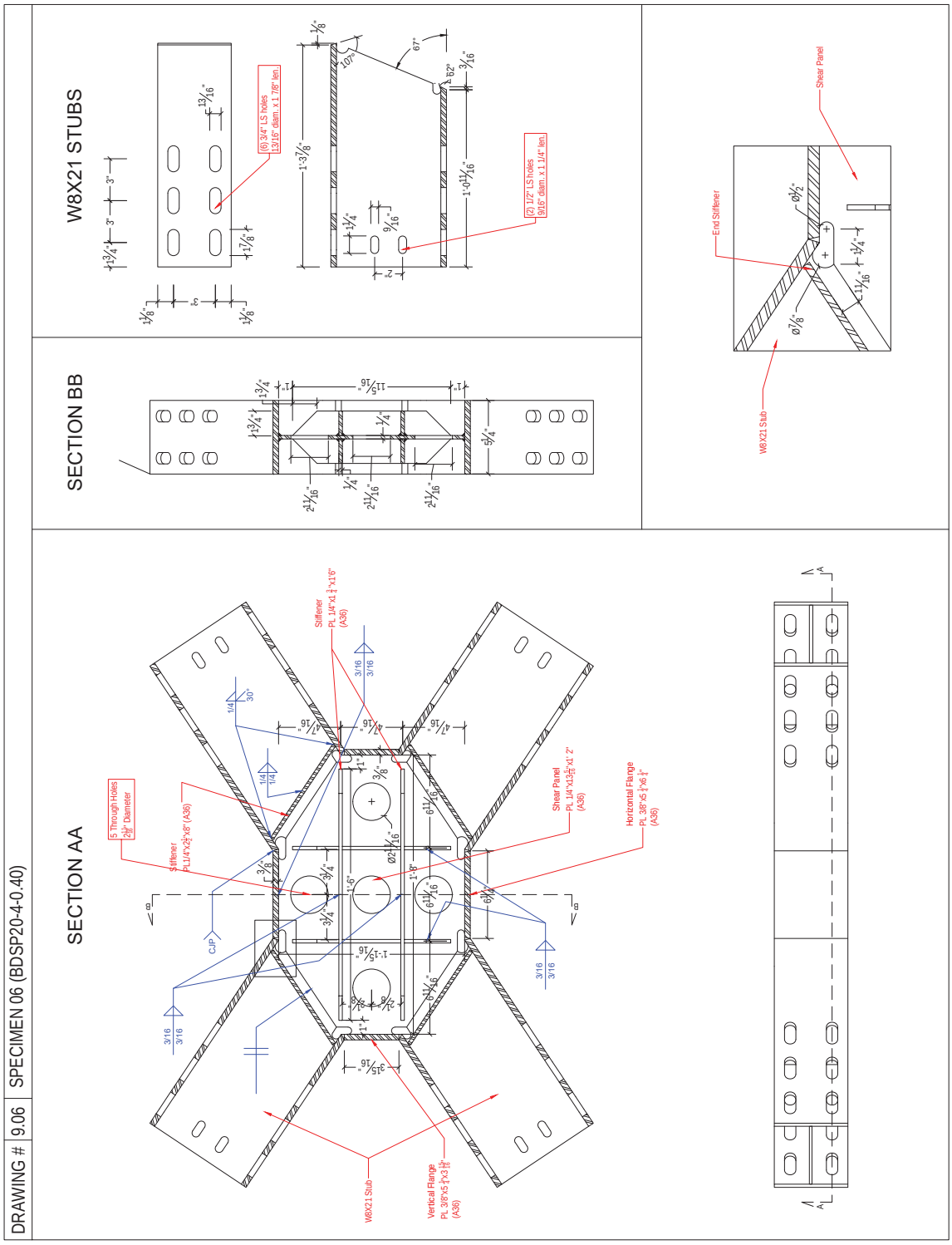

Figure A-15: Specimen BDSP24-2-00

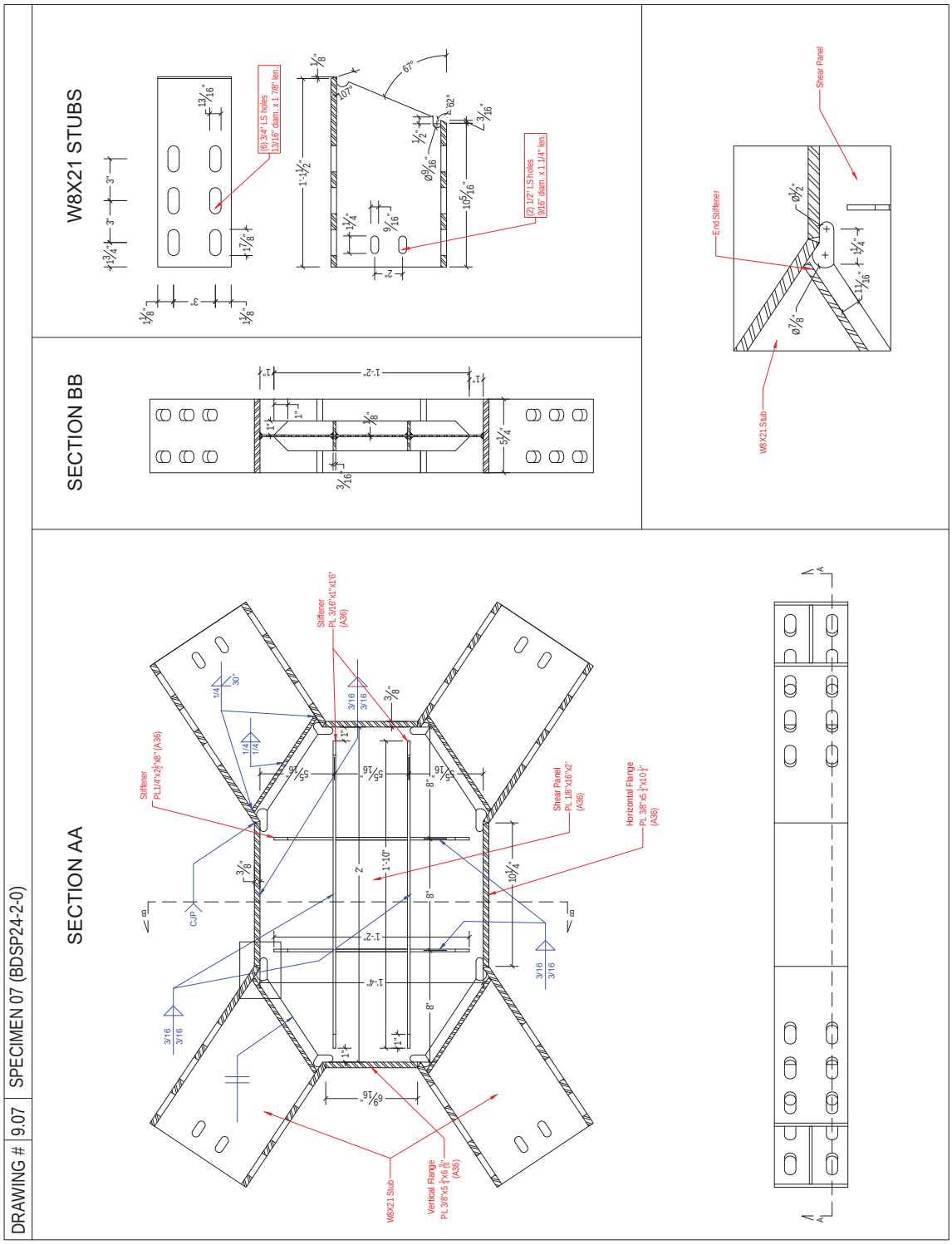

Figure A-16: Specimen BDSP24-2-25

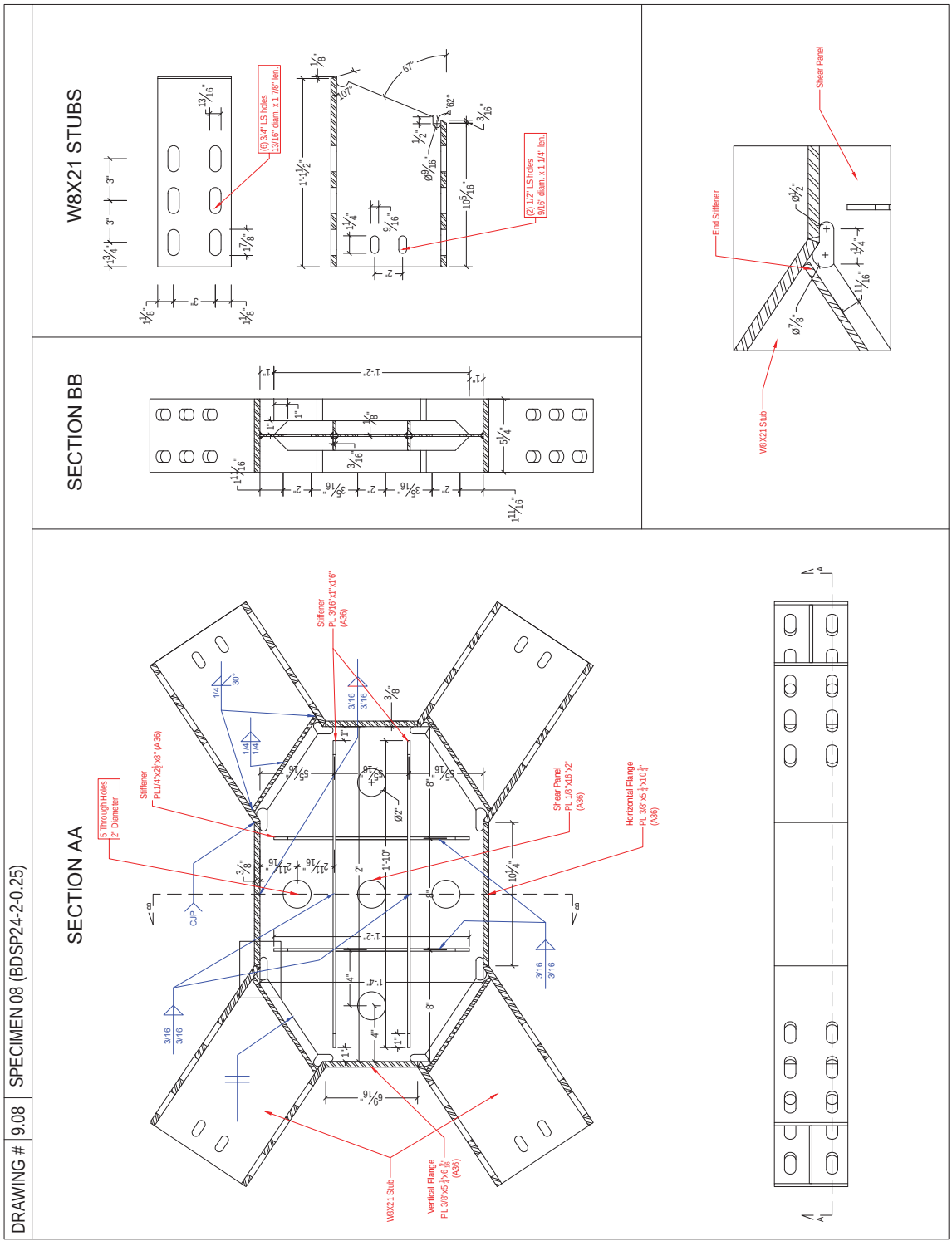

Figure A-17: Specimen BDSP24-2-40

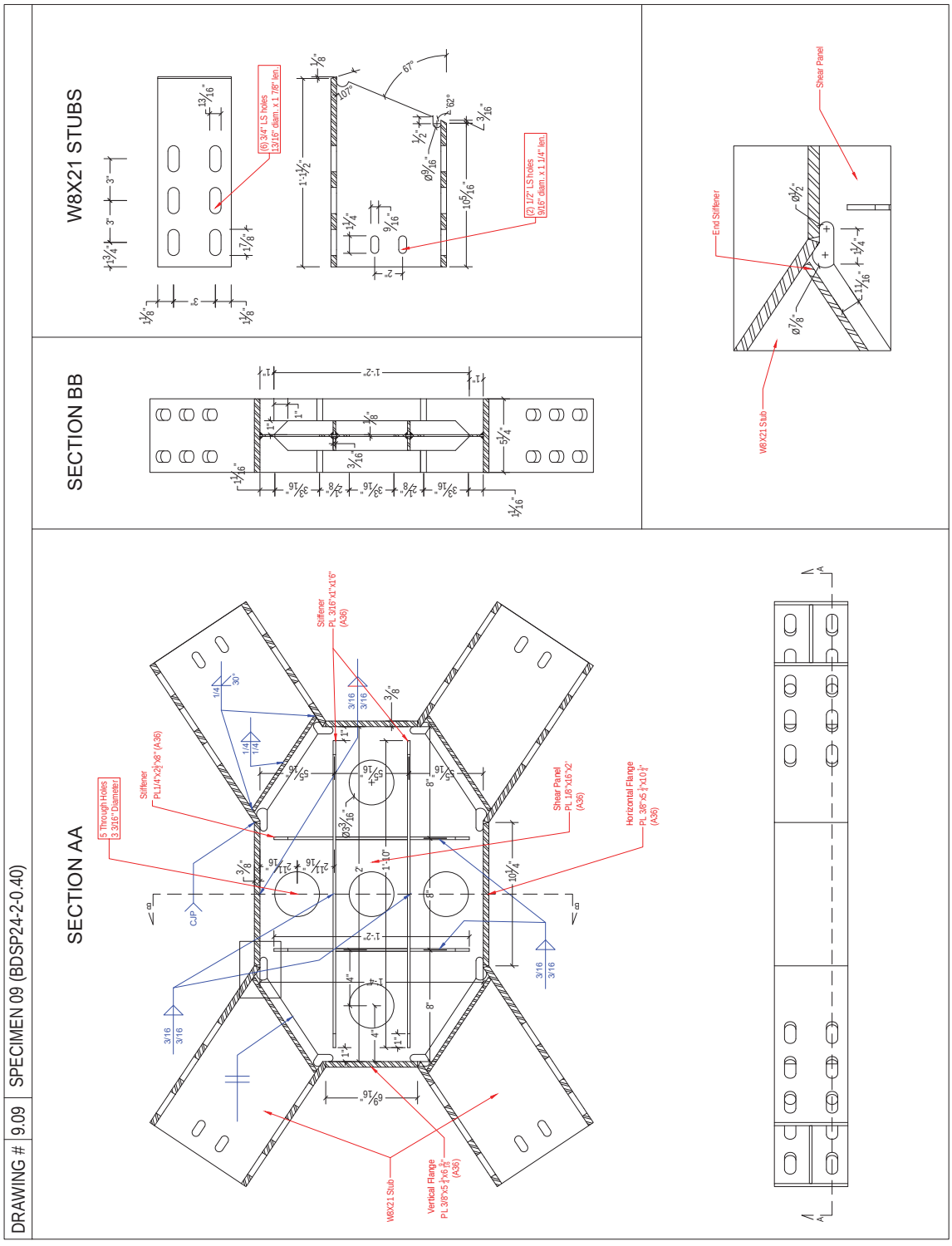

Figure A-18: Specimen BDSP24-3-40

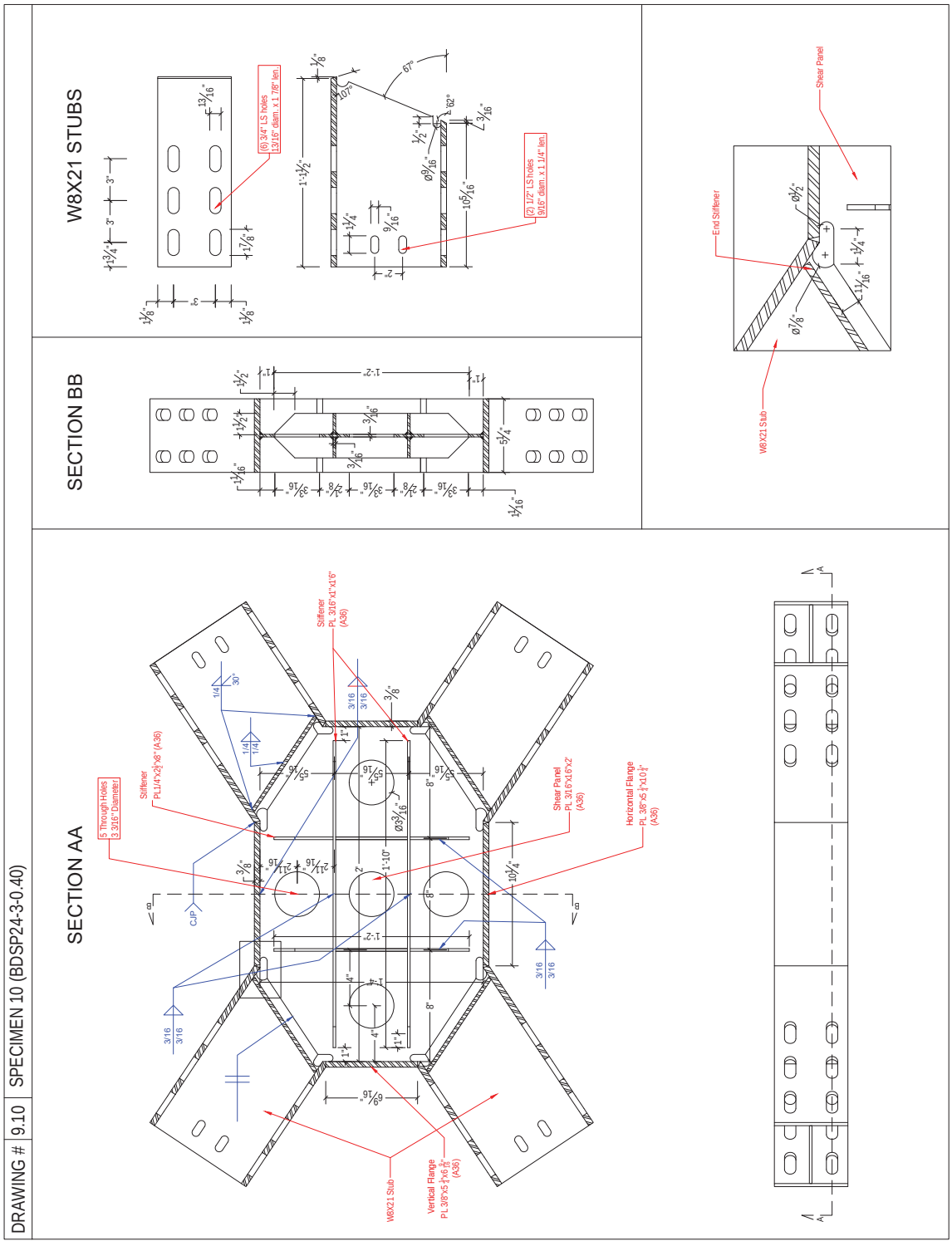

Figure A-19: Strong floor plate

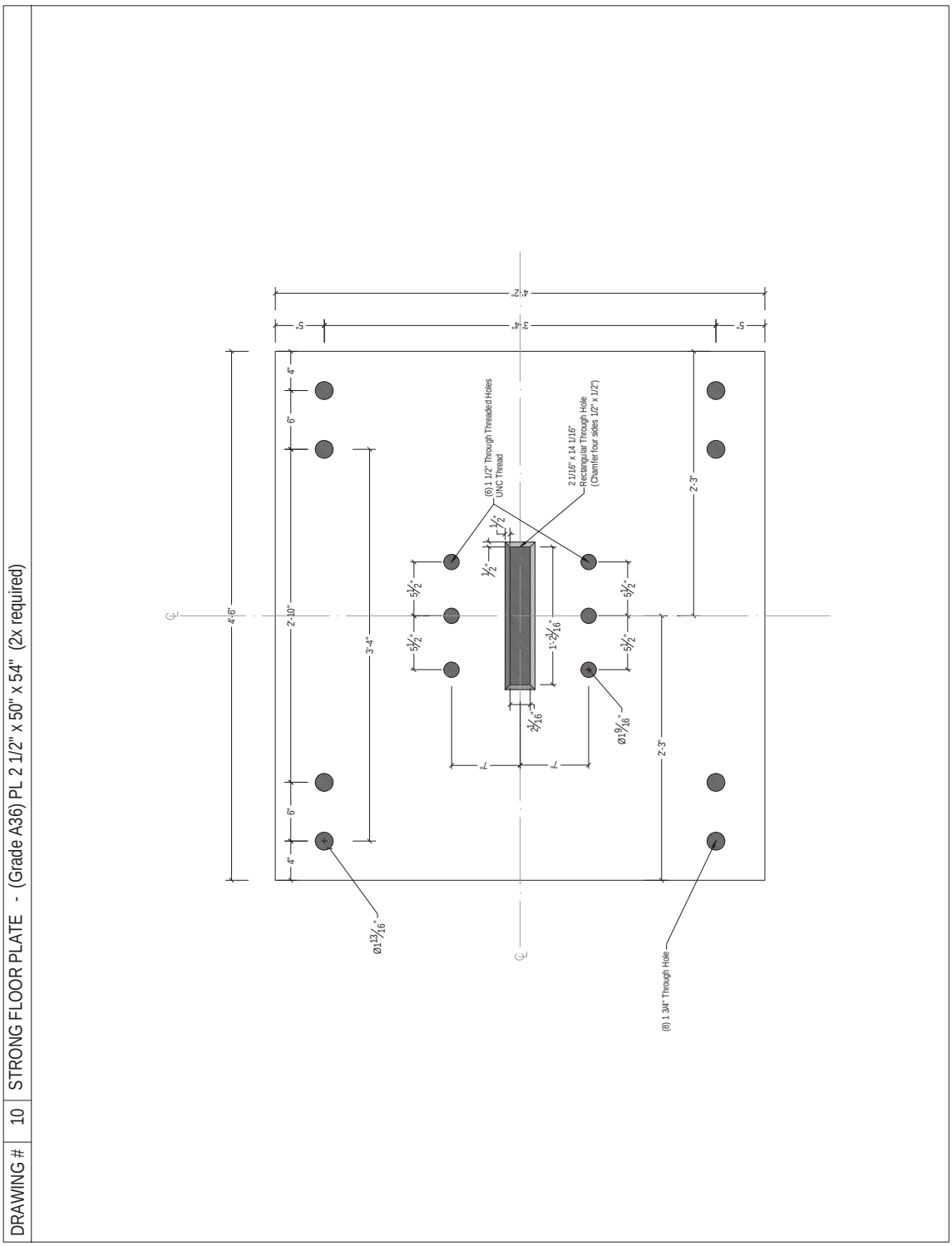

Figure A-20: Shop Drawings - Testing frame

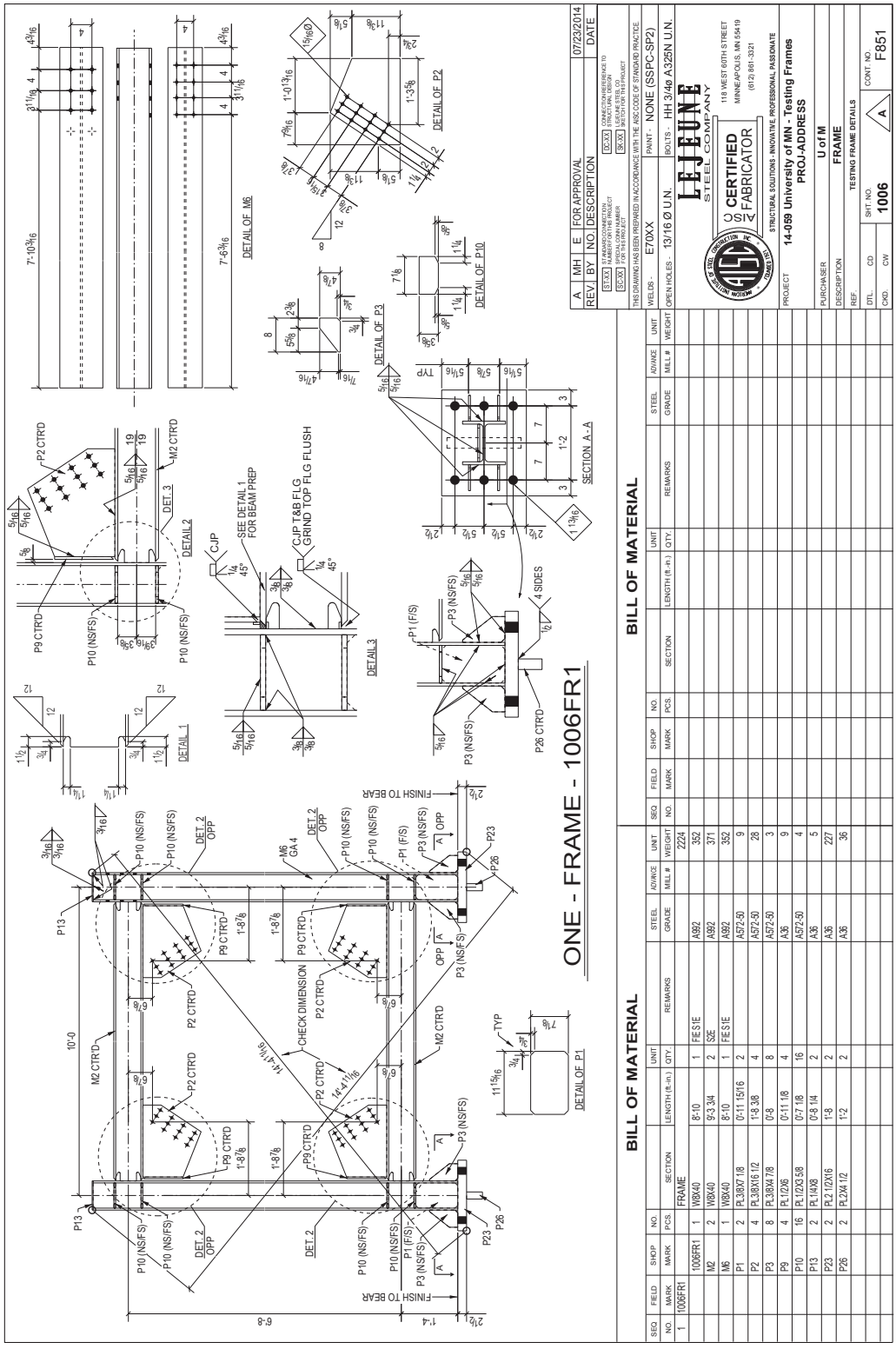

Figure A-21: Shop Drawings - Braces

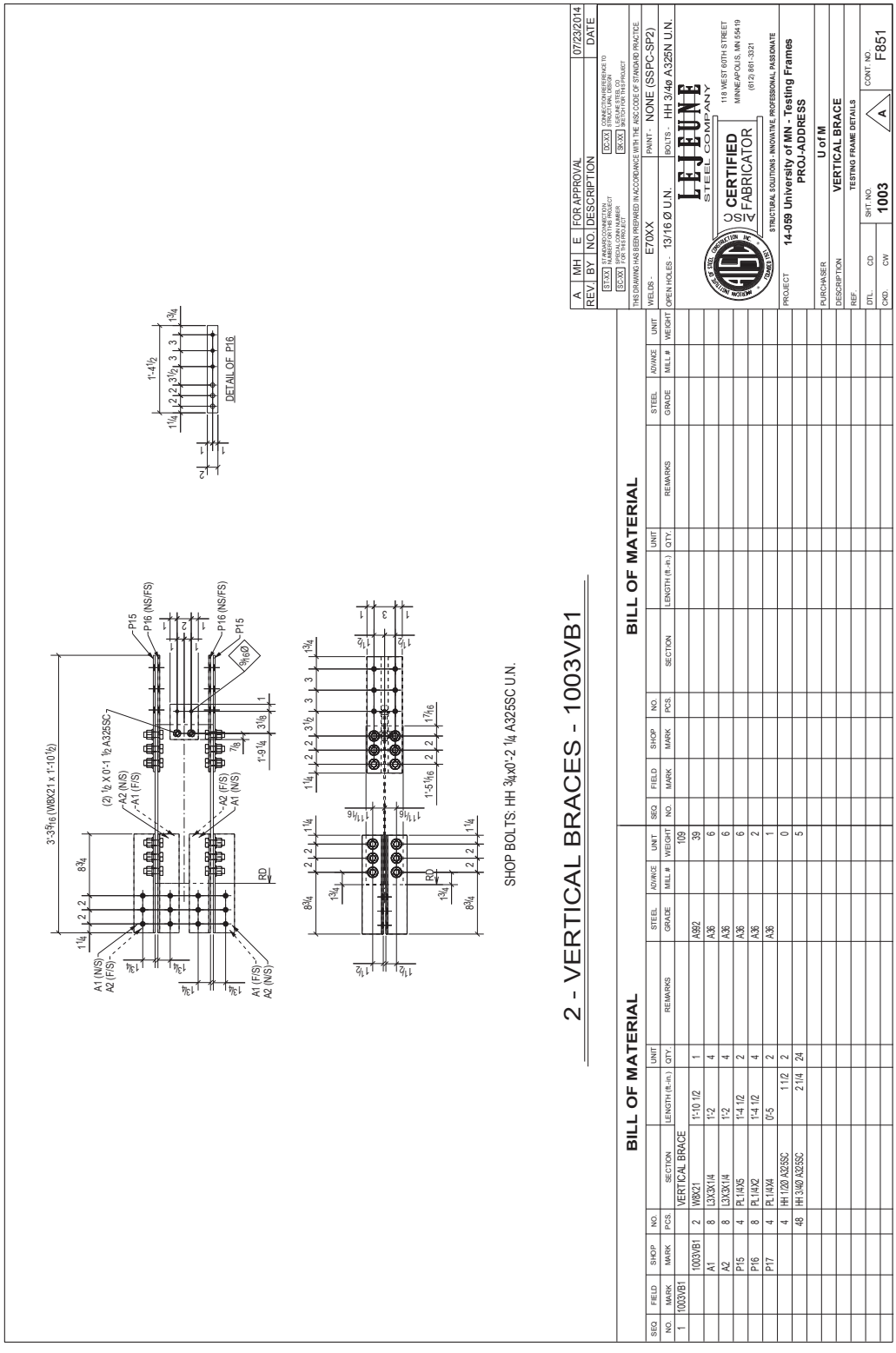

Figure A-22: Shop Drawings – Specimen BDSP20-2-40 (1/2)

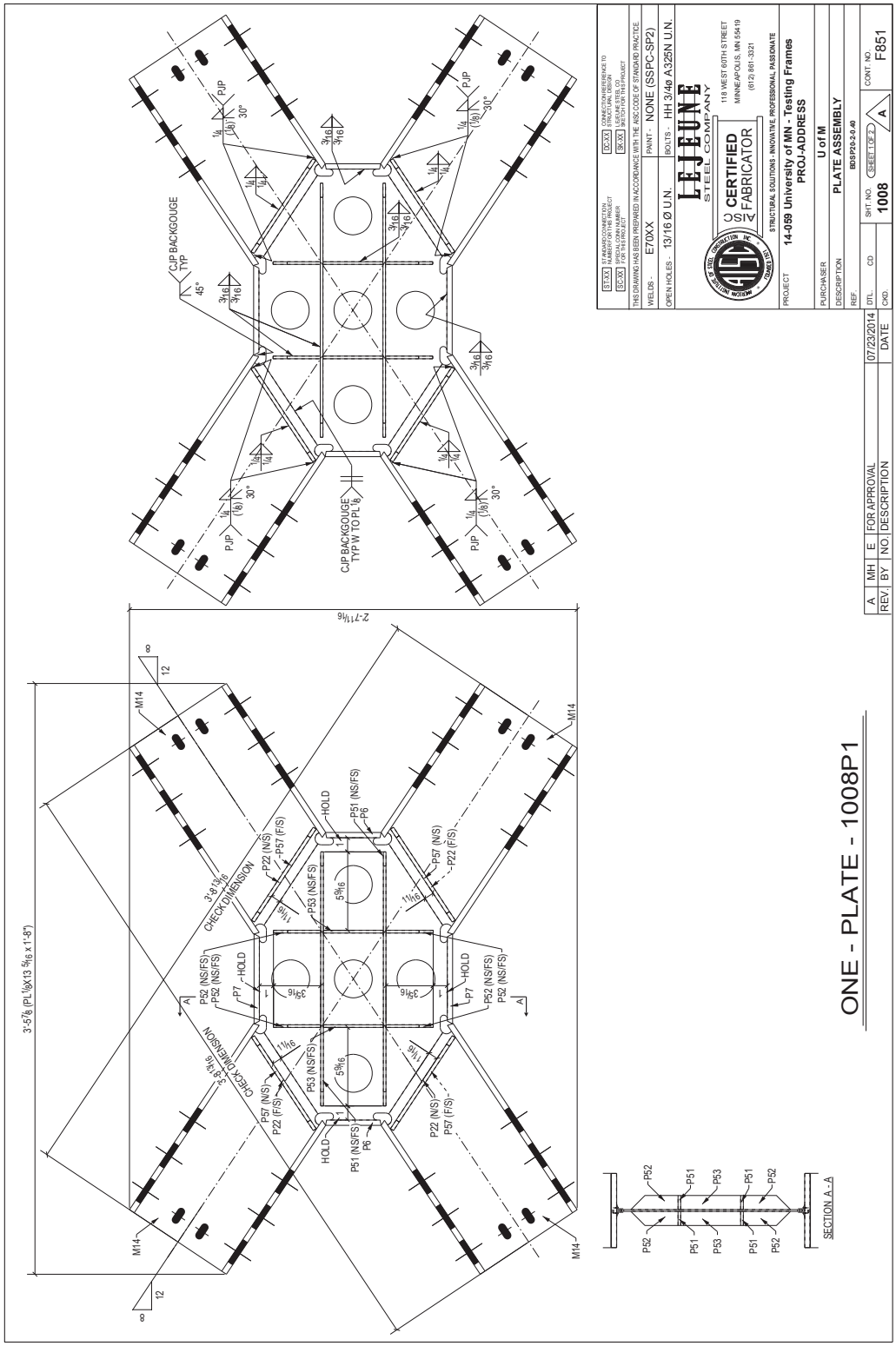

Figure A-23: Shop Drawings – Specimen BDSP20-2-40 (2/2)

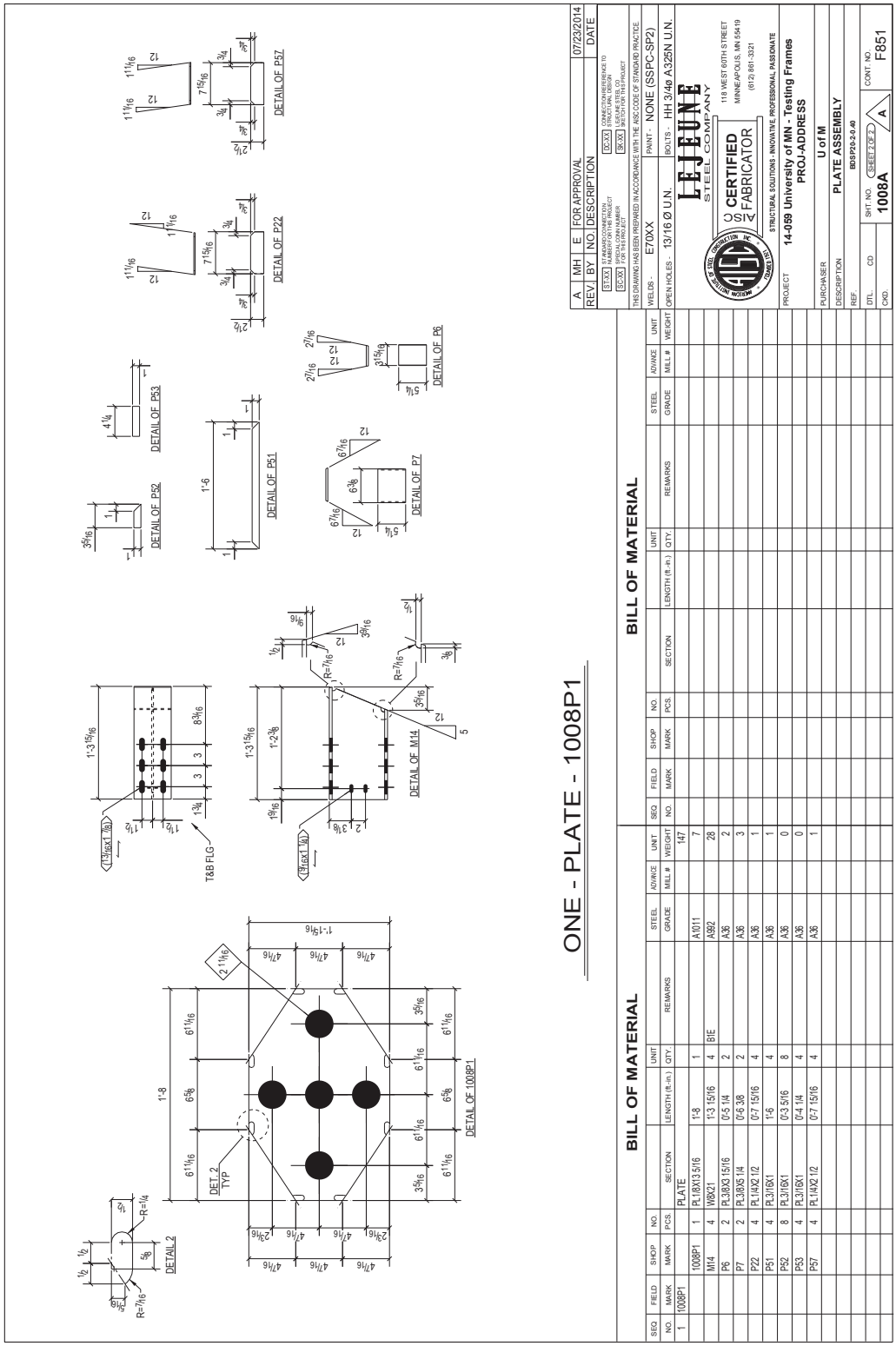

Figure A-24: Shop Drawings – Specimen BDSP24-2-40 (1/2)

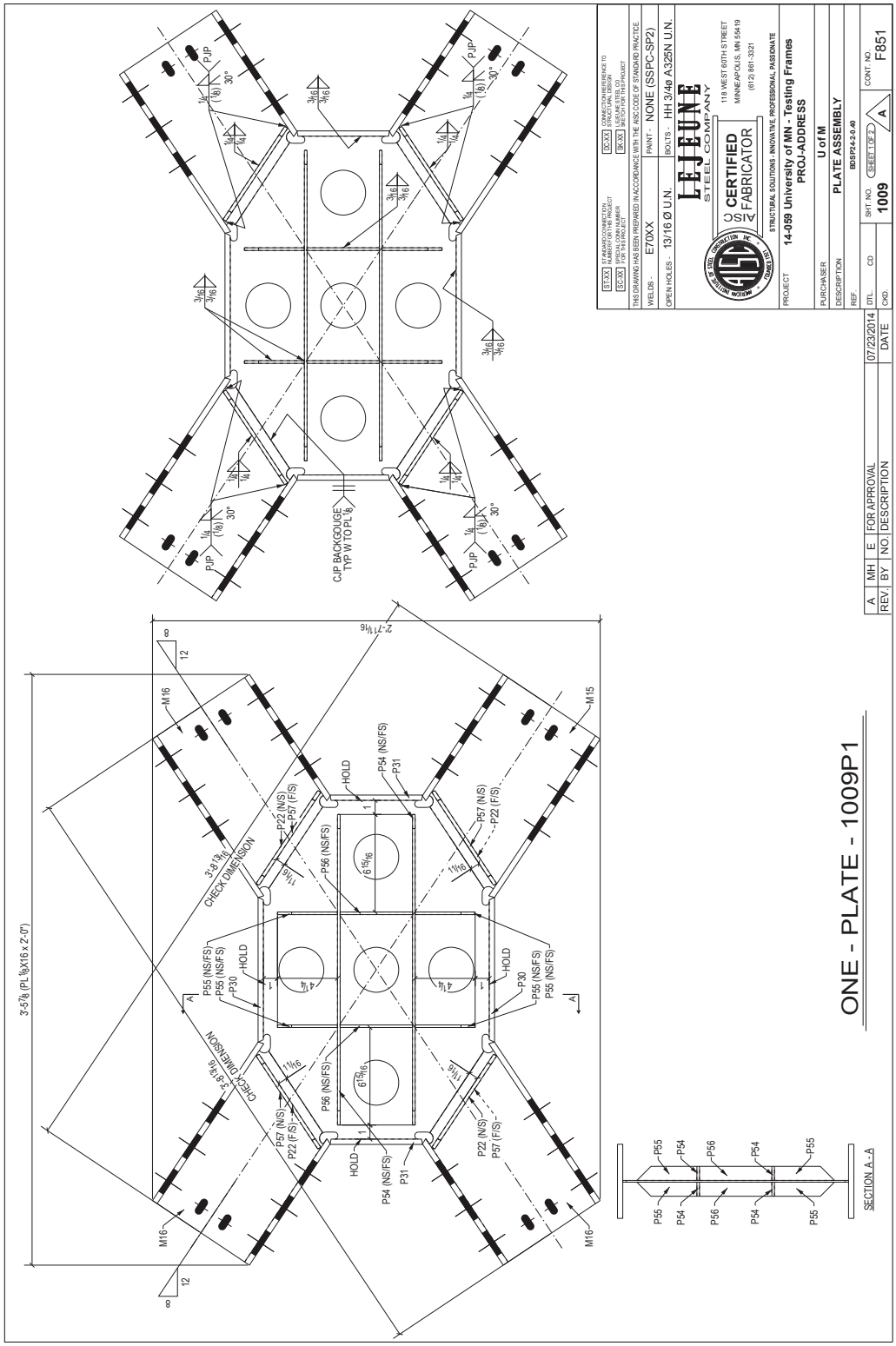

Figure A-25: Shop Drawings – Specimen BDSP24-2-40 (2/2)

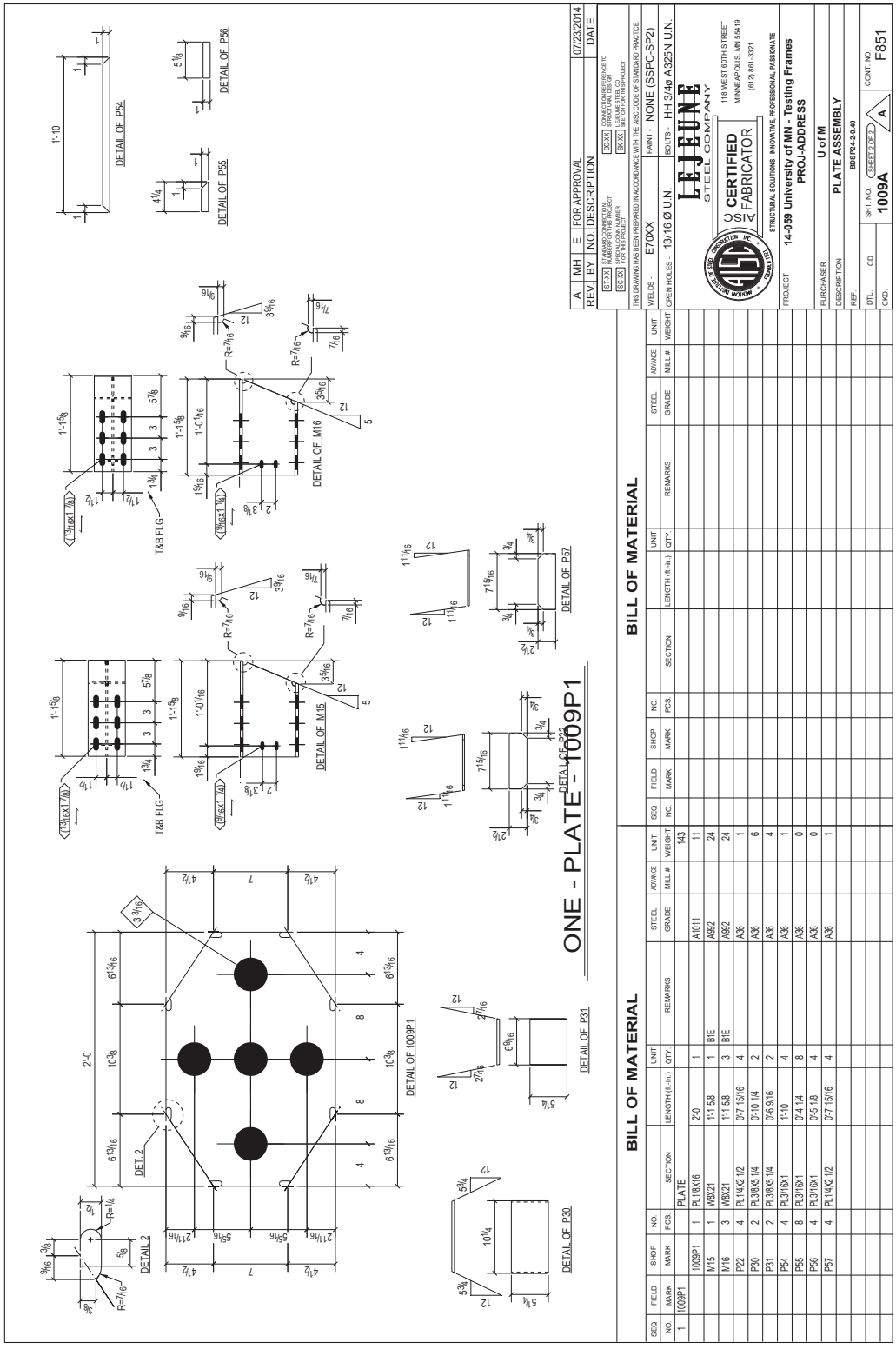

Figure A-26: Shop Drawings – Specimen BDSP20-2-25 (1/2)

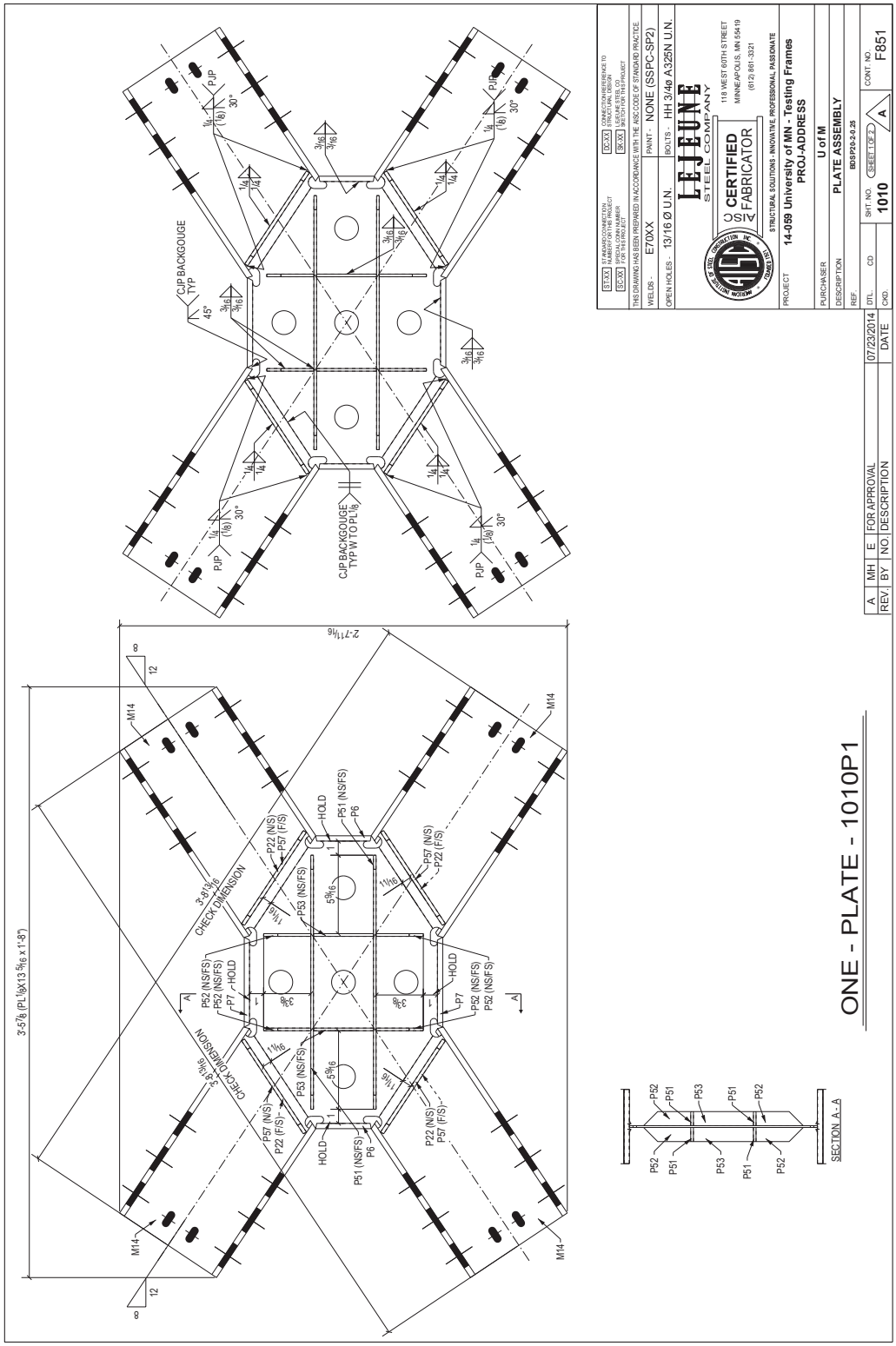

Figure A-27: Shop Drawings – Specimen BDSP20-2-25 (2/2)

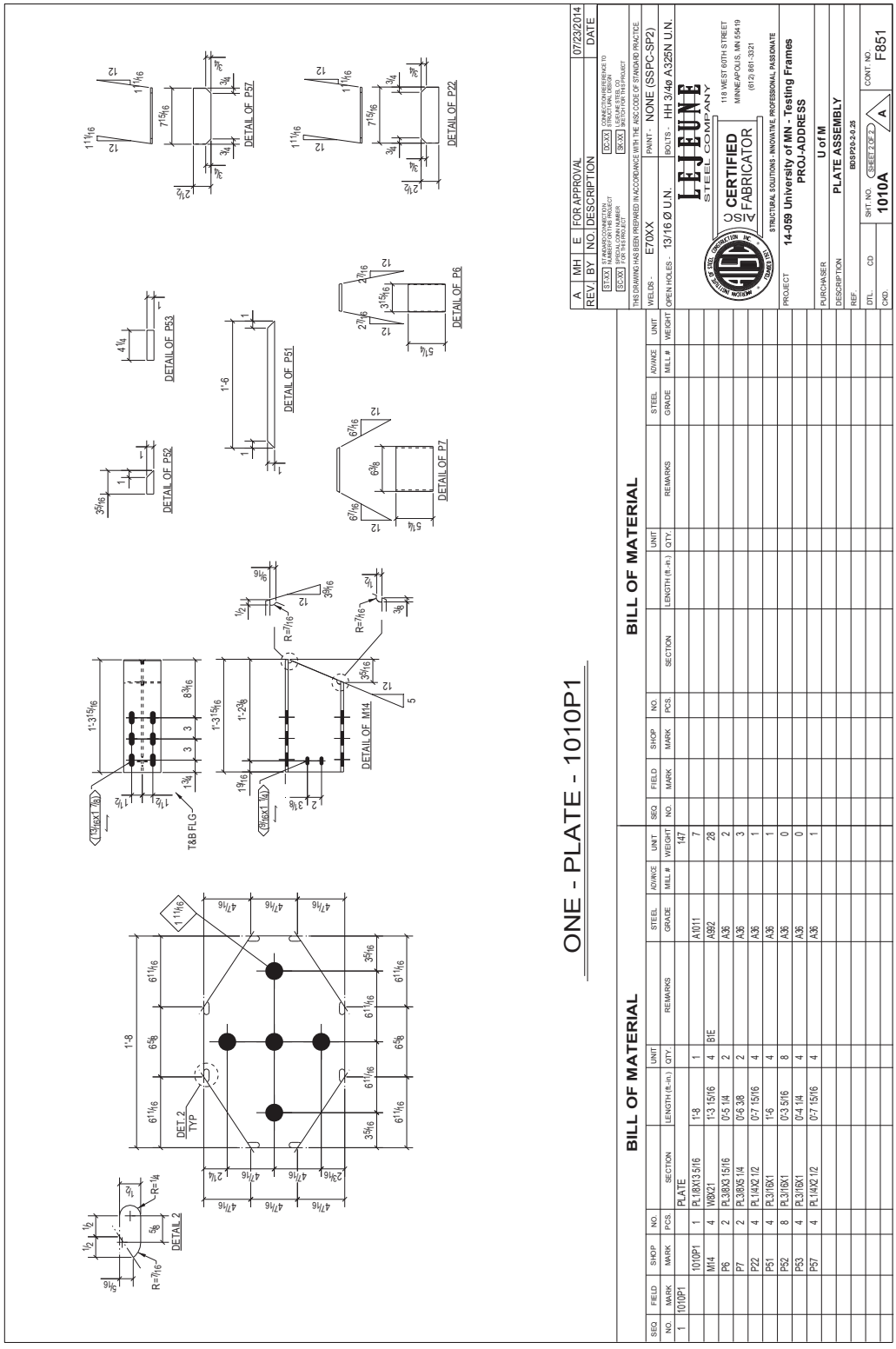

Figure A-28: Shop Drawings – Specimen BDSP20-3-40 (1/2)

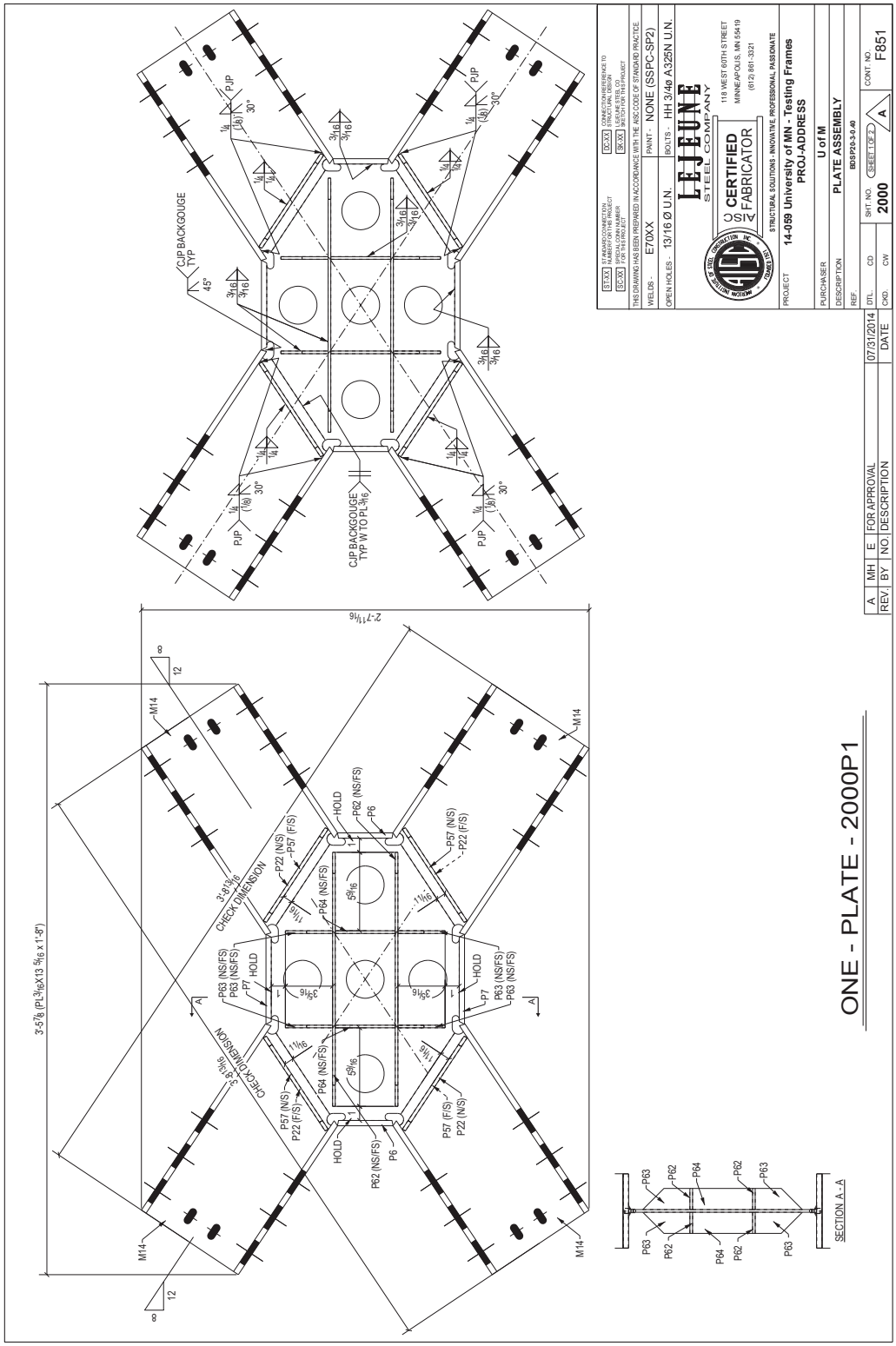

Figure A-29: Shop Drawings – Specimen BDSP20-3-40 (2/2)

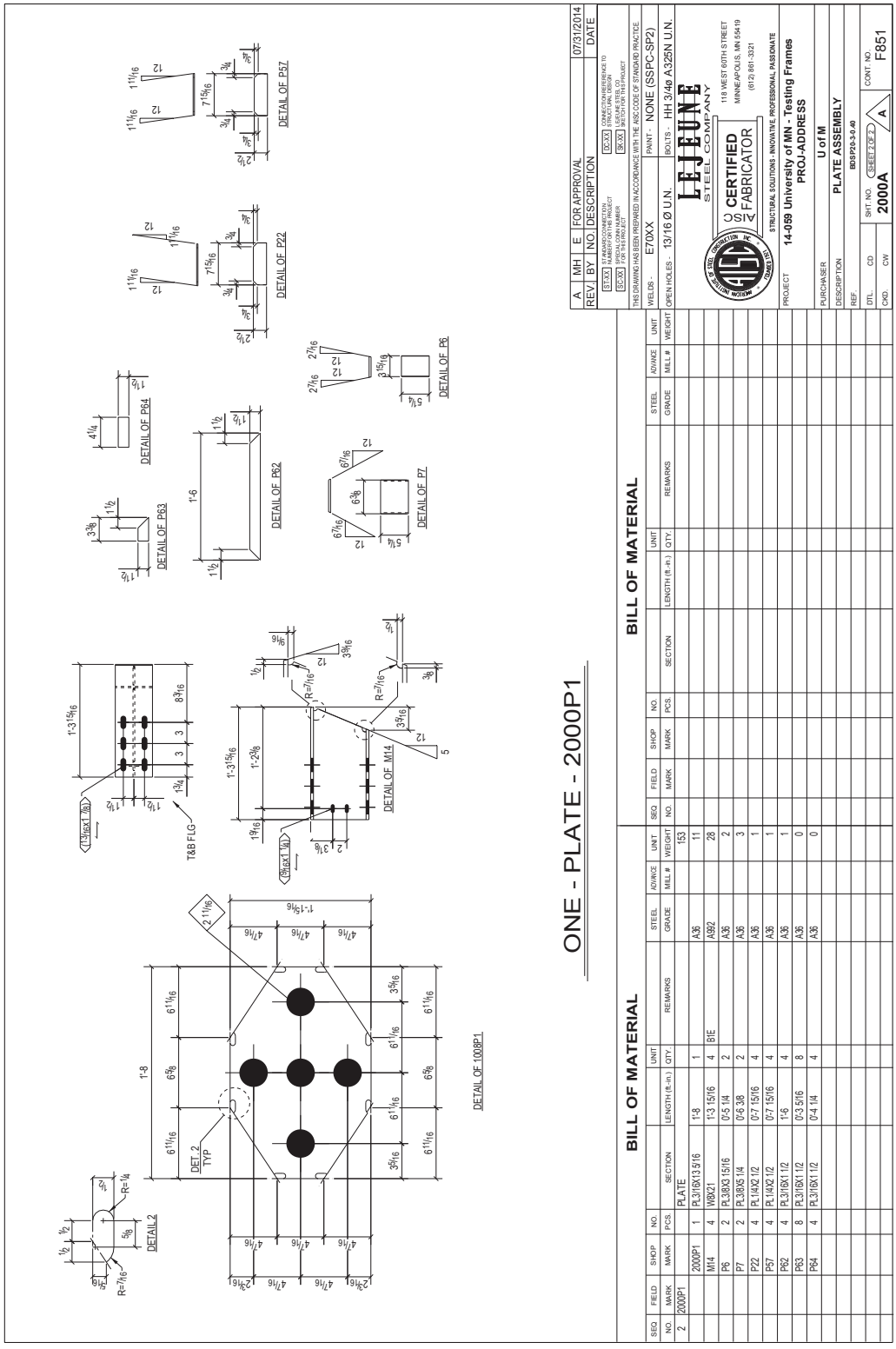

Figure A-30: Shop Drawings – Specimen BDSP24-2-25 (1/2)

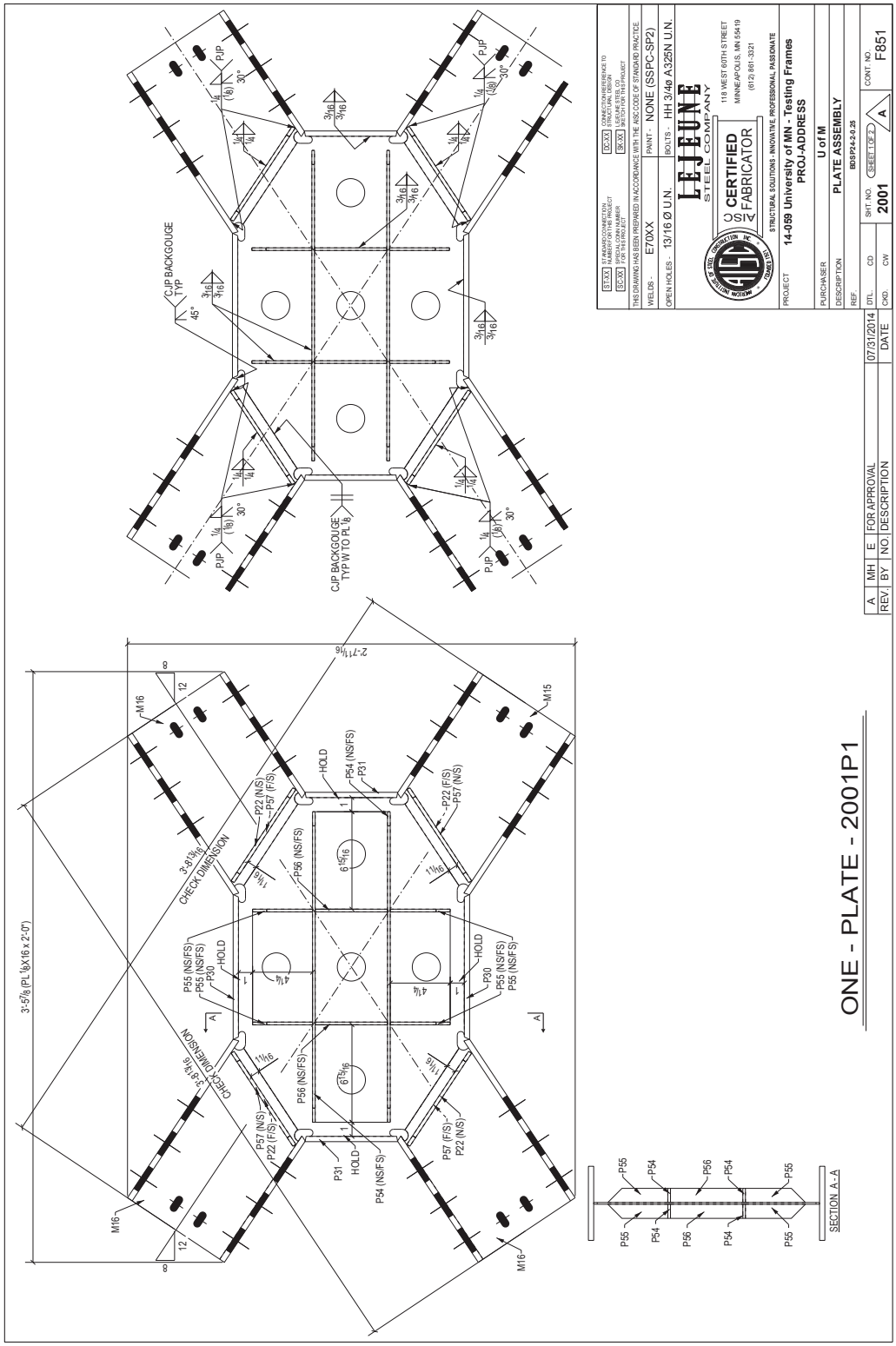

Figure A-31: Shop Drawings – Specimen BDSP24-2-25 (2/2)

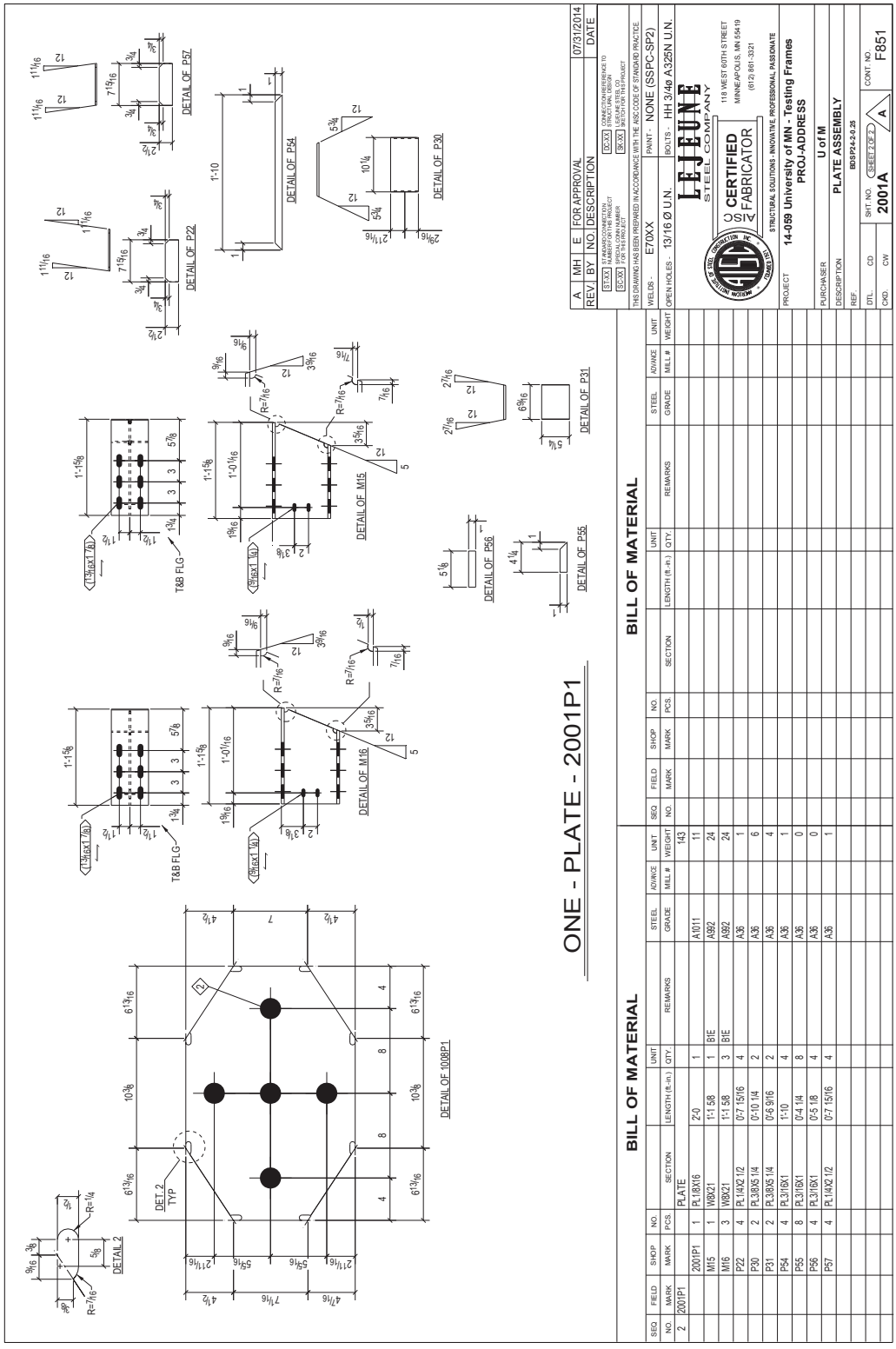

Figure A-32: Shop Drawings – Specimen BDSP20-2-00 (1/2)

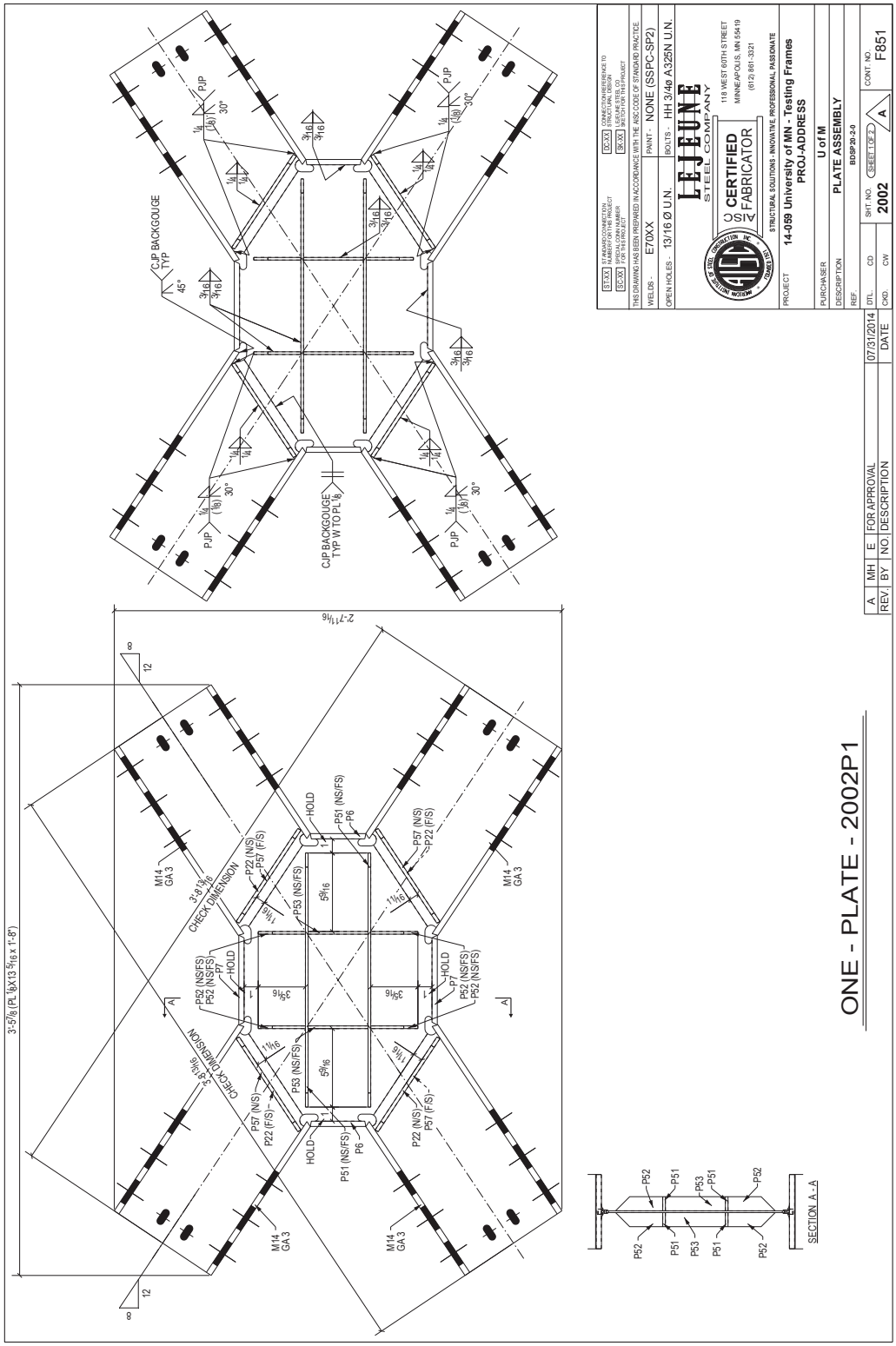

Figure A-33: Shop Drawings – Specimen BDSP20-2-00 (2/2)

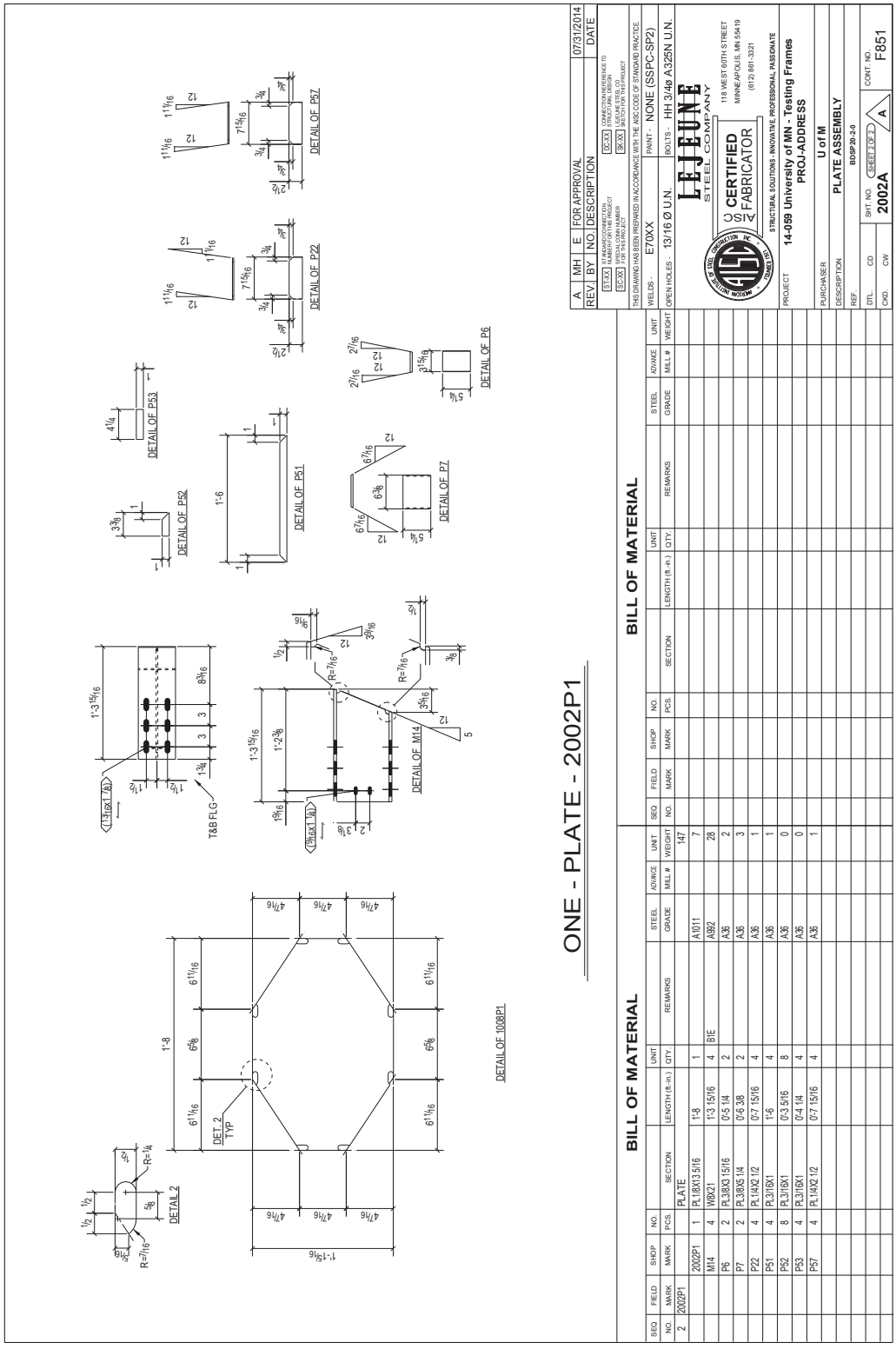

Figure A-34: Shop Drawings – Specimen BDSP24-3-40 (1/2)

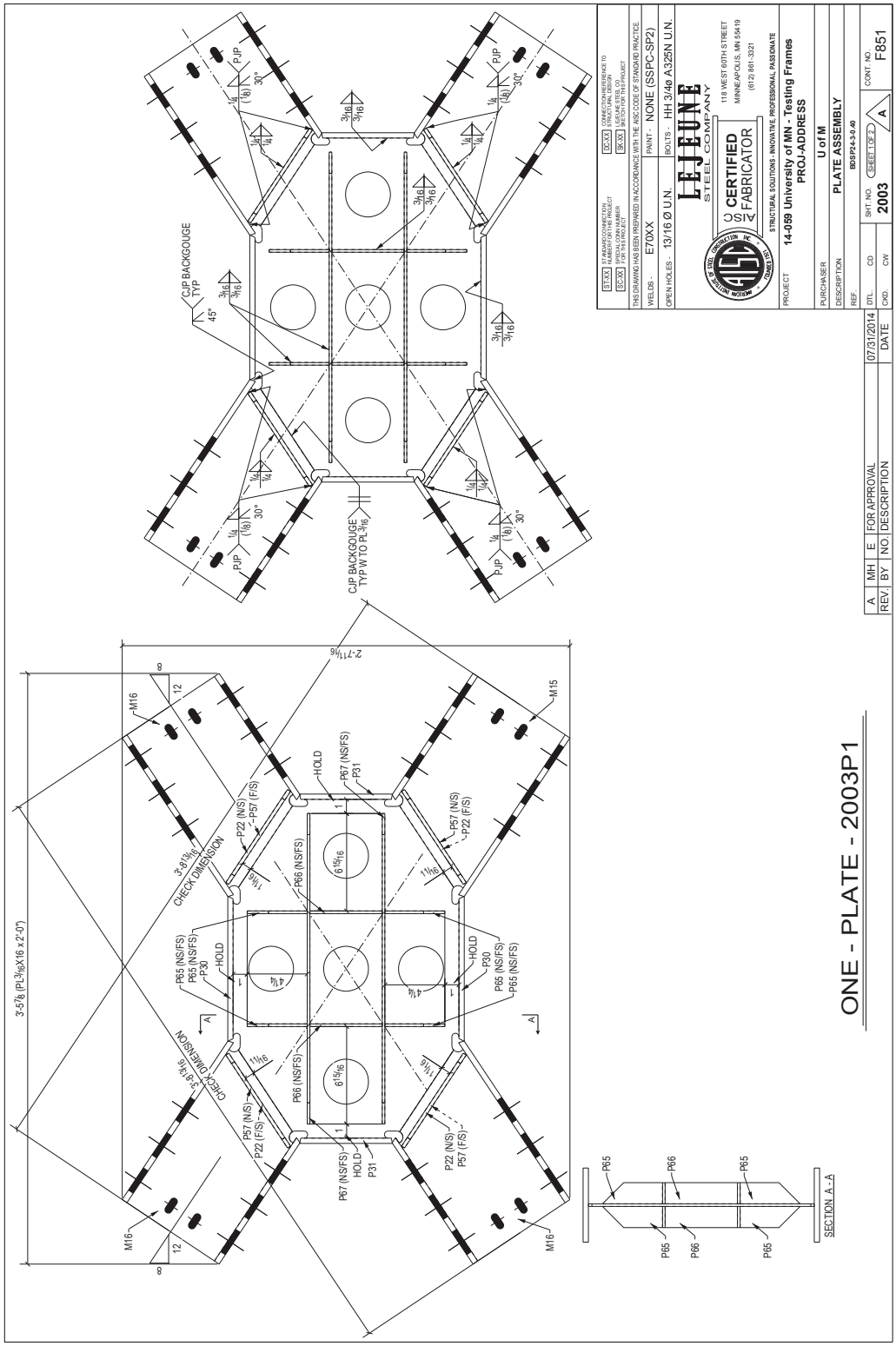

Figure A-35: Shop Drawings – Specimen BDSP24-3-40 (2/2)

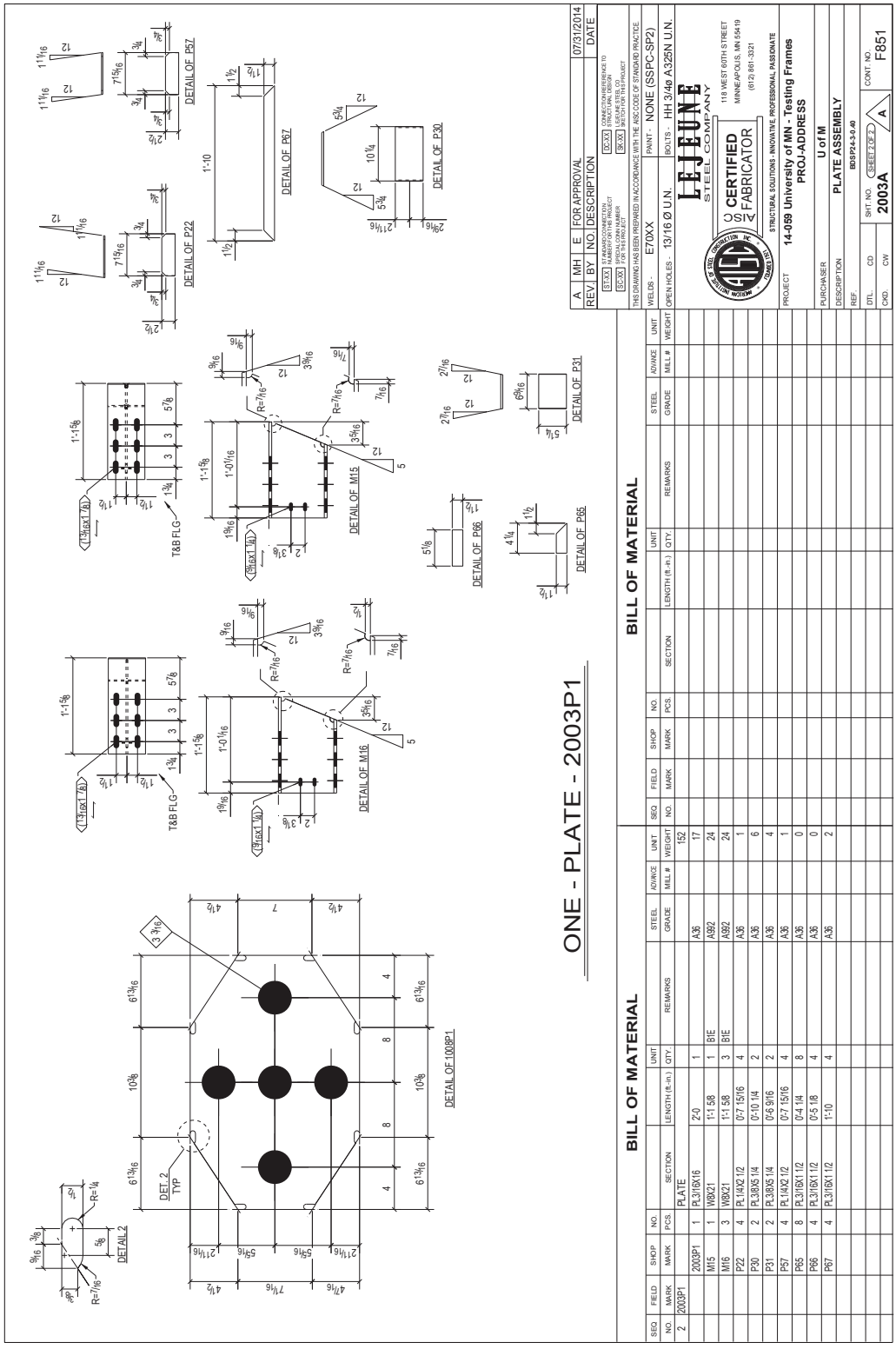

Figure A-36: Shop Drawings – Specimen BDSP20-3-25 (1/2)

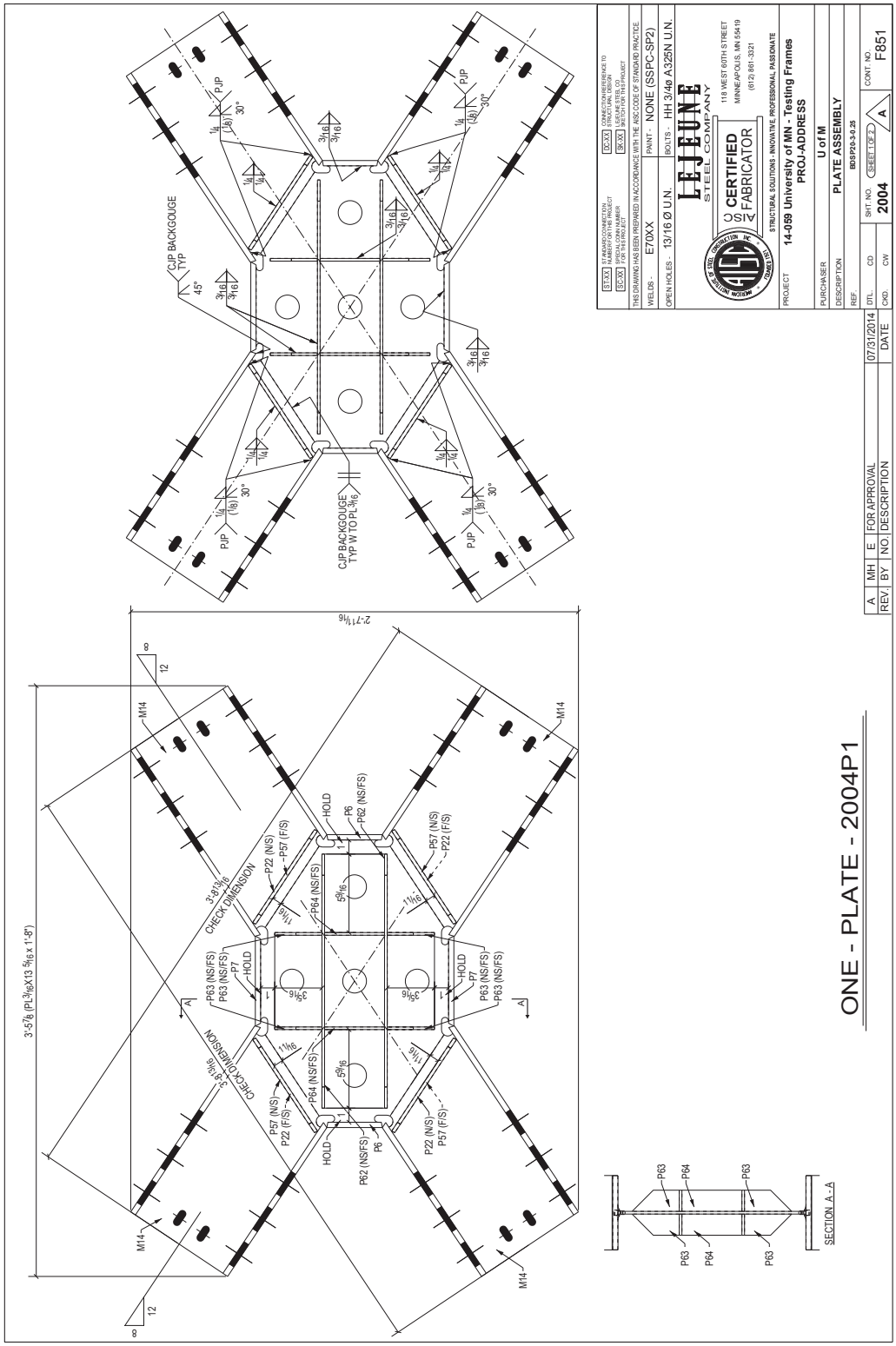

Figure A-37: Shop Drawings – Specimen BDSP20-3-25 (2/2)

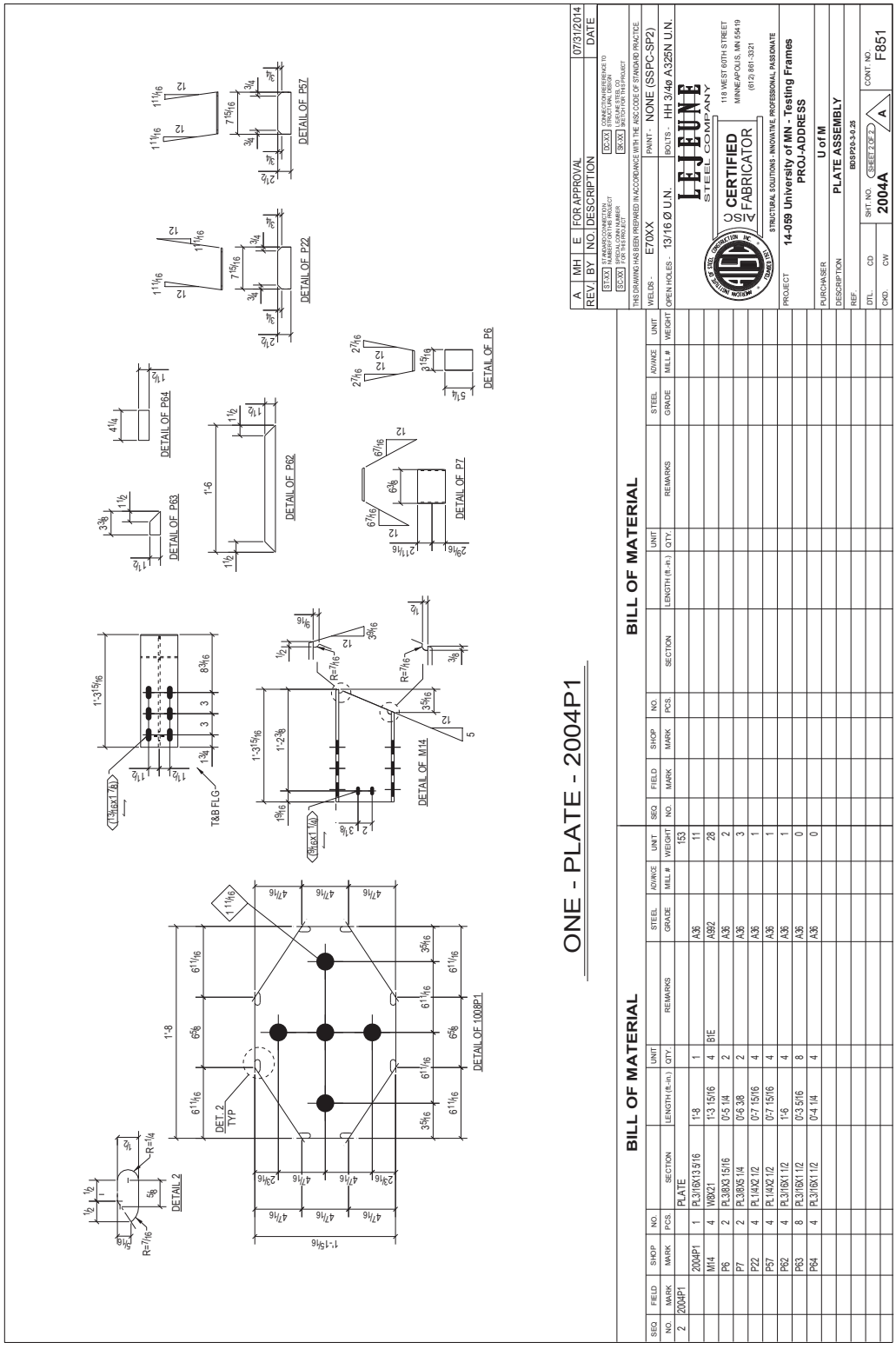

Figure A-38: Shop Drawings – Specimen BDSP20-4-40 (1/2)

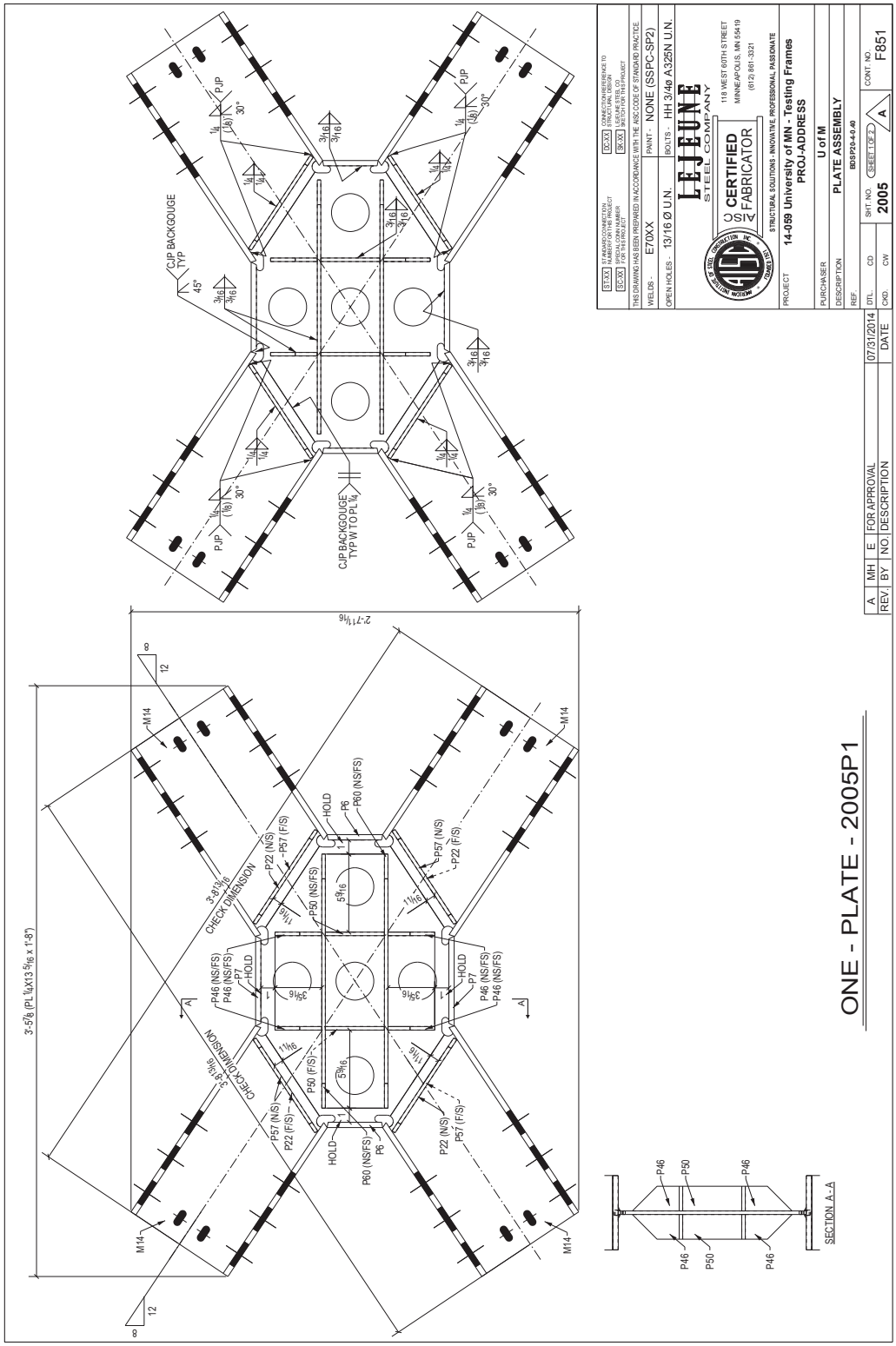

Figure A-39: Shop Drawings – Specimen BDSP20-4-40 (2/2)

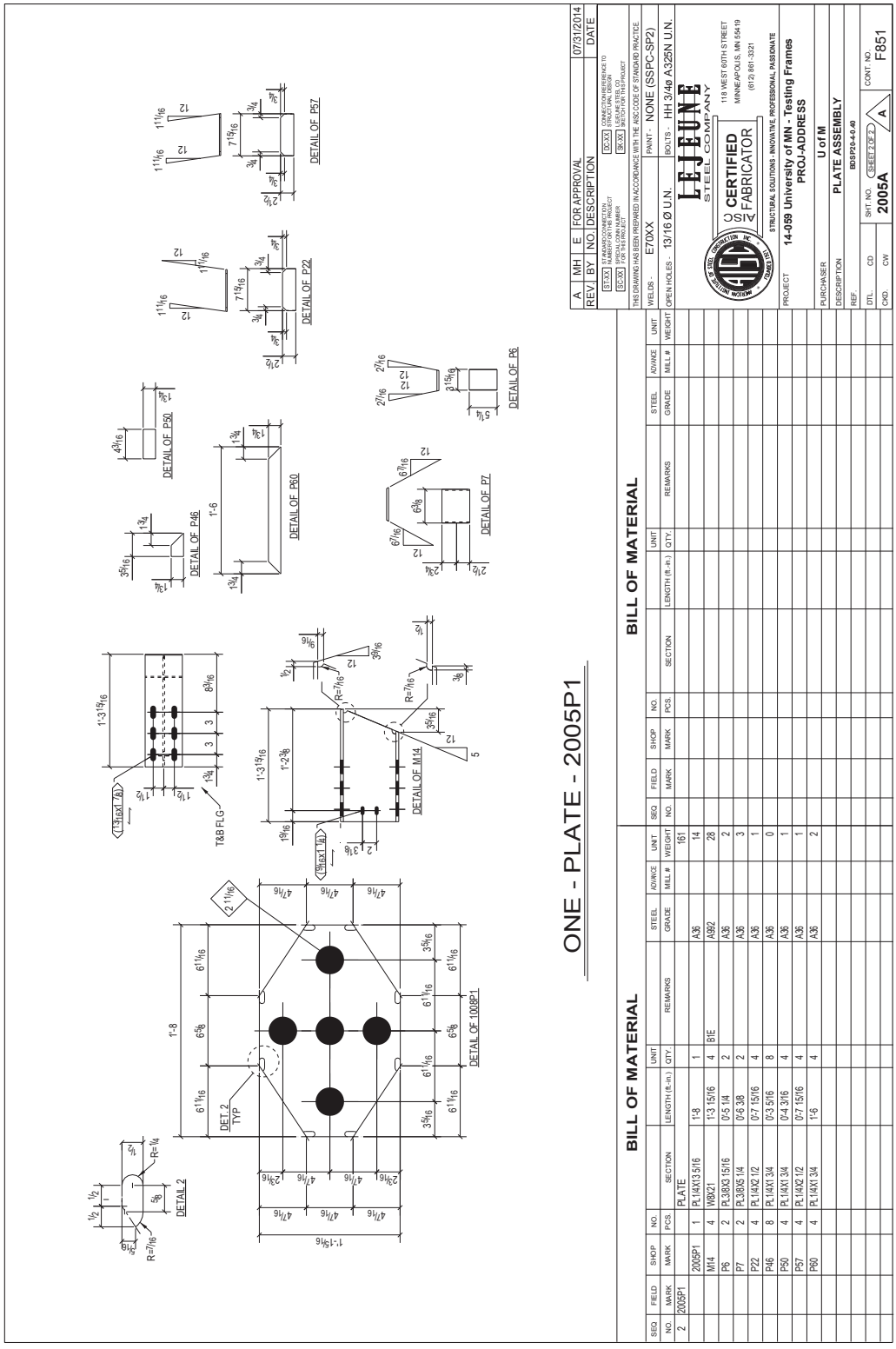

Figure A-40: Shop Drawings – Specimen BDSP24-2-00 (1/2)

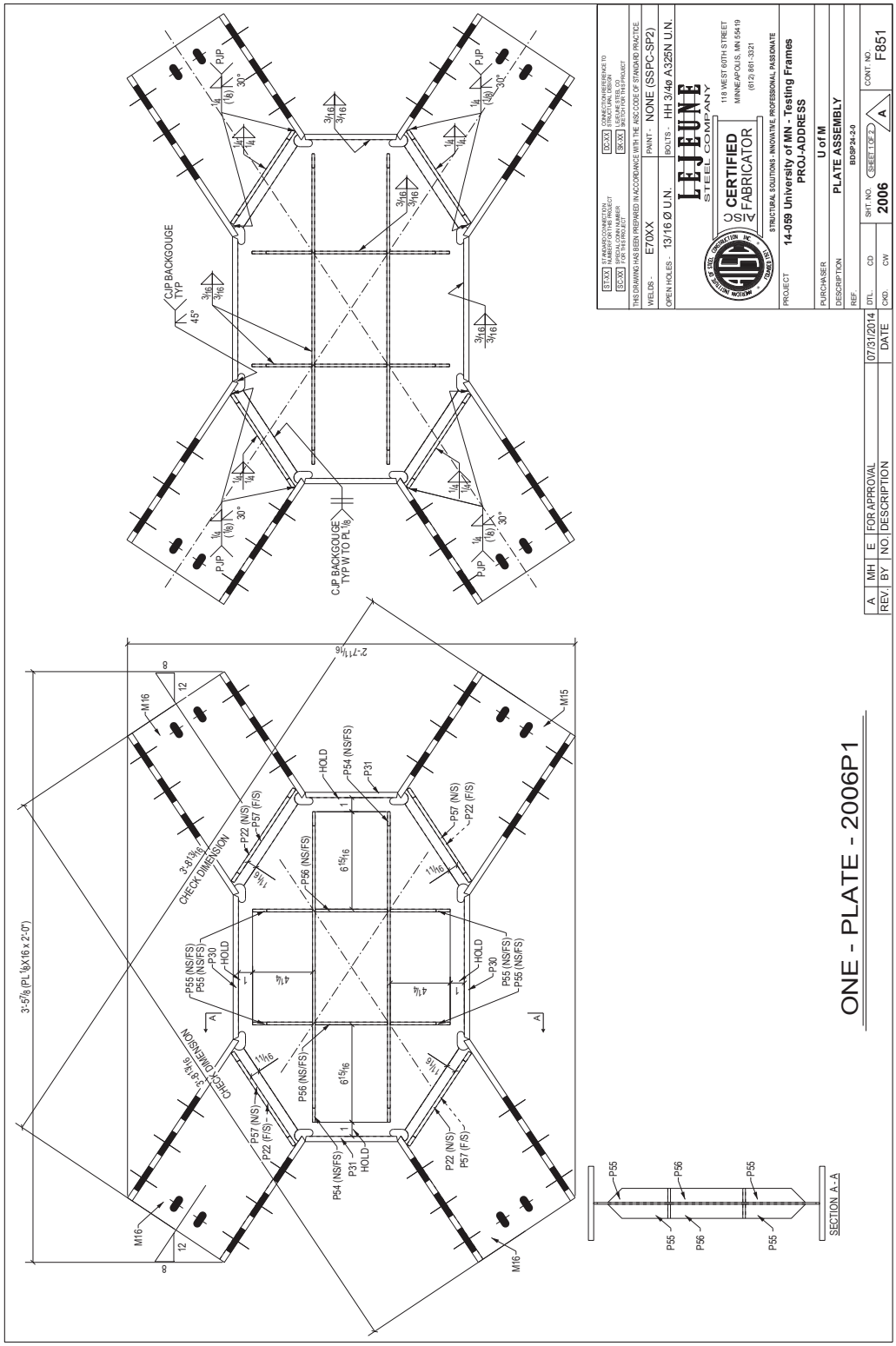

Figure A-41: Shop Drawings – Specimen BDSP24-2-00 (2/2)

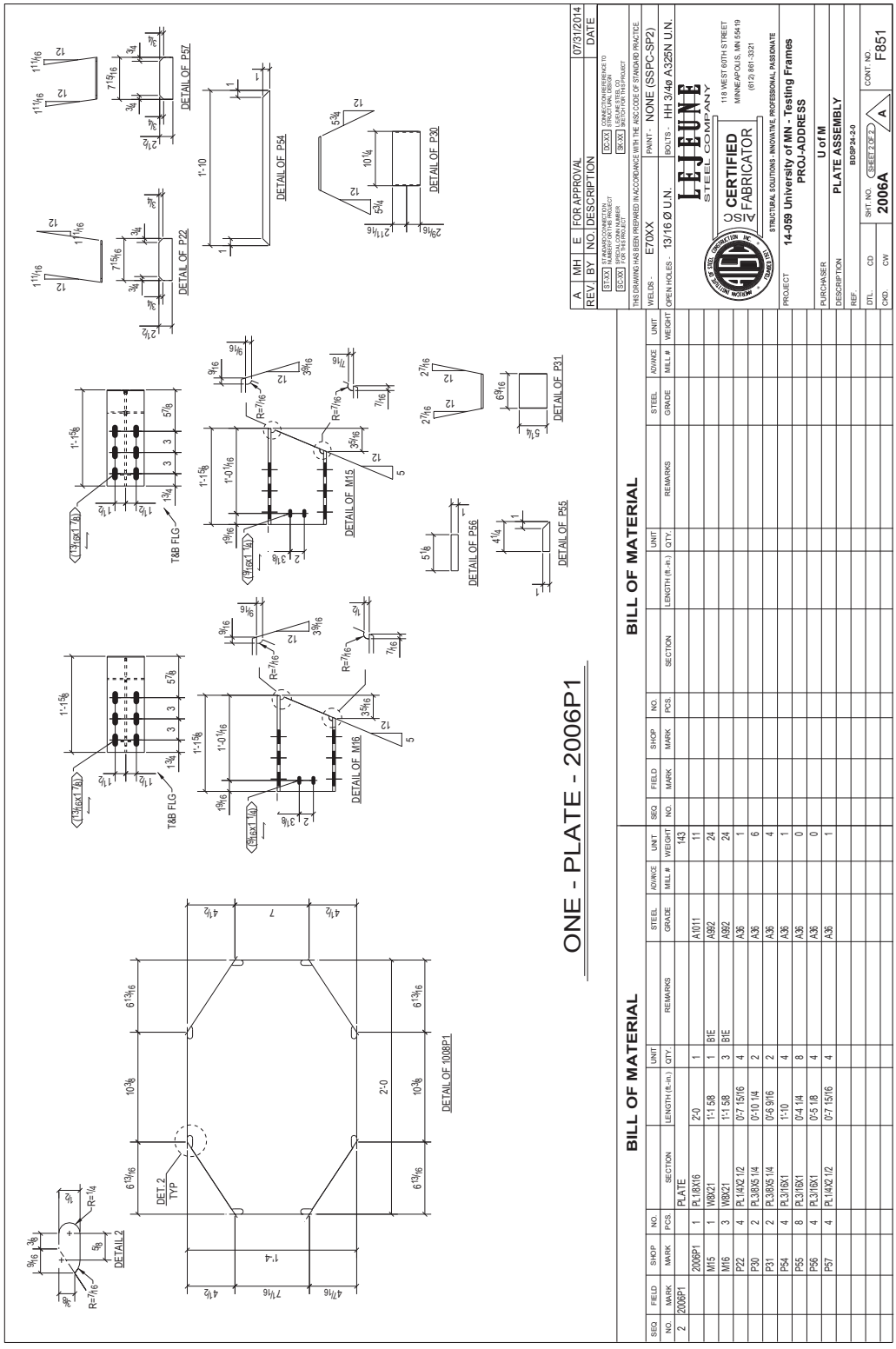

Appendix B
Data Reduction

Raw data was collected by the Data Acquisition system at intervals of 1 second. Data was stored in one file for each day of testing. The following procedures were carried out in processing the raw data:

1. Joining data files for the same test into one single file;
2. Removing pauses in the test for observations;
3. Removing clear sensor malfunctions such as spikes or sudden shifts in measured quantity;
4. Correction of strain gauges measurement creep when tests were paused overnight.

The following section details how all the other quantities, not directly measured, were obtained from the observed measurements.

B.1 Columns

B.1.1 Column axial force

The axial force in the column was calculated at two locations by averaging the value of the two strain gauges, and multiplying it by the modulus of elasticity E (29,000 ksi) and the cross-sectional area of the W8X40 member A_c. Strain gauges locations and naming scheme are shown in Figure B-1**Error! Reference source not found.** and Figure B-2.

$$N_{col} = \frac{\epsilon_o + \epsilon_i}{2} \cdot E\, A_c \qquad \text{(B-1)}$$

B.1.2 Column bending moment

The bending moment around the strong axis at each location on the column is calculated by multiplying the curvature χ_x by the cross-sectional flexural stiffness. The curvature is estimated as the difference between the two measured strains divided by the section depth d.

$$M_{xc} = -\chi_x E I_{xc} = \frac{\epsilon_o - \epsilon_i}{d_c} \cdot E I_{xc} \quad \text{(B-2)}$$

Where I_{xc} is the moment of inertia about the strong axis x.

B.1.3 Column shear

The shear in the column was assumed to be constant in the column. Therefore, it can be calculated dividing the change in bending moment by the distance between the instruments.

$$V_{xc} = \frac{M_{xc,top} - M_{xc,bot}}{s_{g,c}} \quad \text{(B-3)}$$

Where $s_{g,c}$ is the distance between strain gauges on the column.

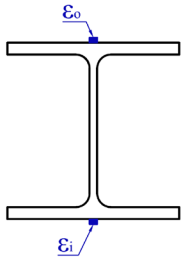

Figure B-1: Columns and beam cross-sectional strain gauges location

Figure B-2: Columns and beam longitudinal strain gauges locations

B.2 Beam

B.2.1 Beam axial force

The axial force in the top beam was calculated at two locations by averaging the value of the two strain gauges and multiplying it by the axial stiffness of the cross-section.

$$N_b = \frac{\epsilon_o + \epsilon_i}{2} \cdot E\ A_b \tag{B-4}$$

Where A_b is the area of the beam section.

B.2.2 Beam bending moment

The bending moment around the strong axis at each location on the beam is calculated following the same approach used for the columns. The curvature is estimated as the difference

between the two measured strains divided by the section depth d_b. The result is given by Equation (B-5):

$$M_{xb} = -\chi_x E I_{xb} = \frac{\epsilon_o - \epsilon_i}{d_b} \cdot E I_{xb} \quad \text{(B-5)}$$

With I_{xb} moment of inertia of the beam around the strong axis.

B.2.3 Beam shear

The strong axis shear in the central portion of the beam (away from the gusset plates) is estimated by assuming constant shear between the strain gauges location. Thus it is calculated as the variation in bending moment divided by the distance between the measuring locations.

$$V_{xb} = \frac{M_{xb,1} - M_{xb,2}}{s_{g,b}} \quad \text{(B-6)}$$

Where $s_{g,b}$ is the distance between the strain gauges.

B.3 Braces

B.3.1 Brace axial force

The strain due to the axial force in the braces is estimated by averaging the measurement of the 4 linear strain gauges installed on the outer surface of the flanges (see Figure 4-14 for gauges type and location). This strain is then multiplied by the cross sectional axial stiffness EA_X where A_X is the area of a W8X21 section. The formula is shown in Equation (B-7):

$$N_i = \frac{\epsilon_{NI} + \epsilon_{NO} + \epsilon_{SO} + \epsilon_{SI}}{4} \cdot E A_X \quad \text{(B-7)}$$

Although brace #3 and #4 were instrumented with additional strain gauge rosettes on web and flanges, for consistency it was decided to only use the strains measured from the four linear strain gauges – common to all the braces – to estimate the axial force. The same logic was used in calculating the bending moments.

B.3.2 Brace bending moments

The strong and weak axis bending moments in the braces were calculated similarly to the columns and beam. However, since two linear strain gauges are installed at each flange of all the braces, the curvature was estimated as the difference between two strains averages divided by the distance between the two groups. The formulas used to calculate the bending moments are shown in Equations (B-8) and (B-9), where d_X is the depth of the braces cross section, $b_{g,X}$ is the distance between two gauges on the same flange (equal to $b_{f,X} - 2 \cdot 0.75in$), and I_{xX} and I_{yX} are the moment of inertia of the braces section around the strong and weak axis respectively. Refer to **Error! Reference source not found.** for the strain gages locations and naming scheme.

$$M_{xi} = -\chi_x \, E \, I_{xX} = \frac{\frac{\epsilon_{NO} + \epsilon_{SO}}{2} - \frac{\epsilon_{NI} + \epsilon_{SI}}{2}}{d_X} \cdot E \, I_{xX} \tag{B-8}$$

$$M_{yi} = -\chi_y \, E \, I_{yX} = \frac{\frac{\epsilon_{NO} + \epsilon_{NI}}{2} - \frac{\epsilon_{SO} + \epsilon_{SI}}{2}}{b_{g,X}} \cdot E \, I_{yX} \tag{B-9}$$

B.3.3 Brace torsional moment

The torsional moment in the brace was estimated by assuming that the bolted slip-critical connections at each end of the brace provide full restraint against warping at their locations. Since the brace is an I-section, which falls into the thin walled sections category, any torsional moment will generate in the section primary torsion (Saint-Venant torsion) and a secondary torsion due to out-of-plane displacements being restrained. However, by taking into account the free length of the brace and its sectional properties (E, G, C_w, J) it can be shown that the contribution of the primary torsion is negligible with respect to the secondary one. Using this model, the torsional moment in braces #3 and #4 was estimated from the shear strains measured on the section flanges using Equation (B-11). The shear strain due to the sole torsion is calculated using Equation (B-10), where

a parabolic distribution of the shear strain over the flanges is used in conjunction with the fact that shear strains caused by secondary torsion flow in opposite directions in the flanges.

$$\gamma_T = \frac{\gamma_{RI} - \gamma_{RO}}{2} \tag{B-10}$$

$$M_{ti} = \frac{2}{3}\tau_T \cdot t_{f,X} \cdot b_{f,X} \cdot d_X = \frac{2}{3}\gamma_T\, G \cdot t_{f,X} \cdot b_{f,X} \cdot d_X \tag{B-11}$$

Where $t_{f,X}$, $b_{f,X}$ and d_X are respectively the flange thickness, flange width and depth of the braces section.

B.3.4 Brace shears

The value of shear forces V_x and V_y is available for the braces instrumented with additional strain rosettes, brace #3 and brace #4. The shear forces were calculated using the shear strains measured by the strain rosettes installed on the webs and flanges of these braces.

The strong axis shear V_x was approximated by assuming that all the shear is resisted by the section web and its projections into the flanges. The distribution of shear stresses inside this area was then evaluated using the Jourawski formula, which results in a quadratic behavior along the section depth. Solving for V_x in the shear formula, and substituting the shear stress with the product of the shear strain by the shear modulus *G* gives Equation (B-13).

$$\overline{\gamma_w} = \frac{\gamma_{RS} + \gamma_{RN}}{2} \tag{B-12}$$

$$V_{xi} = \frac{\tau \cdot t_w \cdot I_x}{S'_x} = \frac{\overline{\gamma_w} \cdot G \cdot t_w \cdot I_x}{S'_x} \tag{B-13}$$

$$S'_x = \frac{d}{2} \cdot t_w \cdot \frac{d}{4} \tag{B-14}$$

Where t_w is the web thickness, S'_x is the first moment of area of the resisting section evaluated at the web center, I_x is the moment of inertia of the considered area, and $\overline{\gamma_w}$ is the average shear strain in the web at the same point.

The weak axis shear is calculated similarly to the strong axis. In this case the flanges of the W8X21 section are assumed to be resisting the whole shear. The shear strain used to compute the stress is the average value of the two shear strains measured in the center of the flanges.

$$\overline{\gamma_f} = \frac{\gamma_{RI} + \gamma_{RO}}{2} \tag{B-15}$$

$$V_{yi} = \frac{\tau \cdot 2t_f \cdot I_y}{S'_y} = \frac{\overline{\gamma_f} \cdot G \cdot 2t_f \cdot I_y}{S'_y} \tag{B-16}$$

$$S'_y = \frac{b_f}{2} \cdot 2t_f \cdot \frac{b_f}{4} \tag{B-17}$$

Where t_f is the flange thickness, S'_y is the first moment of area of the two flanges around the weak axis (evaluated at mid flange), I_y is the moment of inertia of the flanges, and $\overline{\gamma_f}$ is the average shear strain.

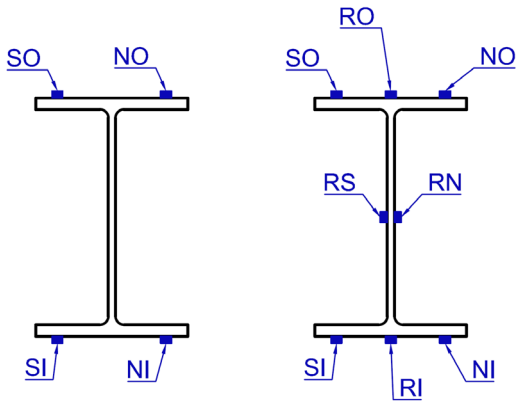

Figure B-3: Braces strain gauges cross-section locations: braces #1-2; braces #3-4

B.4 Average Panel Shear

The average panel shear was calculated using the information from the three LVDTs installed on each specimen. For all the tests, the measurement from the horizontal sensor (LVDT_2) was small enough that it was neglected, thus it was assumed that the distance between the two points stayed constant. Therefore, the average shear angle of the rectangular panel, under the assumption

of small elongations of the diagonals, can be calculated using the measurements from the diagonal LVDTs as:

$$\gamma_{avg} = \frac{1}{2}\frac{\sqrt{a^2 + b^2}}{a \cdot b}(LVDT_3 - LVDT_1) \tag{B-18}$$

Appendix C
Calculations

C.1. Input data

C.1.1 Steel properties

Young Modulus: $E_s = 29000 ksi$

Poisson's ratio: $\nu = 0.30$

Shear modulus: $G_s = \frac{E_s}{2(1+\nu)} = 11154\, ksi$

	Yield stress		*Ultimate stress*	
ASTM Grade A36:	$F_{y1} = 35 ksi$	;	$F_{u1} = 65 ksi$	(conservative value)
BDSP shear stress:	$\tau_y = \frac{F_{y1}}{\sqrt{3}} = 20.2\, ksi$	;	$\tau_u = \frac{F_{u1}}{\sqrt{3}} = 37.5\, ksi$	
ASTM Grade A992:	$F_{y2} = 50 ksi$	;	$F_{u2} = 65 ksi$	

C.1.2 Dimensions

Braced frame

Bay width: $L = 120 in$

Story height: $h = 80 in$

Column pedestal: $h_p = 11\frac{7}{8} in$

Bracing angle: $\alpha = atan\left(\frac{h}{L}\right) = 0.59$

Braces length: $L_X = 24 in$

BDSP

Panel width: $b = 24 in$

Panel web thickness: $t_w = \frac{1}{8} in$

Panel height: $a = b \cdot \frac{h}{L} = 16\, in$

transverse stiffeners: $n_s = 2$

C.1.3 Section properties

W8X40 :	***Beams***	***Columns***
Flange width:	$b_{f.B} = 8.07\,in$	$b_{f.C} = 8.07\,in$
Flange thickness:	$t_{f.B} = 0.56\,in$	$t_{f.C} = 0.56\,in$
Depth:	$d_B = 8.25\,in$	$d_C = 8.25\,in$
Web thickness:	$t_{w.B} = 0.36\,in$	$t_{w.C} = 0.36\,in$
Cross-sectional gross area:	$A_{g.B} = 11.7\,in^2$	$A_{g.C} = 11.7\,in^2$
Moment of inertia x-axis:	$I_{x.B} = 146\,in^4$	$I_{x.C} = 146\,in^4$

W8X21:	***Braces***
Flange width:	$b_{f.X} = 5.27\,in$
Flange thickness:	$t_{f.X} = 0.4\,in$
Depth:	$d_X = 8.28\,in$
Web thickness:	$t_{w.X} = 0.25\,in$
Cross-sectional gross area:	$A_{g.X} = 6.16\,in^2$
Moment of inertia x-axis:	$I_{x.X} = 75.3\,in^4$

C.2. Load-displacement response

C.2.1 Shear panel properties

C.2.1.1 Elastic shear buckling of shear panel web

Plate flexural stiffness: $D = \dfrac{E_s \cdot {t_w}^3}{12 \cdot \left(1 - \nu^2\right)} = 0.43\,ft{\cdot}kip$

Width and height of the subpanels: $b_i = \dfrac{b}{n_s + 1} = 8\,in \;;\; a_i = \dfrac{a}{n_s + 1} = 5.33\,in$

Edge constraint factor: $k_s = 5.34 + 4 \cdot \left(\dfrac{a_i}{b_i}\right)^2 = 7.12$

Critical shear stress: $\tau_{cr} = \dfrac{\pi^2 \cdot k_s \cdot D}{{a_i}^2 \cdot t_w} = 102.5\,ksi$

Critical shear load: $V_{cr} = \tau_{cr} \cdot b \cdot t_w = 307.44\,kip$

C.2.1.2 Linear and ultimate parameters

Yielding shear load: $V_{y1} = \tau_y \cdot b \cdot t_w = 60.62\,kip$

Shear panel elastic stiffness: $K_{BDSP} = \frac{G_s \cdot t_w \cdot b}{a} = 2091\,kpi$

Ultimate shear load: $V_{u1} = \tau_u \cdot b \cdot t_w = 112.58\,kip$

Check slenderness of panel: $\boxed{V_{u1} \le V_{cr} = 1}$

C.2.2 Braced frame properties

C.2.2.1 Elastic properties

Frame lateral stiffness: $K_f = \frac{24 \cdot E_s \cdot I_{x.B} \cdot I_{x.C}}{\left(I_{x.B} \cdot h + I_{x.C} \cdot L\right) \cdot h^2} = 79.39\,kpi$

Gusset plate effective length and width: $L_{gus} = 15in$ $b_{gus} = 10in$

Gusset plate thickness: $t_G = 0.38\,in$

Braces and gusset plates stiffness:

$$K_{br} = \frac{1}{2}\cos(\alpha)^2 \cdot E_s \left(\frac{L_X}{A_{g.X}} + \frac{L_{gus}}{b_{gus} \cdot t_G}\right)^{-1} = 1271\,kpi$$

C.2.3 Global response parameters

Total stiffness of braces and panel: $\boxed{K_{tot} = \left(\frac{1}{K_{BDSP}} + \frac{1}{K_{br}}\right)^{-1} = 791\,kpi}$

Drift at panel yielding: $\boxed{\delta_y = \frac{V_{y1}}{K_{tot}} = 0.077\,in}$

Story drift-index at yielding: $\theta_y = \frac{\delta_y}{h} = 0.096 \cdot \%$

Maximum design drift: $\delta_u = 10 \cdot \delta_y = 0.77\,in$

Shear in the frame at yielding: $V_{y2} = K_f \cdot \delta_y = 6.09\,kip$

Shear in the frame at ultimate: $V_{u2} = K_f \cdot \delta_u = 60.87\,kip$

Total lateral force at yielding: $V_y = V_{y1} + V_{y2} = 66.71\,kip$

Total lateral force at ultimate: $V_u = V_{u1} + V_{u2} = 173.45\,kip$

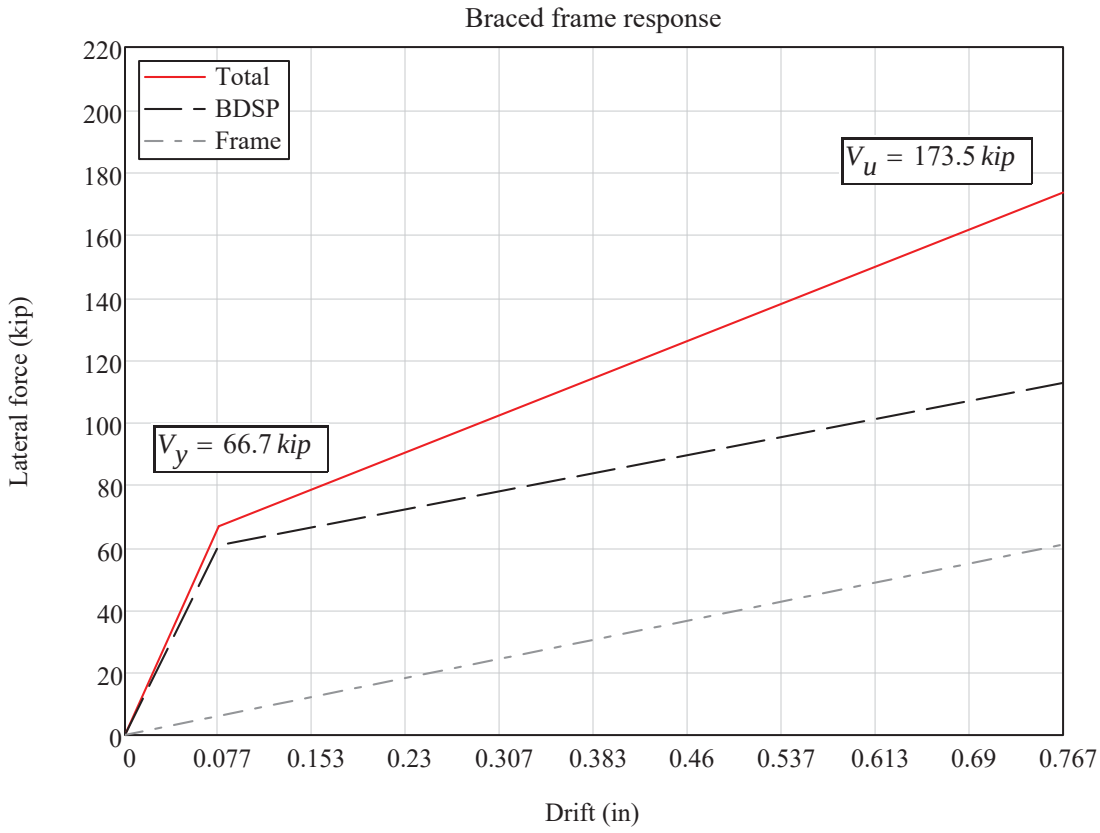

C.3. Member loads

In the following section the demands for the members in the frame are evaluated for two situations.

The first set of demands are calculated under the assumption of a symmetric response of the compression and tension diagonals.

The second group of demands are estimated for the asymmetric or damaged state, where the compression diagonal has lost some its stiffness and the tension members carry most of the load. This last state can be characterized by a factor κ, which is defined as the ratio between the axial force in the tension and compression braces. A value of 1.5 is used here, and it was calibrated from data obtained by finite element simulations.

C.3.1 Members demands in symmetric response

Braces

Axial force: $N_{u.X} = \frac{V_{u1}}{2\,cos(\alpha)} = 67.7\,kip$

Moment: $M_{xu.X} = 0$

Shear: $V_{u.X} = 0$

Beams

Axial force: $N_{u.B} = V_u - \frac{V_{u2}}{2} = 143.0\,kip$

Moment: $M_{u.B} = \frac{V_{u2}\cdot h}{4} = 101\cdot kip\cdot ft$

Shear: $V_{u.B} = \frac{2M_{u.B}}{L} + N_{u.X}\cdot sin(\alpha) = 57.8\,kip$

Columns

Axial force: $N_{u.C} = V_{u.B} = 57.8\,kip$

Moment: $M_{u.C} = \frac{V_{u2}\cdot h}{4} = 101\,ft\cdot kip$

Shear: $V_{u.C} = \frac{2M_{u.C}}{h} = 30.4\,kip$

C.3.2 Members demands in damaged response

Assume a factor $\kappa = 1.5$. These demands will be used later for design of the frame, therefore we want them to be conservative. For this reason the bending moment and shear in the braces, that would otherwise be zero for the model being used, are replaced with estimates obtained from the numerical simulations.

Braces

Axial force: $N_{up.X} = \frac{V_{u1}}{cos(\alpha)} \cdot \frac{\kappa}{\kappa + 1} = 81.2\, kip$

Moment: $M_{xup.X} = 9 kip \cdot ft$

Shear: $V_{up.X} = 4 kip$

Beams

Axial force: $N_{up.B} = V_u - \frac{V_{u2}}{2} = 143.0\, kip$

Moment: $M_{up.B} = \frac{V_{u2} \cdot h}{4} = 101 \cdot kip \cdot ft$

Shear: $V_{up.B} = \frac{2M_{up.B}}{L} + N_{up.X} \cdot sin(\alpha) = 65.3\, kip$

Columns

Axial force: $N_{up.C} = V_{u.B} = 57.8\, kip$

Moment: $M_{up.C} = \frac{V_{u2} \cdot h}{4} = 101\, ft \cdot kip$

Shear: $V_{up.C} = \frac{2M_{u.C}}{h} = 30.4\, kip$

C.4. Members capacity check

The strenght of each member will be checked against the relative loads from the damaged state, calculated in 3.2.
The capacities of the members are calculated following the Specifications (AISC, 2010).

C.4.1 Beams capacity

The beam will be treated as a member in flexure and compression, and will be checked using provisions from Section H1.1 of the Specifications for interaction.

Section properties: $S_{x.B} = 35.5\,in^3$ $Z_{x.B} = 39.8\,in^3$

$r_{ts.B} = 2.31\,in$ $h_{0.B} = 7.69\,in$

$J_B = 1.12\,in^4$ $r_{y.B} = 2.04\,in$

C.4.1.1 Available axial capacity

Effective length factor: $K = 1.0$ (conservative estimate)

Effective length: $KL_b = K \cdot L = 10 \cdot ft$

Check slenderness limit: $\frac{KL_b}{r_{y.B}} = 58.82$

$4.71 \cdot \sqrt{\frac{E_s}{F_{y2}}} = 113.43$ (AISC E3)

Compare slenderness: $\frac{KL_b}{r_{y.B}} < 4.71 \cdot \sqrt{\frac{E_s}{F_{y2}}}$

Elastic buckling stress: $F_e = \frac{\pi^2 \cdot E_s \cdot r_{y.B}^2}{KL_b^2} = 82.7\,ksi$ (AISC E3-4)

Critical stress: $F_{cr} = 0.658^{\frac{F_{y2}}{F_e}} \cdot F_{y2} = 38.8\,ksi$ (AISC E3-2)

Available axial capacity: $\boxed{P_{n.B} = F_{cr} \cdot A_{g.B} = 454.2\,kip}$

C.4.1.2 Available flexural capacity

Plastic limit for unbraced length: $L_p = 1.76 \cdot r_{y.B} \cdot \sqrt{\frac{E_s}{F_{y2}}} = 7.21 \cdot ft$

Inelastic LTB limit:

$$L_r = 1.95 \cdot r_{ts.B} \cdot \frac{E_s}{0.7 \cdot F_{y2}} \cdot \sqrt{\frac{J_B}{S_{x.B} \cdot h_{0.B}} + \sqrt{\left(\frac{J_B}{S_{x.B} \cdot h_{0.B}}\right)^2 + 6.76 \cdot \left(0.7 \cdot \frac{F_{y2}}{E_s}\right)^2}} = 29.9 \cdot ft$$

Member unbraced length $L = 10 \cdot ft$ is between L_p and L_r the section is controlled by inelastic lateral-torsional buckling. Use Equation F2-2 for nominal flexural strength.

Plastic moment: $M_p = Z_{x.B} \cdot F_{y2} = 165.8\, ft \cdot kip$ (AISC F2-1)

Moment gradient factor: $C_b = 3.0$ (reverse curvature)

Inelastic Lateral-Torsional Buckling strength:

$$M_{n.LTB} = C_b \cdot \left[M_p - \left(M_p - 0.7 \cdot F_{y2} \cdot S_{x.B}\right) \cdot \left(\frac{L - L_p}{L_r - L_p}\right) \right] = 474.5\, ft \cdot kip \quad \text{(AISC F2-2)}$$

Available flexural capacity: $\boxed{M_{n.B} = min\left(M_{n.LTB}, M_p\right) = 165.8\, ft \cdot kip}$

C.4.1.3 Interaction formula

Following section H1.1 of the Specifications, use equation H1-1.

Resistance factor for compression: $\phi_c = 0.9$

Design axial strength: $P_c = \phi_c \cdot P_{n.B} = 408.8\, kip$

Resistance factor for flexure: $\phi_b = 0.9$

Design flexural strength: $M_{cx} = \phi_b \cdot M_{n.B} = 149.2\, ft \cdot kip$

Required axial strength: $P_r = N_{up.B} = 143\, kip$

Required flexural strength: $M_{rx} = M_{up.B} = 101.4\, ft \cdot kip$

$\frac{P_r}{P_c} = 0.35$, use Equation H1-1a.

Interaction formula: $\boxed{\frac{P_r}{P_c} + \frac{8}{9} \cdot \left(\frac{M_{rx}}{M_{cx}}\right) = 0.95}$ (AISC H1-1a)

The member has sufficient capacity, since the interaction of flexure and compression is less than the specified limit of 1.0

C.4.2 Columns capacity

The columns will be treated as members in flexure and compression, and will be checked using provisions from Section H1.1 of the Specifications for interaction.

Section properties: $S_{x.C} = 35.5\,in^3$ $Z_{x.C} = 39.8\,in^3$

$r_{ts.C} = 2.31\,in$ $h_{0.C} = 7.69\,in$

$J_C = 1.12\,in^4$ $r_{y.C} = 2.04\,in$

C.4.2.1 Available axial capacity

Effective length factor: $K = 1.0$ (conservative estimate)

Effective length: $KL_c = K \cdot h = 6.67 \cdot ft$

Check slenderness limit: $\frac{KL_c}{r_{y.C}} = 39.22$

$4.71 \cdot \sqrt{\frac{E_s}{F_{y2}}} = 113.43$ (AISC E3)

Compare slenderness: $\frac{KL_c}{r_{y.C}} < 4.71 \cdot \sqrt{\frac{E_s}{F_{y2}}}$

Elastic buckling stress: $F_e = \frac{\pi^2 \cdot E_s \cdot r_{y.C}^2}{KL_c^2} = 186.1\,ksi$ (AISC E3-4)

Critical stress: $F_{cr} = 0.658^{\frac{F_{y2}}{F_e}} \cdot F_{y2} = 44.7\,ksi$ (AISC E3-2)

Available axial capacity: $\boxed{P_{n.C} = F_{cr} \cdot A_{g.C} = 522.8\,kip}$

C.4.2.2 Available flexural capacity

Plastic limit for unbraced length: $L_p = 1.76 \cdot r_{y.C} \cdot \sqrt{\frac{E_s}{F_{y2}}} = 7.21 \cdot ft$

Member unbraced length $h = 6.67 \cdot ft$ is less than L_p, the section is not controlled by LTB. Use Equation F2-1 for nominal flexural strength.

Plastic moment: $M_p = Z_{x.C} \cdot F_{y2} = 165.8\,ft \cdot kip$ (AISC F2-1)

Available flexural capacity: $\boxed{M_{n.C} = M_p = 165.8\,ft \cdot kip}$

C.4.2.3 Interaction formula

Following section H1.1 of the Specifications, use equation H1-1.

Resistance factor for compression: $\phi_c = 0.9$

Design axial strength: $P_c = \phi_c \cdot P_{n.C} = 470.5\,kip$

Resistance factor for flexure: $\phi_b = 0.9$

Design flexural strength: $M_{cx} = \phi_b \cdot M_{n.C} = 149.2\,ft \cdot kip$

Required axial strength: $P_r = N_{up.C} = 57.8\,kip$

Required flexural strength: $M_{rx} = M_{up.C} = 101.4\,ft \cdot kip$

$\frac{P_r}{P_c} = 0.12$, less than 0.2 use Equation H1-1b.

Interaction formula: $\boxed{\frac{P_r}{2P_c} + \frac{8}{9} \cdot \left(\frac{M_{rx}}{M_{cx}}\right) = 0.67}$ (AISC H1-1b)

The member has sufficient capacity, since the interaction of flexure and compression is less than the specified limit of 1.0

C.4.3 Braces capacity

The braces will be treated as members in flexure and compression, even though they are modeled as trusses in the simplified model, to account for the possible bending moment generated by large inelastic drifts. Therefore they will be checked using provisions from Section H1.1.

Section properties: $S_{x.X} = 18.2\,in^3$ $Z_{x.X} = 20.4\,in^3$

$r_{y.X} = 1.26\,in$

C.4.3.1 Available axial capacity

Effective length factor: $K = 2.0$ (conservative estimate)

Effective length: $KL_x = K \cdot L_X = 4 \cdot ft$

Check slenderness limit: $\frac{KL_x}{r_{y.X}} = 38.1$

$4.71 \cdot \sqrt{\frac{E_s}{F_{y2}}} = 113.43$ (AISC E3)

Compare slenderness: $\frac{KL_X}{r_{y.X}} < 4.71 \cdot \sqrt{\frac{E_s}{F_{y2}}}$

Elastic buckling stress: $F_e = \frac{\pi^2 \cdot E_s \cdot r_{y.X}^2}{KL_x^2} = 197.2\,ksi$ (AISC E3-4)

Critical stress: $F_{cr} = 0.658^{\frac{F_{y2}}{F_e}} \cdot F_{y2} = 45\,ksi$ (AISC E3-2)

Available axial capacity: $\boxed{P_{n.X} = F_{cr} \cdot A_{g.X} = 277\,kip}$

C.4.3.2 Available flexural capacity

Plastic limit for unbraced length: $L_p = 1.76 \cdot r_{y.X} \cdot \sqrt{\frac{E_s}{F_{y2}}} = 4.45 \cdot ft$

Member unbraced length $L_X = 2 \cdot ft$ is less than L_p, the section is not controlled by LTB. Use Equation F2-1 for nominal flexural strength.

Plastic moment: $M_p = Z_{x.X} \cdot F_{y2} = 85\,ft \cdot kip$ (AISC F2-1)

Available flexural capacity: $\boxed{M_{n.X} = M_p = 85\,ft \cdot kip}$

C.4.3.3 Interaction formula

Following section H1.1 of the Specifications, use equation H1-1.

Resistance factor for compression: $\phi_c = 0.9$

Design axial strength: $P_c = \phi_c \cdot P_{n.X} = 249.3\,kip$

Resistance factor for flexure: $\phi_b = 0.9$

Design flexural strength: $M_{cx} = \phi_b \cdot M_{n.X} = 76.5\,ft \cdot kip$

Required axial strength: $P_r = N_{up.X} = 81.2\,kip$

Required flexural strength: $M_{rx} = M_{xup.X} = 9\,ft \cdot kip$

$\frac{P_r}{P_c} = 0.33$, greater than 0.2 use Eq.H1-1a.

Interaction formula: $$\boxed{\frac{P_r}{P_c} + \frac{8}{9} \cdot \left(\frac{M_{rx}}{M_{cx}} \right) = 0.43} \qquad \text{(AISC H1-1a)}$$

The member has sufficient capacity, since the interaction of flexure and compression is less than the specified limit of 1.0

C.5. Braces connection to gusset plates

The connection is made using a total of eight L3X3X1/4 with six A325 3/4" bolts per side. The connection is designed not to slip under the maximum expected load. The slip resistance is calculated using Section J3 of the Specifications. The bolted connection is also checked against bearing failure and bolt shear failure in the event that slip occurs.

Bolt diameter: $d_{bolt} = \frac{3}{4} in$

STD and Oversize hole size: $d_{std} = \frac{13}{16} in$ $d_{ov} = \frac{15}{16} in$

Number of bolts: $n_{bolts} = 12$ per flange: $\frac{n_{bolts}}{2} = 6$

Spacing: $s = 2in$

Distance from edge in loading direction: $L_e = 1.25in$

Distance from edge perpendicular to load: $L'_e = 1\frac{3}{8} in$

The design load for each group of four angles is the maximum force expected in the attached flange. It can be calculated as:

$$P_u = \frac{N_{up.X}}{2} + \frac{M_{xup.X}}{d_X - t_{f.X}} = 54.3\, kip$$

C.5.1 Check slip-critical connection strength

Slip resistance from Specifications J3-4. The surfaces of members are left at mill scale and unpainted.

Slip resistance factor: $\phi = 0.85$ (Oversized holes on the gusset plate)

Mean bolt pretension ratio: $D_u = 1.13$

Factor for no fillers: $h_f = 1.0$

Number of shear planes: $n_{sh} = 2$

Slip coefficient: $\mu = 0.3$

Bolt diameter: $d_{bolt} = \frac{3}{4} in$

Minimum bolt pretension: $T_b = 28\, kip$

Slip resistance of one bolt: $R_{ni} = \mu \cdot D_u \cdot h_f \cdot T_b \cdot n_s = 19 \cdot \frac{kip}{bolt}$ (AISC J3-4)

Total resistance: $R_n = \frac{n_{bolts}}{2} \cdot R_{ni} = 113.9\,kip$

Design strength: $\phi R_n = \phi \cdot R_n = 96.82\,kip$

Check capacity: $\boxed{\phi R_n \geq P_u \rightarrow 96.8 \cdot kip \geq 54.3 \cdot kip}$

C.5.2 Check bearing strength and bolt shear strength

C.5.2.1 Bearing strength at bolt holes

The checks are conducted on the gusset plate, since its thickness $t_G = 0.38\,in$ is less than the thickness of two angles leg $2 \cdot t_{Ang} = 0.5\,in$.

For the gusset plate: $F_u = 58ksi$

Clear distance between bolts: $l_{ci} = s - d_{std} = 1.19\,in$

Clear distance of edge bolt: $l_{ce} = L_e - \frac{d_{std}}{2} = 0.84\,in$

Resistance for each field bolt: $R_{ni} = 1.2 \cdot l_{ci} \cdot t_G \cdot F_u = 31\,kip$ (AISC J3-6a)

Resistance for each edge bolt: $R_{ne} = 1.2 \cdot l_{ce} \cdot t_G \cdot F_u = 22.02\,kip$

Resistance for bearing: $R_{n2} = 2.4 \cdot d_{bolt} \cdot t_G \cdot F_u = 39.1\,kip$ (AISC J3-6a)

Resistance of each flange group: $R_n = 2 \cdot R_{ne} + \left(\frac{n_{bolts}}{2} - 2 \right) \cdot R_{ni} = 168\,kip$

Resistance factor: $\phi = 0.75$

Factored strenght: $\phi R_n = \phi \cdot R_n = 126.01\,kip$

Check capacity: $\boxed{\phi R_n \geq P_u \rightarrow 126.0 \cdot kip \geq 54.3 \cdot kip}$

C.5.2.2 Bolt shear strength

Maximum shear stress: $F_{nv} = 54ksi$

Bolt cross-section area: $A_b = 0.44in^2$

Nominal bolt shear strength: $R_n = n_{sh} \cdot F_{nv} \cdot \frac{n_{bolts}}{2} \cdot A_b = 285.12\,kip$

Resistance factor: $\phi = 0.75$

Available strength: $\phi R_n = \phi \cdot R_n = 213.84\,kip$

Check capacity: $\boxed{\phi R_n \geq P_u \rightarrow 214.0 \cdot kip \geq 54.3 \cdot kip}$

C.5.3 Check angles strength

The angles are L3X3X1/4, Grade A36. They are designed for yielding and fracture of the cross-section. No effects from instability are taken into account due to the reduced length of the member.

Section properties

Angle leg width, depth and thickness: $b_{Ang} = 3\,in \quad d_{Ang} = 3\,in \quad t_{Ang} = 0.25\,in$

Area of each angle: $A_{Ang} = 1.44\,in^2$

Yield and ultimate stress: $F_y = 36ksi \quad F_u = 58ksi$

C.5.3.1 Yielding on gross

Resistance factor: $\phi = 0.9$

Gross area of four angles group: $A_g = 4 \cdot A_{Ang} = 5.76\,in^2$

Nominal yield strength: $P_{n.yog} = A_g \cdot F_y = 207.4\,kip$ (AISC J4-1)

Available strength: $\phi P_{n.yog} = \phi \cdot P_{n.yog} = 186.6\,kip$

C.5.3.2 Fracture on net

Resistance factor: $\phi = 0.75$

Net area of four angles group: $A_n = 4 \cdot \left(A_{Ang} - d_{ov} \cdot t_{Ang}\right) = 4.82\,in^2$

Shear lag factor: $U = 0.6$

Effective net area: $A_e = U \cdot A_n = 2.89\,in^2$

Nominal strength: $P_{n.fon} = A_e \cdot F_u = 167.8\,kip$ (AISC J4-2)

Available strength: $\phi P_{n.fon} = \phi \cdot P_{n.fon} = 125.9\,kip$

The strenght of each four angles group is:

$$\boxed{\phi P_n = min\left(\phi P_{n.fon}, \phi P_{n.yog}\right) = 125.9\,kip}$$

Check capacity:

$$\boxed{\phi P_n \geq P_u \rightarrow 126.0 \cdot kip \geq 54.3 \cdot kip}$$

C.5.4 Check dimensions and clearances

Number of bolts per angle leg: $n_{bolts.i} = \frac{n_{bolts}}{4} = 3$

Assuming a separation between the brace end section and the gusset plate edge of $s_{bg} = 0.5in$

Minimum length of angle: $l_{ang} = 2 \cdot \left[2 \cdot L_e + s \cdot \left(n_{bolts.i} - 1\right)\right] + s_{bg} = 13.5\,in$

C.5.4.1 Minimum edge distance on angles

Following Specifications J3.4, check distance from center of hole to edges of connected parts.

$L_{e.min} = 1in$ from Table J3.4 for $d_{bolt} = 0.75\,in$

$L_e = 1.25\,in$ $L_e \geq L_{e.min}$

$L'_e = 1.38\,in$ $L'_e \geq L_{e.min}$

C.5.4.2 Bolt spacing

Following Specifications J3.3, check distance between centers of bolt holes, minimum spacing:

$s_{min} = 2\frac{2}{3} \cdot d_{bolt} = 2\,in$

$s = 2\,in$ $s \geq s_{min} \rightarrow 2 \cdot in \geq 2.0 \cdot in$

C.5.4.3 Clearances for nut and wrench on angles

From Table 7-16 of the Manual, entering and tightening clearance for the bolt size used are:

$C_1 = 1\frac{1}{4}in$ $C_3 = \frac{3}{4}in$

Minimum leg angle width for nut and circular washer to sit on flat:

$d_{min} = L'_e + C_3 + k_{Ang} = 2.75\,in$ where $k_{Ang} = 0.63\,in$

$d_{Ang} \geq d_{min} \rightarrow 3.0 \cdot in \geq 2.75 \cdot in$

Minimum leg angle width for tightening:

$d_{min} = L'_e + C_1 + t_{Ang} = 2.88\,in$ where $t_{Ang} = 0.25\,in$

$d_{Ang} \geq d_{min} \rightarrow 3.0 \cdot in \geq 2.875 \cdot in$

C.5.4.4 Minimum edge distance on braces

The distance from the center of the bolt holes to the brace flange edge in direction perpendicular to loading is dictated by the arrangement of angles and gusset plate thickness.

$$L'_{e.X} = \frac{b_{f.X} - \left(t_G + 2 \cdot d_{Ang} - 2L'_e\right)}{2} = 0.82\,in \quad \text{where} \quad b_{f.X} = 5.27\,in$$

$t_G = 0.38\,in$

$L'_{e.X} < L_{e.min} \rightarrow 0.8225 \cdot in < in$

The resulting edge distance is less than the minimum recommended by the Specifications in J3.3. It is however deemed acceptable by the author, since it is not expected to influence the results and the connection will have enough strength.

C.6 Gusset plate design

Limit states of gusset plate yielding and buckling are considered. For the yielding limit state the Whitmore section is used to determine the effective area that resists that maximum tension force expected in the braces (from the unsymmetric load case). For the limit state of compression buckling, the Thornton Method and the Modified Thornton Method are employed and the strength is compared to the maximum axial compression in the braces (symmetric load case)

C.6.1 Gusset plate yieding

Assume the gusset plate geometry can accomodate the whole Whitmore width.

Design force: $P_u = N_{up.X} = 81.18\,kip$

Initial connection width: $b_0 = d_X + 2 \cdot \left(b_{Ang} - L'_e\right) = 11.53\,in$; $d_X = 8.28\,in$

$b_{Ang} = 3\,in$

$L'_e = 1.38\,in$

Whitmore width: $b_w = b_0 + s \cdot \left(n_{bolts.i} - 1\right) \cdot tan(30deg) = 13.84\,in$

Effective whitmore width: $b_{we} = b_w - 3 \cdot d_{bolt} = 11.59\,in$

Gusset plate thickness: $t_G \equiv \frac{3}{8} in$

Effective area: $A_{we} = b_{we} \cdot t_G = 4.35\,in^2$

Nominal strenght: $R_n = A_{we} \cdot F_{y2} = 217.3\,kip$ $F_{y2} = 50\,ksi$

Available strength in tension:

$\phi = 0.9$ $\boxed{\phi R_n = \phi \cdot R_n = 195.57\,kip}$

$\phi R_n \geq P_u \rightarrow 195.6 \cdot kip \geq 81.18 \cdot kip$

C.6.2 Gusset plate buckling

Design force: $P_u = N_{u.X} = 67.65\,kip$

C.6.2.1 Thornton Method

$L_1 = 1.39\,in$ $L_2 = 13.7\,in$ $L_3 = 10.7\,in$

$b_w = 13.84\,in$

Thornton effective length: $L_t = min\left(L_2, \frac{L_1 + L_2 + L_3}{3}\right) = 8.6\,in$

Slenderness factor: $k = 1.2$
(gusset plate is stiffened on the edge not connected to the column)

Thornton slenderness parameter: $\lambda_t = \frac{k \cdot L_t}{\pi \cdot t_G} \cdot \sqrt{\frac{12 \cdot F_{y2}}{E_s}} = 1.26$

Whitmore area: $A_{we} = 4.35\,in^2$

The critical load according to the Thornton method is:

$$P_{cr} = \begin{cases} \left(0.658^{\lambda_t^2} \cdot A_{we} \cdot F_{y2}\right) & if \ \lambda_t \leq 1.5 \\ \left(\frac{0.877}{\lambda_t^2} \cdot A_{we} \cdot F_{y2}\right) & if \ \lambda_t > 1.5 \end{cases} = 111.87\,kip \quad , \ \lambda_t = 1.26$$

The available strength in compression is then:

$\phi = 0.9$ $\boxed{\phi P_{cr} = \phi \cdot P_{cr} = 100.68\,kip}$

$\phi P_{cr} \geq P_u \rightarrow 100.7 \cdot kip \geq 67.65 \cdot kip$

C.6.2.2 Modified Thornton Method

From gusset plate geometry, the width and length for the Modified Thornton method are:

$b_{mt} = 19.7in$ $L_{mt} = 12.4in$

Slenderness factor: $k = 1.2$
(gusset plate is stiffened on the edge not connected to the column)

Thornton slenderness parameter: $\lambda_{mt} = \frac{k \cdot L_{mt}}{\pi \cdot t_G} \cdot \sqrt{\frac{12 \cdot F_{y2}}{E_s}} = 1.82$

Effective area: $A_{mt} = b_{mt} \cdot t_G = 7.39\,in^2$

The critical load according to the Modified Thornton method is:

$$P_{cr} = \begin{cases} \left(0.658^{\lambda_{mt}^2} \cdot A_{mt} \cdot F_{y2}\right) & if \ \lambda_t \leq 1.5 \\ \left(\frac{0.877}{\lambda_{mt}^2} \cdot A_{mt} \cdot F_{y2}\right) & if \ \lambda_t > 1.5 \end{cases} = 92.79\,kip \quad , \ \lambda_{mt} = 1.82$$

The available strength in compression is then:

$\phi = 0.9$ $\boxed{\phi P_{cr} = \phi \cdot P_{cr} = 83.51\,kip}$

$\phi P_{cr} \geq P_u \rightarrow 83.51 \cdot kip \geq 67.65 \cdot kip$

C.7 Gusset plate-to-beam connection

The forces from the braces are transmitted to the gusset plate and then to the beam by means of longitudinal fillet welds. Since the gusset plate dimensions are controlled by the bolt pattern, use a one pass weld on the whole length of the gusset plate.

In designing the weld, the added capacity provided by the gusset edge stiffener and the welds connecting the stiffener to the beam is conservatively neglected. The eccentricity of the brace axial force, with respect to the weld center of mass, is accounted for by adding the stresses caused by the moment due to the eccentricity to the weld stress demand. With the force translated to the centroid of the weld, section J2.4(a) of the Specifications can be used.

Electrode strenght: $F_{E70} = 70ksi$

Weld nominal size: $D_w = \frac{5}{16}in$

Weld length: $L_w = 20in$

Weld throat area: $A_w = 2L_w \cdot \frac{D_w}{\sqrt{2}} = 8.84\,in^2$

Eccentricity of force: $e_x = \left(\frac{d_C}{2} + 1in + \frac{L_w}{2}\right) \cdot sin(\alpha) - \frac{d_B}{2} \cdot cos(\alpha) = 4.96\,in$

Weld demand forces:

Moment: $M_{uw} = N_{up.X} \cdot e_x = 33.5\,ft \cdot kip$

Longitudinal force: $H_{uw} = N_{up.X} \cdot \cos(\alpha) = 67.5\,kip$

Vertical force: $V_{uw} = N_{up.X} \cdot sin(\alpha) = 45.0\,kip$

Weld stress demands:

Orthogonal stress demand: $f_{wv} = \frac{V_{uw}}{A_w} + \frac{6 \cdot M_{uw}}{L_w \cdot A_w} = 18.76\,ksi$

Parallel stress demand: $f_{wh} = \frac{H_{uw}}{A_w} = 7.64\,ksi$

Magnitude of resultant: $f_{wr} = \sqrt{f_{wv}^{\,2} + f_{wh}^{\,2}} = 20.25\,ksi$

Angle of resultant: $\theta_r = atan\left(\frac{f_{wv}}{f_{wh}}\right) = 67.8 \cdot deg$

Nominal weld strength: $F_{nw} = 0.60 \cdot F_{E70} \cdot \left(1.0 + 0.5 \cdot sin\left(\theta_r\right)^{1.5}\right) = 60.7\, ksi$
(AISC J2-5)

Available weld strength: $\phi = 0.75$

$$\boxed{\phi F_{nw} = \phi \cdot F_{nw} = 45.5\, ksi}$$

Check strength: $\phi F_{nw} \geq 1.40 \cdot f_{wr} \rightarrow 45.5 \cdot ksi \geq 28.4 \cdot ksi$
(the factor of 1.40 is used to account for the uneven distribution of longitudinal stresses)

C.8. Braces-to-BDSP connection

The connection between the braces and the shear panel is realized with steel splice plates on flanges fastened by A490 3/4" bolts. The plates are 1/4" thick, A36 steel plates and 12 bolts for each side. The holes on the shear panel side are long slotted. Therefore the slip strength will be controlled by this end of the connection.
The connection is checked against slip and as a bearing type connection.

The design load is obtained for the unsymmetric (or damaged) load case as:

$$P_u = \frac{N_{up.X}}{2} + \frac{M_{xup.X}}{d_X - t_{f.X}} = 54.3\,kip$$

C.8.1 Slip-critical connection

Slip resistance from Specifications J3-4. The surfaces of members are left at mill scale and unpainted.

Slip resistance factor:	$\phi = 0.60$	(Long-slotted holes)
Mean bolt pretension ratio:	$D_u = 1.13$	
Factor for no fillers:	$h_f = 1.0$	
Number of shear planes:	$n_{sh} = 2$	
Slip coefficient:	$\mu = 0.3$	
Bolt diameter:	$d_{bolt} = \frac{3}{4} in$	
Minimum bolt pretension:	$T_b = 35\,kip$	(ASTM A490 bolts)
Slip resistance of one bolt:	$R_{ni} = \mu \cdot D_u \cdot h_f \cdot T_b \cdot n_s = 23.7 \cdot \frac{kip}{bolt}$	(AISC J3-4)
Total resistance:	$R_n = \frac{n_{bolts}}{2} \cdot R_{ni} = 142.4\,kip$	
Design strength:	$\phi R_n = \phi \cdot R_n = 85.43\,kip$	
Check capacity:	$\boxed{\phi R_n \geq P_u \rightarrow 85.4 \cdot kip \geq 54.3 \cdot kip}$	

C.8.2 Bearing strength of connection

By inspection the connection is deemed verified for bearing. In fact, the bolt pattern is practically equal to the one at the other end of the braces, and the gusset plate, for which all checks were already largely satisfied.

C.8.3 Doubler plates strength

Use 1/4" thick ($t_{dp} = 0.25in$) A36 steel doubler plates ($F_y = 36ksi,\ F_u = 58ksi$). On the outside of the flange one plate with width $b_{dp1} = 7in$ is provided, while on the inner side two 1/4" strips of width $b_{dp2} = 2.5in$ complete the connection.

C.8.3.1 Yielding on gross

Resistance factor: $\phi = 0.9$

Gross area of all the plates: $A_g = \left(b_{dp1} + 2 \cdot b_{dp2}\right) \cdot t_{dp} = 3\,in^2$

Nominal yield strength: $P_{n.yog} = A_g \cdot F_y = 108\,kip$ (AISC J4-1)

Available strength: $\phi P_{n.yog} = \phi \cdot P_{n.yog} = 97.2\,kip$

C.8.3.2 Fracture on net

Resistance factor: $\phi = 0.75$

Net area of four angles group: $A_n = A_g - 4 \cdot d_{bolt} \cdot t_{dp} = 2.25\,in^2$

Effective net area: $A_e = A_n = 2.25\,in^2$ (AISC J4.1)

$A_e < 0.85 \cdot A_g \rightarrow 2.25 \cdot in^2 < 2.55 \cdot in^2$

Nominal strength: $P_{n.fon} = A_e \cdot F_u = 130.5\,kip$ (AISC J4-2)

Available strength: $\phi P_{n.fon} = \phi \cdot P_{n.fon} = 97.9\,kip$

The strenght of each doubler plates group:

$$\boxed{\phi P_n = min\left(\phi P_{n.fon}, \phi P_{n.yog}\right) = 97.2\,kip}$$

Check capacity:

$$\boxed{\phi P_n \geq P_u \rightarrow 97.2 \cdot kip \geq 54.3 \cdot kip}$$

C.8.4 Dimensions fit and clearances

Dimensions and clearances for entering and tightening, as well as checks on fitting of doubler plates in I-sections (web fillet) are verified by inspection on CAD drawings.

C.9. Beam-to-Column connection

The beam-to-column connection is a welded flange welded web (WFWW) connection.

CJP welds are provided at the flanges, therefore their strength will be conrolled by base metal according to the Specifications Table J2.5.

The column is checked for web yielding, web crippling and web compression buckling following Section J10 of the Specifications.

The design loads are the ones from the damage loading case.

Design moment: $M_u = M_{up.B} = 101.45\, ft{\cdot}kip$

Axial force: $P_u = N_{up.B} = 143.02\, kip$

Shear force: $V_u = V_{up.B} = 65.32\, kip$

The concentrated force on the column due to the flanges is calculated by assuming that the flanges resist all the moment (conservative) and a portion of the axial force proportional to their area.

Force in each flange: $$P_{fl} = \frac{M_u}{d_B - t_{f.B}} + P_u \cdot \frac{b_{f.B} \cdot t_{f.B}}{A_{g.B}} = 213.54\, kip$$

where $b_{f.X} = 5.27\, in$, $t_{f.B} = 0.56\, in$, $A_{g.B} = 11.7\, in^2$, $d_B = 8.25\, in$

C.9.1 Concentrated force on the column

C.9.1.1 Flange Local Bending

Following Specifications J10.1 and the column flange thickness $t_{f.C} = 0.56\, in$.

$\phi = 0.90$ $R_n = 6.25 \cdot F_{y2} \cdot t_{f.C}^{\,2} = 98\, kip$

$$\phi R_{n.1} = \phi \cdot R_n = 88.2\, kip$$

$\phi R_{n.1} < P_{fl} \rightarrow 88.2 \cdot kip < 213.5 \cdot kip$

The available strength is less than the demand. Transverse stiffeners are needed for local bending.

C.9.1.2 Web Local Yielding

Following Specifications J10.2 and the column flange thickness $t_{f.C} = 0.56\, in$.

$\phi = 1.00$ $R_n = F_{y2} \cdot t_{w.C} \cdot \left(5 \cdot k_C + t_{f.B}\right) = 95.94\, kip$

$$\boxed{\phi R_{n.2} = \phi \cdot R_n = 95.94\,kip}$$

$$\phi R_{n.2} < P_{fl} \rightarrow 95.94 \cdot kip < 213.5 \cdot kip$$

The available strength is less than the demand. Transverse stiffeners are needed for web yielding.

C.9.1.3 Web Local Crippling

Following Specifications J10.4:

$$\phi = 0.75 \qquad R_n = 0.80 \cdot t_{w.C}^{2} \cdot \left[1 + 3 \cdot \left(\frac{t_{f.B}}{d_C}\right) \cdot \left(\frac{t_{w.C}}{t_{f.C}}\right)^{1.5}\right] \cdot \sqrt{E_s \cdot F_{y2} \cdot \frac{t_{f.C}}{t_{w.C}}} = 172.06\,kip$$

$$\boxed{\phi R_{n.3} = \phi \cdot R_n = 129.04\,kip}$$

$$\phi R_{n.3} < P_{fl} \rightarrow 129.0 \cdot kip < 213.5 \cdot kip$$

The available strength is less than the demand. Transverse stiffeners are needed.

C.9.1.4 Web Compression Buckling

Following Specifications J10.5

$$\phi = 0.90 \qquad R_n = \frac{24 \cdot t_{w.C}^{3} \cdot \sqrt{E_s \cdot F_{y2}}}{h_C} = 212.61\,kip$$

$$\boxed{\phi R_{n.4} = \phi \cdot R_n = 191.35\,kip}$$

$$\phi R_{n.4} < P_{fl} \rightarrow 191.3 \cdot kip < 213.5 \cdot kip$$

The available strength is less than the demand. Transverse stiffeners are needed.

Stiffeners need to be designed for the limit state with the lowest resistance.

$$\boxed{\phi R_n = min\left(\phi R_{n.1}, \phi R_{n.2}, \phi R_{n.3}, \phi R_{n.4}\right) = 88.2\,kip}$$

Flange Local Bending controls.

The required strength for the stiffeners is:

$$\boxed{P_{ts} = P_{fl} - \phi R_n = 125.34\,kip}$$

C.9.1.5 Transverse stiffeners design

Use two A572 steel ($F_y = 50ksi$) transverse stiffeners at each flange, width $b_{ts} = 3.5in$ and thickness $t_{ts} = 0.5in$

The stiffeners satisfy AISC J10.8 dimension requirements:

(1) $b_{ts} + \frac{t_{w.C}}{2} \geq \frac{1}{3} \cdot b_{f.B} \rightarrow 3.68 \cdot in \geq 2.69 \cdot in$

(2) $t_{ts} \geq max\left(\frac{1}{2} t_{f.B}, \frac{b_{ts}}{16}\right) \rightarrow 0.5 \cdot in \geq max(0.28 \cdot in, 0.21875 \cdot in)$

(3) Full depth transverse stiffeners are used

Check for compression, tension will be okay by investigation.

Following AISC J10.8 the effective length can be taken as $KL = 0.75 \cdot h_C = 4.76\,in$ and the cross section shall include the stiffeners as well a strip of the web of width $25 \cdot t_{w.C} = 9\,in$.

Calculate radius of gyration of the cross-section including the stiffeners and the web area:

Moment of inertia weak axis: $I_y = \frac{1}{12} \cdot t_{ts} \cdot \left(b_{ts} + t_{w.C}\right)^3 = 2.4\,in^4$

Area: $A_g = 2 \cdot b_{ts} \cdot t_{ts} + t_{w.C} \cdot \left(25 \cdot t_{w.C}\right) = 6.74\,in^2$

Radius of gyration: $r_y = \sqrt{\frac{I_y}{A_g}} = 0.6\,in$

Slenderness is $KL \cdot r_y^{-1} = 7.98$ and is less than 25, therefore the available strength in compression can be calculated per J4-6:

$\phi = 0.9$ $\quad P_n = F_{y2} \cdot A_g = 337\,kip$

$\boxed{\phi P_n = \phi \cdot P_n = 303.3\,kip}$ $\quad \phi P_n \geq P_{fl} \rightarrow 303.0 \cdot kip \geq 214.0 \cdot kip$

Transverse stiffeners welds

The portion of the demand that goes in the stiffeners and has to be transmitted to the web, is taken equal to:

$$P_i = P_{fl} \cdot \frac{b_{ts} \cdot t_{ts}}{A_g} = 55.4\,kip$$

The maximum length of the fillet weld on the web is limited by the web-flange fillet and k-area, estimated at 0.5" on each side.

Maximum length of fillet weld: $L_{w1} = h_C - 2 \cdot 0.5in = 5.34\,in$

Use weld size: $D_w = \frac{5}{16}in = 0.31\,in$

Nominal strength: $R_n = 0.60 \cdot F_{E70} \cdot \frac{D_w}{\sqrt{2}} \cdot \left(2 \cdot L_{w1}\right) = 99.16\,kip$

Available strength: $\phi = 0.75$ $\boxed{\phi R_n = \phi \cdot R_n = 74.37\,kip}$

$\phi R_n \geq P_i \rightarrow 74.4 \cdot kip \geq 55.4 \cdot kip$

The length of the fillet weld on the flange side of each stiffener is equal to half the flange width minus the fillet length on the flange $k_{1.C} = 0.70in$

Maximum length of fillet weld: $L_{w2} = \frac{b_{f.C}}{2} - k_{1.C} = 3.34\,in$

Weld size: $D_w = \frac{3}{8}in$

Nominal strength: $R_n = 0.60 \cdot F_{E70} \cdot \frac{D_w}{\sqrt{2}} \cdot \left(2 \cdot L_{w2}\right) = 74.28\,kip$

Available strength: $\phi = 0.75$ $\boxed{\phi R_n = \phi \cdot R_n = 55.71\,kip}$

$\phi R_n \geq P_i \rightarrow 55.7 \cdot kip \geq 55.4 \cdot kip$

C.9.2 Web to column weld

The fillet welds on the web are designed to carry a portion of the axial force and all the shear force in the beam section.

Axial force: $N_w = P_u \cdot \frac{t_{w.B} \cdot h_B}{A_{g.B}} = 27.91\,kip$

Shear: $V_w = V_u = 65.32\,kip$

Length of weld: $L_w = h_B = 6.34\,in$

Weld size: $D_w = \frac{5}{16}in$

Resultant of demand: $P_r = \sqrt{N_w^{\,2} + V_w^{\,2}} = 71.03\,kip$

Nominal weld strength: $R_n = 0.60 \cdot F_{E70} \cdot 2 \cdot L_w \cdot \frac{D_w}{\sqrt{2}} = 117.7\,kip$

Available strength: $\phi = 0.75$ $\boxed{\phi R_n = \phi \cdot R_n = 88.29\,kip}$

$\phi R_n \geq P_r \rightarrow 88.3 \cdot kip \geq 71.0 \cdot kip$

C.10. Column foot and base plate

The column extends $h_p = 11.9\,in$ past the lower beam to accomodate the base stiffeners and allow enough clearance for tightening and tensioning of the rods.

The shear demand is equal to half the maximum frame and panel shear combined:

$$V_{base} = \frac{V_{u1} + V_{u2}}{2} = 86.7\,kip$$

The eccentricity between the beam and the base plate creates an additional bending moment at the base of the column:

$$M_{base} = V_{base} \cdot \left(\frac{d_C}{2} + h_p \right) = 115.6\,ft \cdot kip$$

The axial force is equal to:

$$P_{base} = N_{up.C} = 57.82\,kip$$

C.10.1 Column foot shear strength

The foot shear strength is checked against the design shear at the base $V_{base} = 86.73\,kip$ for strength requirements. Following AISC J10.6, doubler plates for shear of the web are provided.

The axial capacity of the foot (compact for compression by inspection) is:

$$P_c = F_{y2} \cdot A_{g.C} = 585\,kip$$

The axial demand is:

$$P_r = P_{base} = 57.82\,kip$$

The nominal shear strength of the foot without doubler plates is:

$$R_n = \begin{cases} 0.60 \cdot F_{y2} \cdot d_C \cdot t_{w.C} & \text{if } P_r \le 0.4 \cdot P_c \\ 0.60 \cdot F_{y2} \cdot d_C \cdot t_{w.C} \cdot \left(1.4 - \frac{P_r}{P_c} \right) & \text{otherwise} \end{cases} = 89.1\,kip$$

where $P_r \le 0.4 P_c \rightarrow 57.8 \cdot kip \le 234.0 \cdot kip$

The available shear strength is:

$$\phi = 0.90 \qquad \boxed{\phi R_n = \phi \cdot R_n = 80.19\,kip}$$

and is less than the shear demand $\phi R_n < V_{base} \rightarrow 80.2 \cdot kip < 86.7 \cdot kip$. Need to provide doubler plates with a minimum shear capacity of:

$$R_{req} = V_{base} - \phi R_n = 6.54\,kip$$

If the plates are made of A572 Gr50 steel, $F_y = 50ksi$ and the required thickness:

$$t_{dp.min} = \frac{R_{req}}{0.90 \cdot 0.60 \cdot F_y \cdot h_C} = 0.04\,in$$

Conservatively provide a $t_{dp} = 0.375in$ doubler plate on each foot, and weld with one-sided full strength fillet welds on all edges (i.e. column flanges, transverse stiffener, base plate).

C.10.2 Anchor rods

The anchor rods are designed to transfer the axial load and bending moment from the column foot to the floor plate. Shear is transferred by the shear key.

Three 1/2" ASTM A193 B7 rods are used on each side, for a total of six rods. The rods are screwed into the matching floor plates threaded holes. The rods are spaced at 5-1/2" on each side and are 14" apart with respect to the column strong axis.

Number of rods per side and total: $n_{rod.i} = 3 \qquad n_{rods} = n_{rod.i} \cdot 2 = 6$

Rods size and grade: $d_{rod} = 1.5in \quad A_{rod} = \frac{\pi \cdot d_{rod}^2}{4} = 1.77\,in^2$

ASTM A193 B7, up to 2-1/2" : $F_u = 125ksi$

Rods spacing: $s_{rod} = 5.5in \qquad L_{rod} = 14in$

Maximum tensile load on each rod: $\boxed{P_{u.rod} = \frac{P_{base}}{n_{rods}} + \frac{1}{n_{rod.i}} \cdot \frac{M_{base}}{L_{rod}} = 42.67\,kip}$

The strength in tension of the rods per Specifications J9 can be calculated using Table J3.2, therefore the nominal tensile strengthis:

Rods nominal tensile stress: $F_{nt} = 0.75 \cdot F_u = 93.75\,ksi$

Rods nominal tensile strength: $R_n = F_{nt} \cdot A_{rod} = 165.67\,kip$ (AISC J3-1)

Rods available tensile strength: $\phi = 0.75$ $\boxed{\phi R_n = \phi \cdot R_n = 124.25\,kip}$

$\phi R_n \geq P_{u.rod} \rightarrow 124.0 \cdot kip \geq 42.7 \cdot kip$

C.10.3 Base plate

The column foot is CJP welded to a 2-1/2" thick A36 steel plate ($t_{bp} = 2.5in$).
The base plate width is $b_{bp} = 16in$, and its length is $L_{bp} = 20in.$

The maximum bending moment in the base plate is obtained by considering the rods as simple supports, and reducing the axial force and bending moment to concentrated forces acting at the flanges.

Force in tension flange at the foot: $P_{u.bp.t} = \frac{P_{base}}{2} + \frac{M_{base}}{d_C} = 197.1\,kip$

Force in comp. flange at the foot: $P_{u.bp.c} = \frac{P_{base}}{2} - \frac{M_{base}}{d_C} = -139.29\,kip$

The bending moment due to this load is calculated for a simply supported beam with span equal to the rods distance $L_{rod} = 14\,in$. The distance between the supports (rods) and the force (flange) is equal to:

Distance rod to flange: $d_{bp} = \frac{L_{rod} - d_C}{2} = 2.88\,in$

Maximum moment due to axial load: $M_1 = \frac{P_{base}}{2} \cdot d_{bp} = 6.93\,ft \cdot kip$

Maximum moment due to moment: $M_2 = \frac{M_{base}}{d_C} \cdot \frac{d_C}{L_{rod}} \cdot d_{bp} = 23.75\,ft \cdot kip$

Design moment: $M_u = M_1 + M_2 = 30.67\,ft \cdot kip$

To avoid or limit damage to the base plate under cyclic loading, design for elastic response. The required thickness for the base plate is then:

Required thickness: $t_{bp.req} = \frac{6M_u}{b_{bp} \cdot F_y} = 2.76\,in^2$

Since base stiffeners will be provided at the base of the column to help in transferring shear force and reduce column rotations, and this design neglected their contribution to the capacity, a reduced base plate thickness, $t_{bp} = 2.5in$, will be provided and expected to work.

C.10.4 Shear key

The shear key is designed to transfer the entire shear force to the floor plates. The contribution to resist shear provided by the base plate friction with the floor plate (rods are pretensioned) is conservatively neglected, since slip due to shear has to be avoided.

The shear key is 14" wide, 2" thick and extends for 2-1/2" into the floor plate. Is made of A36 grade steel and fillet welded on all sides to the base plate with a 1/2" weld.

Dimensions: $b_{sk} = 14in$ $t_{sk} = 2in$ $d_{sk} = 2.5in$ $F_y = 36ksi$

Weld: $D_w = \frac{1}{2}in$ $L_w = \left(b_{sk} + t_{sk}\right)\cdot 2 = 32\,in$ $F_{E60} = 60ksi$

The demands at the base of the shear key, in the base metal and the weld, are:

Shear force: $V_u = V_{base} = 86.73\,kip$

Moment due to bearing forces eccentricity: $M_u = V_u \cdot \frac{d_{sk}}{2} = 9.03\,ft{\cdot}kip$

(assuming a uniform distribution, conservative)

The strength with respect to the limit states of shear yielding and flexural yielding are:

Shear strength: $\phi V_n = 1.00\cdot 0.60\cdot F_y \cdot t_{sk} \cdot b_{sk} = 604.8\,kip$

Nominal yield strength in bending $\phi M_n = 0.9\,\frac{b_{sk}\cdot t_{sk}^{\,2}}{6}\cdot F_y = 25.2\,ft{\cdot}kip$

The shear key has enough capacity for the limit states taken singularly, and by inspection, interaction needs not to be checked.

C.10.4.1 Weld strength

The weld is checked using the provisions of Specifications J2.4(a).
However the checks are conducted with respect to required and available stresses rather than forces.

Assume bending moment is resisted by the welds along the width of the shear key, the depth of the welds cross section is:

$$t' = t_{sk} + D_w = 2.5\,in$$

Stress orthogonal to the weld axis, due to the bending:

$$f_c = \frac{M_u}{b_{sk} \cdot t'} = 3.1\ kpi$$

Stress orthogonal to the weld axis, due to shear:

$$f_v = \frac{V_u}{2 \cdot b_{sk}} = 3.1\ kpi$$

Total stress demand: $f_r = \sqrt{f_v^{\,2} + f_c^{\,2}} = 4.38\ kpi$

Weld nominal strength: $R_n = 0.60 \cdot F_{E60} \cdot 1.5 \frac{D_w}{\sqrt{2}} = 19.09\ kpi$

Weld available strength: $\phi = 0.75$ $\boxed{\phi R_n = \phi \cdot R_n = 14.32\ kpi}$

$\phi R_n \geq f_r \rightarrow 14.3 \cdot kpi \geq 4.38 \cdot kpi$